THE INTERACTIONS OF MUONIUM WITH SILICA SURFACES

by

DALE RICHARD HARSHMAN

B.Sc., Pacific Lutheran University, 1978

M.Sc., Western Washington University, 1980

A THESIS SUBMITTED IN PARTIAL FULFILLMENT OF

THE REQUIREMENTS FOR THE DEGREE OF

DOCTOR OF PHILOSOPHY

in

THE FACULTY OF GRADUATE STUDIES

Department of Physics

We accept this thesis as conforming

to the required standard

THE UNIVERSITY OF BRITISH COLUMBIA

January 1986

In presenting this thesis in partial fulfilment of the requirements for an advanced degree at the University of British Columbia, I agree that the Library shall make it freely available for reference and study. I further agree that permission for extensive copying of this thesis for scholarly purposes may be granted by the head of my department or by his or her representatives. It is understood that copying or publication of this thesis for financial gain shall not be allowed without my written permission.

Department of __Physics__

The University of British Columbia
1956 Main Mall
Vancouver, Canada
V6T 1Y3

Date __17 January 1986__

ABSTRACT

The behavior of muonium on the surface of fine (35 Å mean radius) SiO_2 powders has been studied using the techniques of muon spin rotation (μSR). Results indicate diffusion and trapping behavior of the muonium atoms on the silica surface, which is strongly influenced by the concentration of surface hydroxyl groups. Specifically, the presence of the surface hydroxyl groups has been shown to inhibit the motion of muonium on the silica surface.

These studies have also provided information regarding the origin of the relaxation of the muon spin polarization for muonium on the silica surface. Specifically, a random anisotropic distortion of the muonium hyperfine interaction, induced by the local surface environment of the muonium atom, has been shown to be a principal contributor to the relaxation of the muon ensemble spin polarization, whereas the random local magnetic fields due to the neighboring hydroxyl protons were found to play only a minor role. From this result, the observed strong dependence of the relaxation on the surface hydroxyl concentration has been attributed to an associated hyperfine distortion, induced by the neighboring hydroxyls. A new spin relaxation theory, for the case of random anisotropic hyperfine distortions, has also been developed to explain the data.

Gas adsorption isotherm studies were also performed, with [4]He at 6 K, which show the muonium asymmetry to be strongly influenced by the fractional surface coverage. These results clearly indicate that the muonium formation probability decreases with increasing surface coverage, suggesting that the charge exchange cross section at the silica surface is significant. The implication of these results with regard to the origins of muonium formation

(i.e., surface or bulk formation) is as yet unclear, however, since the precise role played by the adsorbed helium atoms is not known.

These investigations have also been extended to platinum loaded silica, where the first surface reaction of muonium has been observed; the reaction rate of muonium with the surface of oxygen-covered platinum microcrystals was found to be 3.5 ± 0.15 μs^{-1}.

TABLE OF CONTENTS

LIST OF TABLES

LIST OF FIGURES

CHAPTER IV.
EXPERIMENTAL RESULTS AND INTERPRETATIONS

APPENDIX II.
ULTRA-LOW ENERGY MUON PRODUCTION (μSOL)

ACKNOWLEDGEMENTS

CHAPTER I — INTRODUCTION

The work presented in this dissertation concerns the interactions of positive muons (μ^+) and muonium atoms (μ^+e^-, Mu) with the surfaces of finely divided silica powders (35 Å mean radius). This research represents the first detailed investigation of the diffusion and trapping behavior, and the relaxation mechanisms, for muonium on surfaces.

Positive muons and muonium atoms have proven to be ideal microscopic probes of magnetic systems as well as isotopic probes of proton/hydrogen diffusion mechanisms and chemical reactions [1-3]. The motivation for the present work arises because of these features, and the desire to extend the studies of muons and muonium to interactions with a surface environment. This work develops a basic qualitative understanding of the behavior of muonium on surfaces and could conceivably lead to the study of surface magnetism and the extensive use of muonium as an isotopic probe of hydrogen catalysis. Experimental methods such as NMR, ESR, LEED, etc., which are widely used in the study of adatom adsorption, generally require a fairly high density of atoms, which has obvious ramifications with regard to the statistical mechanics of adsorption. In contrast, the μSR (muon spin rotation) techniques [1-3] employed in the present work require observation of one muon (or Mu atom) at a time. This feature of the experimental method allows no possibility for any study of μ^+-μ^+, μ^+-Mu or Mu-Mu interactions; indeed, at presently achievable stopped muon densities, the mutual encounter of two muons or muonium atoms must be an extremely rare occurrence.

Specifically, the present work has provided information concerning the diffusion and trapping behavior of muonium on the silica surface, as well as

the effect of the local surface environment on the hyperfine interaction of the muonium atom. In the case of the latter, a theory has been developed describing the time evolution of the μ^+ spin polarization in muonium for a generally anisotropic hyperfine interaction, which can adequately explain the muonium relaxation data. The behavior of muonium on the silica surface was also found to exhibit a strong dependence on the concentration of surface hydroxyl groups.

A great deal of interest has been generated concerning the interaction of hydrogen atoms with catalytic surfaces. The silica powder used in the present study is typical of those used as support materials for catalysts. Because muonium can be thought of as a light chemical isotope of hydrogen, it is ideally suited for this type of study. In fact, the present work has provided the first study of muonium on platinum loaded silica surfaces, in which the reaction rate of muonium with the oxygen-coated surfaces of the platinum microcrystals was measured.

This dissertation is organized into five chapters and two appendices. The present chapter, Chapter I, is primarily introductory. It provides background information regarding the properties of muons and muonium, the effect of the local environment on the time evolution of the μ^+ spin polarization for both charge states, a brief synopsis of previous experimental and theoretical μSR studies which are pertinent to the present work and a discussion of relevant hydrogen atom experiments.

In Chapter II, the discussion focuses on the specific experimental techniques employed in the present investigation. Included are descriptions of muon production and transport, the μSR apparatus, electronics and data acquisition, target preparation and the methods of data analysis employed.

Chapter III provides a general theoretical discussion concerning the time evolution of the μ^+ spin polarization for the five known muonium spin "relaxation" mechanisms, and the associated spin relaxation functions. Of particular importance are the relaxation functions, for both zero and applied magnetic field, which arise from a random anisotropic distortion of the muonium hyperfine interaction (see Appendix I). These functions are used in the analysis and interpretation of some of the data.

The experimental results are presented and discussed in Chapter IV. These results indicate diffusion and trapping behavior of muonium on the silica surface and suggest a random anisotropic distortion of the muonium hyperfine interaction as a principal contributor to the depolarization of the μ^+ spin on the silica surface.

Finally, Chapter V provides a brief summary of the subject to date, along with a discussion of possible future directions.

Appendix I contains the detailed derivations of the time evolution of the μ^+ spin polarization in muonium subject to a generally anisotropic hyperfine interaction, along with the associated spin relaxation functions described in Chapter III.

Lastly, Appendix II outlines an experiment which is designed to study the interactions of muons and muonium atoms with "macroscopic" surfaces, and draws heavily on knowledge already gained in the study of positrons (e^+) and positronium (e^+e^-, Ps).

I.A Muons and Muonium

Some of the characteristics of muons and muonium are discussed in the following few pages.

I.A.1 Muon Characteristics

The muon (μ^+, μ^-) was first observed [4,5] as a component of cosmic rays in 1937. Muons are unstable leptons, having a rest mass of about 105.7 MeV/c^2, and apart from their finite lifetime can in nearly every respect be considered heavy electrons (or positrons). Some of the properties of muons are given in Table I.1.

The most common source of muons is from the decay of charged pions (π^+, π^-). Pions (spin = 0) decay via weak interaction in the parity nonconserving processes [6]

$$\pi^+ \rightarrow \mu^+ + \nu_\mu \quad \text{and} \quad \pi^- \rightarrow \mu^- + \bar{\nu}_\mu \qquad (I.1)$$

with a free mean lifetime of 26.030(23) nanoseconds (ns). In the rest frame of the pion, the decay is spatially isotropic with the muon and neutrino being emitted in opposite directions. In the case of π^+ decay the muon and neutrino both have negative helicity (i.e., spin antiparallel to momentum), whereas for π^- decay they are both emitted with positive helicity (i.e., spin parallel to momentum). Since neutrinos possess zero (or near zero) rest mass, the momentum of the emitted muon in the rest frame is 29.8 MeV/c, which translates into a kinetic energy of 4.1 MeV.

Like the pion, the muon also decays via the weak interaction, according to the parity violating reactions [6]

$$\mu^+ \rightarrow e^+ + \nu_e + \bar{\nu}_\mu \quad \text{and} \quad \mu^- \rightarrow e^- + \bar{\nu}_e + \nu_\mu \qquad (I.2)$$

with a free mean lifetime of τ_μ = 2.19695(6) µs [7]. In contrast to pion decay, muon decay is spatially anisotropic in the center of mass frame; the muon provides a preferred direction (its spin orientation) as a reference.

Table I.1 Properties of Muons (μ^+, μ^-)

Property (symbol)		Value
Charge	e	$\mu^+, \mu^- = \pm 1.60225 \times 10^{-19}$ Coulombs
Spin	s	1/2
Rest Mass	m_μ	105.6596 MeV/c^2 $= 206.76859(29) \; m_e$ (a)
		$= \quad 0.7570 \quad m_\pi$
		$= \quad 0.1126123(6) \; m_p$ (a)
Mean Free Lifetime	τ_μ	$2.19695(6)$ µs (b)
g-Factor	g_μ	$-2\left[1.001165895(27)\right]$ (c)
Magnetogyric Ratio	γ_μ	$\dfrac{g_\mu e}{2 \; m_\mu c}$ $\quad = 8.5165 \times 10^4 \; s^{-1} \; G^{-1}$
		$= 2\pi \times 13.5544$ kHz/G
Magnetic Moment	μ_μ	$h \, \lvert s_z \rvert \, \dfrac{\gamma_\mu}{2\pi}$ $\quad = 28.0272(2) \times 10^{-18}$ MeV/G
		$= \quad 0.00484 \; \mu_e$
		$= \quad 3.1833417(39) \; \mu_p$ (a)
Compton Wavelength	λ_c^μ	$\dfrac{h}{m_\mu c}$ $\quad = 1.86758$ fm
de Broglie Wavelength	λ_d^μ	$h\left(2\pi m_\mu kT\right)^{-1/2}$ $\quad = 2.99$ Å (300 K)
		$= 25.29$ Å (4.2 K)

(a) D.E. Casperson, et al., Phys. Rev. Lett. **38**, 956 (1977).

(b) K.L. Giovanetti, et al., Phys. Rev. D **29**, 343 (1984).

(c) J.M. Bailey, et al., Phys. Lett. **55B**, 420 (1975).

The maximum momentum of the decay electron is given by the relation

$$m_\mu c^2 = \left[p_e^2 c^2 + m_e^2 c^4 \right]^{1/2} + p_e c \quad ; \quad p_e^{max} = 52.827 \text{ MeV/c} \qquad (I.3)$$

This maximum occurs when both the neutrino and antineutrino are emitted in the same direction, opposite to that of the decay electron. For this case the spins of the neutrino (negative helicity) and the antineutrino (positive helicity) cancel, leaving the positron(electron) to balance the spin of the $\mu^+(\mu^-)$. In weak interactions, the momentum of the $e^+(e^-)$ tends strongly to be (anti)parallel to its spin, so that the high energy $e^+(e^-)$ tends to exit along(opposite) the $\mu^+(\mu^-)$ spin.

Since the topic of this dissertation concerns only positive muons, the discussions henceforth will be constrained accordingly. By neglecting the mass of the positron in comparison with the mass m_μ of the muon, the probability per unit time $dW(\varepsilon,\theta)$ for the emission of a positron of energy E in the elemental solid angle $d\omega$ at an angle θ with respect to the muon spin direction can be expressed as [6]

$$dW(\varepsilon,\theta) = \frac{1}{2\pi\tau_\mu} \left[\varepsilon^2(3-2\varepsilon) \right]\left[1 + P \frac{1-2\varepsilon}{3-2\varepsilon} \cos(\theta) \right] d\varepsilon d\omega \qquad (I.4)$$

where $\varepsilon = E/E_{max} = 2E/m_\mu c^2$ and P represents the degree of polarization of the μ^+ ensemble. Equation I.4 is written in terms of an isotropic average energy spectrum $C(\varepsilon)=\varepsilon^2(3-2\varepsilon)$ and an asymmetry factor $D(\varepsilon)=P(2\varepsilon-1)/(3-2\varepsilon)$, both of which are shown in Figure I.1 for a muon ensemble polarization of P=1.

I.A.2 Thermalization of Positive Muons in Matter

The slowing down of a μ^+ in matter involves several stages of energy
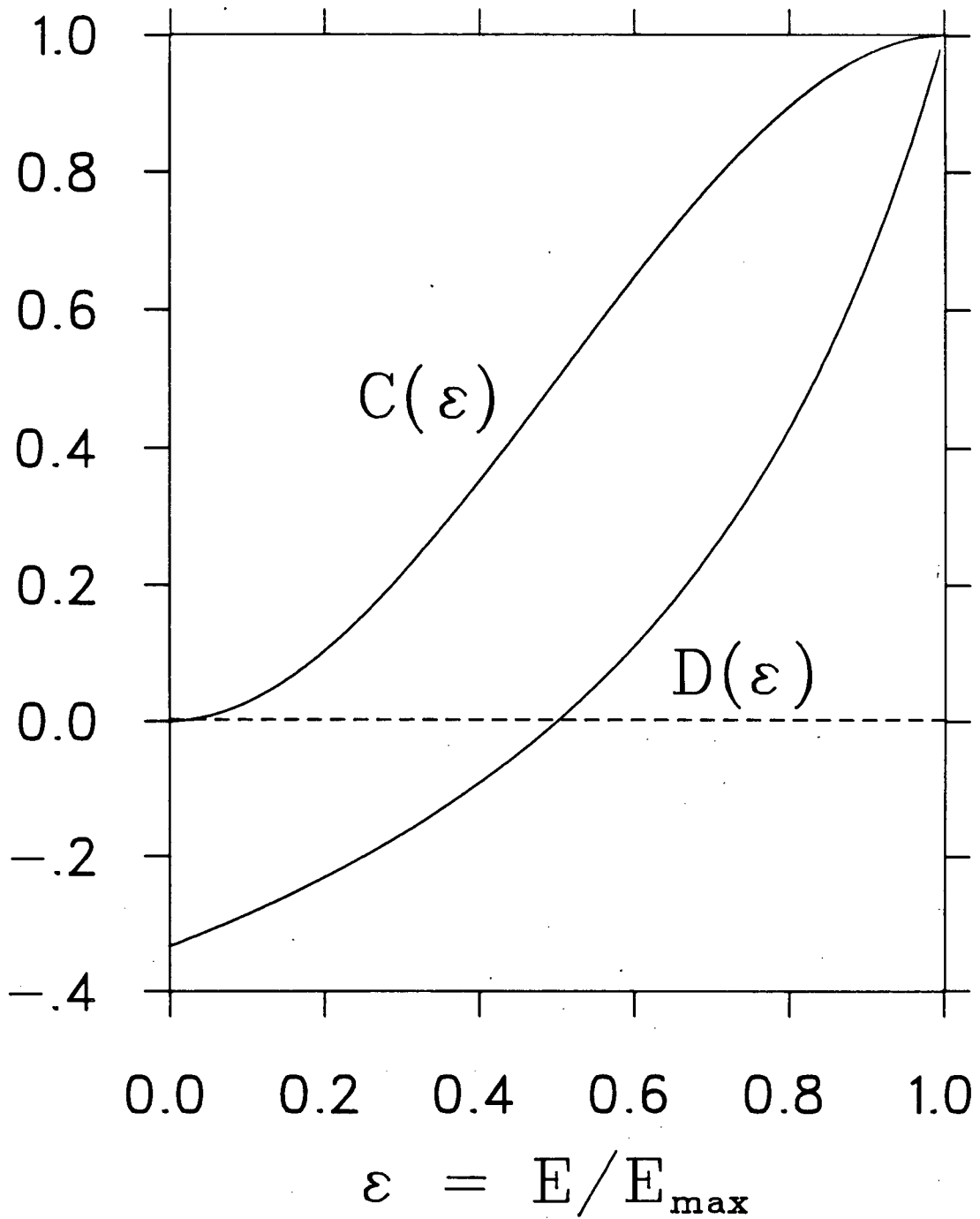
Figure I.1 Positron energy spectrum from muon decay (upper curve) and energy dependence of the asymmetry factor for 100% polarized (P=1) muons (lower curve). The positron energy is given in units of the maximum possible emission energy E_{max} = 52.827 MeV.

loss mechanisms [1]. A high energy μ^+ interacting with matter will first lose energy by scattering with electrons. When the μ^+ velocity approaches that of the valence electrons of the target atoms (corresponding to a μ^+ kinetic energy of 2-3 keV), the energy loss per unit time occurs primarily through ionization, in accordance with the Bethe equation [8]. Below ~2 keV, energy loss still occurs through collisions with electrons, except in this case the Bethe equation does not hold since the electrons now behave as a degenerate gas. In this energy region, a muon can also capture and lose electrons in its interactions with the target medium, forming short-lived neutral hydrogen-like muonium (μ^+e^-) atoms; in many cases, the neutral muonium atom is the favored charge state as the μ^+ velocity drops below the threshold for this capture/loss cycle. The final muonium atom then slows down through subsequent non-ionizing collisions with atoms and/or molecules.

The effect of the slowing down process on the μ^+ spin polarization has been given extensive consideration by many authors [9,10], and found to be negligible in solids, where the charge exchange cycles are much shorter than the hyperfine period. This is, of course, good news if one wishes to study the interaction of the μ^+ spin with its environment. In gases, however, depolarization can indeed occur since the charge exchange cycles may be comparable to the hyperfine period [11,12].

I.A.3 Muonium Formation and Characteristics

The details of muonium (Mu) formation were first discussed in 1952 [13], but it was not until 1960 that direct experimental evidence of its formation was obtained [14]. Some of the properties of muonium are given in

Table I.2. The reduced mass of the electron in muonium is about 0.996 that

for hydrogen, making the Bohr radii and ionization potentials of muonium and

hydrogen essentially the same. Consequently, muonium behaves chemically

like a light isotope of hydrogen [1,15,16], having a rest mass m_{Mu} equal to

0.1131 the rest mass m_H of hydrogen. Unlike hydrogen, however, muonium is a

purely leptonic system whose properties are calculable to extreme precision

entirely from first principles. As a result, the muonium atom is an ideal

system to be used for tests of quantum electrodynamics, and has been widely

employed as such.

A completely general Hamiltonian for the hyperfine interaction between

the μ^+ and e^- spins, in the presence of a magnetic field $\underset{\sim}{B}$ and allowing for

effects due to an anisotropic environment, can be written

$$H_{Mu} = (h/2\pi)\left(\gamma_e \, \underset{\sim}{S}^e_{op} - \gamma_\mu \, \underset{\sim}{S}^\mu_{op}\right) \cdot \underset{\sim}{B} \; + \; (h/2\pi) \, \underset{\approx}{W} : \left(\underset{\sim}{S}^e_{op} \, \underset{\sim}{S}^\mu_{op}\right) \qquad (I.5)$$

where $\gamma_e = 2\pi(\bar{\gamma}_e)$ and $\gamma_\mu = 2\pi(\bar{\gamma}_\mu)$ are the respective magnetogyric ratios of

the electron and the muon, $\underset{\sim}{S}^e_{op}$ and $\underset{\sim}{S}^\mu_{op}$ are the corresponding dimensionless

spin operators and $\underset{\approx}{W}$ is a second rank tensor representing the contact

hyperfine interaction, which has been explicitly generalized here to include

the possibility of an anisotropic Mu atom, as might be imposed by a solid

medium. In vacuum, of course, $\underset{\approx}{W}$ reduces to a constant multiplying the unit

second rank tensor.

For isotropic muonium (i.e., having a spherically symmetric hyperfine

interaction), the eigenvalues of the spin Hamiltonian (Equation I.5) are

given in terms of their respective weak-field quantum numbers (F, m_F) by

the Breit-Rabi formula [17], namely

Table I.2 Properties of Muonium (Mu)

Property (symbol)		Value
Rest Mass	m_{Mu}	$0.1131\ m_H = 207.8\ m_e$
Reduced Mass	m_{Mu}^r	$0.9952\ m_e = 0.9956\ m_H^r$
Bohr Radius	$(a_o)_{Mu}$	$0.5315\ \text{Å} = 1.0044\ (a_o)_H$
Ground State Energy	$(R_\infty)_{Mu}$	$-13.54\ \text{eV} = 0.9956\ (R_\infty)_H$
Magnetogyric Ratio	γ_{Mu}	triplet; $= 8.8 \times 10^6\ s^{-1}\ G^{-1}$ $\approx 2\pi \times 1.4\ \text{MHz/G}$
Hyperfine Frequency	ν_{oo}	theo. $= 4463.3185(6.5)$ MHz (a) expt. $= 4463.30235(52)$ MHz (a)
de Broglie Wavelength	λ_d^{Mu}	$2.979\ \text{Å}\ (300\ K) = 2.967\ \lambda_d^H\ (300\ K)$

(a) D.E. Casperson, et al., Phys. Rev. Lett. <u>38</u>, 956 (1977).

$$E_{F=(\frac{1}{2} \pm \frac{1}{2}),m_F} = -\frac{1}{4} E_0 - (g_\mu \mu_0^\mu)|\underset{\sim}{B}|m_F \pm \frac{1}{2} E_0(1 + 2m_F X + X^2)^{1/2}$$

(I.6)

$$X = (g_e \mu_0^e + g_\mu \mu_0^\mu) \frac{|\underset{\sim}{B}|}{E_0} \qquad \text{and} \qquad m_F = 1, 0, -1$$

where E_0 is the zero field hyperfine energy splitting between the triplet (F=1) and singlet (F=0) states, g_e and g_μ are the respective g-factors and μ_0^e and μ_0^μ are the electron and muon Bohr magnetons. Denoting $\nu_{oo} = E_0/h$ to be the hyperfine-structure interval ($\sim$4463.3 MHz [18]), evaluation of Equation I.6 for the four existing spin coupling states then gives

$$\nu_1 = \frac{1}{h} E_1 = \frac{1}{4} \nu_{oo} + \nu_- \quad ; \quad \nu_2 = \frac{1}{h} E_2 = -\frac{1}{4} \nu_{oo} + [\frac{1}{4} \nu_{oo}^2 + \nu_+^2]^{1/2}$$

$$\nu_3 = \frac{1}{h} E_3 = \frac{1}{4} \nu_{oo} - \nu_- \quad ; \quad \nu_4 = \frac{1}{4} E_4 = -\frac{1}{4} \nu_{oo} - [\frac{1}{4} \nu_{oo}^2 + \nu_+^2]^{1/2}$$

(I.7)

with the definition

$$\nu_\pm = \frac{1}{2} (g_e \mu_0^e \pm g_\mu \mu_0^\mu) \frac{|\underset{\sim}{B}|}{h} = \frac{1}{2} (|\vec{\nu}_e| \pm |\vec{\nu}_\mu|)$$

(I.8)

Choosing the axis of quantization to be along the magnetic field, the energy eigenstates $|j\rangle$ of isotropic muonium can be represented in terms of the individual spin eigenfunctions $|m_\mu, m_e\rangle$ as

$$|1\rangle = |+,+\rangle \qquad ; \quad |2\rangle = s|+,-\rangle + c|-,+\rangle$$

$$|3\rangle = |-,-\rangle \qquad ; \quad |4\rangle = c|+,-\rangle - s|-,+\rangle$$

(I.9)

where the amplitudes s (sine) and c (cosine) are defined as

$$s = \frac{1}{\sqrt{2}} [1 - \frac{x}{(1 + x^2)^{1/2}}]^{1/2} \quad \text{and} \quad c = \frac{1}{\sqrt{2}} [1 + \frac{x}{(1 + x^2)^{1/2}}]^{1/2}$$

(I.10)

$$x = (g_e \mu_0^e - g_\mu \mu_0^\mu) \frac{|\underset{\sim}{B}|}{E_0} = \frac{|\underset{\sim}{B}|}{B_0} = \text{Specific Field Parameter}$$

where one has the normalization condition $s^2 + c^2 = 1$, and B_0 (≈ 1585 G) is the hyperfine field. Note that in zero field, $s = c = 1/\sqrt{2}$ and $\nu_{24} = \nu_{00}$.

I.B Time Evolution of the Muonium Spin State

The four hyperfine states are, in general, unequally populated since the muons arrive with a preferred polarization (directed opposite to the direction of emission from pion decay), while the captured electrons are normally unpolarized. Thus, choosing the spin quantization axis along the initial μ^+ spin polarization direction, half of the Mu ensemble forms in the state $|a_0\rangle = |+,+\rangle$ and the other half in the state $|b_0\rangle = |+,-\rangle$. In a longitudinal field, where the external magnetic field $\underset{\sim}{B}$ is directed along the initial muon polarization, the orientation energy is quantized along this same direction such that the state $|a_0\rangle = |+,+\rangle = |1\rangle$ is an eigenstate of the Hamiltonian, but the state $|b_0\rangle = |+,-\rangle = s|2\rangle + c|4\rangle$ is not. With these designations, half of the muonium ensemble is formed in the "polarized triplet" state $|a_0\rangle$ while the remaining half is formed in the "mixed" state $|b_0\rangle$, and the initial relative populations of the four hyperfine states are given by the probabilities

$$P_1 = \frac{1}{2} \; ; \qquad P_2 = \frac{s^2}{2} \; ; \qquad P_3 = 0 \; ; \qquad P_4 = \frac{c^2}{2} \qquad (I.11)$$

Although the Coulomb interaction which governs the electron capture process has a negligible effect on the μ^+ spin polarization in solids, the hyperfine interaction between the μ^+ spin and the spin of the electron in muonium does give rise to phase oscillations in the superposition $|b_0\rangle$ of the hyperfine states at frequencies on the order of the hyperfine-structure interval ν_{00}.

I.B.1 Muonium in Vacuum

Consider the time evolution of the muon spin polarization in free muonium. In longitudinal field, the polarized triplet eigenstate $|a_0\rangle$ is a

stationary state, while the mixed state $|b_0\rangle$ is a superposition of two

eigenstates. Since the state $|a_0\rangle$ is stationary, one must only determine

the time dependence of state $|b_0\rangle$. Recalling Equation I.7, and defining

$\omega_j = 2\pi\nu_j$ and $\omega_{ij} = 2\pi(\nu_{ij}) = 2\pi(\nu_i - \nu_j)$, one then finds [1]

$$|b(t)\rangle = e^{-i\omega_2 t}\{[s^2 + c^2\exp(i\omega_{24}t)]|+,-\rangle_{\|} + sc[1-\exp(i\omega_{24}t)]|-,+\rangle_{\|}\} \quad (I.12)$$

In zero field, where $s = c = 1/\sqrt{2}$ and $\omega_{24} = \omega_{00} = 2\pi\nu_{00}$, the state $|b(t)\rangle$

oscillates with a frequency ω_{00} between the initial hyperfine state $|+,-\rangle_{\|}$

and the state $|-,+\rangle_{\|}$, in which the muon spin direction is reversed. The

spin polarization of the muons in the state $|b(t)\rangle$ is given by the relation

$\underset{\sim}{P}^{\mu}_{b\|}(x,t)\vec{z} = \langle b(t)|\sigma^{\mu}_3|b(t)\rangle\vec{z}$, where σ^{μ}_3 is the muon Pauli spin matrix for

projections along the quantization axis (z-axis) and $\vec{z}$ is the

corresponding unit vector. By combining this with the 100% polarization of

the muons in the stationary state $|a_0\rangle$, the time dependence of the total

muon ensemble in longitudinal field is given by [1]

$$\underset{\sim}{P}^{\mu}_{\|}(x,t) = \frac{1}{2}[1 + P^{\mu}_{b\|}(x,t)]\vec{z} = \frac{1}{2} + \frac{1}{2}\left[\frac{x^2 + \cos(\omega_{24}t)}{1 + x^2}\right] \quad (I.13)$$

In transverse field (TF), where the external magnetic field $\underset{\sim}{B}$ is

applied perpendicular to the initial muon polarization, the states $|a_0\rangle$ and

$|b_0\rangle$ are not eigenstates and neither one is stationary. In this case, the

initial state vectors $|a_0\rangle$ and $|b_0\rangle$ can be written in terms of the

longitudinal field basis $|m_{\mu},m_e\rangle_{\|}$. By expanding these states in terms of

the isotropic muonium energy eigenstates $|j\rangle$, given in Equation I.9, the

time dependence for each of these two states is found to be [1]

$$|a_0(t)\rangle = \frac{1}{2}[\ e^{-i\omega_1 t}|1\rangle + (s + c)e^{-i\omega_2 t}|2\rangle$$
$$+ e^{-i\omega_3 t}|3\rangle - (s - c)e^{-i\omega_4 t}|4\rangle]$$

$$|b_0(t)\rangle = \frac{1}{2}[-\ e^{-i\omega_1 t}|1\rangle + (s - c)e^{-i\omega_2 t}|2\rangle$$
$$+ e^{-i\omega_3 t}|3\rangle + (s + c)e^{-i\omega_4 t}|4\rangle]$$

(I.14)

Because the magnetic field (B_z) is oriented perpendicular to the initial muon polarization, and since the muonium electron is only interacting with the muon spin, all of the motion of the μ^+ spin in the muonium state is confined to the x-y plane. This being the case, the time evolution of the muon polarization for the entire muonium ensemble is given by the complex quantity

$$\underset{\sim}{P}_{\perp}^{\mu^*}(x,t) = \frac{1}{2}[\langle a(t)|(\sigma_1^\mu + i\sigma_2^\mu)|a(t)\rangle + \langle b(t)|(\sigma_1^\mu + i\sigma_2^\mu)|b(t)\rangle] \qquad (I.15)$$

where σ_1^μ and σ_2^μ are the x and y Pauli spin operators. Here the real part is the μ^+ polarization along the initial $\vec{x}$ direction and the imaginary part represents the μ^+ polarization along the $\vec{y}$ direction, perpendicular to both $\vec{x}$ and $\vec{z}$ (i.e., $\vec{x} \times \vec{y} = \vec{z}$). Substituting the expressions for the state vectors given in Equation I.14 into Equation I.15 then gives the result

$$\underset{\sim}{P}_{\perp}^{\mu^*}(x,t) = \frac{1}{2}\left[c^2(e^{i\omega_{12}t} + e^{-i\omega_{34}t}) + s^2(e^{i\omega_{23}t} + e^{i\omega_{14}t})\right]$$

$$= \exp(i\omega_- t)\cos(\frac{\omega_{oo}}{2}t)\left[\cos(\frac{\omega_{oo}}{2} + \Omega)t - i\delta\sin(\frac{\omega_{oo}}{2} + \Omega)t\right] \quad (I.16)$$

$$\delta = (c^2 - s^2) = \frac{x}{(1 + x^2)^{1/2}} \quad \text{and} \quad \Omega = \frac{1}{2}(\omega_{23} - \omega_{12}) = \frac{\omega_{oo}}{2}[(1 + x^2)^{1/2} - 1]$$

Most of the experiments reported in this dissertation were performed in the low field limit (x ≪ 1). In this limiting case, the real part of

Equation I.16 simplifies to give [1]

$$\text{Re}\{\underset{\sim}{p}_{\perp}^{\mu *}(t)\} \approx \frac{1}{2} \cos(\omega_- t) \left[\cos(\Omega t) + \cos(\omega_{00} + \Omega)t\right] \qquad (I.17)$$

where $\omega_- = 2\pi\nu_-$ as defined in Equation I.8. Since the frequency $(\omega_{00} + \Omega)$ is in general too high to be observed experimentally, except in high transverse fields, Equation I.17 describes a signal with half of the initial μ^+ spin polarization amplitude (asymmetry) which oscillates at the Larmor frequency ω_-, modulated at a beat frequency equal to Ω. A more elaborate formalism is developed elsewhere [19,20] for cases where the muonium electron interacts with its environment.

I.B.2 Interactions with the Environment

The interaction of the μ^+ spin with its environment may in some cases result in a depolarization or a relaxation of the μ^+ spin ensemble. It is instructive at this point to define what is meant by depolarization versus relaxation. The term "depolarization" encompasses all varieties of spin dynamics, including interactions in which the phase coherence of the spin ensemble could in principle be recovered at some later time (e.g., by spin echo techniques); whereas "relaxation" applies to those interactions which result in a strictly irreversible loss of ensemble polarization, such as in the case of a diffusing magnetic probe. Conventionally, however, the term "relaxation" is applied in a somewhat generic fashion and will generally be applied herein in the same manner.

In the case of a bare μ^+, spin relaxation occurs via the interaction of the μ^+ spin with the local magnetic field distribution. In the case of muonium, however, the μ^+ is strongly coupled to the electron so that in weak

magnetic fields the fraction (50%) of muonium that forms in the polarized

triplet (F=1, m_F = +1) state behaves magnetically like a polarized spin-one

object with a magnetic moment on the order of the electron's and is thus

about 103 times more sensitive to local magnetic fields than a bare μ^+.

Because of the rather strong hyperfine coupling, the μ^+ spin polarization is

also sensitive to electric field gradients or other mechanisms that may

distort the muonium electron wavefunction and thereby induce anisotropies

into the muonium hyperfine interaction. It was for this reason that $\underset{\approx}{W}$ was

generalized in Equation I.5. Thus, in addition to interactions with the

local magnetic fields, which can cause depolarization for both bare μ^+ and

Mu, there are four other mechanisms that can induce depolarization or

relaxation of the μ^+ spin in a Mu atom. The five known mechanisms are:

(1) Random Local Magnetic Fields   (depolarization).
(2) Random Anisotropic Hyperfine Distortions (depolarization)
(3) Chemical Reactions   (relaxation, for TF)
(4) Spin Exchange   (relaxation)
(5) Superhyperfine Interactions   (depolarization)

Here the designation of "depolarization" applies only in the case of a

static (non-diffusing) probe (Mu atom). These mechanisms, along with the

corresponding spin relaxation functions, are discussed in more detail in

Chapter III. Of particular importance to the present study are the static

relaxation functions associated with random anisotropic hyperfine

interactions. These functions are derived in detail in Appendix I.

Owing to its relatively light mass, the muon (or Mu atom) may be very

mobile in the stopping medium. This motion or hopping may result in an

effective relaxation rate which differs in magnitude in comparison to the

static value. This difference comes about because the effects of the

interaction(s) governing the time evolution of the μ^+ spin polarization are

averaged by the motion, hence the term "motional averaging". Depending upon the specific interaction(s) and the time scales involved, the motion can produce an effective relaxation rate that has either a reduced magnitude ("motional narrowing") or an increased magnitude ("motional broadening") in comparison to the static value. Relaxations due to chemical reactions or spin exchange are not affected by motional averaging, but relaxations arising from random dipolar fields, random anisotropic hyperfine distortions and superhyperfine interactions are indeed affected.

The traditional example is a μ^+ hopping stochastically in the presence of static nuclear dipoles. Assuming a Gaussian distribution of random local fields, and defining τ_c to be the correlation time of the field fluctuations as sensed by the μ^+, the spin relaxation rate in the limit of fast fluctuations becomes [21]

$$\lambda_\mu \approx \langle \Delta\omega^2 \rangle \, \tau_c \qquad\qquad (I.18)$$

where $\langle \Delta\omega^2 \rangle$ is the second moment of the frequency distribution for the random local field [22].

The effect of hopping on the shape of the relaxation functions arising from random anisotropic hyperfine distortions or superhyperfine interactions is not as straightforward to determine. However, a detailed discussion of this in the case of the former is given in Chapter III.

I.C The Interactions of Muonium with Silica

Much of the work presented in this dissertation stems from earlier studies involving both muonium in bulk silica and on silica surfaces. A brief summary of these studies is therefore presented here, along with

discussions on those points of particular relevance to the present work.

I.C.1 Muonium in Bulk Silica

Extensive studies have been made on muonium in bulk quartz [23-27], where most of the phenomena of interest arise from anisotropic distortions of the muonium hyperfine interaction. Zero field measurements of muonium in single crystal quartz have revealed three frequencies at low temperatures ($\leq$ 77 K). These frequencies, which obey the sum rule $\nu_{13} = \nu_{12} + \nu_{23}$, remain constant but have amplitudes that vary, as the crystal is rotated about the initial muon spin polarization. This result is consistent with an effective spin Hamiltonian in which the hyperfine tensor has three principal axes of symmetry. With this picture, the three observed frequencies then correspond to transitions between three levels, and as such are labelled accordingly. At higher temperatures (near room temperature), the muonium hyperfine interaction has an anisotropy which is symmetric about the c-axis of the crystal due to motional averaging. In this (high temperature) case, the hyperfine tensor $\underset{\approx}{W}$ can be broken down into an isotropic part $\langle W \rangle = \omega_{00}$ and a term $\delta W_c = \delta \omega_c$ associated with a distortion along the c-axis. By denoting S_c^e and S_c^μ as the projections of the e^- and μ^+ spins along the c-axis, respectively, the axially symmetric contact hyperfine Hamiltonian becomes

$$H^{hf} = (h/2\pi)\ \underset{\approx}{W}:\left(\underset{\sim}{S}_{op}^e\ \underset{\sim}{S}_{op}^\mu\right) = (h/2\pi)\left\{\langle W \rangle \left(\underset{\sim}{S}_{op}^e \cdot \underset{\sim}{S}_{op}^\mu\right) + \delta W_c\left(S_c^e\ S_c^\mu\right)\right\} \qquad (I.19)$$

In zero field, with the c-axis oriented perpendicular to the initial muon polarization, an oscillation of 0.412(4) MHz is observed; however, with the c-axis oriented parallel to the initial muon polarization, the oscillation

disappears, as predicted by Equation I.19.

In fused quartz, the zero field hyperfine oscillations are suppressed and the depolarization of the μ^+ spin is enhanced via ensemble dephasing, owing to the the random magnitude, symmetry and orientation of the muonium hyperfine distortion with respect to the initial muon spin. A more general discussion of random anisotropic hyperfine distortions and their effect on the time evolution of the μ^+ spin polarization for static muonium is given is Appendix I.

I.C.2 Muonium on Silica Surfaces

It has long been known that fine insulating powders, such as MgO and SiO_2, can be used in the production of positronium in vacuum [28], even at low temperatures [29]. It is thought that positronium is formed in the powder grains, diffuses rapidly to the surface and finally escapes into the void between the grains.

The analogous phenomena for muonium was first reported in 1978 for fine (35 Å mean radius) evacuated SiO_2 powder [30], where the emergence of muonium into the extragranular region was verified by the introduction of O_2 gas. The Mu spin depolarization rate was observed to increase linearly with O_2 concentration, due to spin exchange interactions with the paramagnetic O_2 molecules, in a manner consistent with results obtained with O_2 in an argon gas moderator at one atmosphere [31], thus demonstrating that the SiO_2 powder acts like a very coarse moderator gas. Later investigations [32-34] concerning Mu in fine oxide powders, namely SiO_2, Al_2O_3 and MgO, show that a certain fraction of the muonium formed finds its way to the extragranular region for all three oxides. Of all the oxides tested, SiO_2 was found to

have the highest formation probability for Mu, (possibly because it was

available in the smallest grain size); and the 35 Å SiO_2 powder was found to

produce the highest yield of extragranular muonium ($\geqslant$97% of Mu formed [30]),

regardless of the ambient temperature of the powder. This last point made

the 35 Å silica powder the obvious candidate for further studies of the

interaction of μ^+ and muonium with surfaces, the subject of this thesis.

I.C.3 Muonium Formation in Fine Silica Powders

The muonium fractions for bulk fused quartz as well as for 35 Å and 70

Å mean radius silica powders are given in Table I.3. As in the case of

positronium formation, muonium formation in fine oxide powders may involve

thermal, epithermal, spur and/or surface processes. Because the atomic

binding energy of positronium is about half that of muonium, it is difficult

to draw a simple analogy between the formation probabilities for the two

atoms. First let us ask whether muonium formation in fine oxide powders is

a bulk or a surface phenomenon; surface formation of positronium has, for

instance, been observed for low energy positrons incident on metal and

metal-oxide surfaces [35]. If muonium formation is indeed surface related,

one would expect the Mu fraction to increase with increasing specific

surface area. From the values given in Table I.3, this effect does not

appear to be particularly dramatic, if it exists at all, suggesting that the

formation of muonium in silica powders takes place primarily in the bulk.

The possibility of some charge exchange ocurring at the silica surface is

not however ruled out.

The next question is whether Mu formation occurs via thermal,

epithermal or spur processes. In the spur model [36], muonium formation

Table I.3 Muonium Fractions (F_{Mu}) and Transverse Field Relaxation Rates
($\lambda_\perp^{Mu}$) for Bulk and Powdered Silica.

Sample	T (K)		F_{Mu} (%)	$\lambda_\perp^{Mu}$ (μs^{-1})
Bulk fused SiO_2	6		79 ± 3	3.3 ± 0.5 (a)
	295		79 ± 3	0.20 ± 0.05 (a)
SiO_2 powder (70 Å)	6	bulk	35 ± 5	4.1 ± 0.7 (b)
		surface	35 ± 5	0.16 ± 0.05 (b)
	295		45 ± 20	0.18 ± 0.03 (c)
SiO_2 powder (35 Å)	6		49 ± 3	0.46 ± 0.03 (b)
	295		61 ± 3	0.18 ± 0.03 (b)

(a) J.H. Brewer, Hyperfine Interactions 8, 375 (1981).

(b) R.F. Kiefl, Ph.D. Thesis, University of British Columbia (1982).

(c) G.M. Marshall, et al., Phys. Lett. 65A, 351 (1978).

The measurements on the 70 Å mean diameter powder were performed in a helium
atmosphere.

comes about when a thermalized μ^+ combines with an electron from the radiation track that it itself produced while stopping. It has been shown, for positronium formed via a spur mechanism, that the application of an electric field inhibits the combination of e^+ with the spur e^- [37]. Similar experiments concerning muonium formation have shown the Mu formation probability in bulk SiO_2 to be independent of applied electric fields of up to 60 kV/cm [38], suggesting that Mu formation in bulk SiO_2 is probably not governed by a spur mechanism. However, the analogous experiments using fine silica powders have not as yet been performed.

For the case of epithermal (or hot atom) formation, the μ^+ undergoes a series of charge-exchange processes as it slows down, as discussed earlier. Recent results [39] on the formation of muonium and "muonated" radicals in liquids, where the spur model is most popular [40], suggest that epithermal processes play a significant role, even in the presence of spurs.

Finally, recent experiments [41] on muonium formation in Al_2O_3 show clear evidence that $\mu^+ \rightarrow Mu$ on a thermal basis over times as long as microseconds at low temperatures (T < 10 K), shortening to picoseconds near room temperature. This process, however, does not seem likely for silica powders since, from Table I.3, the muonium fraction is observed to be temperature independent in bulk fused quartz.

One last point can be made by drawing attention to the fact that there exists a statistically significant discrepancy in the muonium formation probability between fine silica powders and bulk fused quartz. From Table I.3, the muonium fractions F_{Mu} measured at 295 K for the 35 Å radius SiO_2 powder and bulk fused SiO_2 are 61 ± 3% and 79 ± 3%, respectively. In addition, F_{Mu} for bulk fused SiO_2 is found to be independent of temperature

whereas for the 35 Å powder F_{Mu} decreases to 49 ± 3% at 6 K. These results

may be explained by the fact that in powders the Mu atoms have the

possibility of interacting with the grain surfaces. There are two possible

mechanisms associated with the surface that might account for the reduction

of the muonium fraction; covalent bonding, which in zero and longitudinal

field causes no depolarization of the μ^+ spin but which in transverse field

removes muons from the muonium ensemble, or ionization of the muonium atom

at the surface, which has the same effect.

First consider the possibility of covalent bonding. Generally, the

silica surfaces are covered with hydroxyl groups [42,43] and are likely

chemically inert for muonium of thermal energies. It may be energetically

possible for a stopping μ^+ to exchange with a hydroxyl proton; because this

type of process requires non-thermal energies, however, one would not expect

it to be temperature dependent, making it inconsistent with observations.

Now consider the possibility of ionization at the grain surfaces.

Recent positron experiments [44] show that when e^+ of keV energies are

implanted into ionic crystals they are reemitted isotropically from the

solids with a continuum of energies having a maximum approximately equal to

the band gap energy of the solid. This phenomenon has further been shown to

be associated with positronium diffusing to the surface and subsequently

dissociating.

In 1972 it was postulated that Ps could be field-ionized in the process

of leaving a surface [45]. This, however, does not adequately account for

the anomalously large emission energies or the correlation with the band gap

energy of the solid. An alternate explanation [44] is that the positron is

Auger-emitted when the Ps electron falls into an acceptor state at the

surface of the crystal.

It is quite possible that the same mechanism(s) governing e^+ emission may be involved in the interactions of muonium with ionic surfaces such as fine silica powders. A detailed discussion of this particular phenomenon is given in Appendix II, and thus no elaborate explanations will be given here. Suffice it to say that with the model just described the maximum energy of the emitted μ^+, corresponding to the Mu electron recombining with a hole at the bottom of the valence band, can be written as

$$E^{\mu}_{max} = \left(E_g + \Delta E_v\right) - \Phi^{Mu} - R_{\infty} + \Phi^e_- \qquad (I.20)$$

where E_g is the band gap energy, ΔE_v is the width of the valence band, R_{∞} is the binding energy of muonium in vacuum, Φ^e_- is the electron affinity at the bottom of the conduction band and Φ^{Mu} is the muonium work function at the surface. In analogy with positronium studies, the maximum kinetic energy for Mu emission is the negative of its work function, which is given by

$$\Phi^{Mu} = \left(E^{Mu}_b - R_{\infty}\right) + \left(\Phi^e_- + \Phi^{\mu}_+\right) \qquad (I.21)$$

where E^{Mu}_b is the binding energy of muonium at the surface and Φ^{μ}_+ is the μ^+ work function. A negative work function has been postulated for muonium on SiO_2 surfaces [30,33,34]. For SiO_2, $E_g = 10.7$ eV [46] and one may assume a conservative estimate for Φ^{Mu} of 0 ± 1 eV. Substituting these values, along with R_{∞} and rather conservative estimates for ΔE_v and Φ^e_-, into Equation I.20, one can conclude that Mu ionization at the surface of fine silica powders is energetically feasible. However, since one does not expect long-lived holes in the valence band, Equation I.20 is an overestimate.

Assuming this model to be correct, it can be easily argued that this process would indeed be temperature dependent simply because at lower

temperatures a Mu atom will spend a larger fraction of its life on the surface, thereby enhancing the probability of encountering a hole. More extensive measurements of the muonium formation probability have been made as part of this dissertation, for SiO_2 powders as well as for helium coated SiO_2 powders. This is discussed in Chapter IV.

I.C.4 Extragranular Muonium Production

Two models concerning the production of Mu in the extragranular region in fine oxide powders have been put forth; one termed the thermal diffusion (TD) model [30] and another which will be referred to as the direct thermalization (DT) model [33,34]. Both models assume Mu formation to be a bulk phenomenon, but present differing explanations of how the Mu atoms end up in the extragranular region.

The TD model is an adaptation of a model originally applied to positronium diffusion [47], which assumes that the Mu atoms thermalize in the powder grains and then diffuse to the surface where they may be ejected from the surface via a negative work function mechanism. As mentioned earlier, Mu is static in bulk fused SiO_2 below about 50 K [26]. If one assumes that the silica grains are of the same structure as bulk fused SiO_2 and that the grain in which the μ^+ stops remains at the ambient temperature, then the reduced diffusion expected at low temperatures appears to cast doubt on the TD model since it would predict a temperature dependence in the probability for the production of extragranular Mu, in contradiction with existing data. However, local heating of the grains due to the energy deposited by the stopping μ^+ may play an important role in the bulk diffusion and subsequent ejection of the Mu atoms from the oxide grains.

Calculations [48] of this effect estimate an energy deposition of 0.3 keV for muons stopping in a 35 Å radius SiO_2 powder grain; assuming a uniform temperature distribution within the grain, this translates into an average temperature increase of ~300 K. Bear in mind that these calculations are crude and thus only indicate an order of magnitude. At this temperature, Mu is known to diffuse very rapidly (at least in crystalline quartz [26]). Thus the muonium has a high probability of arriving at the surface in a shorter period of time. Furthermore, this temperature corresponds to an average energy of $E_k = (3/2)kT \approx 0.04$ eV for the muonium atom, which may assist in the ejection of Mu from grain surfaces. If the muonium work function Φ^{Mu} is indeed negative at the silica surface, the muonium atoms will escape the powder grains with kinetic energy $E_k + |\Phi^{Mu}|$. Once outside the powder grains (extragranular region), a muonium atom will likely remain outside since it would require only a few elastic collisions for the condition $E_k \ll |\Phi^{Mu}|$ to be met. Thus the TD model can indeed explain the existing data on extragranular muonium production, subject only to the validity of the grain heating hypothesis.

The DT model was originally proposed to circumvent the question of temperature dependent diffusion. This model postulates the existence of a relatively large ($\Phi^{Mu} \sim -2$ eV) negative Mu work function at the surface of the powder grains, which provides the possibility of direct thermalization of the Mu atoms in the extragranular region. This model predicts the extragranular Mu fraction to be temperature independent, in better agreement with experiments, but it is difficult to explain the origin of such a large negative work function.

Recall the expression for the muonium work function Φ^{Mu} given in

Equation I.21. The negativity of Φ^{Mu} is of course influenced by many

factors, however there are two phenomena which are of particular interest.

One involves the distortion of the muonium hyperfine interaction and the

other involves what is termed the "photoelectric size effect". Let us first

consider the effect of the former. If the muonium hyperfine interaction is

distorted by virtue of being on the silica grain surfaces, so that the

isotropic part of the hyperfine interaction is reduced (i.e., ν_{00} less than

the vacuum value), the atomic binding energy of muonium on the surface E_b^{Mu}

would decrease accordingly with respect to the vacuum value R_{∞}, thereby

enhancing the negativity of Φ^{Mu}. Now consider the latter case of

photoelectric size effect. Both the electron work function and

photoelectric yield for small ($<$ 50 Å radius) Ag particles were studied with

results indicating an decrease of a few percent in the electron work

function along with a corresponding increase in the photoelectric yield by a

factor of 10^2 over the macroscopic surface value for the smallest particle

sizes [49]. Depending upon the origin of the interaction, this decrease in

the electron work function may act to enhance the negativity of the muonium

work function Φ^{Mu} for the same material. Thus this effect may also assist

in increasing the probability of extragranular muonium production; however,

no conclusion can be drawn at this time.

I.D The Interactions of Hydrogen and Deuterium with Silica

Although muons are considered to be heavy electrons (or positrons), the

behavior of positive muons and muonium in matter is more reminiscent of

protons and hydrogen than of positrons and positronium. The interactions of hydrogen and deuterium with silica surfaces has been extensively studied; a brief synopsis of what is presently known about the behavior of both hydrogen and deuterium in bulk silica (fused and single crystal) and on silica surfaces will be presented here.

I.D.1 Hydrogen Diffusion in Bulk Silica

Results [50] obtained for hydrogen in single crystal quartz at low ($\leqslant$ 120 K) temperatures, indicate hyperfine anisotropies along three principle axes. Like the observations made for muonium in quartz [23-27], the observed frequencies for hydrogen are assumed to arise from transitions between three levels. This correspondence between muonium and hydrogen suggests that they occupy the same site at low temperatures.

Experiments (ESR) involving the diffusion of protons in single crystal quartz have shown that the recovery of a gamma pulse-induced frequency shift at 306 K follows a $t^{-1/2}$ dependence over an extended period of time (up to 50 seconds), indicative of one-dimensional diffusion [51]. Analysis of this data [52] indicates that protons diffuse preferentially along the optical axis (c-axis) with an activation energy of about 0.25 eV and a diffusion constant of about 5×10^{-6} cm^2/s. As mentioned earlier, one-dimensional diffusion is suspected for muonium in single crystal quartz at this temperature [23-27].

I.D.2 Hydrogen and Deuterium on Silica Surfaces

The effects of ionizing radiation (gamma-rays) on the surface properties of silica-gel have been extensively investigated using ESR

[53,54]. Silica-gel has a rather different structure than powdered silica; it is comprised of large porous particles, whereas the powdered material is composed of non-porous SiO_2 grains, which are in general much smaller in size. In these studies, radiation induced dissociation of the surface hydroxyl (OH) groups was observed along with the subsequent formation of hydrogen atoms which can be stabilized on the silica-gel surface at low temperatures. As the temperature was raised from 123 K to 153 K the hydrogen ESR signal intensity decreased, corresponding to a reduction in the stable H atom population. The adsorbed H atoms were also found to be highly reactive. In particular, chemical reactions with oxygen and ethylene were observed in the temperature range from 123 K to 153 K, which suggests that the H-ethylene reaction involves the formation of an ethyl radical. Measurements of the spin-lattice relaxation time and line width in the presence of oxygen indicate that the average separation between adsorbed H and an oxygen molecule is about 10 Å. The authors suggest that the hydrogen atoms are located in deep "microslits" where the oxygen molecules cannot penetrate. Weak ESR sidebands, possibly due to hyperfine interactions between unpaired electrons and the hydroxyl protons, were also observed and found to be dependent upon pretreatment of the silica-gel. In particular, samples degassed at 200-300 °C for 8 hours prior to irradiation were found to exhibit a signal with a g-value identical to that of the diphenylpicryl hydrazyl radical, and a structure apparently due to the hyperfine interaction between the odd electron of the radical and the hydroxyl protons. This was verified by replacing the hydrogen atoms of the surface OH groups by deuterium. The signal obtained for samples degassed at 500 °C prior to irradiation was indicative of an enhancement in the bulk formation

of F-centers due to the capture of electrons by oxygen lattice vacancies.

In 1975, measurements [55] were made of the hyperfine interval v_{00} for both hydrogen and deuterium adsorbed on the surface of fused quartz at room temperature. Results indicate reductions in v_{00} of 0.12% and 0.13% for hydrogen and deuterium, respectively. In addition to the reduction in the isotropic hyperfine interaction, an anisotropic hyperfine interaction (distortion) was also introduced, producing hyperfine splittings differing by < 0.4% from the vacuum values; this anisotropy has been attributed to an electric field at the surface. The perturbation of the hydrogen atom hyperfine interaction due to an electric field has been discussed in some detail elsewhere [56,57].

The interactions of gas-phase deuterium atoms with silica surfaces have been studied [58] with results showing evidence for a chemical reaction of D atoms with with these surfaces, signaled by the formation of SiO-D bonds. Both Cab-O-Sil and porous Vycor glass (amorphous) surfaces were studied. For Cab-O-Sil, the formation of SiO-D groups was accompanied by a corresponding decrease in SiO-H groups, suggesting an exchange reaction favoring liberation of the lighter isotope. In the case of Vycor glass, however, no significant decrease in the SiO-H group population was observed. The Cab-O-Sil surface used in the ESR studies of deuterium on silica was the same surface used in the present work on muonium.

The text up to this point has been a general introduction to muons and muonium atoms and their characteristics, and has provided a review of the results of previous studies involving muonium and hydrogen in bulk silica and on silica surfaces. The present work will now be considered in more detail, beginning with a discussion of the experimental technique.

CHAPTER II — EXPERIMENTAL TECHNIQUE

II.A Accelerators and Beamlines

At the present time, there are three "meson factories" in existence: (1) Los Alamos Meson Physics Facility (LAMPF), (2) Schweizerisches Institut für Nuklearforschung (SIN) and (3) Tri-University Meson Facility (TRIUMF). All three facilities currently support rather large scale μSR research programs. In addition, CERN, Brookhaven, JINR, Gatchina (Leningrad) and the BOOM facility at KEK also support ongoing μSR research. The experiments described in this dissertation were conducted on the M9 and M20 secondary channels of the TRIUMF cyclotron facility.

II.A.1 The TRIUMF Cyclotron Facility

The present layout of the TRIUMF facility is shown in Figure II.1. The TRIUMF accelerator [1-6] is a sector focussed H^- cyclotron capable of accelerating protons to energies ranging from 180 to 520 MeV at maximum currents of 170 μA at 520 MeV [7]. The proton beam has a 100% "macroscopic" duty cycle and a microscopic time structure consisting (normally) of a 5 ns burst every 43 ns.

The proton beam is extracted with essentially 100% efficiency by passing the H^- ions through a thin carbon "stripper" foil thus stripping off the two electrons and effectively reversing the charge of the ions. The extracted proton energy is selected by the radial position of the stripper foils. The resulting protons then swerve out of the machine through three available extraction ports. A more detailed discussion of the recombination magnet and beam optics associated with the extraction system is given
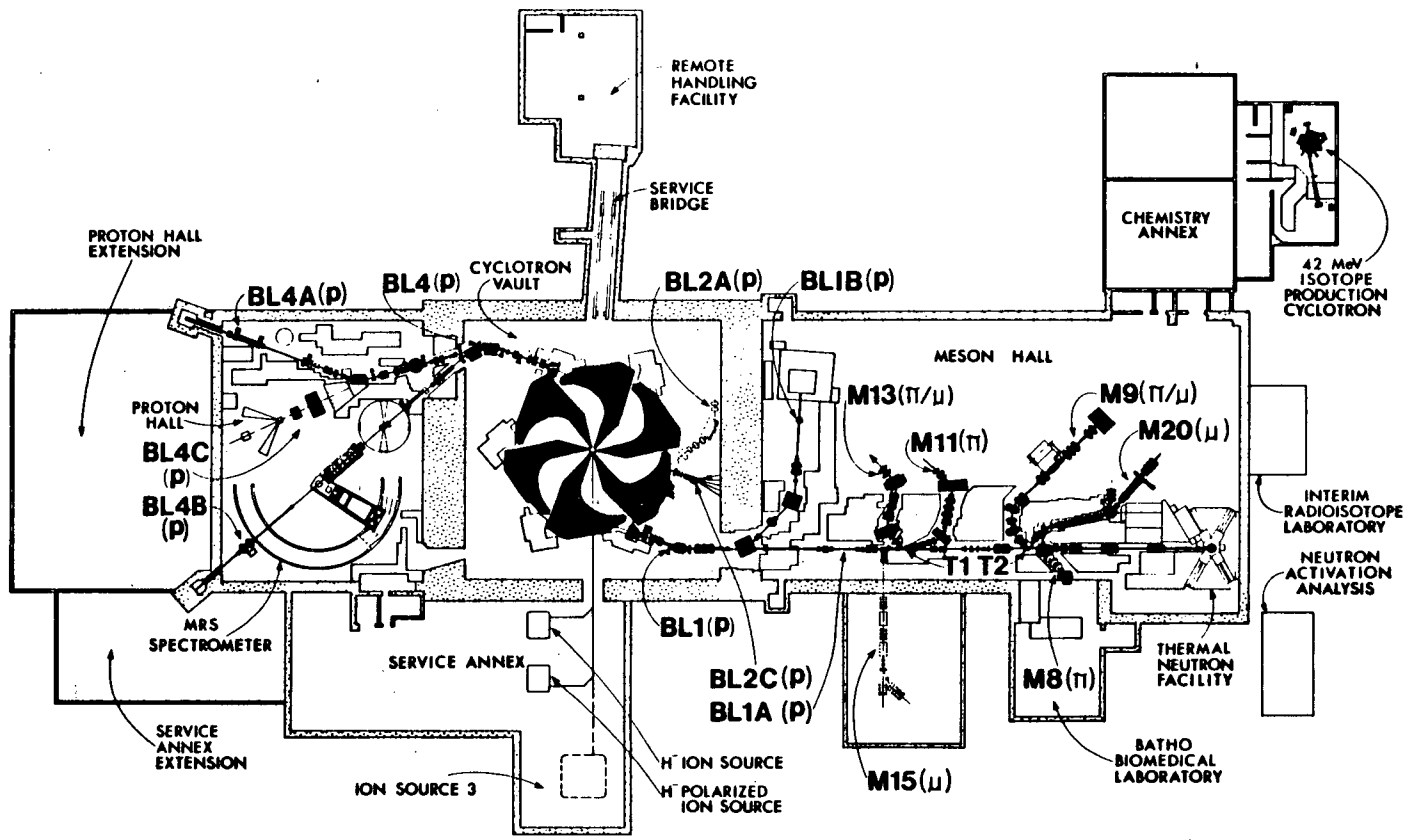
Figure II.1   TRIUMF Cyclotron Facility and Experimental Halls

elsewhere [8].

During high intensity (unpolarized) operation, a proton beam is extracted down Beam Line 4 and then transmitted at currents as low as 1 nA down Beam Line 4B (maximum 1 μA) or 4A (maximum 10 μA). Both of these channels are utilized for nucleon experiments at energies between 180 and 520 MeV. In addition, a 20 to 30 μA proton beam can be extracted down Beam Line 2C for isotope research and production. Finally, a 130 to 140 μA, 500 MeV proton beam is extracted down Beam Line 1A and passed through two pion production targets (1A-T1 and 1A-T2) and ultimately dumped into a molten lead target at the T.N.F. (Thermal Neutron Facility). Low intensity (polarized) beam operation is usually shared between 4B, 4A and 1B.

Typically, the pion production target at 1A-T1 is a 10 mm thick (long) water cooled pyrolitic graphite strip and the one at 1A-T2 is a 100 mm thick (long) water cooled beryllium strip. Pions are produced at these targets via nuclear reactions. Six secondary channels are currently operational along Beam Line 1A. Three channels simultaneously extract π-mesons or muons at 1A-T1: M13 [9], M11 and a newly commissioned channel, M15, that extracts positive muons in the momentum range 21 - 29.8 MeV/c. The length of the M15 channel prohibits pion transport. Three secondary channels simultaneously extract π-mesons or muons at 1A-T2: M8, is dedicated to π⁻ cancer therapy, M9 [10] primarily (in recent years) to the TPC (Time Projection Chamber) and M20 [14] is used principally for μSR experiments.

II.A.2 Muon Production and Transport

To begin this discussion of muon production and transport, we focus our attention on the M20 secondary channel [14]. The M20 channel (shown in

Figure II.2) is mainly a decay muon channel which views the 1A-T2 target at
55° with respect to the primary proton beam direction. It consists of a
injection system incorporating two quadrupole doublets (Q1&2, Q3&4)
separated by a 42.5° bending magnet (B1), which has an acceptance of 12 msr.
In addition to providing the particle collection, this system selects the
momentum of the particles emitted from the pion production target at 1A-T2
and focuses them at the slits (SL1). The injection system is followed by a
ten quadrupole decay section which is designed to collect and transport
muons produced by pions that decay in flight along its length. The
particles that emerge from the decay section are collected by a quadrupole
doublet (Q7 & Q8) and focused through a second bending magnet (B2) which has
two exit ports, one (M20-A) at 75° and the other (M20-B) at 37.5° to the
secondary beam direction before the B2 bender. A Wien filter or
crossed-field velocity separator is incorporated into M20-B and used to
reduce the positron contamination of the beam and may also be used as a
"spin rotator".

Muons can be transported through M20 in any one of three operational
modes; "conventional", "cloud", or "surface / subsurface". Conventional
muons (μ^+ or μ^-) are produced by pions decaying in flight along the length
of the decay section between B1 and B2. In its rest frame, the pion decay
is spatially isotropic and the resulting muons have a momentum of 29.8
MeV/c. The decay muons born in the direction of the pion momentum in the
lab frame are termed "forward muons" and those born in a direction opposite
to the pion momentum are called "backward muons". From relativistic
kinematics, the lab frame momenta are typically ~140 MeV/c and ~86 MeV/c,
respectively. The decay section of M20 is designed to transmit only those

<u>Figure II.2</u> The M20 secondary channel showing both legs (A and B).

muons having a small angular divergence from the initial pion momentum (i.e., backward and forward muons). This feature not only narrows the two available conventional momenta, but also gives rise to a high (85%) polarization. The M20 channel can be tuned to transport backward muons through either M20-A or M20-B with low positron contamination. In addition, a "simultaneous" tune is available which simultaneously delivers "low - contamination" backward and forward decay muons to M20-A and M20-B, respectively. Because conventional muons are produced from an extended source (pions decaying in flight along the length of the decay section) the beam spot size at the final focus is generally rather large. The measured beam parameters [11] for M20 operating in backward mode and simultaneous mode are given in Tables II.1(a) and II.1(b), respectively.

Cloud muons (μ^+ or μ^-) are produced by pions decaying in flight between the production target at 1A-T2 and B1. In this mode, both backward and forward muons are present. However, because the injection system does not discriminate on the angular divergence of decay muons as much as does the decay section between B1 and B2, the beam polarization is relatively low (50-60%). At present, there are no calculated or measured beam parameter values for cloud muons on the recently rebuilt version of M20; but on M9 the beam polarization for cloud muons at 77 MeV/c is ~30%.

Surface muons [12] (only μ^+) are produced from π^+ that decay at rest on the surface of the pion production target. Muons produced in this manner have several advantages over cloud or conventional muons. Unlike cloud muons, for example, surface muons include only the forwardly-decaying component. This feature, coupled with the acceptance of the injection system and the kinematics of π^+ decay, gives rise to two important

Table II.1(a)   Backward Decay Muons at 75° (M20-A) and 37.5° (M20-B)

Beam Parameters		M20-A	M20-B
Total Flux	μ^+	2.5 x 10^6/sec	----
	μ^-	5.9 x 10^5/sec	----
Central Luminosity	μ^+	2.9 x 10^4/sec/cm^2	----
	μ^-	----	----
Central Momentum (P)		86.4 MeV/c	----
Momentum Spread ($\Delta P/P$)		9.6%	----
Electron Contamination	μ^+	0.3%	----
	μ^-	1.3%	----
Polarization		85%	----
Beam Spot (fwhm)	x	7.2 cm	----
	y	9.5 cm	----
Divergence	x	63 mr	----
	y	70 mr	----

Table II.1(b)   Simultaneous Decay Muons on M20

Beam Parameters		M20-A	M20-B
Total Flux	μ^+	1.6 x 10^6/sec	1.6 x 10^6/sec
	μ^-	3.6 x 10^5/sec	4.6 x 10^5/sec
Central Luminosity	μ^+	1.6 x 10^4/sec/cm^2	3.0 x 10^4/sec/cm^2
	μ^-	----	----
Central Momentum (P)		85.5 MeV/c	----
Momentum Spread ($\Delta P/P$)		6.7%	----

All rates are for a 100 μamp proton beam incident on a 10 cm Be target

characteristics of surface μ^+: (1) surface μ^+ are at least 99.9% polarized
in a direction opposite to the beam momentum and (2) the surface μ^+ beam
momentum distribution has a sharp "edge" at a momentum of 29.8 MeV/c, which
translates into a kinetic energy of 4.1 MeV. Because of their low and well
defined energy, surface μ^+ have a high (~140 mg/cm^2) stopping density and a
rather small range spread.

Another advantage of surface μ^+ arises because the μ^+ originate
directly from the pion production target. This feature provides a rather
small source for surface μ^+ in comparison to the extended conventional muon
source. In the case of surface μ^+, the production target is imaged at the
final focus thereby producing a small (~2 cm diameter) beam spot. Owing to
the low energy and monochromatic nature of the surface muon beam, surface
muons have a high stopping density as well. The small beam spot and high
stopping density of surface μ^+ make it possible to stop muons in small
and/or low density targets. In particular, the work described in this
dissertation involves the use of low density SiO_2 powder targets and could
not have been carried out without a high intensity surface μ^+ beam. The
measured beam parameters for M20 operating in surface mode are given in
Table II.2.

By tuning the channel to lower momenta, it is possible to collect and
transport μ^+ which are produced by π^+ decaying inside the pion production
target. These muons are, for lack of a better term, called subsurface
muons. Consider the cross section in the pion stopping distribution having
a width Δy and located inside the production target a distance y from the
emitting surface. The decay μ^+ emitted from π^+ stopped in this region, must
traverse the distance y through the production target before reaching the

Table II.2   Surface Muons at 75° (M20-A) and 37.5° (M20-B)

Beam Parameters		M20-A	M20-B
Total Flux		2.7×10^6/sec	1.5×10^6/sec
Central Luminosity		1.6×10^5/sec/cm^2	----
Central Momentum (P)		29.4 MeV/c	----
Momentum Spread ($\Delta P/P$)		6.4%	7.1%
Electron Contamination (e^+/μ^+)		40/1	40/1
Polarization		100%	100%
Beam Spot (fwhm)	x	4.5 cm	----
	y	4.3 cm	----
Divergence	x	---	----
	y	---	----

All rates are for a 100 μamp proton beam incident on a 10 cm Be target

emitting surface. Thus the μ^+ are degraded by the production target before being collected and transported down the beamline. The range R_o of the decay μ^+ is approximated by [13]

$$R_o = k_o P_o^{7/2} \qquad \text{(II.1)}$$

where P_o is the initial μ^+ momentum (in this case, 29.8 MeV/c) and k_o is a constant that depends upon the stopping medium (i.e., the production target). It can then be easily argued that the subsurface μ^+ rate is proportional to the range R_o multiplied by the appropriate decay factor.

The utility of subsurface muons is easily understood by now considering the stopping distribution of the transported subsurface μ^+ beam of momentum $P < 29.8$ MeV/c. Similar to μ^+ in the production target, the range R of the transported beam is given approximately by [13]

$$R = kP^{7/2} \qquad \text{(II.2)}$$

where the constant k depends on the sample in which the beam is stopped, (i.e., $k \approx 140 \text{mg/cm}^2 \, (29.8 \text{ MeV/c})^{-7/2}$, for surface μ^+). For a given spread in momentum and taking range straggling into consideration (typically ~10% of the range [14]), an estimate of the total stopping spread ΔR is then given by

$$\Delta R \approx \left[(0.1)^2 + (3.5 \, \Delta P/P)^2 \right]^{1/2} R$$
$$= k \left[(0.1)^2 + (3.5 \, \Delta P/P)^2 \right]^{1/2} P^{7/2} \qquad \text{(II.3)}$$

From this it is obvious that decreasing the momentum bite results in only a limited reduction in the stopping spread ΔR, while decreasing the momentum yields a dramatic decrease in ΔR. Thus the use of subsurface muons makes it

possible to tune for a desired stopping range spread ΔR.

An attempt is now being made to produce a low energy (0 to ~10 keV) μ^+ beam by utilizing the knowledge gained in low energy positron production research and drawing the appropriate analogies. Recent measurements [15] show that when e^+ of keV energies are implanted into LiF and NaF, they are reemitted isotropically from the solids with a continuum of energies having a maximum approximately equal to the alkali halide band gap. Details regarding the physics involved and a description of the prototype apparatus to test for the analogous μ^+ phenomenon are given in Appendix II.

II.B The μSR / MSR Technique

The experiments reported in this dissertation were performed using the conventional time-differential μSR technique [16-18]. In this type of measurement one records the arrival time t_μ of the μ^+ and its subsequent decay at time t_e, and then constructs a time histogram for the intervals defined by $\Delta t = (t_e - t_\mu)$. This technique requires the ability to unambiguously associate a given e^+ with the muon from which it was emitted. Normally, this requirement is satisfied by allowing only one muon at a time to be present in the sample.

In general, the time-differential μSR spectrum observed in a direction defined by the unit vector $\vec{n}$ with respect to the beam momentum can be expressed as

$$N(t) = N_o e^{-t/\tau_\mu} \left[1 + A_\mu \vec{P}_\mu(t) \cdot \vec{n} + A_{Mu} \vec{P}_{Mu}(t) \cdot \vec{n} \right] + B \qquad (II.4)$$

where N_o is a normalization constant, τ_μ is the mean muon lifetime, A_μ and A_{Mu} are the initial instrumental asymmetries for the μ^+ and muonium

signals, respectively, $\vec{P}_\mu(t)$ represents the muon spin polarization for the μ^+ signal and $\vec{P}_{Mu}(t)$ is the corresponding quantity for the muonium state and the constant B is a time independent background.

II.B.1 Zero and Longitudinal Field (ZF and LF)

In zero field, one acquires information regarding the time dependence of the μ^+ spin polarization by observing and comparing the μSR spectra at angles $\theta=0°$ and $\theta=180°$ with respect to the initial muon spin direction. A schematic representation of this is given in Figure II.3(a). In these directions, the observed μSR spectra are

$$\theta = \quad 0°; \quad N^0(t) \quad = N_o^0 \; e^{-t/\tau_\mu} \left[1 + A_\mu^0 \; G_{zz}^\mu(t) + A_{Mu}^0 \; G_{zz}^{Mu}(t) \right] + B^0$$

$$\theta = 180°; \quad N^{180}(t) = N_o^{180} e^{-t/\tau_\mu} \left[1 - A_\mu^{180} G_{zz}^\mu(t) - A_{Mu}^{180} G_{zz}^{Mu}(t) \right] + B^{180}$$

$$(II.5)$$

where the time evolution of the muon spin for the μ^+ and Mu signals are represented by the two zero field relaxation functions, $G_{zz}^\mu(t)$ and $G_{zz}^{Mu}(t)$, respectively.

II.B.2 Transverse Field (TF)

In weak transverse fields ($B_\perp \ll B_0$), the evolution of the muon spin polarization in muonium can be treated using perturbation theory [16]. In this approximation, triplet muonium $|a(t)\rangle = |1\rangle$ precesses in a sense opposite to that of a free μ^+ in the same field, with a Larmor frequency $\vec{\omega}_{Mu} = - 103\vec{\omega}_\mu$, while for Mu in the mixed state $|b(t)\rangle = s|2\rangle + c|4\rangle$ the μ^+ spin polarization oscillates at a high frequency which is on the order of

Figure II.3(a)
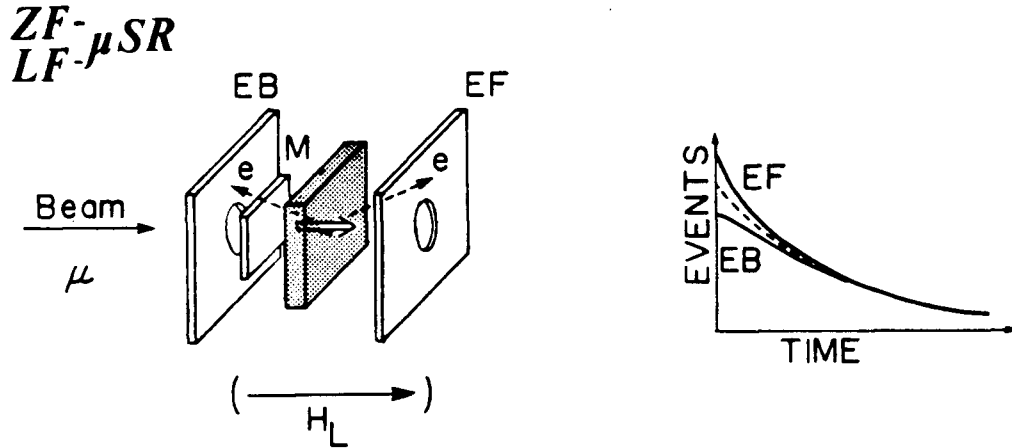
Figure II.3(b)
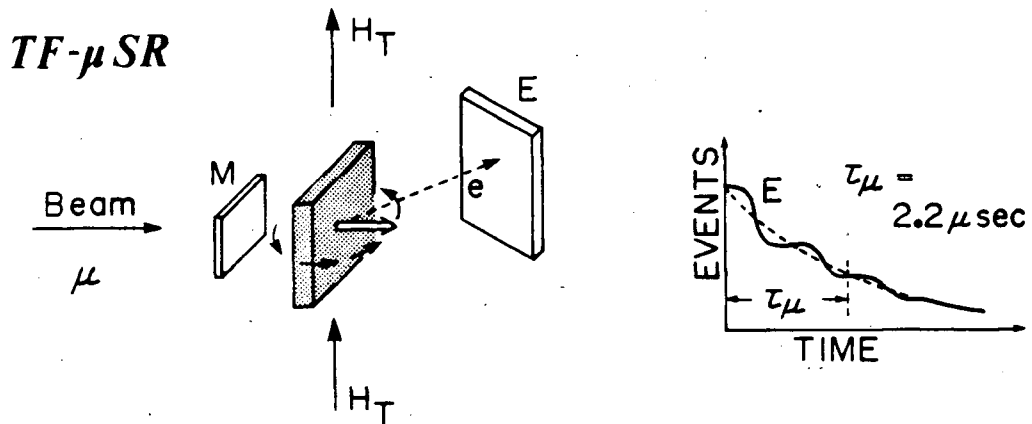
Figure II.3 Schematic representations of the μSR techniques; Figure II.3(a) shows the zero and longitudinal field configuration and Figure II.3(b) shows the corresponding diagram for transverse magnetic field. Figures taken from Y.J. Uemura, Ph.D. Thesis, University of Tokyo, 1981.

the hyperfine frequency ω_{00}. However, since the experimental timing resolution is typically about 2 ns, the hyperfine oscillation is generally not observable, making this half of the muonium ensemble appear to be completely depolarized. The transverse field geometry is schematically represented in Figure II.3(b). In very weak fields ($B_\perp \lesssim 10$ G), the transition frequencies ν_{12} and ν_{23} are approximately equal and thus the μSR positron spectra take the simple form

$$N^i(t) = N^i_o e^{-t/\tau_\mu} \left[1 + A^i_\mu G^\mu_{xx}(t) \cos\left(\omega_\mu t - \Phi^i_\mu\right) + A^i_{Mu} G^{Mu}_{xx}(t) \cos\left(\omega_{Mu} t + \Phi^i_{Mu}\right) \right] + B \tag{II.6}$$

where Φ^i_μ and Φ^i_{Mu} are the muon and muonium phase angles, defined by the orientation of the particular telescope with respect to the initial muon spin direction, $G^\mu_{xx}(t)$ is the transverse field relaxation function for the μ^+ signal and $G^{Mu}_{xx}(t)$ is the corresponding function for muonium.

II.C Experimental Apparatus and Data Acquisition

During the course of these experiments, both the experimental apparatus and data acquisition system have evolved. Since it is not possible to describe the different stages of development here, only the present state of affairs is discussed in any detail.

II.C.1 The μSR Spectrometer

The μSR ("Eagle") spectrometer, shown in Figure II.4, was designed to take full advantage of the properties of surface muons. One of the most important design constraints arises because of the relatively short range
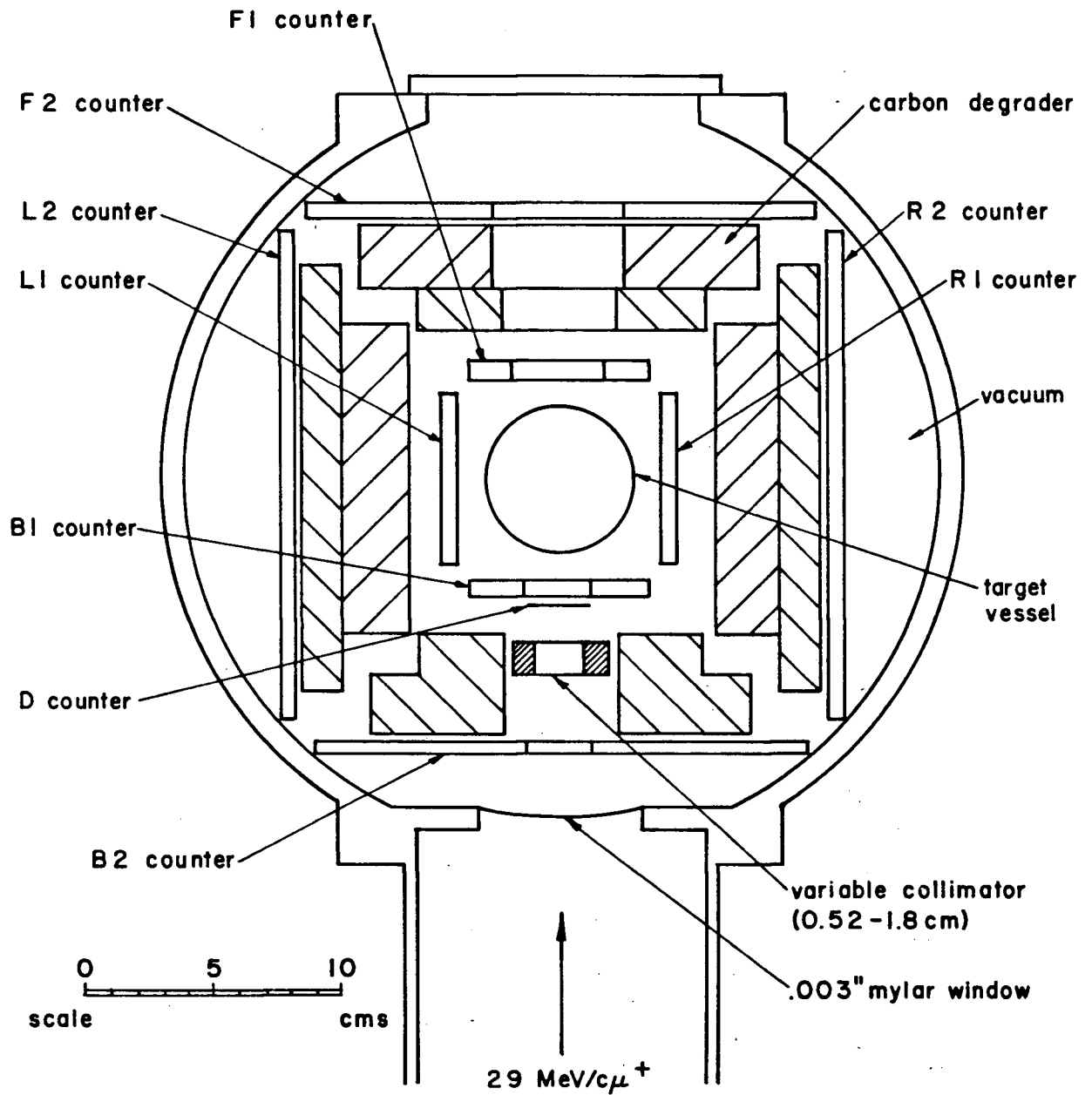
Figure II.4   The "Eagle" μSR spectrometer.

($\sim$140 mg/cm^2) and large multiple scattering of surface μ^+, which dictates

the requirement of minimizing the amount of mass in the beam path. To this

end, the spectrometer is evacuated to a pressure of $\sim$5 microns with both the

counter array and sample situated inside. The spectrometer vacuum is

isolated from the beam line and cyclotron vacuum by a 76 μm (0.003") mylar

window through which the μ^+ enters the spectrometer.

After entering the spectrometer, the positive muons pass through a

variable collimator and are detected by a 0.305 mm (0.012") thick

scintillator ("D" counter) before finally stopping in the target assembly.

Four positron telescopes, each comprised of two 6.35 mm (0.25") plastic

scintillators (B1-B2, F1-F2, R1-R2, L1-L2), are arranged around the target

assembly, perpendicular (B and F telescopes) and parallel (R and L

telescopes) to the beam direction. The B telescope (up stream) is provided

with a 5 cm hole in its center to pass the μ^+ beam. The F telescope (down

stream) is also provided with a 5 cm hole, primarily intended to pass beam

positrons thereby reducing possible backgrounds due to beam contamination.

The positron telescope array subtends a total solid angle of about $\frac{2}{3}(4\pi)$

steradians. The two counters comprising each of the four positron

telescopes are separated by a 2.5 cm thick graphite moderator. This has the

effect of increasing the positron asymmetry by cutting off the low energy

end of the of the Michel spectrum [16] and helps prevent scattered beam

(29.8 MeV/c) positrons from firing one of the positron telescopes. The

light produced in the counters (scintillators) is transmitted through the

bottom of the vacuum chamber via UVT Lucite light guides and then detected

and amplified by RCA 8575 photomultipliers.

The variable collimator (2.5 cm thick brass), immediately upstream of

the D-counter, provides four easily selectable collimator diameters (5.2, 8.0, 10.8 and 18.0 mm) and serves to define the incoming μ^+ beam. The collimator is positioned between the B1 and B2 counters such that decay positrons from μ^+ stopped in the collimator have only a small probability of firing both counters of the B-telescope, which would result in a bad event.

The present spectrometer has four pairs of coils which provide magnetic fields in three orthogonal directions. A pair of water-cooled Helmholtz coils, having a mean diameter of 56 cm and a B/I factor of 4.63 G/A, provides a magnetic field in the "transverse-vertical" direction (i.e, transverse to the incident muon momentum and vertical in the lab frame). In principle, these coils can produce 6.5 kG, however because of the small turning radius of surface muons in a magnetic field and the geometry of the spectrometer itself, the apparatus is limited to fields below about 500 G.

A pair of air-cooled coils, not in Helmholtz configuration, provide a field in the "longitudinal" direction (i.e., along the incident muon momentum) from 0-12 G. When connected in series, the coils have a B/I factor of about 1 G/A. With this arrangement, one can study the longitudinal polarization of the μ^+ spin as a function of time by observing the decay spectrum in the F and B telescopes.

The remaining two pairs of coils are air-cooled and provide small (~1 G) bucking fields in the "transverse-horizontal" (i.e., transverse to the incident muon momentum and horizontal in the lab frame) and longitudinal directions. These bucking coils are used to achieve zero field plus or minus ~100 mG; however, they do not automatically compensate for time dependent drifts which may introduce small field fluctuations (~0.2 G) over several hours.

The limitations of the Eagle spectrometer, namely the inability to do research in a high (> 500 G) field or a stable zero field environment, will be overcome with the commissioning of a new apparatus dubbed "Omni" which is currently under construction. This apparatus has three pairs of water-cooled Helmholtz coils that produce magnetic fields in three orthogonal directions; longitudinal, transverse-vertical and transverse-horizontal. The longitudinal coils are capable of producing high fields (⩽ 6 kG) while the other two can produce maximum fields of only ~ 100 G. The longitudinal orientation of the high field coils makes possible research in high fields, since the μ^+ enter the spectrometer along the field lines and thus their trajectories, except for focusing effects, remain unaffected. The two low field Helmholtz pairs can of course be operated independently to produce fields of up to ~ 100 G in the two transverse directions; however, they will be utilized primarily as bucking coils. A feedback system coupling all three Helmholtz pairs along with two strategically placed 3-dimensional Hall probes will be used to produce a stable, time independent zero field environment with a stability of ~10^{-4} G, limited by the sensitivity of the Hall probes.

II.C.2 Electronics and Logic

The time-differential data acquisition electronics has evolved during the course of the present study, primarily due to the introduction of the LeCroy 4204 TDC. From a μSR point of view, the 4204 possesses several attractive features. Two of the more important attributes are its buffer memory and a nominal time resolution of 156.25 ps. With the incorporation of a buffer memory, the 4204 TDC effectively combines all the functions

performed by the TRIUMF B080 1 GHz TDC and EG&G C212 pattern unit, as

employed in the previous system [19]. This feature greatly reduces the

event processing dead time.

The signals from the photomultipliers are transmitted along ~30 m of

coaxial cable before being discriminated and routed through the NIM logic

shown in Figure II.5. A μ^+ entering the spectrometer first passes through

the D-counter thereby generating a pulse at a time t_μ which both starts

the TDC and also triggers a pileup gate that defines the time window T for

the subsequent decay e^+ event. At a later time t_e the μ^+ decays, emitting

a positron preferentially along its spin direction. If the decay e^+ is

detected by one of the four positron telescopes, within the preselected time

window T (typically 10 μs), a pulse is generated which stops the TDC. If a

decay e^+ is not detected within the time T, the TDC is automatically reset.

Constant fraction discriminators (CFD) were used on the critical timing

signals. The discriminated pulses from the counters comprising the four

positron telescopes are routed into four separate coincidence units. The

two-fold coincidences ($e^+E_i = E_i1 \cdot E_i2$, etc.) ensure that accepted events

correspond to decay positrons that pass through both telescope counters and

the carbon degrader separating them. The third coincidence, shown in Figure

II.5, was not employed in the present study. The outputs of the four

coincidence units are logically "OR-ed", with the resulting pulse serving as

the TDC stop. Simultaneous with stopping the TDC, pulses from each of the

four telescopes are also routed to set identification bits in NIM-ECL

converter units, thereby identifying which e^+ telescope was fired. The data

are written into the PDP-11 memory via a CAMAC computer-logic interface

which is serviced by a Bi-Ra Microprogrammed Branch Driver (MBD-11). The
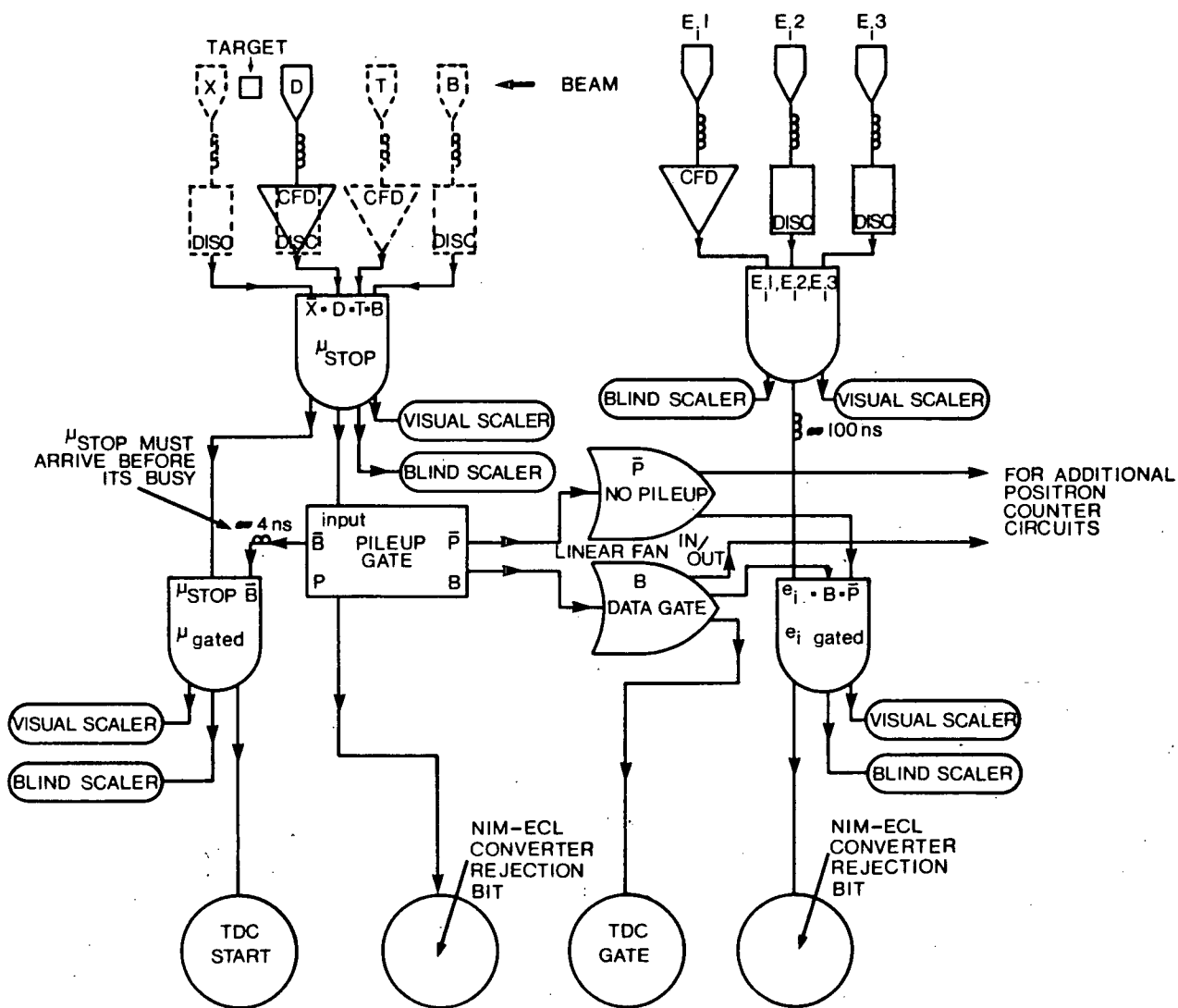
Figure II.5 Data acquisition electronics. Only the circuit for one positron telescope is shown.

MBD reads the memory buffer of the 4204 TDC, identifies the telescope that generated the event, and then performs the necessary functions required to increment the histogram bin corresponding to the measured time interval $(t_e - t_\mu)$. To guard against possible loss of data due to computer failure, the data are periodically updated on an RL02 disk.

The requirement of having only one μ^+ present in the sample at a time is fulfilled with the use of the pileup gate (model: GP 100/N EG&G Ortec). The pileup gate (data gate) is triggered on an incident μ^+ pulse in the D-counter and latched for a preset time T (normally set to 4-8 muon lifetimes). If a positron is detected during the data gate period T, a "good" event is logged and the appropriate histogram updated. There are however "bad" events that, if left unsuppressed, would introduce distortions into the spectra. The two most important processes that produce "bad" events are early second μ^+ events ($\mu-\mu-e$), where the second μ^+ arrives during the period T but before t_e, and late second μ^+ events ($\mu-e-\mu$), where the second μ^+ arrives after t_e. In earlier versions of the data aquisition electronics [19] the $\mu-\mu-e$ events were rejected in logic by vetoing multiple clock stops, thereby causing the clock to time out. The $\mu-e-\mu$ events on the other hand, which must be rejected after the clock has stopped, were rejected in software by setting a fake pattern in the now obsolete C212 unit when the second μ^+ was detected. The C212 and TDC were then read and cleared by the MBD. With the new system incorporating the 4204 TDC, the $\mu-\mu-e$ events are still rejected in the same manner as in the earlier version. The $\mu-e-\mu$ events, however, are rejected in the TDC itself which rejects multiple hit events. Thus the incorporation of the 4204 TDC into the data aquisition electronics has made it possible to process all

"bad" event rejection in hardware thereby greatly reducing the event processing dead time.

The rejection of the $\mu-\mu-e$ events places a restriction on the maximum rate at which one can take data using the time-differential technique. Since the time structure of the TRIUMF cyclotron has a period of 43 ns, which is much smaller than the muon lifetime, one can assume that the incident muons arrive with a time distribution closely described by Poisson statistics. From this assumption, and denoting the incident rate μ^+ by R_o the "good" event rate R_g is given by [19]

$$R_g = R_o \exp(-2R_o T) \tag{II.7}$$

For $R_o = (2T)^{-1}$, the "good" event rate R_g is maximized. With a typical gate width of 8 μs, the maximum "good" event rate occurs for a μ^+ stop rate R_o of about 62 kHz. This translates into a positron event rate of 2k-3k e^+/s per positron telescope. The logic level diagram for a "good" event is shown in Figure II.6, and a more detailed discussion of bad events and their effect on μSR spectra can be found elsewhere [19].

II.C.3 Targets

The SiO_2 powder used in these experiments was chosen because of its high specific surface area (390 ± 40 m^2/g [20]) and high yield (61 ± 3%) of extragranular muonium previously observed at 300 K [21] and at 6 K [22,23]. Some of the physical characteristics of this powder are given in Table II.3. The surfaces of these powders normally have ~4.5 chemisorbed hydroxyl (OH) groups per nm^2, corresponding to about half of the surface Si atoms being associated with a surface hydroxyl [20]. When evacuated at room temperature
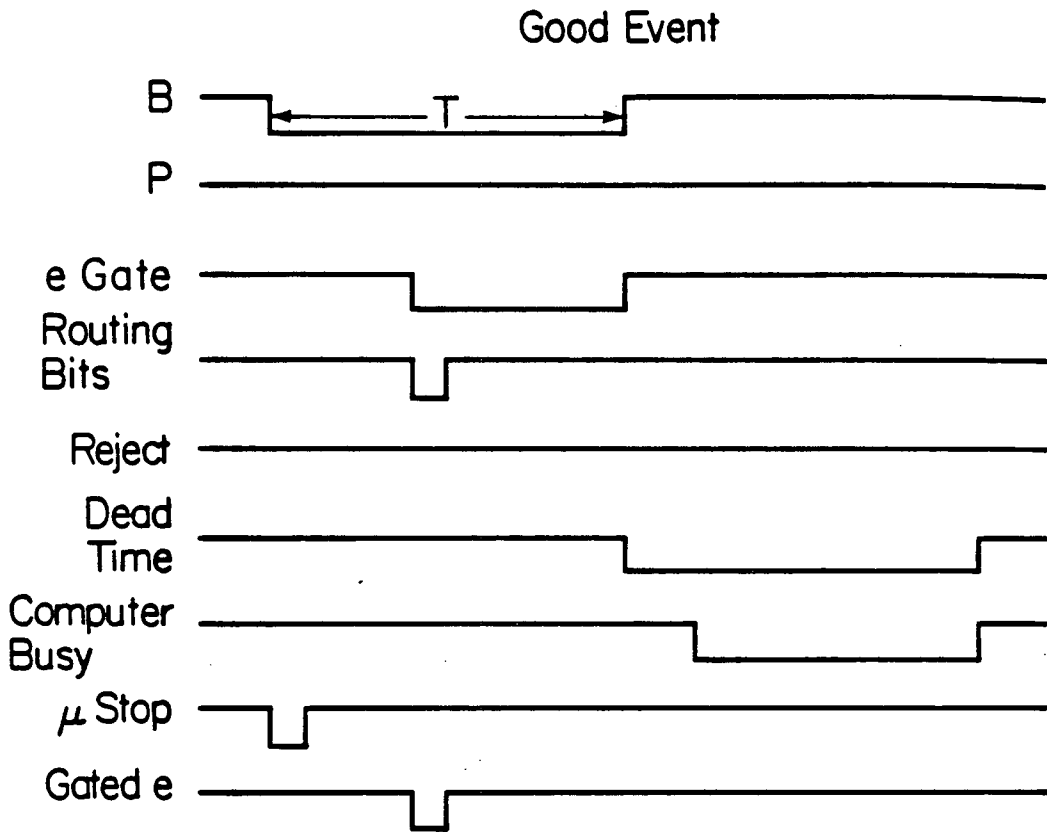
Figure II.6 Logic level diagram for a "good" event.

Table II.3 Physical Characteristics of the SiO_2 Powder

Property	Value
Supplier	Cabot Corporation, 125 High Street, Boston, MA., 02110 (U.S.A.)
Serial Number	EH-5
Density (unpacked)	0.033 gram/cm^3
Specific Surface Area	390 +/- 40 m^2/gram
Mean Grain Size	35 Angstrom (mean radius)
Major Impurities	Na 20-40 ppm P < 300 ppm Other < 30 ppm
Hydroxyl Concentration	average 3.5-4.5 groups per nm^2 maximum (calc.) 7.8 groups per nm^2

The above values are taken from reference [20].

(in a vacuum equal to 10^{-2} Torr) or heated above 110°C, the powder surfaces undergo "reversible dehydration". In this process, the surface hydroxyls combine to form H_2O which, when released, leaves behind additional siloxane groups (Si-O-Si). Above about 800 °C this hydrolysis is completed and the powder begins to sinter. The term reversible dehydration means that the powder surfaces can be restored to their original state by either exposure to air or immersion in water; with the target geometry used in the present study, this restoration process takes about 24 hours in air, subject to the ambient atmospheric moisture. It is therefore possible to vary the surface density of hydroxyls, and indeed study the reactions of various molecules with the surface hydroxyl groups [24-26]. The thermogravimetric analysis curve (measured at one atmosphere), for the SiO_2 powder used in the present study, is shown in Figure II.7.

Four targets were prepared with the SiO_2 powder essentially unaltered from the manufacturer's specifications. Five other targets were prepared with the same SiO_2 powder, but in this case hydrogen-reduced, with four of these having a non-zero platinum loading. The platinum loaded samples were prepared at Arizona State University, according to procedures described elsewhere [27]. Briefly, the loading procedure involves first physisorbing H_2PtCl_6 onto the SiO_2 powder surfaces. This molecule is then reduced in a hydrogen atmosphere at 500 °C, via the reaction $H_2PtCl_6 + 2H_2 \rightarrow Pt^0 + 6HCl$, to produce surface Pt atoms. Because of the high temperatures, the Pt atoms move about on the silica surface and eventually begin aggregating. Five levels of platinum loading were chosen for the catalyst samples; 0.0%, 0.001%, 0.01%, 0.1% and 1.0% by weight. All samples were characterized by well-known gas adsorption techniques at Stanford University. The specific
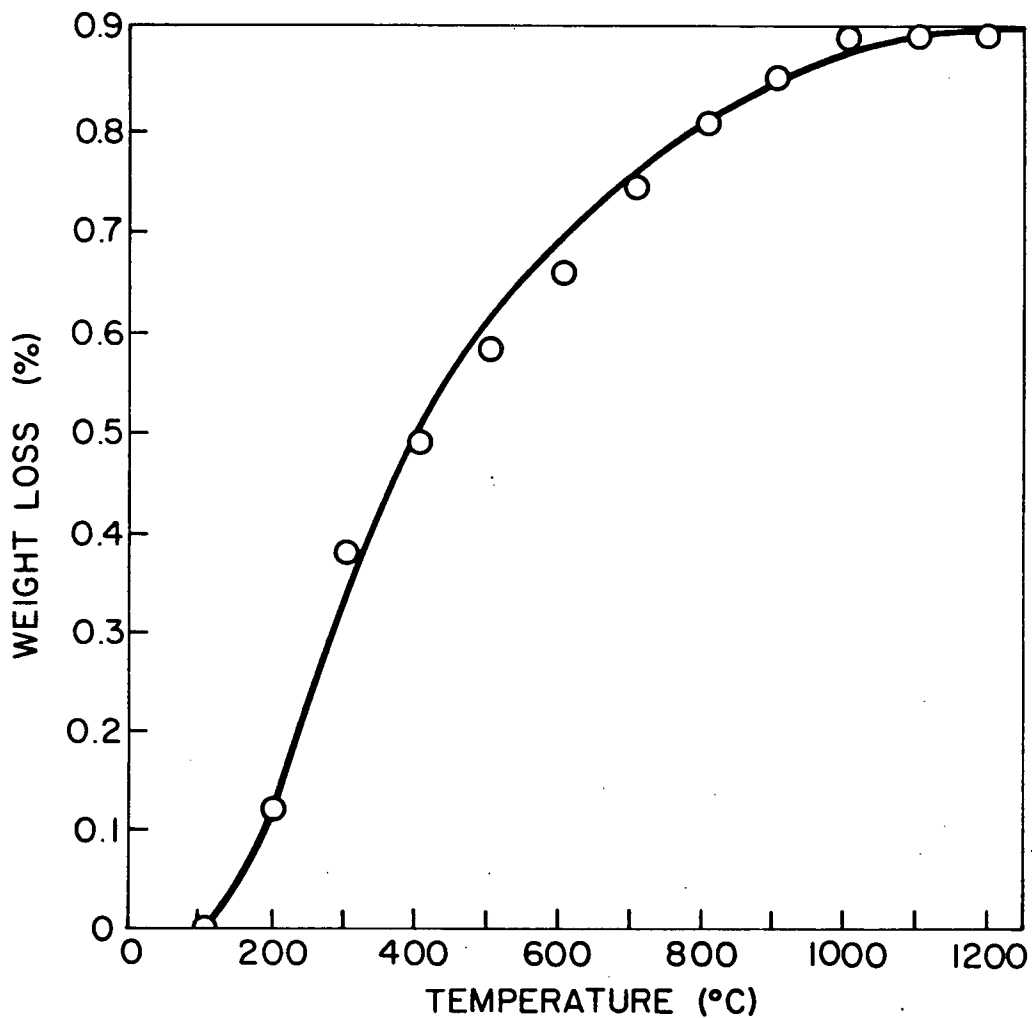
Figure II.7 Thermogravimetric analysis of Cab-O-Sil. Above 110 °C, the weight loss is caused by a gradual loss of water as the hydroxyls undergo condensation. Figure taken from reference [20].

surface area of the SiO_2 support, which had been hydrogen-reduced during the sample preparation, was measured using the B.E.T. adsorption isotherm technique [28] (in this case, N_2 at 77 K) and found to be 320 ± 20 m^2/g. This is somewhat smaller than the manufacturer's specification of 390 ± 40 m^2/g for the unreduced SiO_2 powder. Platinum dispersions (# of Pt atoms at surface / total # of Pt atoms in sample) were measured in both the 0.1% and 1.0% Pt loaded samples by hydrogen chemisorption [29], and were found to be 1.0 ± 0.02 and 0.39 ± 0.02, respectively. The percentage of the total surface area of the loaded catalysts which is attributable to the Pt atoms is then 0.08% for the 0.1% sample and 0.34% for the 1.0% sample.

The targets were prepared by compressing the SiO_2 powder into stainless steel vacuum vessels, onto which a 25 μm or 50 μm stainless window was then TIG (Tungsten Inert Gas) welded or electron beam welded. Welded stainless steel targets were used both for cleanliness and because of the need to prepare some of the samples by baking in vacuum at high temperatures. All heat treatments were performed in vacuum for a period of 10-12 hours prior to the experiments. The targets were evacuated through a 110 cm length of 0.635 cm (0.25") outer diameter (0.4 cm I.D.) stainless steel tubing, using a diffusion pump. The pumping system was isolated from the target assembly by a liquid nitrogen cold trap, to reduce the possibility of contamination arising from backstreaming. The pressure at the input of the diffusion pump was measured to be 10^{-6} Torr, whereas the ultimate pressure at the target (after baking at T > 110 °C) was measured to be 10^{-5} - 10^{-6} Torr. Although "low-magnetic" steels (types 316-L and 321) were used, there still existed some remnant magnetization, which was found to introduce a small relaxation of the muonium spin due to induced field inhomogeneity. Specific details

regarding the targets used in this work are given in Table II.4. All but
one of the targets used in the present study had 25 μm TIG welded windows.
The exception was target $SiO_2(3)$, which had a 50 μm electron beam welded
window.

II.C.4 Cryogenics

The evacuated samples were inserted through the top of a Janis ^{4}He
gas-flow cryostat (model: 10DT Super-VariTemp) which provides a uniform
low-temperature environment, variable from 1.8 to 300 K. The Janis cryostat
is mounted through the top of the Eagle spectrometer with the cryostat tail
extending down between the four positron telescopes. To minimize the mass
in the beam path the tail outer vacuum shield is removed, making the
cryostat insulating vacuum contiguous with the Eagle vacuum chamber. The
muons enter the cryostat by first passing through a 76.2 μm (0.0003")
aluminized mylar heat shield and then a 0.127 mm (0.005") mylar window
separating the helium gas thermal bath of the "sample space" from the
insulating vacuum.

The temperature is regulated by adjusting the vaporizer heater current
and the ^{4}He flow rate through a needle valve. The heater is incorporated
into a PID [30] temperature feedback system along with the thermometer
(mounted on the outside of the target vessel) which monitors the sample
temperature. For temperatures in the range 300 K - 75 K, a calibrated
platinum resistor was used, and for the range 100 K - 1.8 K, a calibrated
germanium resistor was employed. Some question may arise as to whether the
thermometers measure the "true" temperature of the sample (i.e., is the
sample at thermal equilibrium with the helium thermal bath). This was

Table II.4(a) SiO_2 Targets

Targets	Characteristic	Value
$SiO_2(1)$ • (Vol. = 4.48 ± 0.05 cm^3)	Mass of Powder Packing Density Surface Area	1.50 ± 0.05 g 0.335 ± 0.015 g/cm^3 585 ± 79.5 m^2
$SiO_2(2)$ (Vol. = 4.48 ± 0.05 cm^3)	Mass of Powder Packing Density Surface Area	0.50 ± 0.05 g 0.112 ± 0.012 g/cm^3 195 ± 39.5 m^2
$SiO_2(3)$ (Vol. = 6.63 ± 0.05 cm^3)	Mass of Powder Packing Density Surface Area	0.72 ± 0.05 g 0.109 ± 0.008 g/cm^3 281 ± 48.3 m^2
$SiO_2(4)$ (Vol. = 6.08 ± 0.05 cm^3)	Mass of Powder Packing Density Surface Area	1.76 ± 0.05 g 0.289 ± 0.011 g/cm^3 686 ± 89.8 m^2

Table II.4(b) Platinum Loaded SiO_2 Targets

Targets	Characteristic	Value
Pt(1) (0.0% loading) (Vol. = 4.38 ± 0.05 cm^3)	Mass of Powder Packing Density Surface Area	1.50 ± 0.08 g 0.61 ± 0.03 g/cm^3 480 ± 25.6 m^2
Pt(2) (0.001% loading) (Vol. = 4.38 ± 0.05 cm^3)	Mass of Powder Packing Density Surface Area	1.50 ± 0.08 g 0.61 0.03 g/cm^3 480 ± 25.6 m^2
Pt(3) (0.01% loading) (Vol. = 4.38 ± 0.05 cm^3)	Mass of Powder Packing Density Surface Area	1.50 ± 0.08 g 0.61 ± 0.03 g/cm^3 480 ± 25.6 m^2
Pt(4) (0.1% loading) (Vol. = 4.38 ± 0.05 cm^3)	Mass of Powder Packing Density Surface Area	1.50 ± 0.08 g 0.61 ± 0.03 g/cm^3 480 ± 25.6 m^2
Pt(5) (1.0% loading) (Vol. = 4.38 ± 0.05 cm^3)	Mass of Powder Packing Density Surface Area	1.50 ± 0.08 g 0.61 ± 0.03 g/cm^3 480 ± 25.6 m^2

tested experimentally by first stepping through the temperature range in increasing steps, and then repeating these measurements in reverse order. The data were found to be quite insensitive to the order in which the temperature points were taken, indicating that the sample was indeed in thermal equilibrium with the helium bath of the cryostat.

III.C.5 Gas Handling

Figure II.8 shows the gas handling system used for physisorbing or chemisorbing controlled amounts of different gases onto the sample surface. By altering the surface characteristics in this fashion, and observing the associated change in the muonium behavior, one gains further insight into the relaxation and diffusion behavior of muonium on surfaces. In the present study, ^{4}He is deposited on the silica surfaces. The gas handling apparatus is quite typical for the purpose at hand and consists of a doser volume V_d (three different doser volumes were used for these experiments, 41.9 ± 0.16 cm^3, 36.5 ± 0.6 cm^3 and 28.2 ± 0.5 cm^3), a standard volume V_s (1331 ± 28 cm^3) and a metering valve V_4 on the output. The pressure in the system is monitored by a Baratron gauge (MKS model: 220BHS-2A1-B-1000) capable of measuring pressures in the range 0-100 Torr. This gauge is accurate to within 0.15% of the reading and is also temperature compensated with an associated error of 0.01% F.S./Δ°C. The latter source of error was not taken into account in the data analysis, and no "zero drift" in the gauge was observed. The dead volume in the output section after valves V_4 and V_5 was measured to be 35 ± 2 cm^3, not including the targets.

During gas deposition, the sample temperature was kept low enough to ensure that any gas atoms reaching the surface would be adsorbed; for ^{4}He on
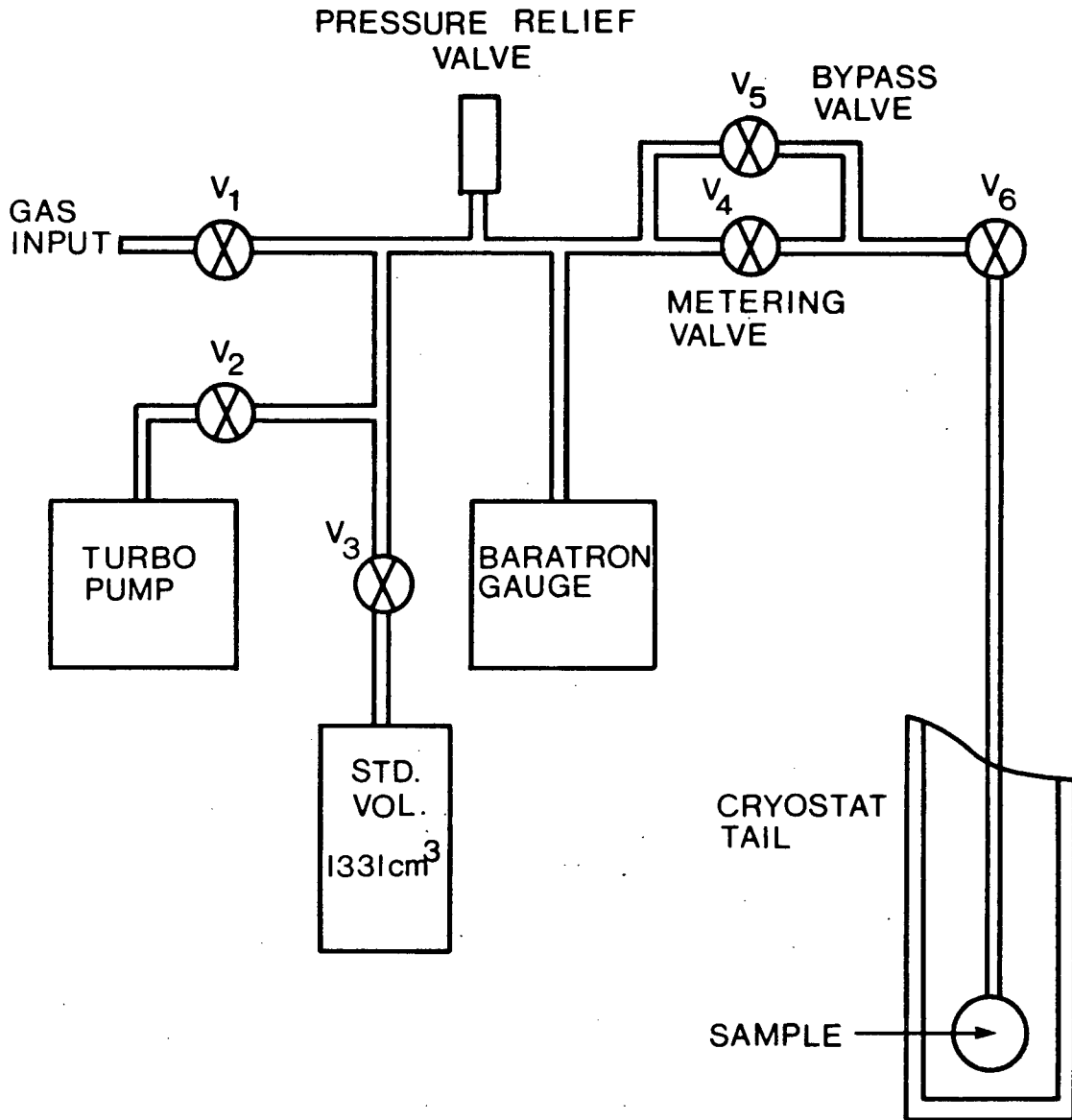
Figure II.8 Gas handling system.

SiO_2, the temperature was typically kept below 10 K. To estimate the amount of gas required for fractional or complete monolayer coverage, one calculates the change in pressure ΔP in the doser volume, according to the simple equation

$$\Delta P = f \frac{A}{\sigma_x V_d} RT \tag{II.8}$$

where f is the fraction of the surface area to be covered, A is the surface area of the sample, R is the gas constant (1.036×10^{-19} torr cm^3 K^{-1}), σ_x is the area covered by an adsorption atom or molecule X ($\sim 10^{-15}$ cm^2, for helium on silica), V_d is the doser volume of the system and T is the doser volume temperature.

For physisorption of atoms and molecules, the following gas handling procedure was used:

(1) With V_1, V_3, V_4, V_5 and V_6 closed, open V_2 and evacuate the system using the turbo pump.

(2) Once the system is evacuated, close V_2.

(3) Open V_1 to pressurize doser volume to desired level.

(4) Once the desired pressure is attained, close V_1 and note pressure on the Baratron gauge.

(5) Open V_4 or V_5 (depending on requirements placed on flow rate).

(6) Open V_6 and wait for the system to come to equilibrium, (may take 30 minutes).

(7) Note pressure on Baratron gauge.

(8) Take data.

(9) Note pressure once again to ensure that the system was near equilibrium.

(10) Repeat this procedure as many times as necessary to achieve the desired surface coverage.

Because one is normally dealing with small quantities of gas and small flow rates, the temperature of the sample is only briefly perturbed by this procedure; such temperature fluctuations were normally unobservable.

II.D Data Analysis

The MINUIT [31] minimization package was used to provide least-squares fits to the data and to generate the statistical errors on the function parameters.

II.D.1 Transverse Field Spectra

For the transverse field data, the raw spectra were fit separately, with the function given in Equation II.6. In these fits, the transverse field muonium relaxation function was assumed to be of the form

$$G_{xx}^{Mu}(t) = \exp\left[-(\lambda_\perp^{Mu} + \lambda_o)t\right] \tag{II.9}$$

where λ_o $(\ll \lambda_\perp^{Mu})$ is the relaxation rate due to field inhomogeneity and was determined by a measurement at low temperature (~ 6 K) with several monolayers of ^{4}He on the grain surfaces; earlier experiments [22,23] on fine alumina powders have shown that Mu is protected from the depolarization centers on the oxide surface by just such a helium film. The two parameters of interest to the present study are the initial muonium asymmetry A_{Mu}^i and the relaxation rate $\lambda_\perp^{Mu}$. The fitted asymmetries for each positron telescope were treated independently, whereas the relaxation rates were combined in a weighted average.

II.D.2 Zero and Longitudinal Field Spectra

For the zero and longitudinal field data, the F and B spectra were

first treated separately by removing the respective backgrounds using the

"t<0" time bins. After this, they were combined to form an asymmetry

spectrum defined by

$$ASY = \frac{\left[N^B(t) - B^B\right] - \left[N^F(t) - B^F\right]}{\left[N^B(t) - B^B\right] + \left[N^F(t) - B^F\right]} \qquad (II.10)$$

in which the muon lifetime is automatically divided out. The resulting

spectrum was then fit using Equation II.10 with the appropriate relaxation

function assumed.

In practice, the two telescopes do not in general have the same solid

angle, with respect to the target, or efficiencies. These differences are

parameterized in terms of a relative efficiency parameter $\alpha_o = N_o^F/N_o^B$. The

associated correction is given by the equation

$$ASY_{(corr)} = \frac{(1 + \alpha_o)ASY - (1 - \alpha_o)}{(1 + \alpha_o) - (1 - \alpha_o)ASY} \qquad (II.11)$$

The resulting asymmetry spectrum is then referred to as a "corrected

asymmetry".

CHAPTER III -- THEORY OF MUONIUM RELAXATION

To obtain a clear interpretation of the experimental results, it is important to understand the different relaxation mechanisms through which the μ^+ spin may be depolarized. For muonium, the ensemble spin polarization can be lost through interactions with the environment by means of the five relaxation mechanisms:

    (1)   Random Local Magnetic Fields
    (2)   Random Anisotropic Hyperfine Distortions
    (3)   Chemical Reactions
    (4)   Spin Exchange
    (5)   Superhyperfine Interactions

In this chapter, these mechanisms, along with the associated spin relaxation functions, are discussed. The effect of diffusion on these relaxation functions is also considered. Since the mixed state $|b_0\rangle$ is normally unobservable, this discussion will be restricted to the half of the muonium ensemble initially in the polarized triplet state $|a_0\rangle$.

III.A Spin Relaxation Functions

For a muonium atom, the expectation value of the μ^+ spin polarization is defined by the equation

$$\langle \underset{\sim}{S}^\mu_{op}(t) \rangle = \text{Tr}\{\underset{\sim}{S}^\mu_{op}(t)\ [\tfrac{1}{4} U^\mu + (\underset{\sim}{S}^\mu_{op}(0) \cdot \underset{\sim}{S}^\mu_{in})]U^e\ \rho_s(0)\}$$

$$= \frac{1}{4}\text{Tr}\{\underset{\sim}{S}^\mu_{op}(t)\ \rho_s(0)\} + \text{Tr}\{(\underset{\sim}{S}^\mu_{op}(t)\ \underset{\sim}{S}^\mu_{op}(0)\ \rho_s(0)) \cdot \underset{\sim}{S}^\mu_{in}\}$$

(III.1)

where U^μ and U^e are the unit operators for the μ^+ and e^- spins, respectively, $[\tfrac{1}{4} U^\mu + (\underset{\sim}{S}^\mu_{op}(0) \cdot \underset{\sim}{S}^\mu_{in})]U^e$ is the initial spin density operator associated with the spin dynamics of the muon, $\rho_s(0)$ is the initial spin density matrix for the environment and $\underset{\sim}{P}^\mu_{in} = 2 \cdot \underset{\sim}{S}^\mu_{in}$ is the incoming muon spin

polarization vector. In general, the first term in Equation III.1 reduces
to zero because the trace over any spin vector operator is zero. This makes
it possible to express the expectation value, $\langle S_{\sim op}^{\mu}(t) \rangle$, in terms of a second
rank spin-spin autocorrelation tensor $g(t)$, defined as

$$
\begin{aligned}
\underset{\sim}{g}(t) &= Tr\{ S_{\sim op}^{\mu}(t) \; S_{\sim op}^{\mu}(0) \; \rho_s(0) \} \\
&= Tr\{ \exp[iHt(2\pi/h)] \; S_{\sim op}^{\mu}(0) \; \exp[-iHt(2\pi/h)] \; S_{\sim op}^{\mu}(0) \; \rho_s(0) \}
\end{aligned}
\tag{III.2}
$$

where H is the spin Hamiltonian of the system. With this, Equation III.1
can be written as

$$
\langle S_{\sim op}^{\mu}(t) \rangle = \underset{\sim}{g}(t) \cdot S_{\sim in}^{\mu}
\tag{III.3}
$$

where the time evolution of the μ^{+} spin polarization is completely
determined by the motion tensor $g(t)$. In zero and longitudinal field, $\underset{\sim}{g}(t)$
is defined as the relaxation tensor. In transverse field, however, this
tensor includes oscillatory terms corresponding to Larmor precession which
are omitted in the definition of the transverse field relaxation tensor.

III.A.1 Random Local Magnetic Fields (RLMF)

In the context of the spin-spin interaction between a magnetic probe
and some weak dipolar field distribution, the spin Hamiltonians for triplet
muonium and for positive muons are mathematically equivalent, except that
the former has a magnetic moment which is ~103 times greater than the
latter.

The general spin Hamiltonian for a muonium atom, in the polarized
triplet state, interacting with N nuclear spins is given by the equation

$$
H = \sum_{j=1}^{N} \left(H_j^d + H_j^q \right) + H^z
\tag{III.4}
$$

where H_j^d represents the dipolar interactions between the muonium atom and

the N neighboring nuclei, H_j^q represents the quadrupolar interactions of the

nuclear spins (due for instance to electric field gradients induced by the

presence of the muonium atom) and H^z are the Zeeman terms. Note that any

dipolar interactions among the nuclear spins have been neglected. Because

of the desire to treat triplet muonium the same as a positive muon, one

defines $\underset{\sim}{S}_{op}$ to be the spin operator of the magnetic probe (μ^+ or Mu, etc.)

and γ_s (= $2\pi\bar{\gamma}_s$) as the corresponding magnetogyric ratio. By further

defining $\underset{\sim}{J}_{op}^j$ as the spin operator of the jth nucleus, and γ_J (= $2\pi\bar{\gamma}_J$) as the

corresponding magnetogyric ratio, the Zeeman term is written as

$$H^z = (h/2\pi) \gamma_s(\underset{\sim}{S}_{op} \cdot \underset{\sim}{B}) - \sum_{j=1}^{N} (h/2\pi) \gamma_J(\underset{\sim}{J}_{op}^j \cdot \underset{\sim}{B}) \qquad (III.5)$$

In addition, the dipolar terms can be written

$$H_j^d = (h/2\pi)^2 (\gamma_s \gamma_j)(r_j)^{-3} [(\underset{\sim}{S}_{op} \cdot \underset{\sim}{J}_{op}^j) - 3(\vec{n}_j \cdot \underset{\sim}{S}_{op})(\vec{n}_j \cdot \underset{\sim}{J}_{op}^j)] \qquad (III.6)$$

and the quadrupole terms are

$$H_j^q = (h/2\pi) \frac{\omega_q}{3} [3(\vec{n}_j \cdot \underset{\sim}{J}_{op}^j)^2 - J(J + 1)] \qquad (III.7)$$

where $\vec{n}_j$ is the unit vector in the direction from the muonium spin to the

j^{th} nucleus located at a distance r_j, $J(J + 1)$ is the eigenvalue of the

operator $\underset{\sim}{J}_{op}^j$ and ω_q represents the strength of the quadrupolar interaction.

The zero and low field (external field $\ll$ local field) spin relaxation

functions for a magnetic probe interacting with a random local magnetic

field were first discussed in 1967 [1,2]. In this formulation, the

quadrupole interactions are assumed to be negligible and the dipolar

interactions, which are in general described by a quantal local magnetic

field operator, are approximated by a static (continuous) effective local

dipole field $\vec{H}$. With these assumptions, the dipolar interaction term takes the simple form

$$\sum_{j=1}^{N} H_j^d = (h/2\pi) \, \gamma_s \left(\underset{\sim}{S}_{op} \cdot \vec{H} \right) \tag{III.8}$$

The effective field distribution is further assumed to be isotropic, with the magnitude of each component being distributed according to a continuous Gaussian distribution function of width Δ/γ_s, given by

$$f^G(H_i) = \frac{\gamma_s}{\sqrt{2\pi} \, \Delta} \exp\left[-\frac{\gamma_s^2 \, H_i^2}{2\Delta^2} \right] \quad ; \quad i = x, \, y, \, z \tag{III.9}$$

and

$$f^G(|H|) = \left[\frac{\gamma_s}{\sqrt{2\pi} \, \Delta} \right]^3 \exp\left[-\frac{\gamma_s \, |H|^2}{2\Delta^2} \right] \left[4\pi \, |H|^2 \right] \tag{III.10}$$

where Δ is the second moment of the field distribution [3]. Assuming this distribution, the zero field spin relaxation function of a magnetic probe in a system of static local dipolar fields is found to be [1,2]

$$g_{zz}^G(t) = \frac{1}{3} + \frac{2}{3} \left(1 - \Delta^2 t^2 \right) \exp\left(-\frac{1}{2} \Delta^2 t^2 \right) \tag{III.11}$$

which is the familiar static Gaussian Kubo-Toyabe function. In Equation III.11, The 1/3 component corresponds to the component of the local field directed parallel to the initial μ^+ spin polarization (i.e., the beam direction, z-axis), while the damped oscillation of the 2/3 component arises from the x and y components (i.e., normal to the incident muons polarization) of the random local field.

The application of a longitudinal field B_L (directed along the z-axis) can be used to effectively "decouple" the magnetic probe spin from the static local fields, thereby quenching the depolarizing effects of the dipolar interaction. For small longitudinal fields, one obtains the

expression [1,2]

$$g_{zz}^{G}(t,\omega_L) = 1 - \frac{2\Delta^2}{\omega_L^2} \left[1 - \exp\left(-\frac{1}{2}\Delta^2 t^2\right)\cos(\omega_L t)\right]$$

$$+ \frac{2\Delta^4}{\omega_L^3} \int_0^t d\tau \, \exp\left(-\frac{1}{2}\Delta^2\tau^2\right) \sin(\omega_L\tau) \qquad\qquad (III.12)$$

where, $\omega_L = \gamma_s B_L$. This function is shown for various values of ω_L in Figure III.1. Positive muons and the techniques of μSR are ideally suited for studying relaxation functions in any (or zero) external magnetic field, and thus provided the first experimental observation [4] of the Kubo-Toyabe function given in Equation III.11.

In the limit of "randomly ordered" moments (i.e., distributed randomly in the lattice), the local magnetic field distribution at the μ^+ site approximates a Lorentzian distribution [5-7]. The Lorentzian field distribution (HWHM = a/γ_s), can be written as

$$f^L(H_i) = \frac{\gamma_s}{\pi}\left[\frac{a}{a^2 + \gamma_s^2 H_i^2}\right] \quad ; \quad i = x, y, z \qquad\qquad (III.13)$$

and

$$f^L(|H|) = \frac{\gamma_s^3}{\pi^2}\left[\frac{a}{(a^2 + \gamma_s^2 |H|^2)^2}\right]\left[4\pi|H|^2\right] \qquad\qquad (III.14)$$

For the case of static local fields, the zero field spin relaxation function takes the form [8]

$$g_{zz}^L(t) = \frac{1}{3} + \frac{2}{3}(1 - at)\exp(-at) \qquad\qquad (III.15)$$

As in the case of the Gaussian Kubo-Toyabe function, given in Equation III.11, the static Lorentzian function $g_{zz}^L(t)$ exhibits the characteristic time dependent 1/3 component. Furthermore, an applied longitudinal field
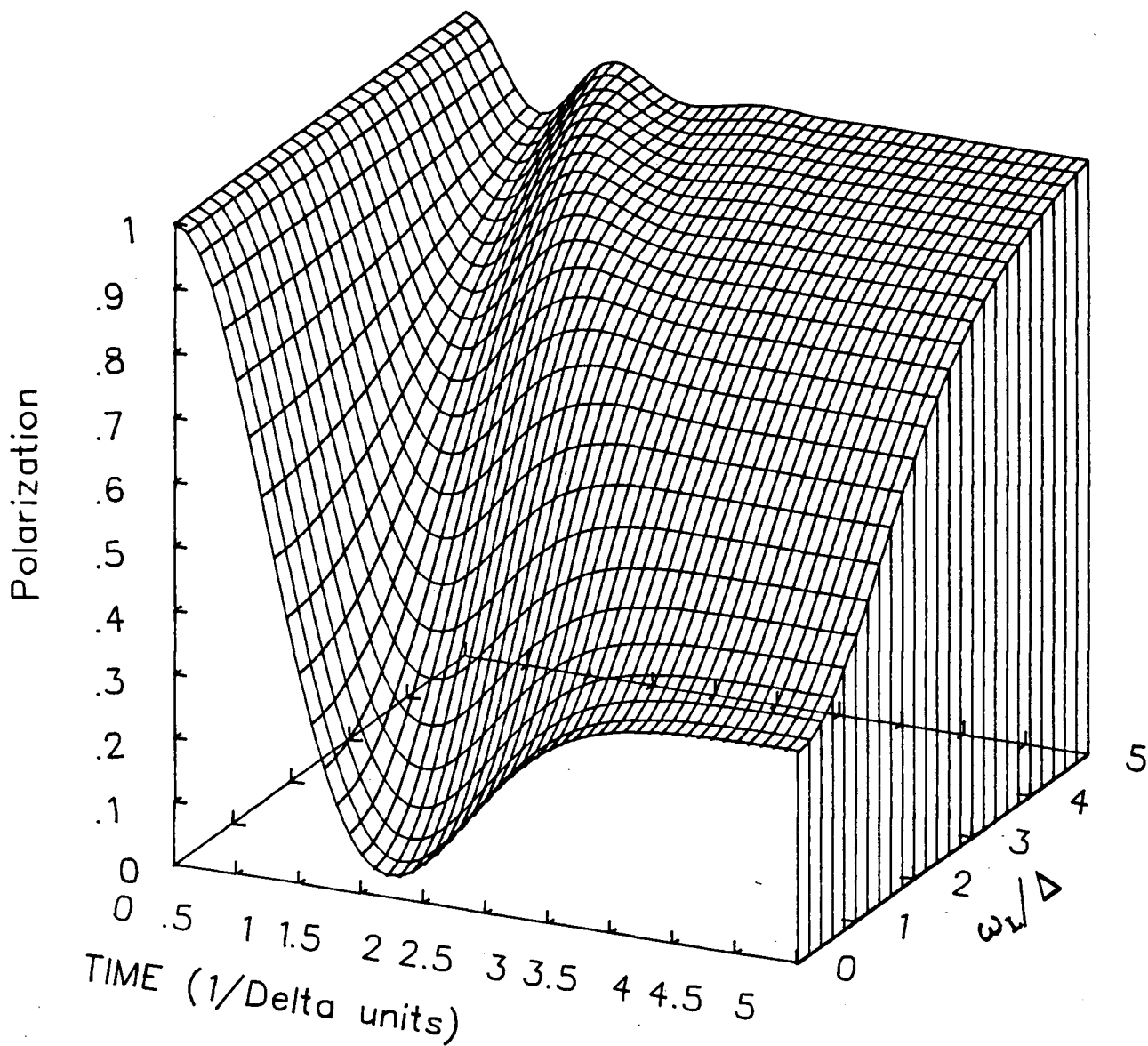
Figure III.1 Static longitudinal field spin relaxation function for a Gaussian random local field, plotted for various values of ω_L/Δ.

$B_L > H_i$ will effectively "decouple" the spin-spin interaction between the magnetic probe and the random fields according to the equation [8]

$$g_{zz}^L(t,\omega_L) = 1 - \frac{a}{\omega_L}\left[j_1(\omega_L t)\exp(-at)\right] - \left(\frac{a}{\omega_L}\right)^2\left[j_0(\omega_L t)\exp(-at)\right]$$
$$- a\left[1 + \left(\frac{a}{\omega_L}\right)^2\right]\int_0^t d\tau\left[j_0(\omega_L\tau)\exp(-a\tau)\right] \qquad (III.16)$$

where j_0 and j_1 denote Spherical Bessel functions, and $\omega_L = \gamma_s B_L$. This function is shown in Figure III.2 for selected values of ω_L.

The exact quantum mechanical solution for the time dependence of the μ^+ spin polarization, assuming the Hamiltonian of Equation III.4, has also been investigated [9-11]. The zero field relaxation functions $g_{zz}(t)$ obtained are found to deviate from the Kubo-Toyabe function, given in Equation III.11, at long times ($t \gg 2/\Delta$). This deviation, which manifests itself as extra oscillations in the long time tail, can be understood intuitively by noting that the exact quantum mechanical solutions allow spin-flip transitions involving the μ^+ and neighboring nuclei which, in the dilute limit, appear as coherent oscillations. This type of relaxation function has recently been observed experimentally for μ^+ in alkali fluorides [12], with results suggesting the μ^+ to be localized along the ⟨110⟩ axis, between two ^{19}F nuclei.

The corresponding transverse field function, for a magnetic probe interacting with local magnetic fields, is discussed in both the static and dynamic limits in section III.B.

III.A.2 Random Anisotropic Hyperfine Distortions (RAHD)

In condensed media, the muonium hyperfine coupling may be perturbed due to the electrostatic interaction between the muonium electron and the
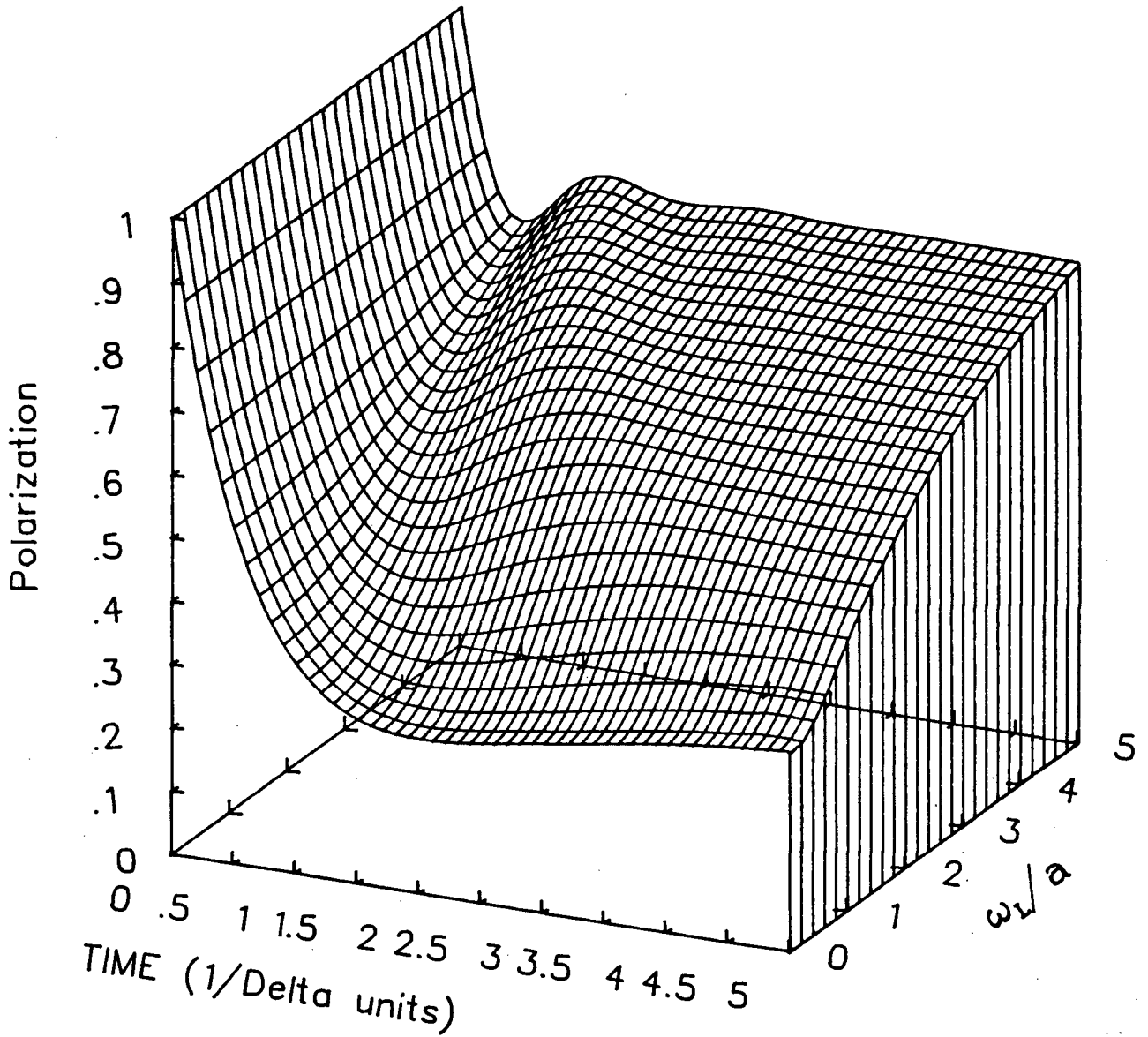
Figure III.2 Static longitudinal field spin relaxation function for a Lorentzian random local field, plotted for various values of ω_L/a.

lattice. As discussed in section I.C.1, a classic example of this interaction is the case of muonium in bulk quartz. The resulting change in the ground state wavefunction is transmitted to the μ^+ via the magnetic dipole-dipole coupling of the μ^+ and e^- spins. The contribution to the total Hamiltonian due to the hyperfine-lattice interaction is implicitly included in the $\underset{\sim}{W}$ tensor of the hyperfine term of the Hamiltonian

$$H = (h/2\pi)\left(\gamma_e \, \underset{\sim op}{S^e} - \gamma_\mu \, \underset{\sim op}{S^\mu}\right) \cdot \underset{\sim}{B} + (h/2\pi) \, \underset{\sim}{W} : \left(\underset{\sim op}{S^e} \, \underset{\sim op}{S^\mu}\right) \qquad \text{(III.17)}$$

If the distortion of the hyperfine coupling is isotropic, a shift in the hyperfine-structure interval ν_{00} will occur, along with a corresponding shift in the energy eigenvalues. The zero field eigenfunctions for the system will however remain functionally unaltered from the vacuum hyperfine states so that no additional time dependence of the μ^+ spin polarization is induced. In general, however, the distortion may have some anisotropic components, and in this case one observes dramatic effects even in zero field.

The time evolution of the μ^+ spin polarization for a generally anisotropic muonium hyperfine interaction is discussed in some detail in Appendix I. The approach that is taken involves expanding the hyperfine tensor $\underset{\sim}{W}$ in terms of spherical harmonics and using the expansion coefficients ω_{Lm} to parameterize the distortion. Because the hyperfine tensor $\underset{\sim}{W}$ involves only dipole-dipole and contact interactions, both of which have reflection symmetry, the antisymmetric part of the expansion is identically zero. Although interactions of this type may produce different distortions in the electron wavefunction of each muonium atom, they do not lead to a true (irreversible) relaxation of the muon spin vector for the individual muonium atoms. For an ensemble of muonium atoms, however,

depolarization can occur via ensemble dephasing, provided that there is a random distribution in the distortions of individual muonium atoms in the enemble. To describe the ensemble relaxation, an approximation of $\text{Tr}\{\rho_s(0)\}$ is adopted, where each of the ω_{2m}'s is assumed to be distributed according to some distribution function $f_{2m}(\omega_{2m})$. With this approximation, one has

$$\text{Tr}\{\rho_s(0)\} \approx \prod_m \int_{-\infty}^{\infty} d\omega_{2m} \, f_{2m}(\omega_{2m}) \qquad \text{(III.18)}$$

The motion tensor for the ensemble is then approximated by

$$\mathbf{g}(t) \approx \prod_m \int_{-\infty}^{\infty} d\omega_{2m} \, f_{2m}(\omega_{2m}) \, \text{Tr}\{\underset{\sim}{S}_{op}^{\mu}(t) \, \underset{\sim}{S}_{op}^{\mu}\} \qquad \text{(III.19)}$$

where the trace over the muon spin operators is included in the integral. The spin relaxation functions associated with a specific distortion symmetry are then calculated by averaging over the appropriate ω_{2m} distributions.

Of particular interest to the present study are the zero and transverse field spin relaxation functions for a randomly oriented system such as in the case of muonium in bulk fused quartz or on the surface of fine silica powders. To calculate these functions, one must also average over all possible orientations. Consider the combination of a cylindrical distortion coupled with a planar distortion, which are parameterized by the frequencies ω_{20} and ω_{22}^M, respectively. Assuming each of these frequencies to be distributed according to a Lorentzian or Lorentzian-like distribution with zero average, as discussed in Appendix I, one has

$$f(\omega_{20}, \omega_{22}^M) = \left\{\frac{1}{\pi}\frac{\sigma_{20}}{(\omega_{20})^2 + (\sigma_{20})^2}\right\}\left\{\frac{4}{\pi}\frac{\sigma_{22}^M \, \omega_{22}^M}{[(\omega_{22}^M)^2 + (\sigma_{22}^M)^2]^2}(2\pi)^{-1}\right\} \qquad \text{(III.20)}$$

where σ_{20} and σ_{22}^M represent the respective widths (HWHM) of the frequency distributions. Ignoring the mixed state component of the muonium ensemble,

the polarized triplet muonium static relaxation function in zero field is found to be

$$g_{zz}^{rh}(t) = \frac{1}{6} \left(1 - \frac{1}{2} \overset{M}{\sigma}_{22} t\right) \exp\left(-\frac{1}{2} \overset{M}{\sigma}_{22} t\right)$$
$$+ \frac{1}{3} \left(1 - \frac{1}{4} \overset{M}{\sigma}_{22} t\right) \exp\left[-\frac{1}{4}(\overset{M}{\sigma}_{22} + 3\sqrt{2/3}\, \sigma_{20}) t\right]$$

(III.21)

This result can be better understood by considering the two cases of a purely cylindrical distortion and a purely planar distortion, separately. If one neglects the planar component of the hyperfine distortion, Equation III.21 becomes

$$g_{zz}^{rh}(t; \sigma_{20}) = \frac{1}{6} + \frac{1}{3} \exp\left[-\frac{3}{4}\sqrt{2/3}\, \sigma_{20} t\right]$$

(III.22)

Notice that as $t \to \infty$, this function tends to 1/6, (or 1/3 of the initial polarization of the triplet muonium ensemble). The time independent 1/6 component of the total ensemble spin polarization (residual polarization) arises because there exists a non-trivial zero frequency. This can be understood intuitively by drawing an analogy with random dipolar fields and noting that for a random hyperfine interaction, the cylindrical distortion axis will be directed along the z-axis (i.e., along the initial muon spin polarization) 1/3 of the time on average.

If on the other hand one neglects the cylindrical component of the hyperfine distortion, Equation II.21 becomes

$$g_{zz}^{rh}(t; \overset{M}{\sigma}_{22}) = \frac{1}{6} \left(1 - \frac{1}{2} \overset{M}{\sigma}_{22} t\right) \exp\left(-\frac{1}{2} \overset{M}{\sigma}_{22} t\right)$$
$$+ \frac{1}{3} \left(1 - \frac{1}{4} \overset{M}{\sigma}_{22} t\right) \exp\left(-\frac{1}{4} \overset{M}{\sigma}_{22} t\right)$$

(III.23)

Notice here that as $t \to \infty$, this function approaches zero. This result simply reflects the fact that, unlike a cylindrical distortion, a planar distortion generates no non-trivial zero frequencies.

From considering these two limiting cases, it is obvious that the planar component of the distortion is responsible for driving the function $g_{zz}^{rh}(t)$ in Equation III.21 to zero at long times. A typical example of this function, along with the two limiting cases is plotted in Figure III.3.

In an external magnetic field $\underset{\sim}{B}$, the problem of calculating the relaxation functions for a random anisotropic hyperfine interaction becomes somewhat more difficult, especially for a randomly oriented system. There are, however, a few simple limiting cases that can be treated. Consider, for example, triplet muonium in the limit of "high fields" (i.e., $\omega_{Mu} \gg \sigma_{2m}$ and $x \ll 1$). In this limit, the isotropic frequencies dominate so that the Hamiltonian can be approximated by its diagonal elements alone (secular approximation). These calculations are given in Appendix I for the case of a randomly oriented system. Results for the longitudinal field case show that, in this limit, a longitudinally applied field will completely decouple the random anisotropic hyperfine interaction. In the transverse field case, one obtains (omitting the Larmor precession part) the relaxation function

$$g_{xx}^{rh}(t) = (2\pi)^{-1} \int_0^\pi d\beta \, \sin\beta \int_0^{\pi/2} d\theta \qquad \text{(III.24)}$$

$$\times \left\{ \exp\left[-\frac{3}{8} \sin^2\beta \, \sigma_{22}^M \cos(\theta)t\right] \exp\left[-\frac{3}{8} \sqrt{2/3} \, \sigma_{20} \, |3\cos^2\beta - 1|t\right] \right\}$$

For early times ($t \to 0$), one can expand the integrand to obtain the short time behavior and approximate the relaxation function with the expression

$$g_{xx}^{rh}(t) \approx \frac{1}{2} \exp\left[-\left(\frac{\sqrt{2}}{6} \sigma_{20} + \frac{2}{\pi\sqrt{6}} \sigma_{22}^M\right)t\right] \qquad \text{(III.25)}$$

The exact solution of Equation III.24, calculated numerically, as well as the expansion approximation given in Equation III.25 are plotted for
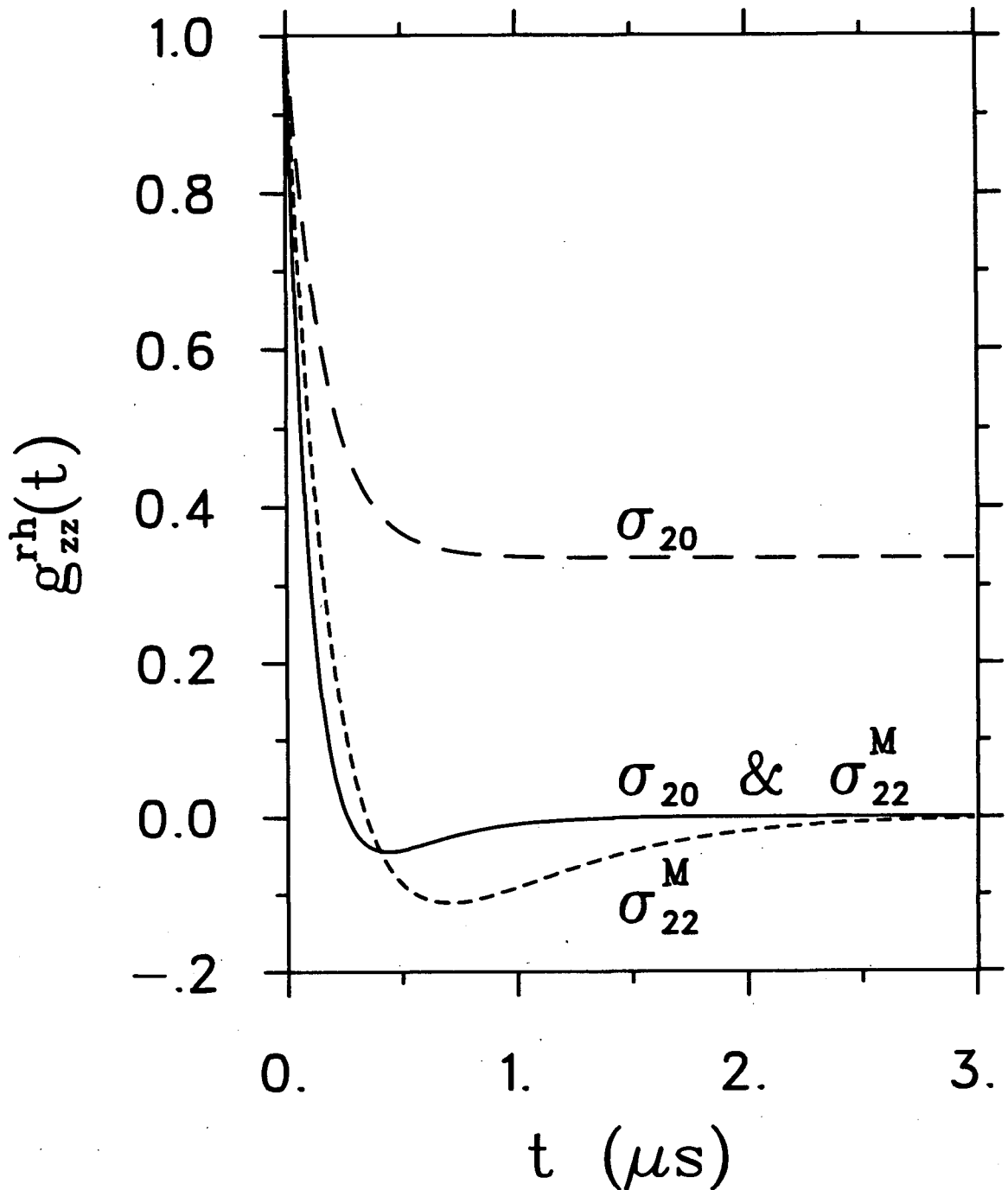
Figure III.3 Static zero field RAHD relaxation functions assuming Lorentzian frequency distributions with zero averages. The cylindrical component of the distortion is represented by the long-dashed curve (σ_{20} = 10 μs^{-1}), whereas the planar distortion component (σ_{22}^{M} = 10 μs^{-1}) is represented by the short-dashed curve. The solid line is the combined relaxation function for equal cylindrical and planar components ($\sigma_{20} = \sigma_{22}^{M}$ = 10 μs^{-1}). All three curves have been normalized to equal 1 at t=0.

comparison as a function of time in Figure III.4. Notice that at early times, these two functions are virtually indistinguishable in shape.

The assumption of a Lorentzian (or Lorentzian-like) distribution may not in general be appropriate, simply because a Lorentzian distribution has an infinite second moment. A more appropriate approximation may be made by assuming a modified Lorentzian, with a Gaussian damping. The affect of assuming this frequency distribution will of course be reflected in the shape of the calculated relaxation function, and can most easily be understood by considering the simple example of a purely cylindrical hyperfine distortion. In this case one defines the distribution

$$f(\omega_{20}) = (\pi \, e^{\lambda^2} \text{erfc}(\lambda))^{-1} \, [\frac{\sigma_{20}}{\omega_{20}^2 + \sigma_{20}^2}] \, \exp[-(\omega_{20}^2/\sigma_{20}^2)\lambda^2] \qquad \text{(III.26)}$$

where λ is a damping parameter (typically less than one), and $\text{erfc}(\lambda)$ is a complimentary error function. Using this definition, the static zero field relaxation function is found to be

$$g_{zz}^{rh}(t,\lambda;\sigma_{20}) = \frac{1}{6} + (6 \, \text{erfc}(\lambda))^{-1} \{e^{-\sigma_{20}'t} \, \text{erfc}(\lambda - \sigma_{20}'t/(2\lambda))$$
$$+ \, e^{+\sigma_{20}'t} \, \text{erfc}(\lambda + \sigma_{20}'t/(2\lambda))\} \qquad \text{(III.27)}$$

where $\sigma_{20}' = \sqrt{2/3} \, \sigma_{20}$. This function has been calculated and is plotted in Figure III.5 for $\lambda = 0.0$ and 0.1. Note that for small values of λ, this function is virtually indistinguishable from the function derived using a standard Lorentzian distribution (Figure III.3). However, as λ is increased, the initial decay begins to mimic a Gaussian shape. Because of this, one should be able to put an upper limit on λ for data exhibiting an exponential-like initial decay shape.
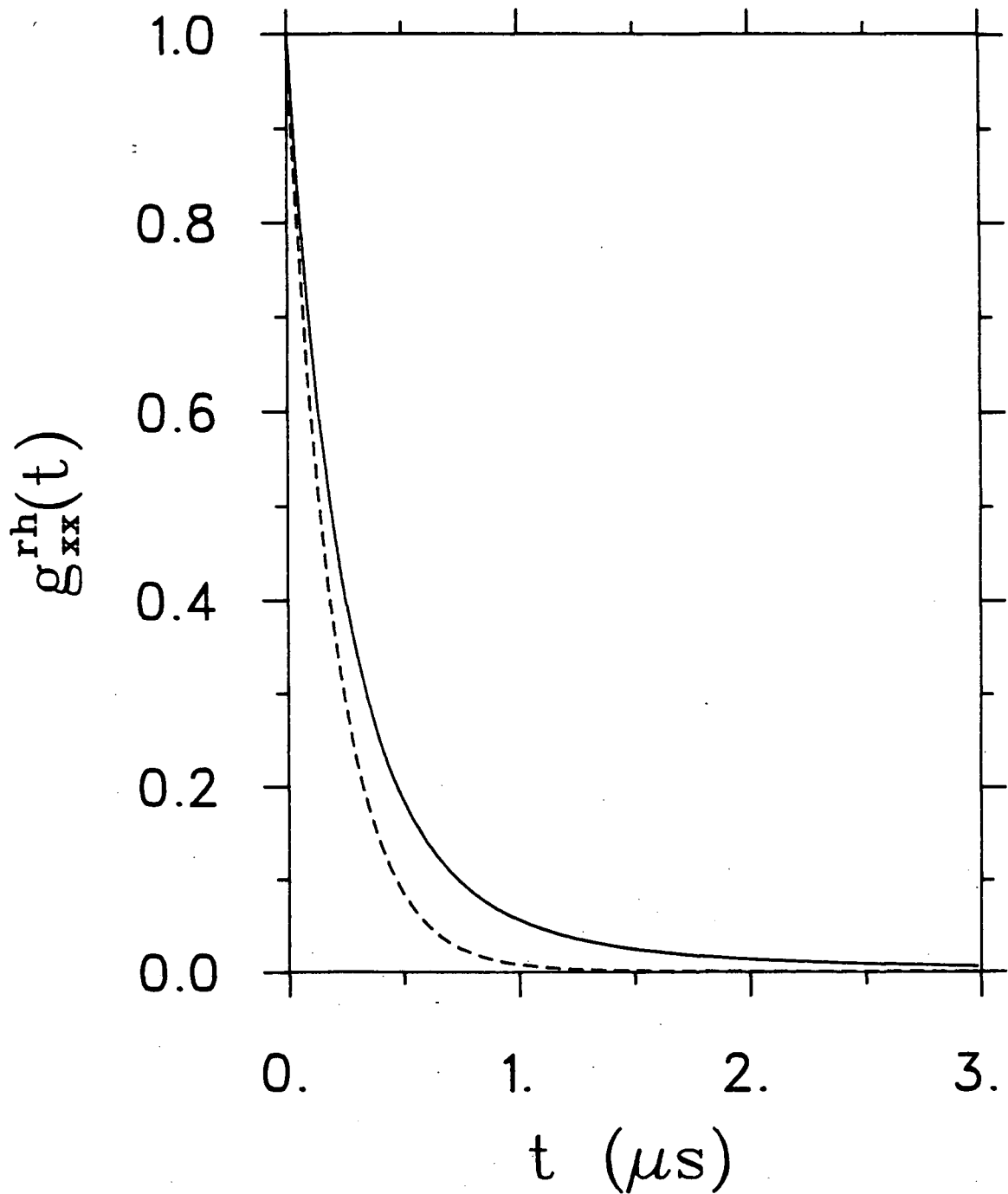
Figure III.4 Static transverse field RAHD relaxation function. The solid curve is the exact solution of Equation II.24, calculated numerically, and the dashed curve is the expansion approximation of Equation II.25. Both functions have been evaluated for $\sigma_{20} = \sigma_{22}^{M} = 10 \ \mu s^{-1}$ and have been nomalized to equal 1 at t=0.
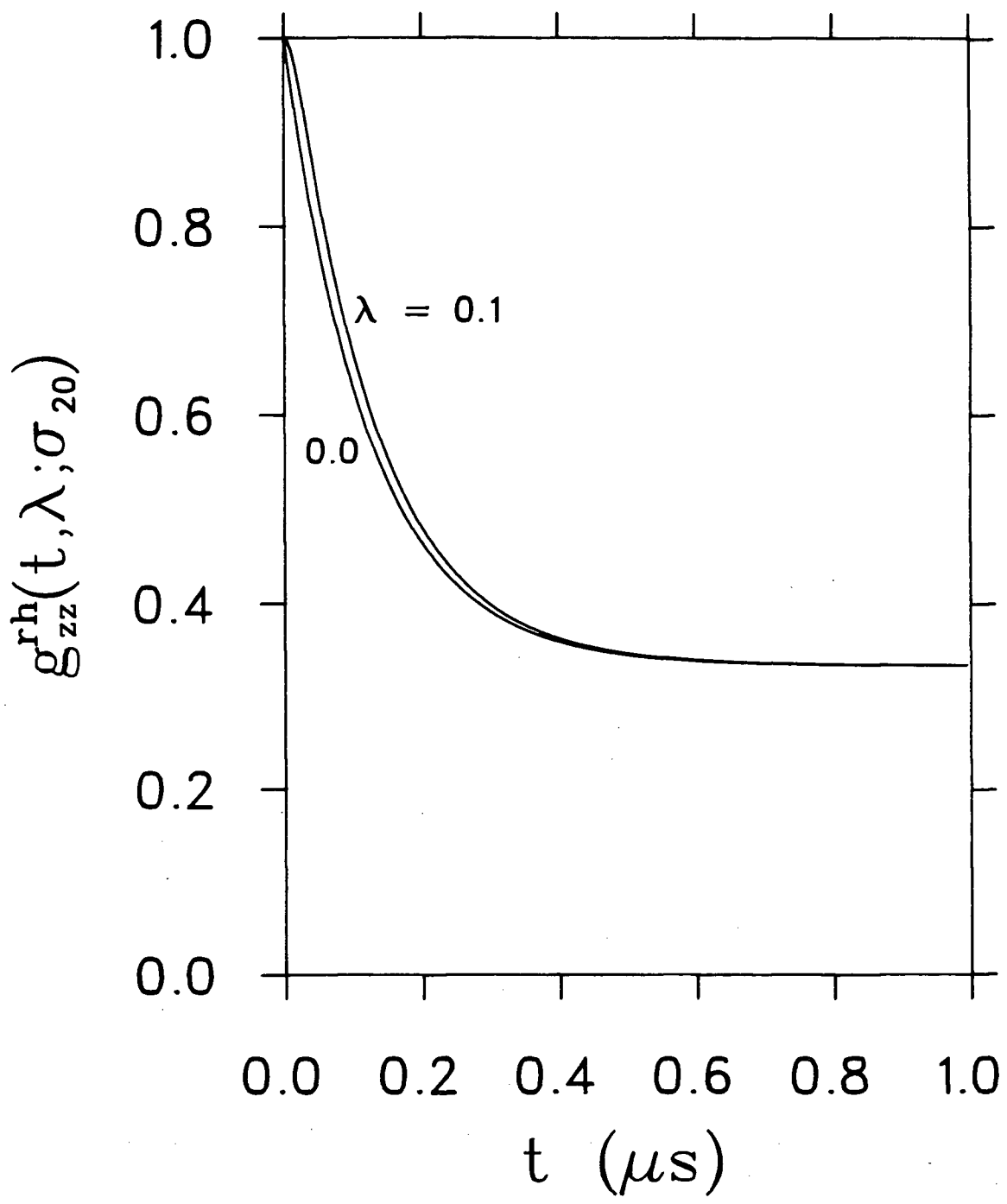
<u>Figure III.5</u> Static zero field RAHD spin relaxation function for a pure cylindrical distortion, assuming the form of Equation III.27. The function is plotted for two values of the damping parameter λ, 0.0 and 0.1, for the case of $\sigma_{20} = 10 \ \mu s^{-1}$. The curves have been normalized to equal 1 at t=0.

An interesting point can now be made by comparing the initial slopes of the zero field relaxation function given in Equation III.21 and the high transverse field function of Equation III.24. By defining m_{zf} and m_{tf} to be the initial slopes of the zero and transverse field relaxation functions, one can define the ratio

$$\frac{m_{zf}}{m_{tf}} \approx \sqrt{3}\ \frac{[1 + 4/\sqrt{6}\ (\sigma_{22}^M/\sigma_{20})]}{[1 + \sqrt{12}\ \frac{1}{\pi}(\sigma_{22}^M/\sigma_{20})]} \approx \sqrt{3} \qquad \text{(III.28)}$$

Thus, one finds that $m_{zf} > m_{tf}$, indicating that the depolarization rate is faster in zero field than in transverse field. This important result can be understood by considering the problem in terms of dimensionality; in zero field, all three components (x,y,z) of the hyperfine distortion contribute to the relaxation of the μ^+ spin, whereas in high transverse field, one is able to make a secular approximation to the Hamiltonian and effectively ignore all but the isotropic and cylindrical (z-axis) components.

For Mu in bulk silica, the μ^+ spin polarization relaxes via random anisotropic hyperfine distortions (RAHD) [13]; interactions with ^{29}Si nuclei (4.6%, isotopic) are relatively insignificant. In an amorphous environment such as bulk fused silica, the hyperfine distortions are distributed randomly both in orientation and magnitude. It is also known that muonium is static in bulk quartz below about 50 K [13]. Because of these two features, Mu in bulk fused silica provides an excellent test case for the zero and transverse field RAHD spin relaxation functions developed here.

The zero and longitudinal field spectra for muonium in bulk fused quartz at 7.0 ± 0.1 K are plotted in Figure III.6. The curve through the zero field data is a fit of Equation II.10 to the data, assuming the static RAHD function of Equation III.21. The fit gave a Chi-square of 86.2 for 53
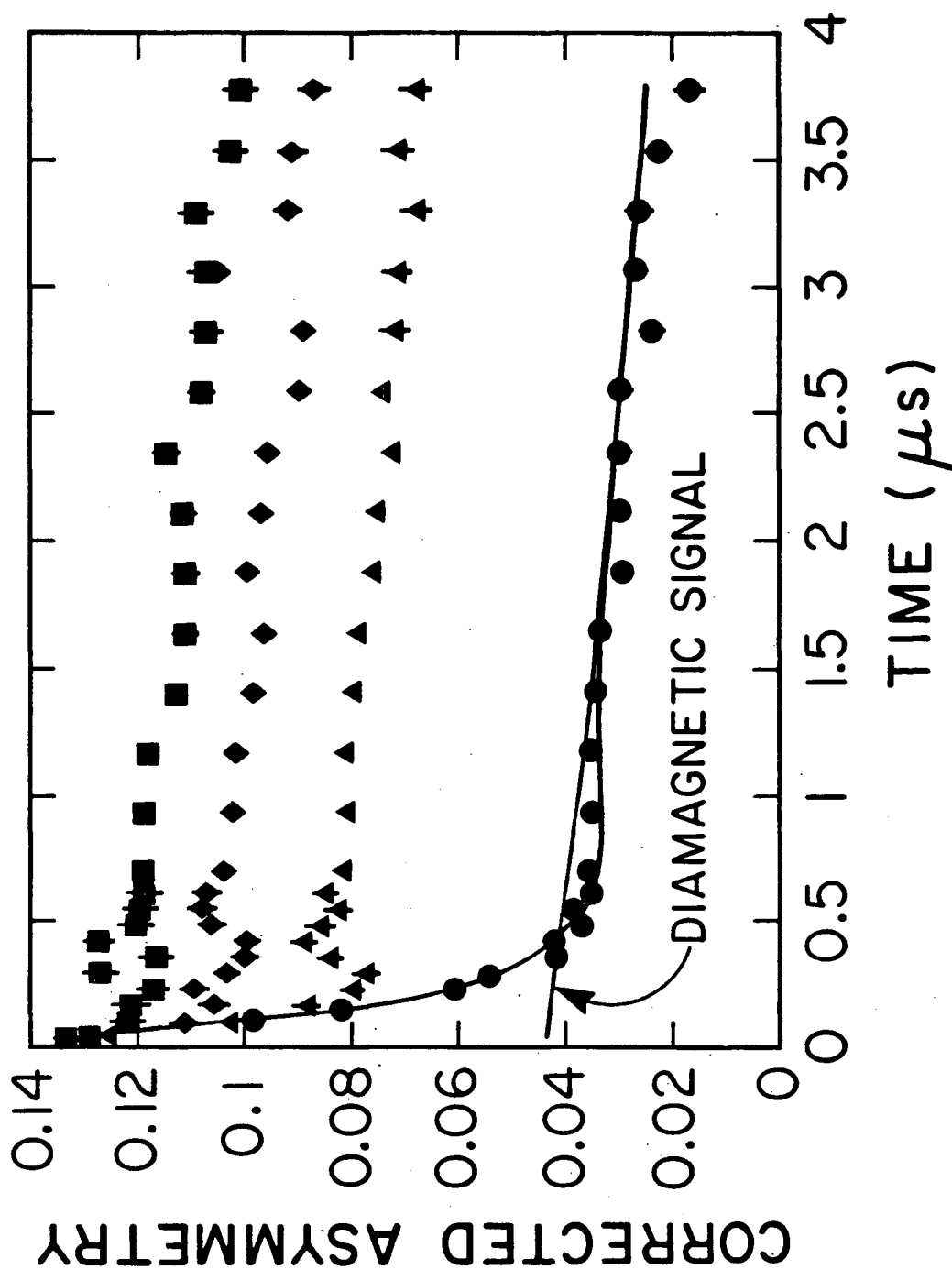
Figure III.6 Zero and longitudinal field data for muonium in bulk fused
quartz at 7±1 K. The line through the zero field data (circles) is a fit of
the RAHD function to the data. The longitudinal field data shown are for
0.5 G (triangles), 1.0 G (diamonds) and 2.0 G (squares).

degrees of freedom and the fitted results for the cylindrical and the planar

distortion parameters were 5.7 (+1.5/−1.2) μs^{-1} and 6.2 (+0.54/−0.52) μs^{-1},

respectively. The triplet muonium asymmetry parameter was allowed to vary

in the fit and found to be 0.118 (+0.0030/−0.0030). Recall that the muonium

asymmetry reflects the fraction of muonium formed in the sample; the result

obtained here is consistent with the corresponding value obtained in low

transverse field.

As has been discussed, a random hyperfine interaction can be almost

completely decoupled in longitudinal field for $\omega_{Mu} \gg \sigma_{2m}$. From the fit of

the zero field 7 K data, this translates into a longitudinal field on the

order of a few Gauss. As can be seen in Figure III.6, the decoupling

behavior is consistent with this.

Finally, by substituting the values for σ_{20} and σ_{22}^{M} obtained in the

zero field fit into the approximation for the transverse field function

given in Equation III.25, one obtains a transverse field relaxation rate

$\lambda_{\perp}^{Mu}$ of 2.9 ± 0.5 μs^{-1}, which is consistent with existing transverse field

data [13].

Although a Lorentzian distribution of frequencies does reproduce the

basic features of the quartz data, it is probably not the most realistic

assumption. Perhaps using the type of distribution defined in Equation

III.26 would be better, but there is at present no obvious physical argument

or model that can be used to help decide what the correct distribution

should be.

III.A.3 Chemical Reactions (CH)

The coherence of the spin polarization of the μ^+ in the muonium state

can (in transverse field) be lost through collisions of the muonium atoms
with molecules which result in chemical reactions forming diamagnetic
products [14]. With this mechanism, the muon spin polarization must decay
exponentially. In the gas phase, the transverse field relaxation function
is given by the expression

$$g_{xx}^{ch}(t) = \exp\left[- \lambda_{\perp}^{ch} t\right] = \exp\left[-\left(\eta \bar{v} \sigma_{ch}\right) t\right] \qquad \text{(III.29)}$$

where η is the number of interacting molecules per unit volume, $\bar{v}$ is the
mean relative velocity between the muonium atom and the molecules and σ_{ch} is
the cross section for the reaction.

In transverse field, a μ^+ precesses about 103 time slower than triplet
muonium in the same field, such that if a chemical reaction produces a μ^+ in
a diamagnetic environment, the μ^+ is effectively removed from the precessing
muonium ensemble. In zero and longitudinal field, however, such reactions
produce no observable relaxation since the μ^+ spin remains polarized along
the z-axis regardless of whether the μ^+ is in the muonium state or in a
diamagnetic state.

III.A.4 Spin Exchange (SE)

In collisions with paramagnetic molecules, hyperfine transitions such
as $|m_{\mu}, m_e\rangle = |+, +\rangle \rightarrow |+, -\rangle$ can take place. As in the case of chemical
reactions in transverse field, the decay of the muon spin polarization due
to spin exchange is found to vary exponentially with time so that, in
transverse field, the relaxation function is written

$$g_{xx}^{se}(t) = \exp\left[- \lambda_{\perp}^{se} t\right] = \exp\left[-\left(\frac{f}{2} \eta \bar{v} \sigma_{se}\right) t\right] \qquad \text{(III.30)}$$

where η is again the number density of interacting molecules, $\bar{v}$ is the mean relative velocity between the muonium atom and the molecules, σ_{se} is the spin exchange cross section and f is a factor which depends on both the spin of the paramagnetic molecules and the orientation of the external magnetic field with respect to the initial muon spin polarization.

In longitudinal field, where the quantization axis is along the initial muon spin polarization, spin exchange causes hyperfine transitions with a probability of $s^2c^2 = (1 + x^2)^{-1}$. Thus in terms of the specific field parameter x, the spin exchange relaxation function for muonium in a longitudinal field is written as [14,15]

$$g_{zz}^{se}(t,x) = \exp\left[- \lambda_{\parallel}^{se} t\right] = \exp\left[-(\frac{f}{2} \eta \bar{v} \sigma_{se})(1 + x^2)^{-1} t\right] \qquad \text{(III.31)}$$

Transverse field studies [16] of the temperature dependence of the spin exchange reaction of muonium with O_2 (S=1) and NO (S=1/2) have shown that the factor f to equal 8/9 for O_2 and 3/4 for NO, whereas in longitudinal field studies [15] the factor f was found to equal 64/27 and 2 for O_2 and NO, respectively.

III.A.5 Superhyperfine Interactions (SHF)

The time evolution of the muon spin polarization in the muonium state can also be influenced by the superhyperfine interactions between the unpaired electron of the muonium atom and neigboring nuclei with non-zero magnetic moments. To describe this interaction, one first defines a coordinate system with the muon located at the origin, the electron positioned at radius $\vec{s}$, the interacting nucleus located at radius $\vec{R}$ (directed along the z'-axis), and the distance between the electron and the

nucleus defined by the vector $\vec{r}$ which originates from the electron. A schematic diagram of this is shown in Figure III.7. With these designations, the Hamiltonian for the superhyperfine (SHF) interaction between the electron and a nucleus of spin $\underset{\sim}{J}_{op}$ can be written as [17]

$$H^{shf} = (a - b) \left(\underset{\sim}{S}^e_{op} \cdot \underset{\sim}{J}_{op} \right) + 3b \left(S^e_{z'}, J_{z'} \right) \tag{III.32}$$

where $S^e_{z'}$ and $J_{z'}$ are the respective z'-components of the electron and the nuclear spins and the superhyperfine parameters (a & b), corresponding to a "contact"-like term and dipole-dipole term, respectively, are defined as

$$a = \frac{8}{3} \pi \left(g_e \mu^e_o \; g_J \mu^J_o \right) |\Psi(\vec{R})|^2$$

and $\hspace{8cm}$ (III.33)

$$b = \frac{1}{2} \left(g_e \mu^e_o \; g_J \mu^J_o \right) \int d^3\vec{r} \; |\Psi(\vec{s})|^2 \left[\frac{3 \, \cos^2(\tau) - 1}{r^3} \right]$$

Here g_J and μ^J_o are the g-factor and Bohr magneton of the neighboring nucleus, respectively, and τ is the angle defined by the vectors $\vec{r}$ and $\vec{R}$.

Take as an example an isotropic superhyperfine interaction of muonium with a single nucleus of spin J (>1), in zero magnetic field. In this case one has b=0 and z=z' such that the total Hamiltonian can be written in the form

$$H = \left(H^{hf} + H^{shf} \right) = \underset{\approx}{W} : \left(\underset{\sim}{S}^e_{op} \underset{\sim}{S}^\mu_{op} \right) + a \left(\underset{\sim}{S}^e_{op} \cdot \underset{\sim}{J}_{op} \right) \tag{III.34}$$

The four eigenvalues of this Hamiltonian are

$$\lambda_1 = \frac{1}{4} (h/2\pi)\omega_{00} + \frac{a}{2} J \quad ; \quad \lambda_3 = \frac{1}{4} (h/2\pi)\omega_{00} - \frac{a}{2} (J + 1)$$

$$\lambda_{2,4} = -\frac{1}{4} \left[(h/2\pi)\omega_{00} + a \right] \pm \frac{1}{2} \left\{ \left[(h/2\pi)\omega_{00} - \frac{a}{2} \right]^2 + J(J + 1)a^2 \right\}^{1/2} \tag{III.35}$$

where ω_{00} is the hyperfine-structure interval of the perturbed muonium atom,
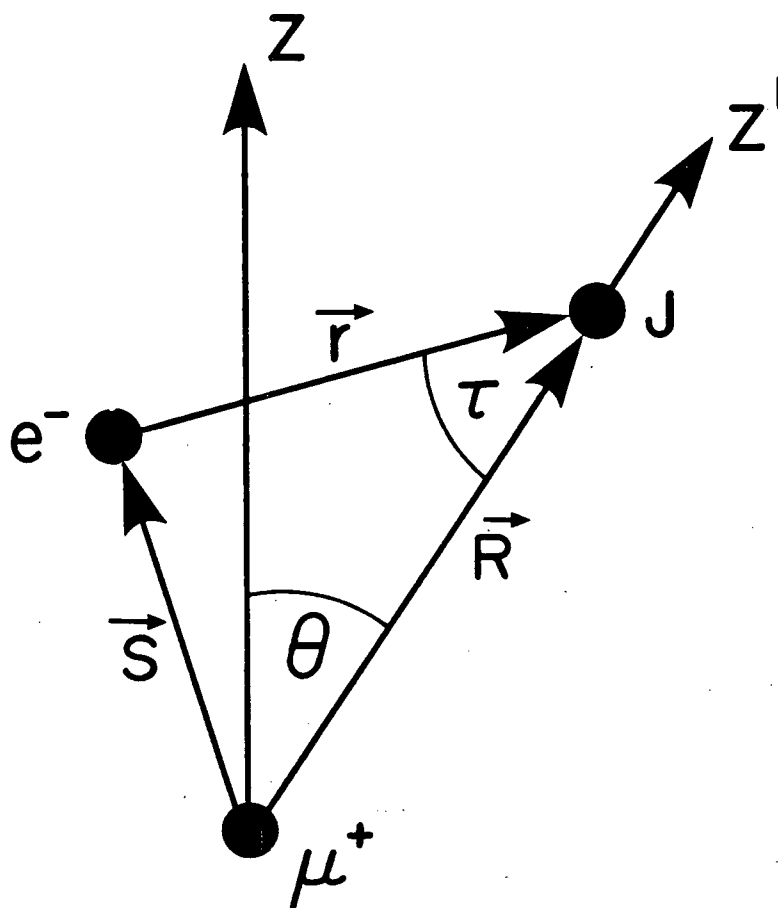
Figure III.7 Diagram representing the superhyperfine interaction. Taken from reference [17].

and the corresponding transition frequencies between the eigenstates are defined as $\omega_{ij} = (2\pi/h)(\lambda_i - \lambda_j)$. Since to a first approximation, $\lambda_1 \approx \lambda_2 \approx \lambda_3 \approx (1/4)(h/2\pi)\omega_{00}$, the transition frequencies ω_{14}, ω_{24} and ω_{23} are of order ω_{00}. Frequencies of order ω_{00} are generally not experimentally observable in zero field due to timing limitations. Bearing this in mind, an approximation can be made by ignoring the oscillatory terms involving these frequencies, which simply implies ignoring the singlet state. Assuming a relatively large value of J, one then obtains an approximate relation for the zero field relaxation function of the observable muonium ensemble, namely

$$g_{zz}^{shf}(t) \approx \frac{1}{6} \left\{ 1 + \cos(\omega_{12}t) + \cos(\omega_{23}t) \right\} \tag{III.36}$$

Comparison to muonium in vacuum shows that the time-independent part of $g_{zz}^{shf}(t)$ (residual polarization) is reduced from 1/2 to 1/6.

The contact term of the superhyperfine interaction requires the interacting nucleus to be within about one Bohr radius of the muon. Because of this, one would expect a superhyperfine interaction to be much stronger than a simple dipole-dipole interaction, and therefore more difficult to decouple in longitudinal field.

III.B Dynamical Relaxation Functions

Up to now the discussions on spin depolarization for a magnetic probe in a solid have assumed the magnetic probe to be static with respect to its environment. Owing to its relatively light mass, however, the muon (or muonium atom) may be very mobile in the stopping medium. This motion or hopping may alter the shape of the relaxation function in comparison to the static case. This phenomenon comes about because the effects of the

interaction(s) which govern the time evolution of the μ^+ spin polarization in the solid are averaged by the motion of the probe (μ^+, Mu, etc.), hence the term "motional averaging".

III.B.1 Gaussian-Markovian Process

In the case of a magnetic probe hopping stochastically in the presence of static nuclear dipoles, the motion induces a modulation or fluctuation of the local field as sensed by the magnetic probe. In the original research of Kubo and Toyabe [1,2] the modulation of the local field is assumed to follow a "Gaussian-Markovian" process, where the correlation of the fluctuating field is characterized by the equation

$$\langle H_i(t) \, H_i(0) \rangle = \frac{\Delta^2}{\gamma_\mu} \exp(-t/\tau_c) \qquad \text{(III.37)}$$

where $\tau_c = 1/\nu$ is the correlation time of the field fluctuation. Assuming a Gaussian random process automatically implies that the fluctuation of the local field is determined by the cumulative effect of a large number of random processes, each of which induces a gradual change in the local field. The Gaussian-Markovian assumption has also been applied to the case of a magnetic probe interacting with a Gaussian local field in a strong external transverse external magnetic field, yielding the analytic result

$$G_{xx}^G(t,\nu) = \exp\{-\Delta^2/\nu^2 \left[\exp(-t\nu) - 1 + t\nu \right]\} \qquad \text{(III.38)}$$

which is the familiar formula of Kubo and Tomita [18]. It is obvious that this expression behaves properly in the slow modulation limit ($\nu/\Delta \ll 1$), where the relaxation function exhibits a Gaussian shape, as well as in the fast modulation limit ($\nu/\Delta \gg 1$), where the shape resembles an exponential decay. This function is plotted for various values of Δ/ν in Figure III.8.
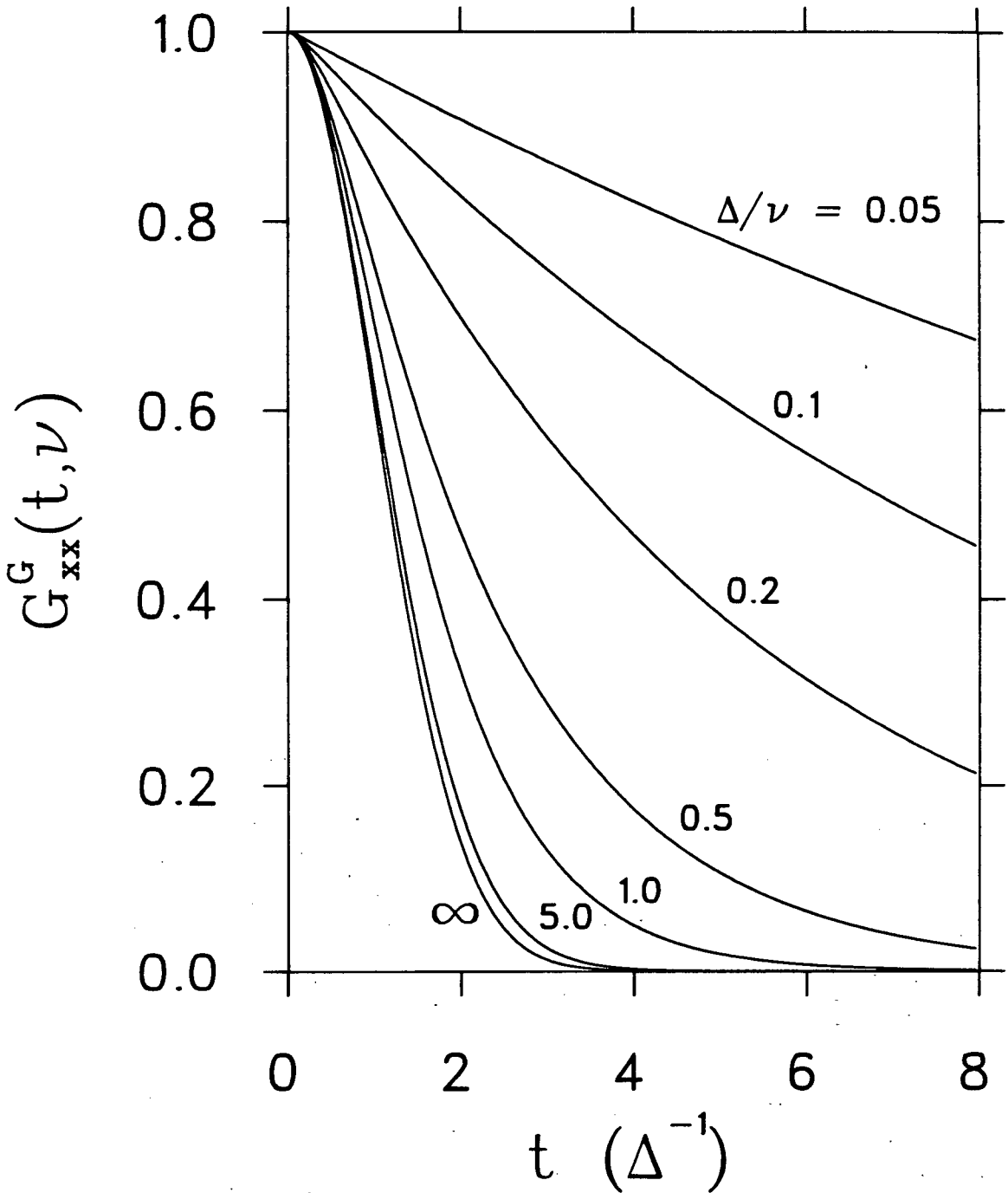
Figure III.8 Dynamic Kubo–Tomita high transverse field spin relaxation function (Gaussian-Markovian process) plotted for various values of Δ/ν.

The assumption of a Gaussian-Markovian process may not, however, be a good one, particularly for the case of diffusion in the presence of traps. This is because a magnetic probe jumping from site to site with a hopping frequency ν would likely sense a sudden change in the local field distribution and not an adiabatic or gradual one. This type of behavior is idealized by the "Strong Collision Model" [19].

III.B.2 Strong Collision Model

In the strong collision model, the local field sensed by the magnetic probe is assumed to change abruptly upon collision, with the local field distribution before and after this collision being completely uncorrelated. In this approximation, the time evolution of the dynamical relaxation function $G_{ii}(t,\nu)$ is constructed from an infinite series of discrete static relaxation functions according to the equation

$$G_{ii}(t,\nu) = \sum_{n=0}^{\infty} g_{ii}^{(n)}(t,\nu) \qquad \text{(III.39)}$$

where $g_{ii}^{(n)}(t,\nu)$ is the relaxation function for the magnetic probes that jump n times in time t. The first term (n=0) in the series of Equation III.39 is easily understood to be

$$g_{ii}^{(o)}(t,\nu) = \exp(-\nu t)\, g_{ii}(t) \qquad \text{(III.40)}$$

where $\exp(-\nu t)$ is the probability that the magnetic probe does not hop in time t, and $g_{ii}(t)$ is the static relaxation function. The following term in the series describes the process in which the magnetic probe hops at time t_1 $(0 < t_1 < t)$ and is expressed as

$$g_{ii}^{(1)}(t,\nu) = \nu \int_{o}^{\infty} dt_1 \; e^{-\nu(t-t_1)} \, g_{ii}(t-t_1) \, e^{-\nu t_1} \, g_{ii}(t_1) \qquad \text{(III.41)}$$

By introducing the Laplace transforms

$$f_{ii}(s) = \int_o^\infty dt\, e^{-st} g_{ii}(t) \quad \text{and} \quad F_{ii}(s) = \int_o^\infty dt\, e^{-st} G_{ii}(t) \quad \text{(III.42)}$$

the exact solution in the frequency domain becomes

$$F_{ii}(s,\nu) = \sum_{n=o}^\infty \nu^n\, f_{ii}^{n+1}(s+\nu) = \frac{f_{ii}(s+\nu)}{1 - \nu f_{ii}(s+\nu)} \quad \text{(III.43)}$$

To obtain the time domain dynamical relaxation function $G_{ii}(t,\nu)$, for a specific static relaxation function $g_{ii}(t)$, one must calculate the inverse Laplace transform of Equation III.43.

The time domain dynamical transverse field relaxation function $G_{xx}^G(t,\nu)$, for the case of a magnetic probe interacting with a Gaussian random local field, has been numerically calculated [20] using a strong collision formula similar to that of Equation III.43. This calculation was performed using the "Korrektur-Verfahren" (Iteration Procedure) method [21,22]. Comparison of the relaxation functions obtained in this manner with the Gaussian-Markovian approximation of the Kubo-Tomita formalism [18], given in Equation III.38, reveals that the two cases are nearly identical except that the strong collision function exhibits a slightly slower decay rate. This discrepancy is particularly noticable in the limit of slow hopping (ν/Δ or $\nu/a \ll 1$, for a Gaussian or Lorentzian distribution, respectively). However, the difference between the relaxation function obtained using the strong collision approximation and that obtained assuming a Gaussian-Markovian process is so small that the simple analytic expression of Equation III.38 is generally preferred for data analysis.

The dynamical zero field spin relaxation function $G_{zz}^G(t,\nu)$ for the case

of a magnetic probe interacting with a Gaussian random local field has also

been calculated [4] using the strong collision model given in Equation

III.43. This function is plotted in Figure III.9 for various values of Δ/ν.

Comparison of Figure III.9 with the Gaussian-Markovian curves of Kubo-Toyabe

[1,2] indicates that, as in the case of the transverse field function

$G_{xx}^G(t,\nu)$, the zero field curves generated with the strong collision model

decay at a slightly slower rate than those based on the Gaussian-Markovian

approximation, particularly in the limit of slow hopping ($\nu/\Delta \ll 1$).

The modulation of the local field has a marked effect on the shape of

the long time tail of the relaxation function as well. As has already been

discussed, the zero field static relaxation functions for both Gaussian and

Lorentzian random local field distributions, exhibit a 1/3 recovery of the

asymmetry at long times. For slow modulations of the local field, this

recovery is suppressed, and for Gaussian random local field, follows the

asymptotic form

$$G_{zz}^G(t,\nu) \approx \frac{1}{3} \exp\left(-\frac{2}{3}\nu t\right) \quad ; \text{ for } t \gg 3/\Delta \qquad \text{(III.44)}$$

where the factor of 2/3 in the exponent can be understood intuitively by

noting that, on average, 1/3 of the longitudinal (z-axis) polarization is

preserved for each hop. In the limit of fast fluctuations ($\nu/\Delta \gg 1$), the

Gaussian line shape begins to mimic an exponential, due to motional

narrowing, such that

$$G_{zz}^G(t,\nu) \approx \exp\left(-2\Delta^2 t/\nu\right) \qquad \text{(III.45)}$$

which tends to zero at long times.

Application of the strong collision model of Equation III.43 to the

problem of a magnetic probe interacting with a Lorentzian local field
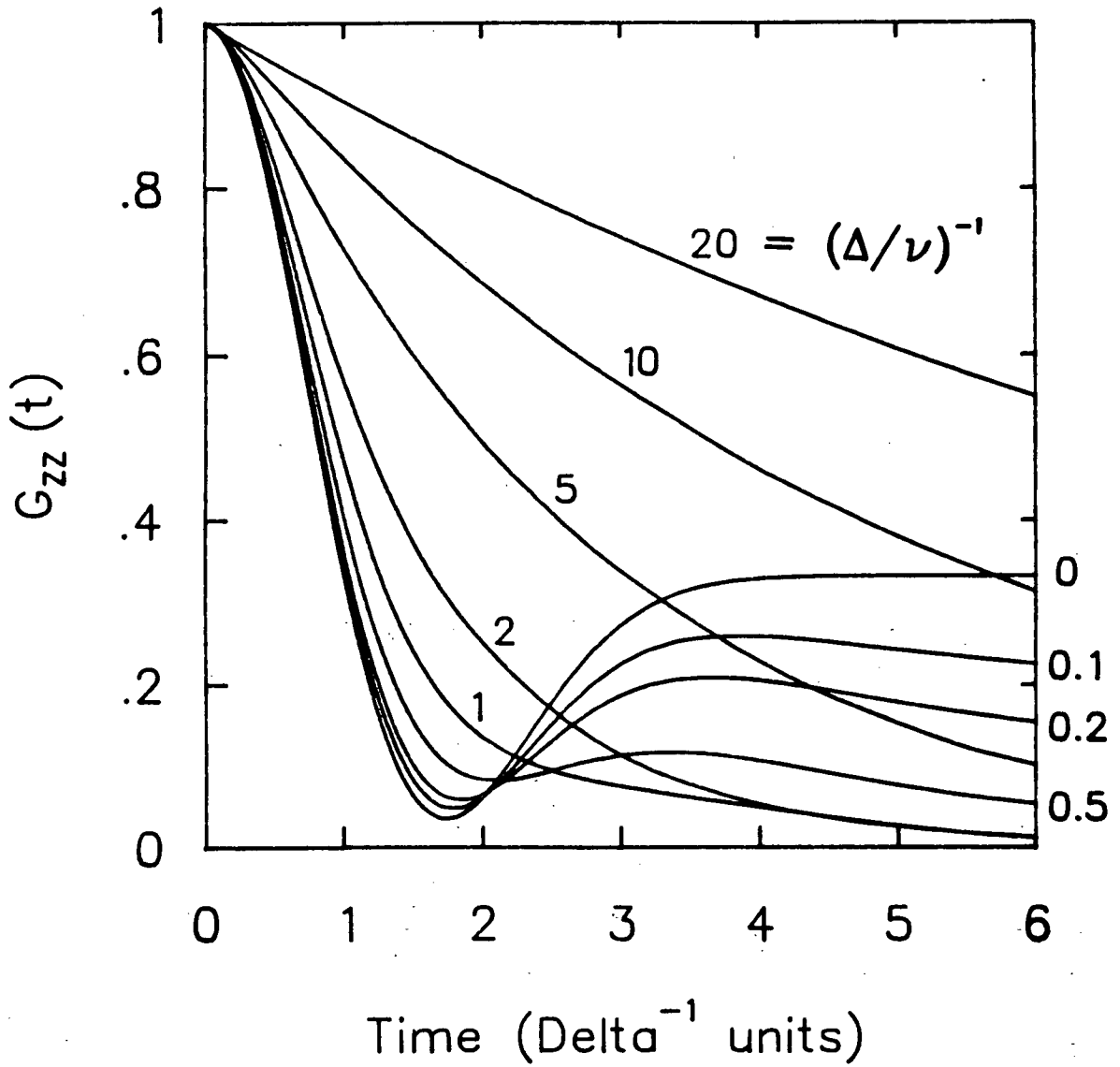
Figure III.9 Dynamic zero field Gaussian Kubo–Toyabe spin relaxation function (Strong Collision Process) plotted for various values of Δ/ν.

yields the corresponding dynamical zero field relaxation function $G_{zz}^{L}(t,\nu)$. This function is shown in Figure III.10 for various values of a/ν. A major feature to make note of is that, unlike its Gaussian counterpart, the function $G_{zz}^{L}(t,\nu)$ does not exhibit a motional narrowing effect. In fact, the initial decay rate is quite independent of the hop frequency. In the limit of slow hopping, and for $t \gg 3/\Delta$, one obtains an equation similar to Equation III.44, whereas in the limit of fast fluctuations, $(\nu/a \gg 1)$, the relaxation function takes the form

$$G_{zz}^{L}(t,\nu) \approx \exp\left(-4at/3\right) \tag{III.46}$$

This, like the Gaussian case, tends to zero at long times; however, it has the peculiar feature of being independent of ν, as explained above.

Thus, the zero field technique has been shown to be a powerful tool for studying the diffusion and trapping behavior of a magnetic probe interacting with a random local field (Gaussian or Lorentzian) distribution. Comparison of Figures III.9 and III.8 also reveals the advantage provided by the zero field technique, as opposed to the transverse field (precession) method, for such studies.

Additional discrimination between static and dynamic systems can also be obtained using longitudinal field, where the relaxation function would still exhibit an exponential decay at long times, even in relatively high magnetic fields. This behavior can be understood by considering the case of muonium in the intermediate and high field limits, in the context of the strong collision assumption of Equation III.43. The static longitudinal field relaxation function can be obtained by combining Equations AI.109 and AI.110 with the definitions of Equation AI.21. For longitudinal fields of
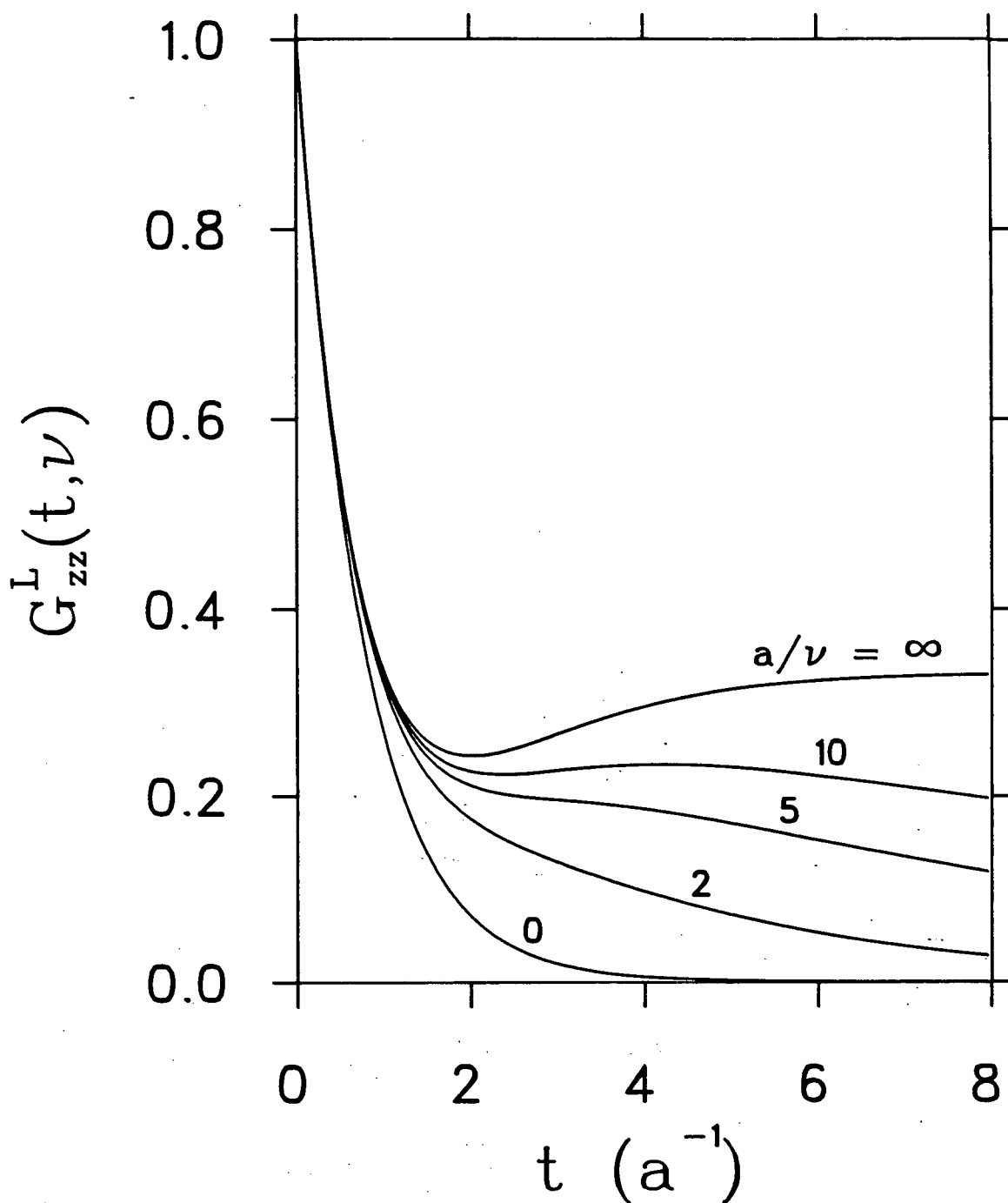
Figure III.10 Dynamic zero field Lorentzian Kubo-Toyabe spin relaxation function (Strong Collision Process) plotted for various values of a/ν.

intermediate strength ($0 < \lambda < \pi/2$), the observable static longitudinal "relaxation function" (omitting the modulating time part) is written

$$g_{zz}(t,\lambda) \propto \frac{1}{2}(1 + \cos^2\lambda) \quad ; \qquad \lambda = \arcsin[1/(1+x^2)^{1/2}] \qquad \text{(III.47)}$$

where $x\ (= |\underline{B}|/B_0)$ is the specific field parameter, defined in Equation I.10. From the strong collision model, one then writes in frequency space

$$F_{zz}(s+\nu) = \frac{1 + \cos^2\lambda}{2(s+\nu) - \nu(1-\cos^2\lambda)} \qquad \text{(III.48)}$$

and by taking the inverse Laplace transform of Equation III.48, one obtains the relaxation function

$$G_{zz}(t,\nu,\lambda) = \frac{1}{2}(1+\cos^2\lambda)\ \exp\left[-\frac{\nu}{2}(1-\cos^2\lambda)t\right] \qquad \text{(III.49)}$$

Notice that only for the extreme high field limit ($\lambda \to 0$, $x \to \infty$), is the relaxation completely decoupled for muonium, unless $\nu = 0$. This argument can be extended to any relaxation mechanism, as long as the "high field" (secular approximation) limit applies. In the present work, $x \ll 0.01$.

Since the strong collision model can be applied to any static relaxation function, the dynamical spin relaxation functions for the case of a random hyperfine interaction can also be obtained using Equation III.43. Taking the Laplace transform of the static zero field relaxation function of Equation III.21 gives

$$f_{zz}^{rh}(s) = \frac{1}{6}\left[s + \frac{1}{2}\sigma_{22}^M\right]^{-1} - \frac{1}{6}\left(\frac{1}{2}\sigma_{22}^M\right)\left[s + \frac{1}{2}\sigma_{22}^M\right]^{-2} \qquad \text{(II.50)}$$
$$+ \frac{1}{3}\left[s + \frac{1}{4}(\sigma_{22}^M + 3\sqrt{2/3}\ \sigma_{20})\right]^{-1} - \frac{1}{3}\left(\frac{1}{4}\sigma_{22}^M\right)\left[s + \frac{1}{4}(\sigma_{22}^M + 3\sqrt{2/3}\ \sigma_{20})\right]^{-2}$$

Substituting this expression into Equation III.43, one can numerically calculate the inverse Laplace transform to obtain the time domain relaxation function $G_{zz}^{rh}(t,\nu)$. This function is shown in Figure III.11 for selected
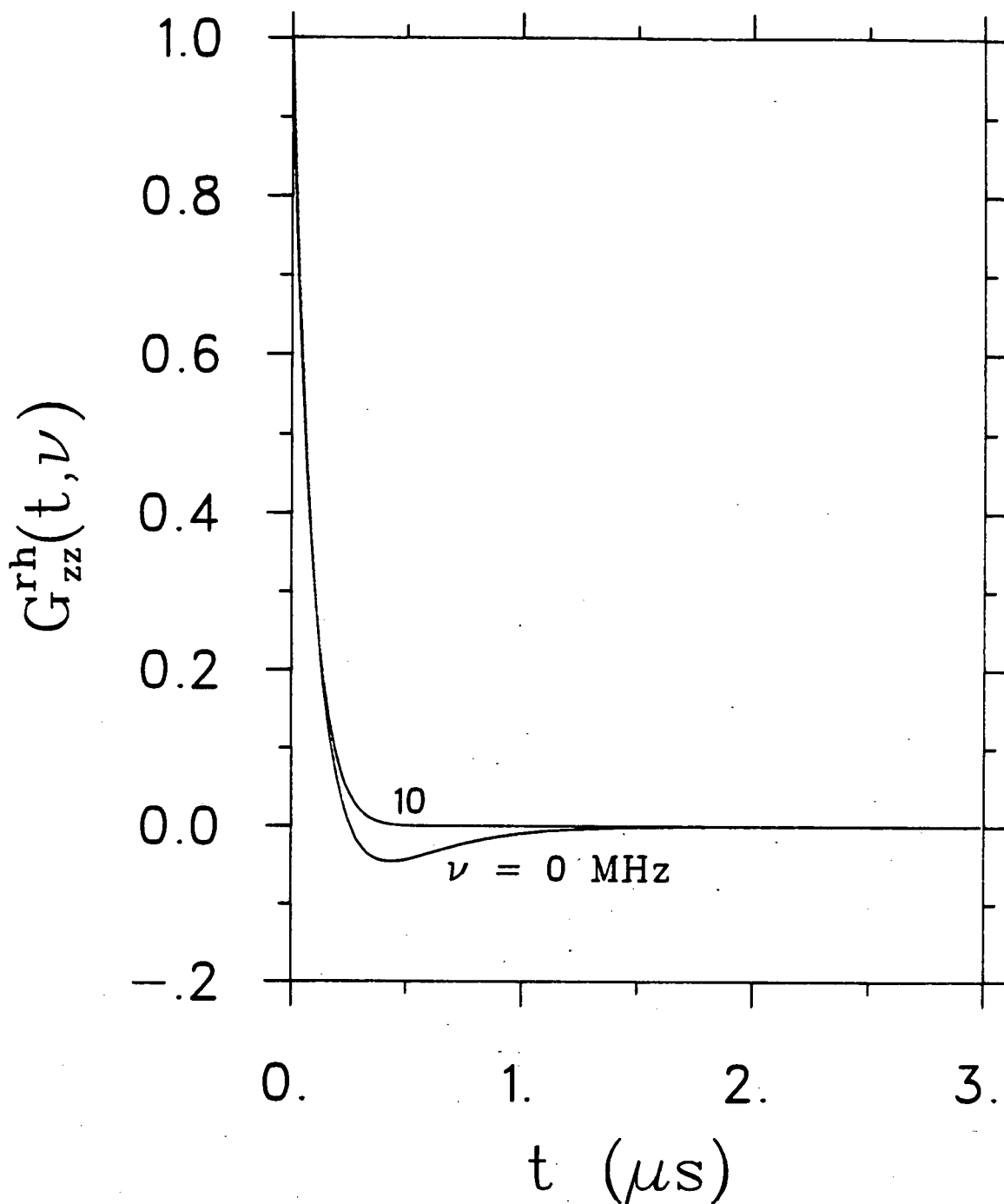
Figure III.11 Dynamic zero field Lorentzian RAHD spin relaxation function (Strong Collision Process) plotted for selected values of the hop rate ν, where $\sigma_{20} = \sigma_{22}^{M} = 10 \ \mu s^{-1}$. The function is normalized to equal 1 at t=0.

values of ν, where both σ_{20} and σ_{22}^M are equal to 10 μs^{-1}. As in the case

of a magnetic probe interacting with a Lorentzian random local field

distribution (Figure III.10), the initial decay rate of the function shown

in Figure III.11 is completely unaffected by the hop rate ν. This feature,

which is somewhat counter-intuitive, arises directly from the assumption of

Lorentzian or Lorentzian-like frequency distributions. This behavior is

also independent of the dimensionality of the distribution since in the case

of a Lorentzian random local field the distribution is three-dimensional,

whereas for random hyperfine distortions one has both a one-dimensional

cylindrical component distribution plus a two-dimensional planar component

distribution. Thus the behavior shown in Figure III.11 implies that for

Lorentzian and Lorentzian-like distributions (of all dimensions), the shape

at early times is independent of the motion of the magnetic probe. It is

particularly instructive to consider the two limiting cases of either a

totally cylindrical or totally planar distortion. In Figure III.12 the

relaxation function generated by assuming only a cylindrical distortion of

the muonium hyperfine interaction (i.e., $\sigma_{22}^M = 0$) is plotted. The effect of

motion on this component of the relaxation function is to suppress the long

time tail, even for small hop rates; for sufficiently high hop rates, this

long time tail tends to zero. The case of a purely planar distortion (i.e.,

$\sigma_{20} = 0$) is shown in Figure III.13. Since in the static limit this function

already tends to zero, the effect of hopping is not very noticeable at long

times. Instead, the effect of hopping on the relaxation function is more

evident at early times, where it serves to reduce the depth of the minimum.

This same procedure can be applied to calculate the dynamical

transverse field relaxation function $G_{xx}^{rh}(t,\nu)$. Taking the Laplace transform
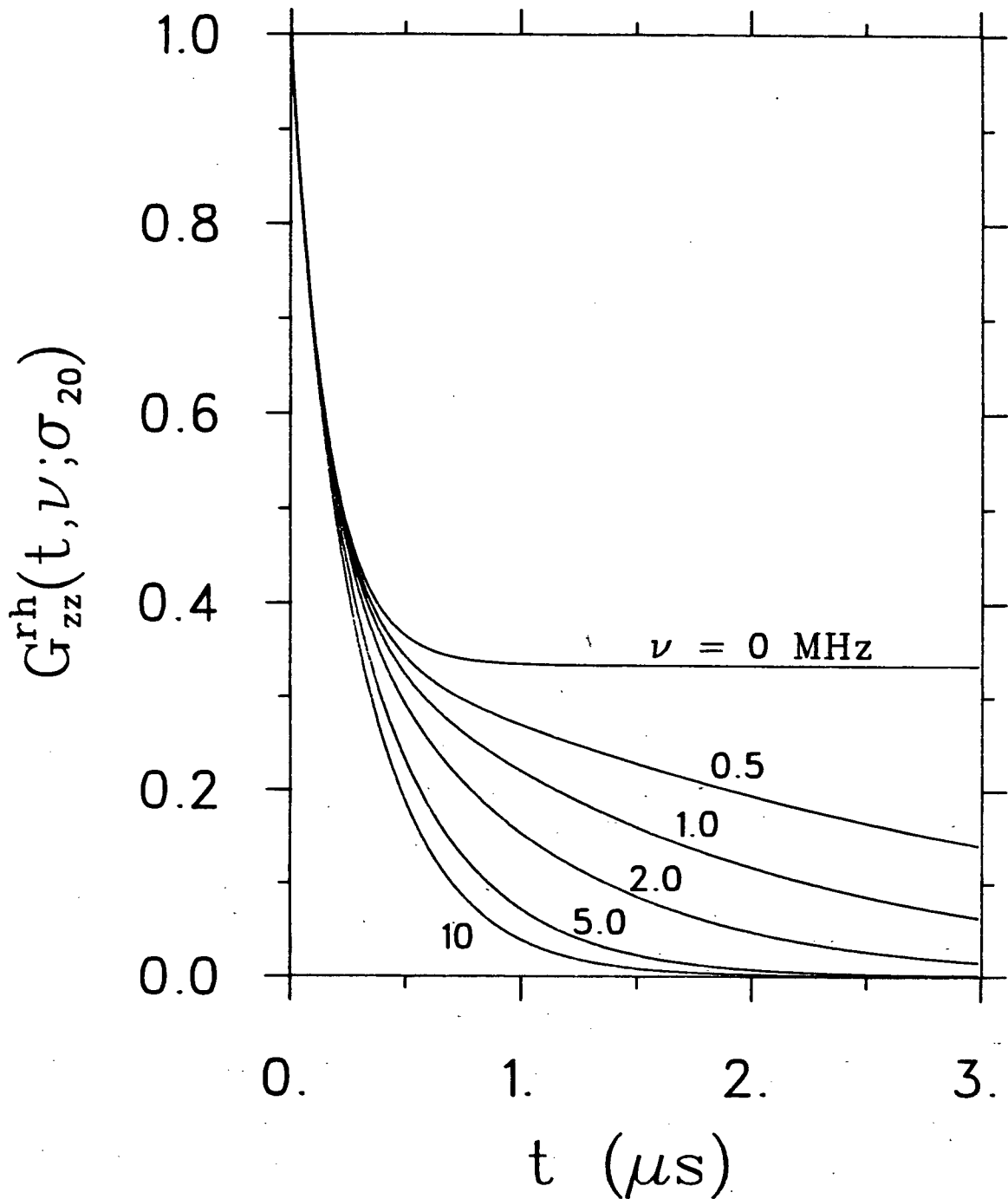
Figure III.12 Dynamic zero field Lorentzian RAHD spin relaxation function for a pure cylindrical distortion (Strong Collision Process) plotted for selected values of the hop rate ν, where $\sigma_{20} = 10 \ \mu s^{-1}$. The curves have been normalized to equal one at t=0.
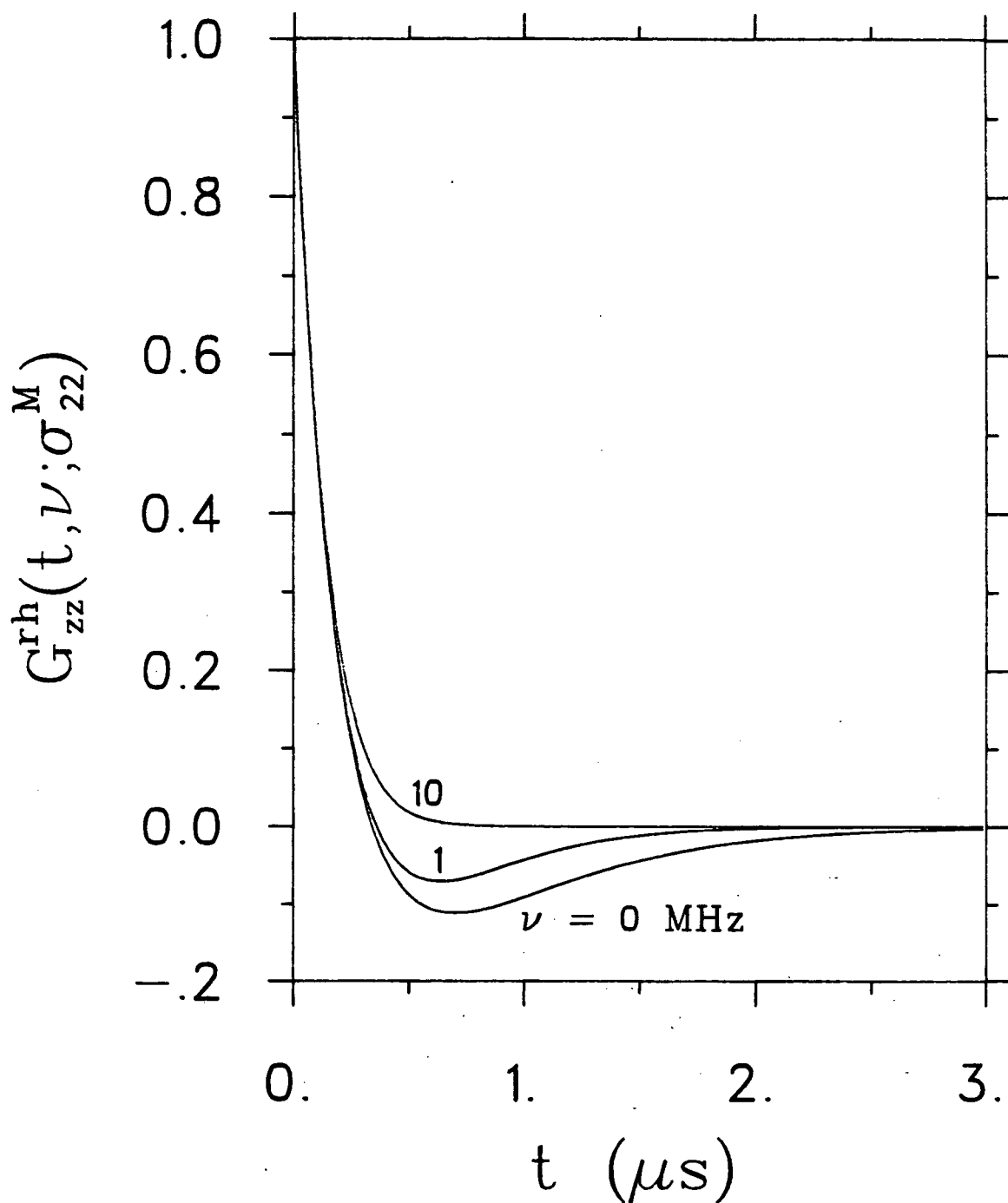
Figure III.13 Dynamic zero field Lorentzian RAHD spin relaxation function for a pure planar distortion (Strong Collision Process) plotted for selected values of the hop rate ν, where $\sigma_{22}^{M} = 10 \ \mu s^{-1}$. The curves have been normalized to equal one at t=0.

of the approximation in Equation III.25, one obtains

$$f_{xx}^{rh}(s) = \frac{1}{2} \left\{ s + \left[\frac{\sqrt{2}}{6} \sigma_{20} + \frac{2}{\pi\sqrt{6}} \sigma_{22}^{M} \right] \right\}^{-1} \qquad \text{(III.51)}$$

Substituting this into Equation III.43 and numerically calculating the inverse Laplace transform yields a time domain function which is completely independent of the hop frequency ν.

The dynamical relaxation functions corresponding to random anisotropic hyperfine interactions have thus far been calculated assuming the distortion parameters to be distributed according to Lorentzian (or Lorentzian-like) distributions of dimension less than three. These functions have been found to exhibit no motional dependence at early times, owing to the assumption of Lorentzian and Lorentzian-like distributions. If instead one assumes the same distortion symmetries, but chooses a different frequency distribution which has a finite second moment, such as the distribution defined in Equation III.26, one would expect the resulting functions to eventually motionally narrow. The strong collision dynamical function derived by assuming the "modified Lorentzian" distribution of Equation III.26 has been calculated numerically and is shown in Figure III.14 for various values of the hop rate ν. Notice that for small hop rates, this function exhibits no ν dependence at early times, but as ν is increased, motional narrowing becomes more apparent. As mentioned, however, there is no obvious physical argument that can enable one to decide which distribution is most suitable.

III.B.3 Diffusion in the Presence of Traps

Thermally activated diffusion and trapping of positive muons at defects and impurities has been observed by many authors [23,24]. Two theories have
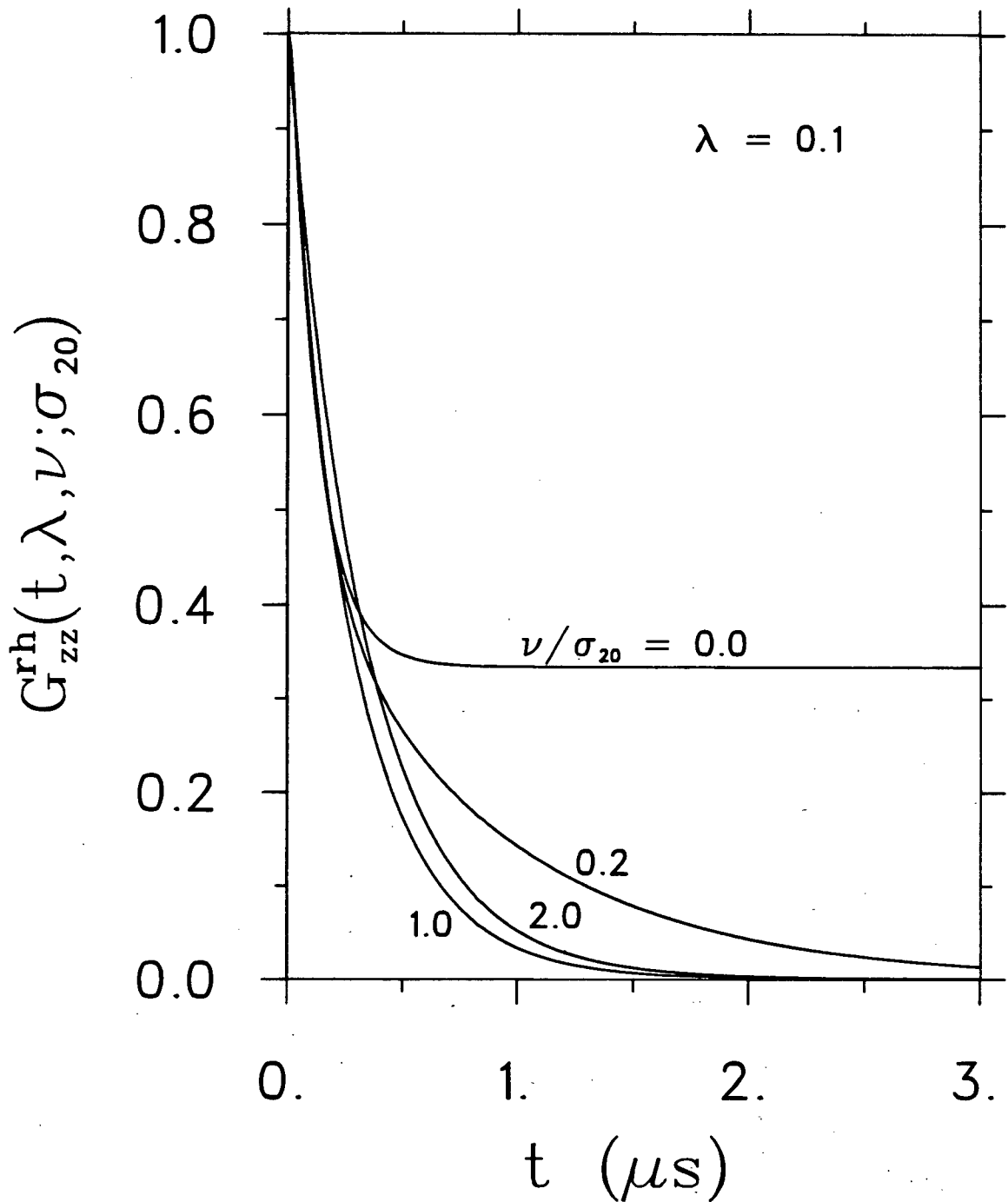
Figure III.14 Dynamic zero field modified Lorentzian RAHD spin relaxation function for a pure cylindrical distortion (Strong Collision Process) plotted for selected values of the hop rate ν, where $\sigma_{20} = 10 \ \mu s^{-1}$ and the parameter $\lambda = 0.1$. The functions are normalized to equal one at t=0.

been proposed to explain the effect of such phenomena on the μ^+ spin

polarization, one suggested by Kehr et al. [20] and another put forth by

McMullen and Zaremba [25] and Petzinger [26,27]. Both of these theories can

be extended to a muon in the muonium state as well. In the case of the

former theory, a strong collision process is assumed, making this formalism

applicable to any relaxation mechanism, whereas the latter case only applies

to muons or triplet muonium interacting with a local dipolar field.

The latter theory has been used in the present work in the analysis of

some of the transverse field data. It assumes a Gaussian approximation for

the frequency distribution due to dipolar fields and expresses the spin

relaxation function in terms of time dependent site occupation probabilities

and autocorrelation functions. The inclusion of the time dependent site

occupation probabilities allows for the possibility that the muons are not

in thermal equilibrium with respect to their site occupancy. Using

second-order time dependent perturbation theory, the transverse field spin

relaxation function for a multi-state system can be written as [26,27]

$$G_{xx}^{Mu}(t) = \exp[-\Gamma(t)] = \exp\left[-\sum_{i=1}^{\eta} \sigma_i^2 \int_o^t dt' \int_o^{t'} dt'' \, N_i(t'')\phi_{ii}(t'-t'')\right] \quad \text{(III.52)}$$

Here the sum extends over η states; σ_i^2 is the second moment of the frequency

distribution for the ith state, N_i is the time dependent probability for the

occupation of the ith state and $\phi_{ii}(t)$ is the corresponding site

autocorrelation function.

The evaluation of Equation III.52 can be facilitated by introducing a

dimensionless linewidth parameter α [28], defined as

$$\alpha = \int_o^\infty dt \, \exp\left(-t/\tau_\mu\right)\left[d\Gamma(t)/dt\right] \quad \text{(III.53)}$$

where τ_μ is the mean muon lifetime. For simplicity, stochastic hopping is assumed so that the functions $\phi_{ii}(t)$ are given by an exponential of the form $\exp(-t/\tau_i)$, where τ_i is the mean dwell time in the ith state. By combining Equations III.52 and III.53, one obtains the simple result

$$\alpha = \sum_{i=1}^{\eta} \sigma_i^2 \, \pounds\{N_i(t)\} \, \left(\frac{1}{\tau_\mu} + \frac{1}{\tau_i}\right)^{-1} \tag{III.54}$$

where $\pounds\{N_i(t)\}$ is the Laplace transform of the ith state occupation probability, with the implicit transform variable $s = 1/\tau_\mu$. For the case of an exponential relaxation, $\Gamma(t) = \alpha t/\tau_\mu$, and for a Gaussian relaxation, $\Gamma(t) = \frac{1}{2}\alpha t^2/\tau_\mu^2$. Thus, the problem of calculating the relaxation function for a multi-state system has been reduced to determining the $\pounds\{N_i(t)\}$, which are in general the solutions to a specified set of rate equations.

CHAPTER IV -- EXPERIMENTAL RESULTS AND INTERPRETATIONS

Previous to the present work it was shown [1-3] that muonium escapes the grains of fine oxide powders, including the silica powders used in the present study, and resides in the extragranular region and on the grain surfaces. This phenomenon was further shown to be totally independent of the ambient temperature of the powder grains (see section I.C). Because of the large specific surface area (390 ± 40 m^2/g [4]) and the high yield of extragranular muonium, provided by the 35 Å silica powder, this material was chosen for the present study of the interactions (i.e., surface diffusion, desorption and spin relaxation mechanisms) of muonium with surfaces.

Zero, longitudinal and transverse field μSR techniques have been used in the present work to study the behavior of muonium on silica surfaces (section IV.A). In the initial stages of this work (section IV.A.1), transverse field ($<$ 10 G) data were taken to investigate the temperature dependence of the transverse field muonium relaxation rate for several surface hydroxyl concentrations. These studies were prompted by the hypothesis that a dipole-dipole interaction between muonium and the hydroxyl protons might be a principal contributor to the relaxation of the μ^+ spin polarization for muonium on the silica surface. Assuming this hypothesis to be correct, a three-state model was also developed, which describes the diffusion and trapping of muonium on the silica surface and includes the possibility of desorption. A second set of experiments were then performed (section IV.A.2), using zero and longitudinal field techniques, to obtain information on the shape of the relaxation as well as the decoupling behavior. This information was used to discriminate between different

relaxation mechanisms, and prompted the development of a new relaxation theory, involving random hyperfine anisotropies, which is used to interpret some of the data. A third set of experiments (section IV.B), again in transverse field, were done to study the effect of fractional surface coverages of helium on the surface diffusion and trapping behavior of muonium. Finally (section IV.C), transverse field data were taken to investigate the interactions of muonium with the surfaces of platinum loaded catalysts. These experiments provided the first observation of the chemical reaction of muonium with surfaces (in this case platinum), and also suggested a possible origin for one of the surface sites for muonium on the silica surface.

The results of these experiments are individually subtle; however, they do allow one to construct an unbroken chain of logic leading to some clear deductions concerning which spin relaxation mechanism(s) are operable for muonium on the silica surface.

IV.A Muonium on Silica Surfaces

As in bulk quartz, the μ^+ spin polarization for muonium on the silica surface may experience relaxation due to random anisotropic distortions of the muonium hyperfine interaction. However, significant contributions to the total spin relaxation may also arise from other relaxation mechanisms such as random local magnetic fields (due mainly to the surface hydroxyl protons) or perhaps spin exchange interactions (with any paramagnetic impurities). In this section, data are presented and arguments are put forth to extract information concerning the motion of the muonium atoms on the silica surface as well as the origin of the relaxation interaction.

IV.A.1 Transverse Field Results

The transverse field muonium relaxation rate $\lambda_\perp^{Mu}$ is shown as a function of inverse temperature for two sample preparations in Figure IV.1; the circles are the data obtained for sample $SiO_2(1)$ prepared at 110 °C and the squares represent the date taken with sample $SiO_2(3)$ prepared at 600 °C. Let us first consider the 110 °C data. Qualitatively, these data are interpreted as follows: The plateau below about 8 K is due to muonium "localized" in a host adsorption site (by which is meant a very common shallow potential well), and the peak which occurs at about 25 K is taken to be due to trapping at less common depolarization centers (trap sites). From the low temperature plateau to the minimum at about 16 K, $\lambda_\perp^{Mu}(T)$ decreases because of motional narrowing due to hopping of the muonium atom between host sites. Between the minimum and the 25 K peak, the hopping becomes sufficiently rapid for the muonium atom to reach the trap sites before it decays. As the temperature is increased beyond the peak temperature, $\lambda_\perp^{Mu}(T)$ is seen to decrease monotonically. This decrease is attributed to detrapping and eventual desorption of the muonium atom from the grain surfaces.

If one pictures the silica powder target as a uniform distribution of spherical particles of radius R and mass density ρ_o, packed to an overall mass packing density ρ, the maximum collision frequency of the Mu atoms with the grain surfaces is easily shown to be (see Appendix III)

$$F(T) = \frac{N}{V_f}\left(\pi R^2\right)\bar{v} = \frac{3}{R}\left(\frac{k}{2\pi m_{Mu}}\right)^{1/2}\left(\frac{\rho_o}{\rho} - 1\right)^{-1} T^{1/2} \qquad (IV.1)$$

where N is the number of spherical particles in the sample, V_f is the free
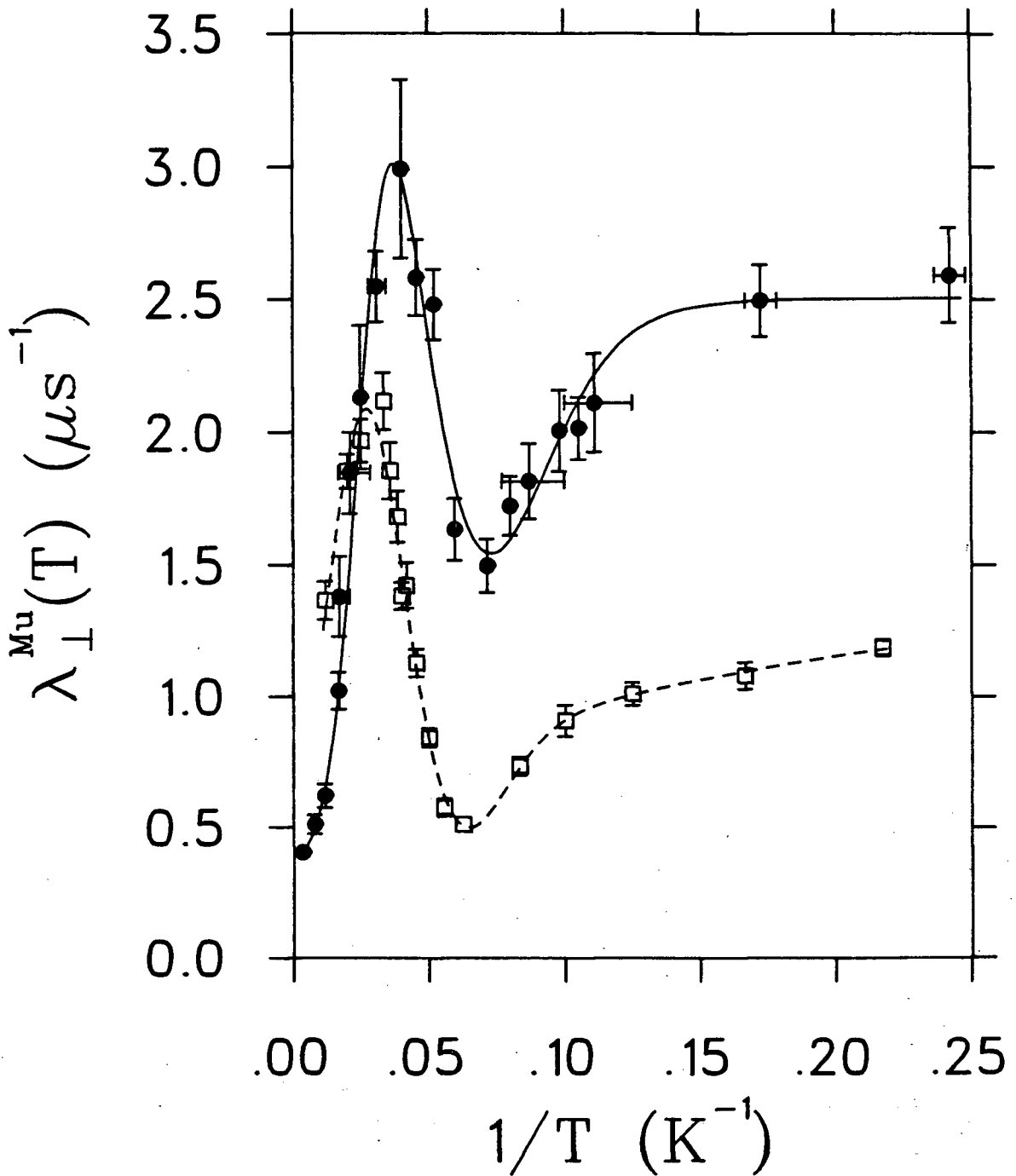
Figure IV.1 Transverse field muonium relaxation rate as a function of
inverse temperature for muonium on the surfaces of fine silica powders (mean
grain radius 35 Å) with samples prepared at 110 °C (filled circles) and at
600 °C (open squares). The lines shown are fits of the three-state model
described in the text.

volume of the sample $(V - V_{solid})$ and $\bar{v}$ is the mean thermal velocity of the muonium atom. In the case of SiO_2, $\rho_o \approx 2.2$ g/cm^3. From Equation IV.1, one might expect $\lambda_\perp^{Mu}(T)$ to exhibit some dependence on the packing density ρ, which would presumably be more evident at higher temperatures. In order to test for a possible packing density dependence of $\lambda_\perp^{Mu}(T)$, transverse field measurements were made using sample $SiO_2(2)$, which has a mass packing density of about 1/3 that of sample $SiO_2(1)$, prepared at 110 °C. Comparison of the these results with those obtained for the higher packing density reveals no significant differences below ~65 K, leading one to conclude that the relaxation rate is largely independent of the target packing density in the temperature and packing ranges studied. This result is consistent with the idea that at low temperatures, the muonium atoms are constrained primarily to motion on the surfaces of the silica grains. These data are tabulated in Appendix IV.

Now consider the temperature dependence of $\lambda_\perp^{Mu}$ for sample $SiO_2(3)$ prepared at 600 °C, also shown in Figure IV.1, for which the surface hydroxyl concentration is reduced. These data indicate the same general diffusion and trapping behavior as originally observed for sample $SiO_2(1)$ prepared at 110 °C; however, there are some important differences. In particular, one observes that the reduction in the concentration of surface hydroxyl groups is accompanied by a decrease in $\lambda_\perp^{Mu}$. Moreover, this effect seems to be more evident at lower (< 30 K) temperatures. In addition to the observed general reduction in $\lambda_\perp^{Mu}$, the position of the "trapping peak" is seen to shift to higher temperatures with reduced hydroxyl concentration. This shift in position can for instance be attributed to a decrease in the

detrapping frequency, arising in turn from the hydrolysis process. These results clearly indicate that the surface hydroxyls play an important role in the depolarization of the μ^+ spin for muonium on the silica surface. The precise role played, however, may not be simply to provide a dipole-dipole interaction. A few data points were also taken with sample $SiO_2(4)$, prepared at 600 °C, which reproduce the same behavior as observed for sample $SiO_2(3)$ prepared at the same temperature.

The temperature dependence of the average muonium hyperfine-structure interval $\bar{v}_{00}$ was also studied, using the same silica powder prepared at about 110 °C, over the temperature range 17 K < T < 300 K [5]. These measurements were made in high transverse field (~500 G) and are shown in Figure IV.2. Above ~100 K, the values obtained for $\bar{v}_{00}$ are consistent with the vacuum value (~4463.3 MHz), indicating that the muonium atoms spend the majority of their time in the extragranular region. Below ~100 K, $\bar{v}_{00}$ decreases rapidly to a value of 4437 ± 4 MHz at 17.0 ± 0.1 K, a change of about −0.6%. This effect has been attributed to adsorption of muonium on the silica surface and may be compared to the room temperature results of −0.12% and −0.13% observed for hydrogen and deuterium, respectively (see section I.D.2). These measurements are sensitive only to the isotropic part of the hyperfine interaction and thus provide no information regarding any anisotropic components. However, if one is correct in assuming that the observed distortion is due to muonium adsorbed onto the silica surface, it is easily argued that the resulting hyperfine interaction would be anisotropic, and thus induce a relaxation of the μ^+ spin polarization.

Operating under the assumption that a dipole-dipole interaction between the hydroxyl protons and the muonium atoms is a major contributor to the
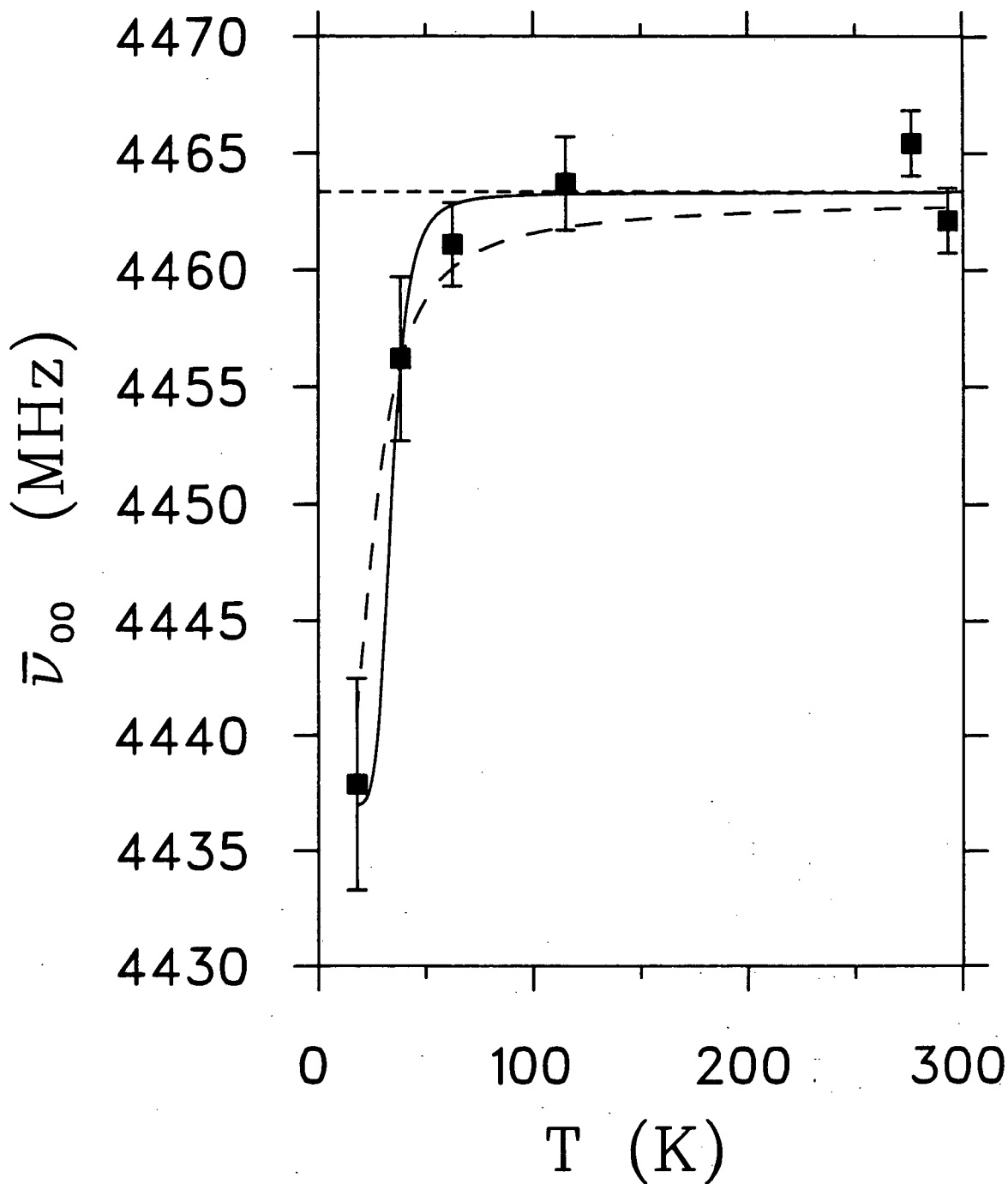
<u>Figure IV.2</u> Hyperfine-structure interval versus temperature for muonium
interacting with the silica surface (~110 °C preparation). The curves
through the points are fits to the data using Equation IV.6.

spin depolarization of the muonium ensemble, a three-state model was developed [6,7]. This model utilizes a previously developed multi-state diffusion and trapping theory [8-10], which is described in Chapter III.

To describe the transverse field data shown in Figure IV.1, one chooses a model which characterizes the muonium occupation sites on the surface in terms of equivalent trapping sites of relative concentration C_t and a remaining fraction $1-C_t$ of equivalent host sites. Since there is also a finite temperature dependent probability for desorption, the situation can be represented by a three-state model in which muonium atoms have the possibility of occupying either of the two adsorbed states or the desorbed state. By denoting the occupation probabilities for the host sites, the trap sites and the desorbed state as N_o, N_t and N_f, respectively (which obey the normalization condition $N_o + N_t + N_f = 1$) one can define the following set of coupled rate equations:

$$\begin{bmatrix} \dot{N}_o \\ \dot{N}_t \\ \dot{N}_f \end{bmatrix} = \begin{bmatrix} -(\nu_o C_t + \nu_{of}) & \nu_t(1-C_t) & \nu_{fo}(1-C_t) \\ \nu_o C_t & -[\nu_t(1-C_t) + \nu_{tf}] & \nu_{ft} C_t \\ \nu_{of} & \nu_{tf} & -[\nu_{fo}(1-C_t) + \nu_{ft} C_t] \end{bmatrix} \begin{bmatrix} N_o \\ N_t \\ N_f \end{bmatrix} \quad \text{(IV.2)}$$

Here ν_o and ν_t are the surface hop rate and detrapping rate, ν_{fo} and ν_{ft} are the host and trap site adsorption rates and ν_{of} and ν_{tf} are the desorption rates. In Equation IV.2, the hop rate from a host site to a trap site is assumed to be equal to the hop rate ν_o between host sites. Applying the normalization condition, one can then obtain the Laplace transform solutions to Equation IV.2. Assuming Arrhenius behavior, the surface hopping and detrapping rates are respectively

$$\nu_o = \nu_1 \exp\left(-E_o/kT\right) \quad \text{and} \quad \nu_t = \nu_2 \exp\left(-E_t/kT\right) \tag{IV.3}$$

where E_o and E_t are the respective activation energies. Similarly, the desorption rates are defined as

$$\nu_{of} = \nu_3 \exp\left\{-(E_o + E_f)/kT\right\} \quad \text{and} \quad \nu_{tf} = \nu_4 \exp\left\{-(E_t + E_f)/kT\right\} \tag{IV.4}$$

where the quantity $E_i + E_f$ is the desorption energy for the ith state. Finally, the associated adsorption rates are defined as

$$\nu_{fo} = F(T)\, P_o(T) \quad \text{and} \quad \nu_{ft} = F(T)\, P_t(T) \tag{IV.5}$$

Here $P_o(T)$ and $P_t(T)$ are the trapping probabilities for the host and trap sites, respectively, and $F(T)$ is the collision frequency of the muonium atoms with the grain surfaces, given in Equation IV.1. This three-state model was used to fit the transverse field data for both the 110 °C and 600 °C preparations, assuming an initial condition of $N_o = N_t = 0$ and $N_f = 1$. Other initial conditions were tried as well, but the fitted parameters were found to be independent of the initial conditions assumed. The resulting curve is shown in Figure IV.1 and the fitted parameters are given in Table IV.1(a). Because of the expected low concentration of trap sites, the effect on $\lambda_\perp^{Mu}(T)$ of direct desorption from the traps was assumed negligible (i.e., $\nu_4 = 0$). In addition, the trapping probabilities $P_o(T)$ and $P_t(T)$ were both set equal to unity. This model has also been used to fit the data for the 600 °C preparation. The resulting curve is shown in Figure IV.1 and the fitted parameters are given in Table IV.1(b). In this fit, some of the parameters were not well determined, owing to the lack of data above 85 K. Because of this, only a few error estimates were obtained.

As can be seen from Figure IV.1, this simple model describes the data

Table IV.1(a)   Fit Results for Sample $SiO_2(1)$ Prepared at 110 °C

Parameter	Value	Error	$(\chi^2/\text{deg.fr.} = 10.5/11)$	
ν_1	87	+86 / −37		μs^{-1}
ν_2	11.2	+6.6 / −2.8		μs^{-1}
ν_3	441	+889 / −230		μs^{-1}
E_o	63	+10 / −8		K
E_t	118	+25 / −17		K
E_f	212	+108 / −43		K
σ_o^2	1.02	+0.06 / −0.06		μs^{-2}
σ_t^2	18.9	+3.6 / −5.8		μs^{-2}
C_t	0.66	---		%

Table IV.1(b)   Fit Results for Sample $SiO_2(3)$ Prepared at 600 °C

Parameter	Value	Error	$(\chi^2/\text{deg.fr.} = 11.6/8)$	
ν_1	0.548	---		μs^{-1}
ν_2	4.21	+0.42 / ---		μs^{-1}
ν_3	1557	+2.3 / ---		μs^{-1}
E_o	8.37	+0.021 / ---		K
E_t	93	+3.5 / ---		K
E_f	97	---		K
σ_o^2	0.61	+0.12 / −0.12		μs^{-2}
σ_t^2	4.39	---		μs^{-2}
C_t	0.52	---		%

quite well. Of course, the relaxation interaction assumed here is much simpler than the actual interaction, and some of its features may obscure the physical parameters (hop rates, activation energies, etc.) deduced from this model. However, the qualitative explanation afforded by this model is satisfactory. For example, by comparing the fit results obtained for the two preparations (see Table IV.1), one observes that the activation energies are significantly reduced for the 600 °C preparation as compared to the 110 °C preparation. This is particularly noticeable for E_o. In addition, ν_1 for the 600 °C preparation is smaller than that for the 110 °C preparation. To understand what implications this has with respect to the motion of the muonium atoms on the silica surface, it is instructive to plot the surface hop rates ν_0 (defined in Equation IV.3) as a function of temperature, for both sample preparations. The resulting curves are are shown in Figure IV.3. Comparison of the two curves in Figure IV.3 suggests that the presence of the hydroxyl groups serves to inhibit surface diffusion of the Mu atoms at low temperatures. Another important difference is that ν_2 is significantly smaller for the 600 °C preparation as opposed to the 110 °C preparation, indicating a reduction in the detrapping rate. The reduced detrapping rate is responsible for the observed shift of the trapping peak to higher temperatures, as suggested earlier.

The data in Figure IV.2, showing the temperature dependence of the hyperfine-structure interval, have been fit assuming the model of a Mu atom thermalized in a system with total area A and total free volume V_f. This situation is represented by the equation [2]

$$\bar{\nu}_{oo} = \nu_{oo}^s \left[1 + \frac{V_f}{A}(1/\lambda_d^{Mu})\exp(-E/kT) \right] + \nu_{oo}\left[1 + \frac{A}{V_f}(\lambda_d^{Mu})\exp(E/kT) \right] \qquad (IV.6)$$
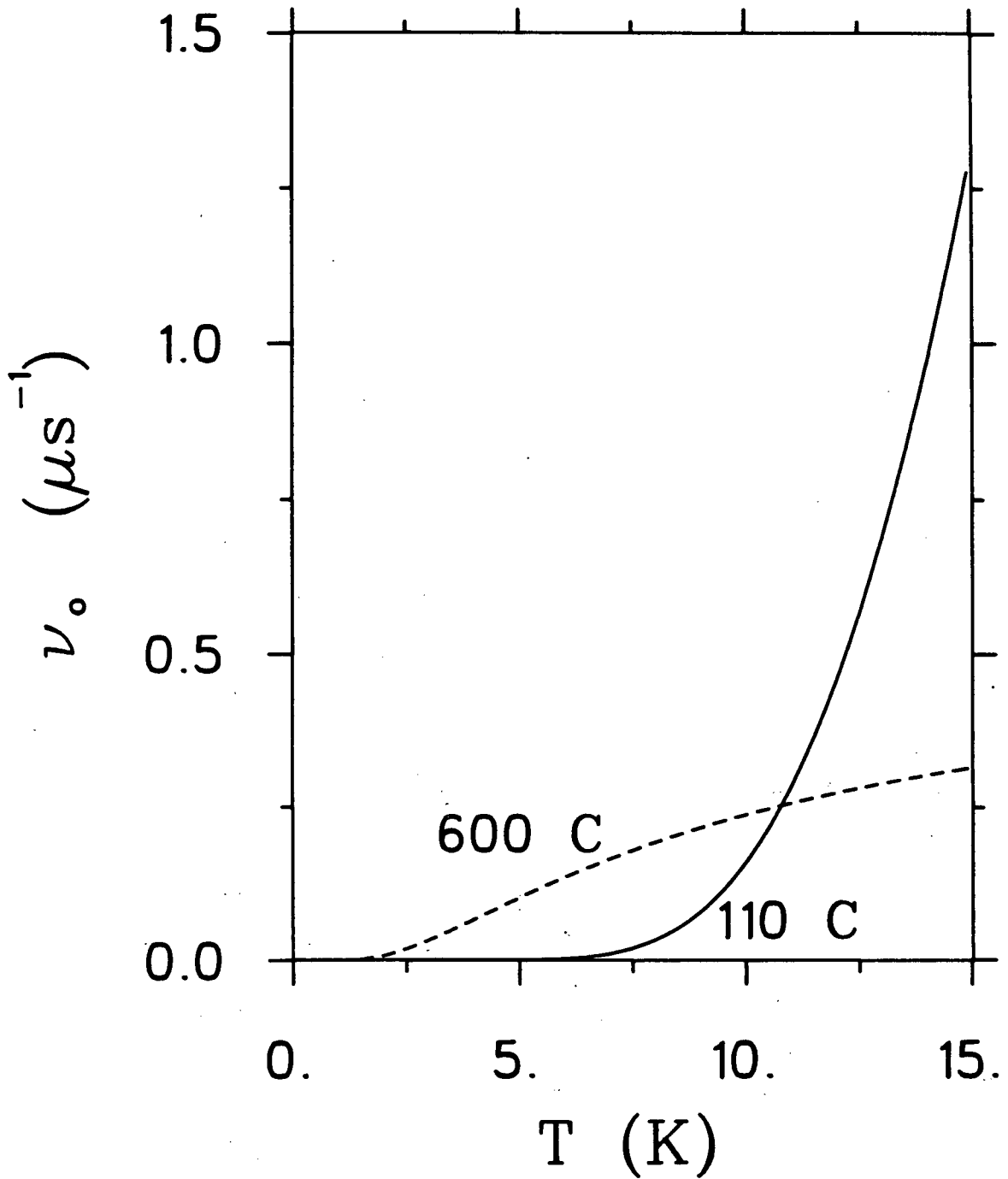
Figure IV.3 Surface hop rate ν_0 versus temperature, calculated from Equation IV.3, using the fitted parameters of Table IV.1. The solid line corresponds to the 110 °C preparation, and the dashed curve corresponds to the 600 °C preparation.

where v_{oo}^S is the hyperfine-structure interval for muonium on the silica

surface, v_{oo} is the vacuum value, λ_d^{Mu} is the thermal de Broglie wavelength

and E is the activation energy for desorption. In the fits, v_{oo}^S was fixed

at 4437 MHz, the value measured at the lowest temperature. The dashed curve

is obtained by fixing the ratio A/V_f at a value of 6.24×10^5 cm^{-1}

(calculated using the model of Appendix III) and fitting the activation

energy E. This fit gave a Chi-square of 5.66 for 5 degrees of freedom and

an activation energy of 76 (+35.4/-12.8) K. The solid line is obtained by

setting the activation energy E equal to the sum $E_f + E_o$ (= 275 K),

calculated using the values from the three-state model fit given in Table

IV.1(a), and fitting the ratio A/V_f. This fit gave a Chi-square of 4 for

5 degrees of freedom and a value of A/V_f = 3587 (+2865/-1960) cm^{-1}, two

orders of magnitude less than that given by the model calculation. This

result is not surprising since the model calculation is an overestimate,

owing to the tendency for the silica powder grains to aggregate.

IV.A.2 Zero and Longitudinal Field Results

The zero and longitudinal field asymmetry spectra taken at 7.0 ± 0.2 K

for sample SiO$_2$(4), prepared at 110 °C, are shown in Figure IV.4. According

to the interpretation of the associated transverse field data of Figure

IV.1, these data correspond to the static limit. Notice that the zero field

spectrum exhibits an initial exponential-like decay and tends to zero at

long times. Notice also that the relaxation is almost completely decoupled

for longitudinal fields of only a few Gauss. From the discussions in

Chapter III one recalls that, for relaxations due to random local magnetic
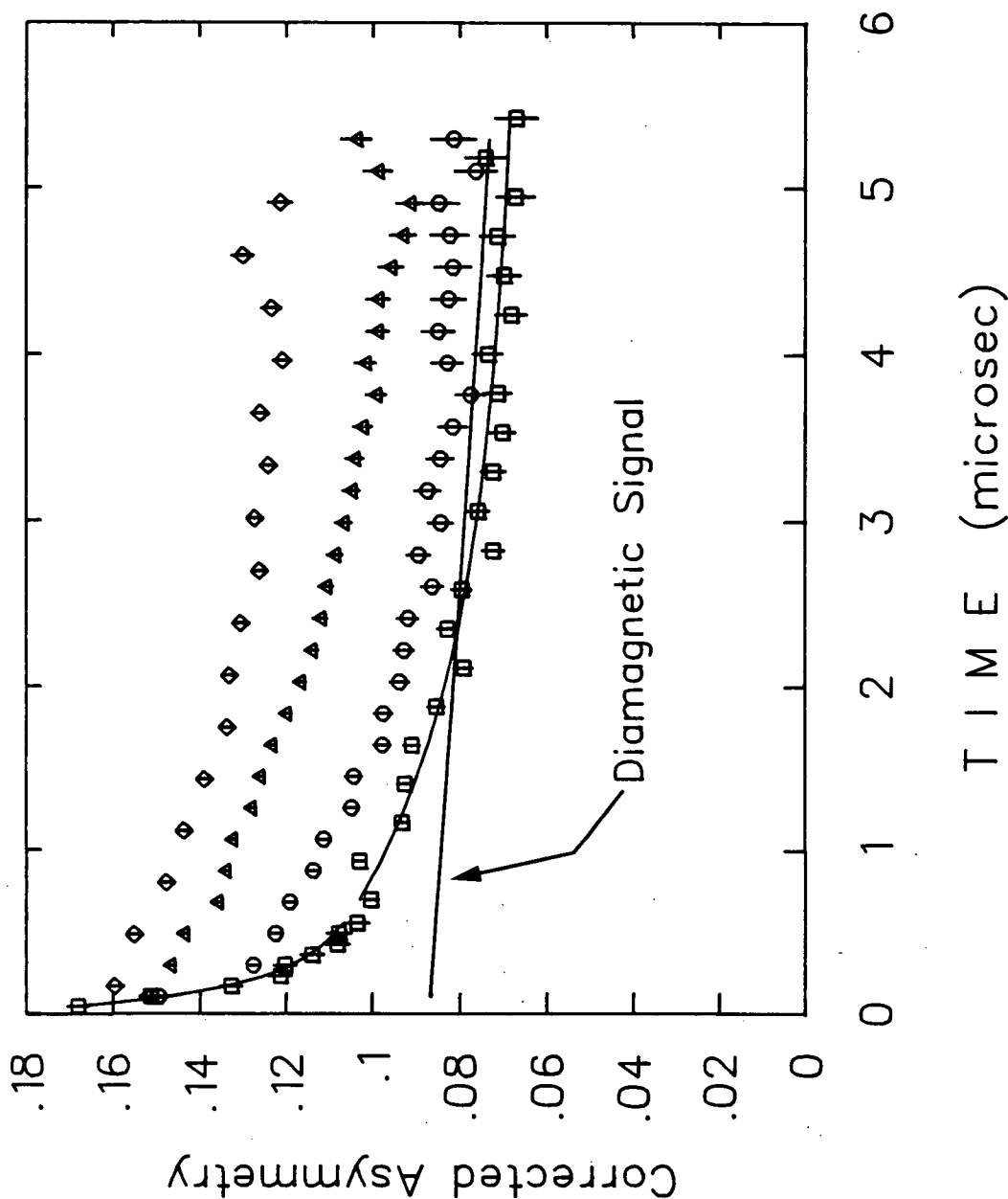
Figure IV.4 Zero and longitudinal field asymmetry spectra for muonium on
the silica surface (110 °C preparation) at 7.0 ± 0.2 K. The zero field data
are represented by the square symbols and are compared to data taken at
three different longitudinal fields; the circles correspond to 1.0 G, the
triangles to 3.0 G and the diamonds to 10.0 G. The curve through the zero
field data is a fit to the data using the static zero field relaxation
function of Equation III.21.

fields (RLMF), the relaxation function exhibits an initial Gaussian shape
unless one is in the fast hopping limit or in the limit of "randomly
ordered" moments. It has also been shown in Chapter III that in the static
limit, any form of relaxation due to random local magnetic fields would
exhibit a 1/3 recovery of the initial μ^+ spin polarization at long times.
Since the data for muonium on the silica surface below about 7 K shows no
long time recovery, one has only two possibilities:

(1) The dipole moments (hydroxyl protons) are randomly ordered,
     and the muonium atoms are not static on the silica surface.

(2) A dipole-dipole coupling is not the principal interaction
     governing the time evolution of the μ^+ spin polarization.

The first of these possibilities is difficult to reconcile with the fact
that there are about 4 hydroxyl groups per nm^2 on the silica surface, which
translates into one hydroxyl for every other Si atom. With such a large
concentration, the limit of randomly ordered moments would be difficult to
justify. Moreover, even if this were accepted, along with the concomitant
Lorentzian distribution of random local magnetic fields, the postulation of
diffusing muonium is inconsistent with the observed shape of the relaxation
function in longitudinal field. Recall from Chapter III that for a static
muonium atom interacting with a random local field, the spin relaxation can
be completely decoupled in a longitudinal field on the order of the local
dipolar field; whereas for a dynamic system, the relaxation would continue
to exhibit a decay at long times, even in high longitudinal fields. The
data shown in Figure IV.4 show the relaxation to be almost completely
decoupled for very small fields, which is inconsistent with what one would
expect for a dynamic probe. From this argument one may conclude that a
random dipolar interaction is not the principal relaxation mechanism for

muonium on the silica surface. The fact that the data in Figure IV.4 shows

the relaxation to be easily quenched in low field, however, leads one to

suspect a random anisotropic hyperfine distortion (RAHD) as a likely

candidate. One can easily argue that the relaxation function for a dynamic

muonium atom, interacting via a random anisotropic hyperfine interaction,

would also exhibit a decay at long times, even in high longitudinal fields.

Thus if one assumes a relaxation due to RAHD, the low temperature zero and

longitudinal field data shown in Figure IV.4 indicates muonium to be in the

static limit, in agreement with the interpretation of the transverse field

data of Figure IV.1.

Let us now consider whether a random anisotropic hyperfine interaction

alone can adequately explain the data. In this case, an exponential-like

decay is expected as long as the frequencies are distributed according to a

Lorentzian distribution function. As discussed in Appendix I and in Chapter

III, a 1/3 residual polarization is expected in the static limit for a

cylindrically distorted random hyperfine interaction. Thus, as in the case

of random local fields, a cylindrical distortion of the muonium hyperfine

interaction is not sufficient to explain the data. If, however, one

includes a planar distortion component as well, one obtains a function which

has the required exponential-like initial decay, and also tends to zero at

long times (Equation III.21). The curve in Figure IV.4 is a fit of Equation

II.10, assuming the relaxation function of III.21, to the data. The fit

gave a Chi-square of 45.1 for 28 degrees of freedom, and the fitted results

for the cylindrical and planar distortion frequencies (distribution widths)

were found to be 12.1 (+1.59/-1.33) μs^{-1} and 0.86 (+0.085/-0.090) μs^{-1},

respectively. The muonium asymmetry (for triplet muonium) was allowed to

vary in the fit and was found to equal 0.103 (+0.0047/-0.0042). This value

is consistent with that obtained for the corresponding transverse field data

(taken with the same sample and preparation).

As has already been discussed, the effects of a random anisotropic

hyperfine interaction can be effectively decoupled for $\omega_{Mu} \gg \sigma_{2m}$. From the

results of the zero field fit, this translates into a field on the order of

a few Gauss, which is consistent with the data in Figure IV.4.

By substituting the values of σ_{20} and σ_{22}^M obtained in the zero field

fit, into the transverse field approximation of Equation III.25, one obtains

a transverse field relaxation rate λ_1^{Mu} of 3.1 ± 0.38 μs^{-1}. This result is

consistent with the relaxation rate determined for the associated transverse

field data, shown in Figure IV.1.

The zero and longitudinal field asymmetry spectra taken at 3.6 ± 0.2 K,

using sample $SiO_2(3)$ prepared at 600 °C, are shown in Figure IV.5. As in

the case of the data for the 110 °C preparation, the zero field spectrum

exhibits an exponential-like decay and also tends to zero at long times.

The curve through the zero field data is a fit of Equation II.10 to the

data, assuming the static random anisotropic hyperfine distortion function

of Equation III.21. The fit gave a Chi-square of 87.3 for 53 degrees of

freedom, and the fitted results for the cylindrical and the planar

distortion parameters were found to be equal to 4.4 (+0.8/-0.9) μs^{-1}, and

1.8 (+0.2/-0.15) μs^{-1}, respectively. The muonium asymmetry was allowed to

vary in the fit and found to equal 0.069 (+0.0023/-0.0022). This value is

consistent with that obtained for the corresponding transverse field data,

but it is significantly less than that found for sample $SiO_2(4)$ prepared at
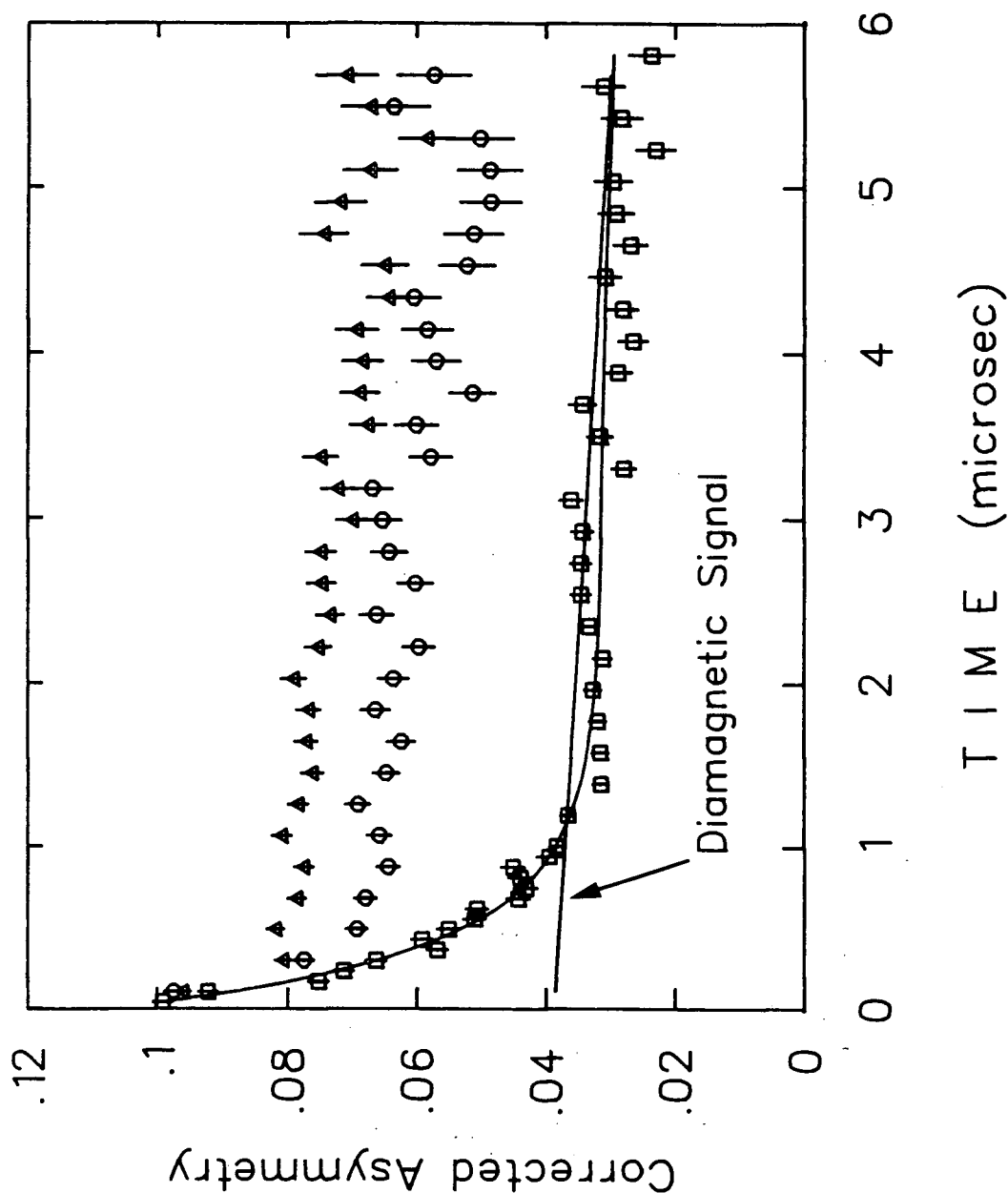
Figure IV.5 Zero and longitudinal field asymmetry spectra for muonium on the silica surface (600 °C preparation), at 3.6 ± 0.2 K. The zero field data are represented by the square symbols and are compared to data taken at two different longitudinal fields; the circles correspond to 0.2 G and the triangles to 0.5 G. The curve through the zero field data is a fit to the data using the zero field static relaxation function of Equation III.21.

110 °C. This difference arises simply because the window on sample $SiO_2(4)$ is 25 μm thick, whereas the window on sample $SiO_2(3)$ is 50 μm thick. More muons are therefore stopped in the window for sample $SiO_2(3)$, thereby adding to the diamagnetic fraction observed. A comparison of the distortion parameters obtained here with those obtained for the 110 °C preparation indicates a correspondence between the muonium hyperfine distortion and the concentration of surface hydroxyl groups; the cylindrical component σ_{20} increases, while the planar component σ_{22}^M decreases, with increasing hydroxyl concentration. This result is rather interesting because it suggests that the presence of the hydroxyl groups affects the local environment of the muonium atom in a manner which induces an associated distortion symmetry in the muonium hyperfine interaction. Moreover, the fact that the observed distortion for the 110 °C preparation is shown to have an enhanced cylindrical component and a diminished planar component, relative to the 600 °C preparation, suggests that the electrostatic interaction between the muonium atom and the hydroxyl groups is repulsive. Although this interpretation does adequately explain the observed behavior, one cannot exclude the possibility that this result could merely be a manifestation of a combined relaxation involving both random hyperfine anisotropies and random dipolar fields.

By substituting the values of σ_{20} and σ_{22}^M for the 600 °C preparation into Equation III.25, the transverse field relaxation rate $\lambda_{\perp}^{Mu}$ is calculated to be 1.5 ± 0.25 μs^{-1}. This result is again consistent with the associated transverse field data.

Data were also obtained with sample $SiO_2(3)$ (prepared at 600 °C), in

the dynamic region from 6 K to 20 K. The zero and longitudinal field data

taken at 16.0 ± 0.1 K (where the muonium atoms are believed to be hopping

between the host sites) are shown in Figure IV.6. The zero field data for

this temperature exhibit a slight decrease in the initial decay (motional

narrowing) as compared to the static case of Figure IV.5, but there is no

indication of the σ_{22}^M minimum. The absence of a minimum is predicted by the

dynamical model derived from the static formula of Equation III.21 and the

strong collision model of Equation III.43 (see Figures III.10 - III.12);

however, the observed motional narrowing effect is inconsistent with this

function. This inconsistency merely reflects the fact that the distortion

frequencies are only approximately distributed according to a Lorentzian

distribution, and this approximation breaks down when motion is introduced.

The transverse field results indicate two different types of adsorption

sites (host and trap sites) for muonium on the silica surface. Thus far it

has been concluded that the depolarization of the μ^+ spin for muonium in

the host sites (at low temperatures) is largely due to random anisotropic

hyperfine distortions, with possibly a small contribution arising from the

random local magnetic fields produced by the hydroxyl protons.

To decipher which relaxation mechanism(s) are operating at the trap

sites, zero and longitudinal field data were taken at the high temperature

peak, where muonium is presumed trapped. The data taken at 25 ± 0.5 K, for

sample $SiO_2(4)$ prepared at 110 °C, are shown in Figure IV.7. A comparison

of this data with the low temperature data of Figure IV.4, where the muonium

atoms are thought to be primarily in the host sites, shows two distinctly

different decoupling behaviors for the two sites. Specifically, the

relaxation at the host sites is almost completely decoupled (quenched) for a
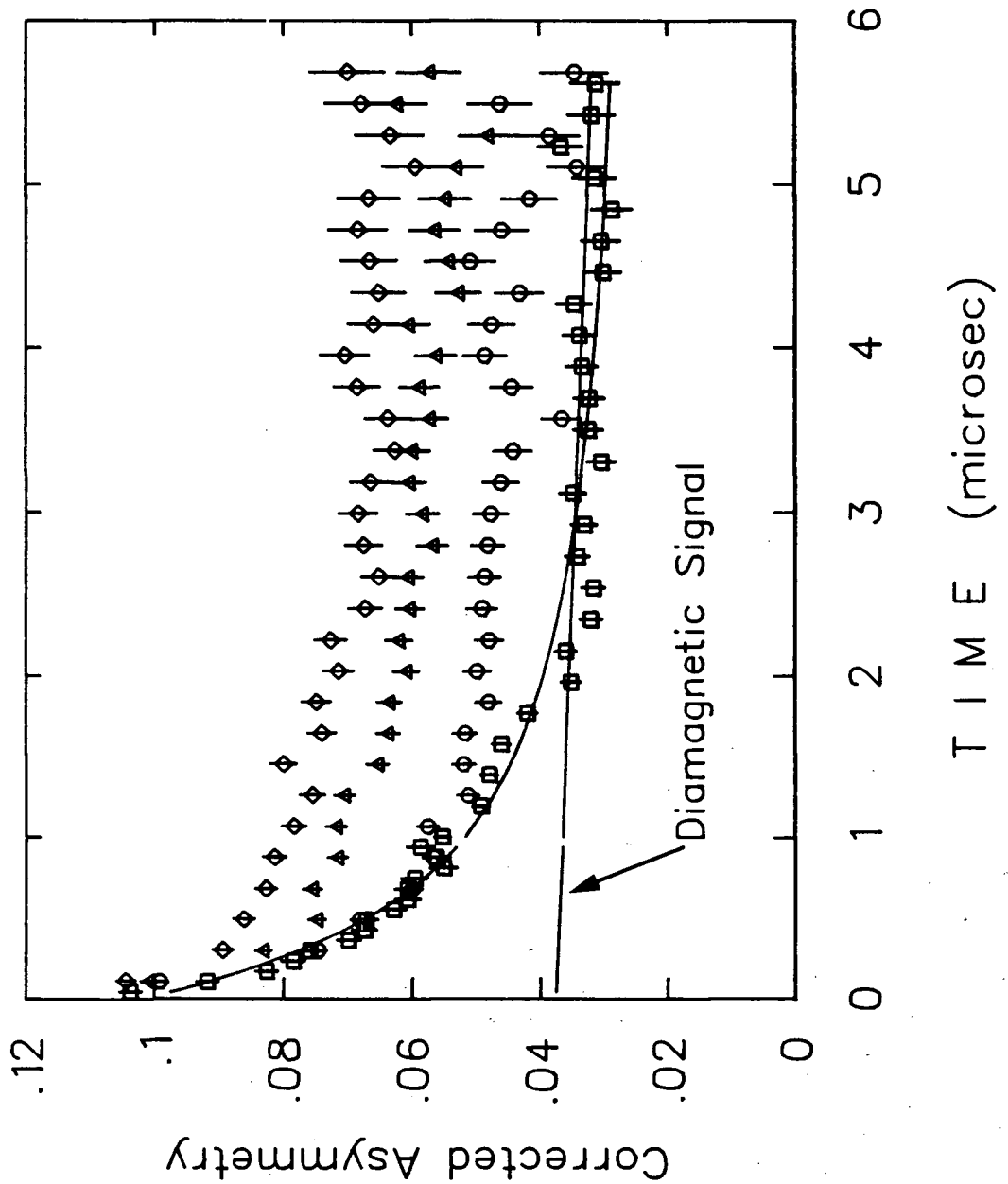
Figure IV.6 Zero and longitudinal field asymmetry spectra for muonium on the silica surface (600 °C preparation), at 16.0 ± 0.1 K. The zero field data are represented by the square symbols and are compared to data taken at three different longitudinal fields; the circles correspond to 0.2 G, the triangles to 0.5 G and the diamonds to 1.0 G.
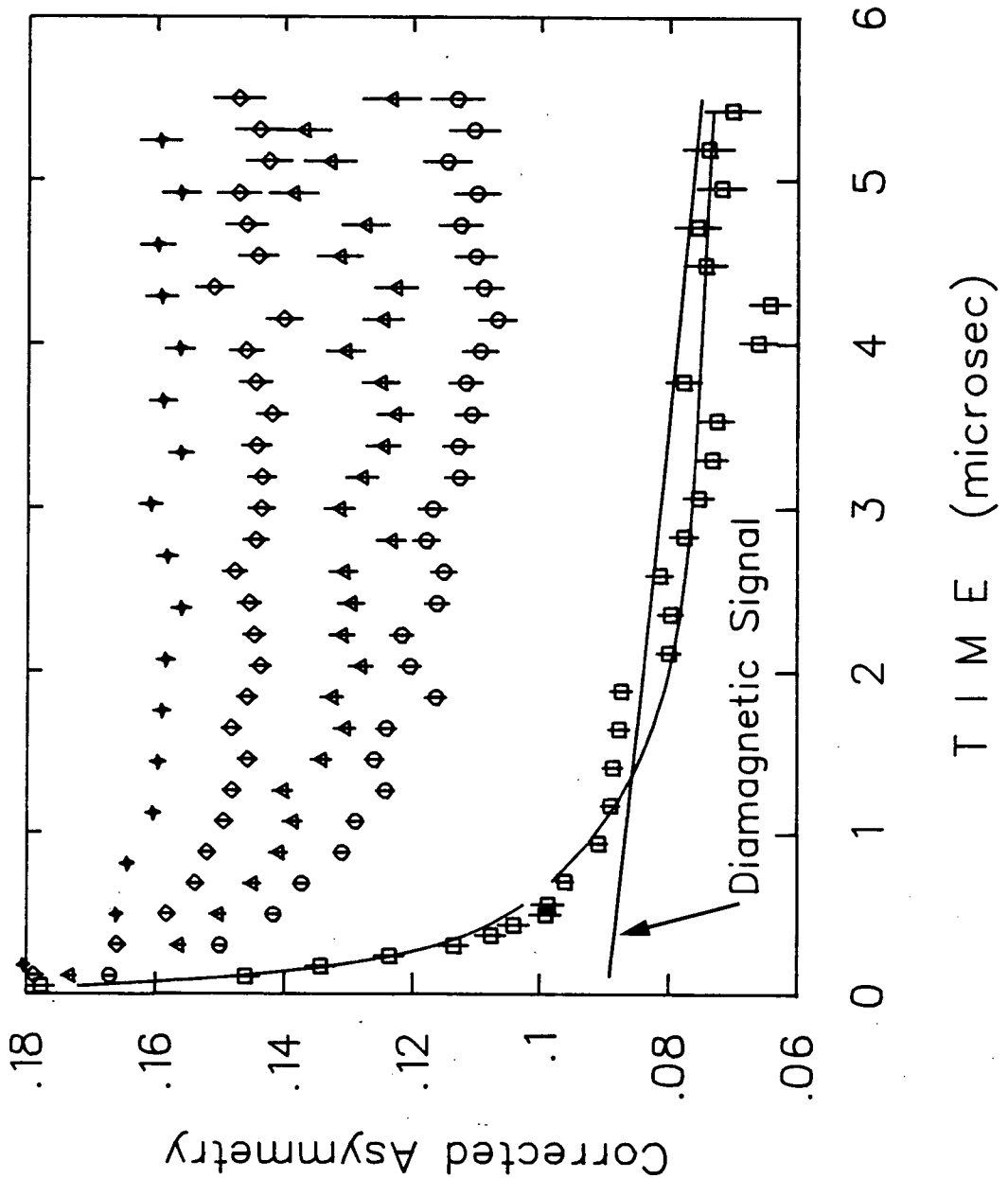
Figure IV.7 Zero and longitudinal field asymmetry spectra for muonium on the silica surface (110 °C preparation), at 25.0 ± 0.5 K. The zero field data are represented by the square symbols and are compared to data taken at four different longitudinal fields; the circles correspond to 4.0 G, the triangles to 10.0 G, the diamonds to 25.0 G and the crosses to 45.0 G. The curve through the zero field data is a fit to the data using the zero field static relaxation function of Equation III.21.

longitudinal field of only 2.0 G, whereas at the trap sites there remains a small unquenched component, even up to 45 G. The curve through the zero field data is a fit of Equation II.10 to the data, assuming the static zero field relaxation function of Equation III.21. The fit gave a Chi-square of 83.8 for 28 degrees of freedom, and the cylindrical and planar components were found to be equal to 13 (+1.4/-1.2) μs^{-1} and 1.47 (+0.098/0.096) μs^{-1}, respectively. The triplet muonium asymmetry was also fitted and found to be 0.11 (+0.0043/-0.0041). The corresponding data taken at 30 ± 0.5 K, for sample $SiO_2(3)$ prepared at 600 °C, is shown in Figure IV.8. A comparison of Figures IV.7 and IV.8 indicates that the relaxation may be more easily quenched for the 600 °C preparation than for the 110 °C preparation. The curve through the zero field data is a fit of Equation II.10, assuming the static zero field function of Equation III.21. The fit gave a Chi-square of 39.1 for 38 degrees of freedom, and the cylindrical and planar distortion parameters were found to be 7 (+1/-0.9) μs^{-1} and 1.04 (+0.075/-0.074) μs^{-1}, respectively. The triplet muonium asymmetry was also fitted and found to be 0.076 (+0.0063/-0.0059). The associated transverse field relaxation rates, calculated from Equation III.25, are also consistent with the respective transverse field data for both the 110 °C and 600 °C preparations.

These results suggest that the nature of the relaxation in the trap sites may be a function of the surface preparation. A paramagnetic ion, for instance, which is somehow neutralized by baking at high temperatures, might explain this data. The most likely candidate for this is an Fe^{3+} ion. In the Cab-O-Sil EH-5 material, iron impurities are quoted as being less than 2 ppm [11]; however, recent measurements have set this level at ~6 ppm [12]. This possibility is discussed further in section IV.C.
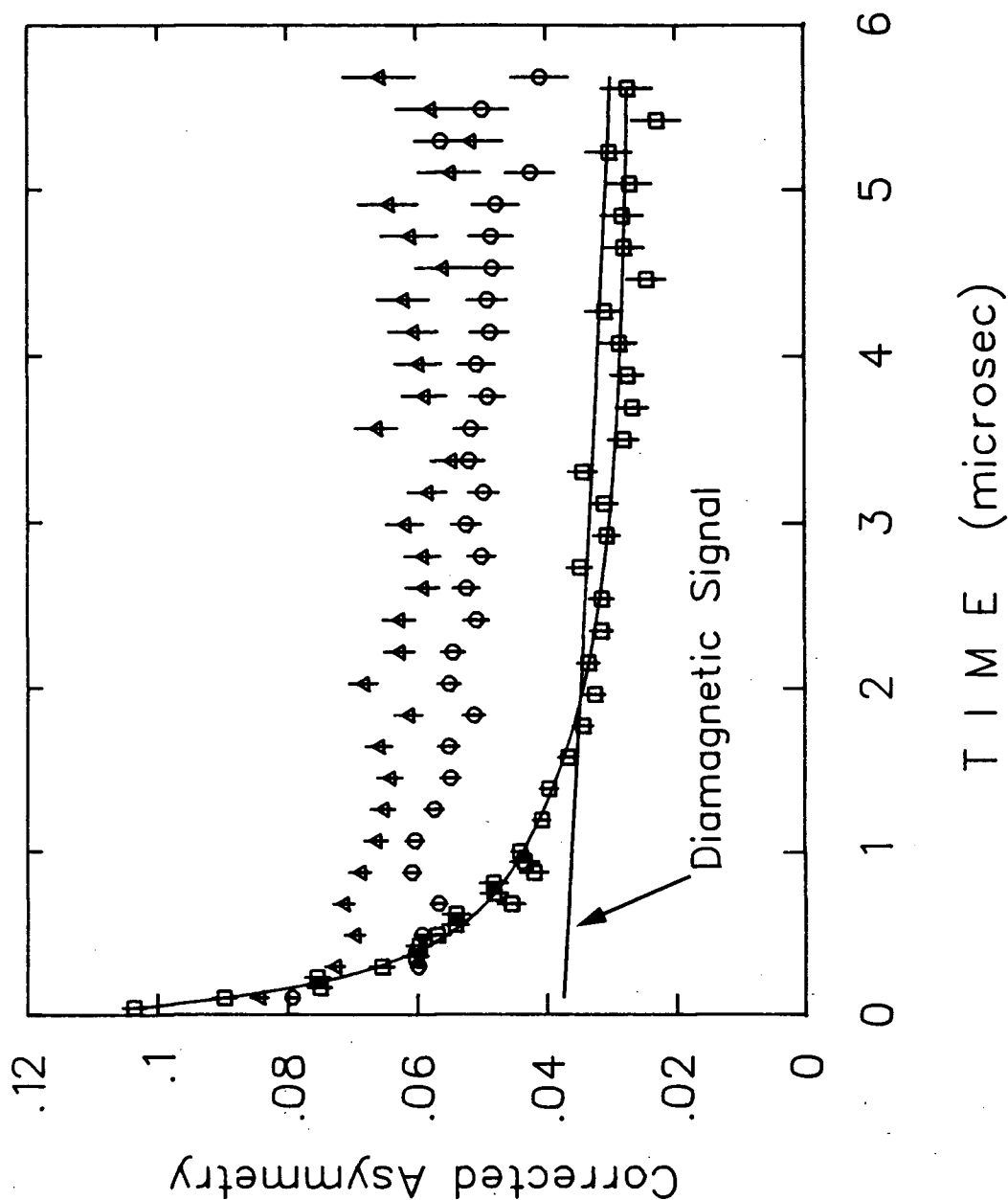
Figure IV.8 Zero and longitudinal field asymmetry spectra for muonium on
the silica surface (600 °C preparation), at 30.0 ± 0.5 K. The zero field
data are represented by the square symbols and are compared to data taken at
two different longitudinal fields; the circles correspond to 0.5 G and the
triangles to 2.0 G. The curve through the zero field data ia a fit to the
data using the static zero field relaxation function of Equation III.21.

IV.B Muonium on the Surface of Helium Coated Silica

Gas adsorption isotherms were measured using ^{4}He at 6.0 ± 0.1 K,

concomitant with measurements of the transverse field muonium relaxation

rate and the muonium formation probability. The gas deposition was

performed according to the procedure given in Chapter II.

IV.B.1 Relaxation Rate Versus ^{4}He Coverage at 6 K

The transverse field relaxation rate $\lambda_\perp^{Mu}$ for sample $SiO_2(4)$ prepared at

110 °C and for sample $SiO_2(3)$ prepared at 600 °C is plotted as a function of

the specific volume V_s in Figure IV.9. By definition, the specific volume

is the volume of gas, measured at STP, divided by the surface area of the

target. From this data, it is obvious that the dependence of $\lambda_\perp^{Mu}$ on surface

coverage is a strong function of the sample preparation. In particular, the

110 °C data are observed to decrease monotonically with increasing coverage,

while the 600 °C data show a peak in the coverage dependence. Furthermore,

this peak has a maximum which is equal (within the uncertainties) to the

trap site relaxation rate for the 600 °C data, shown in Figure IV.1.

Interpretation of the 110 °C data is straightforward. At zero

coverage, the muonium atoms are stationary in the host sites on the silica

surface. As the coverage is increased from zero, the probability of a Mu

atom interacting with the silica surface decreases because there is less

exposed surface area.

Interpretation of the 600 °C data is not so trivial. A model can be

developed around the assumption that the baking procedure produces fissures

in the surfaces of the silica grains. These fissures are further assumed to

act as deep potential wells which have the same relaxation mechanism as the
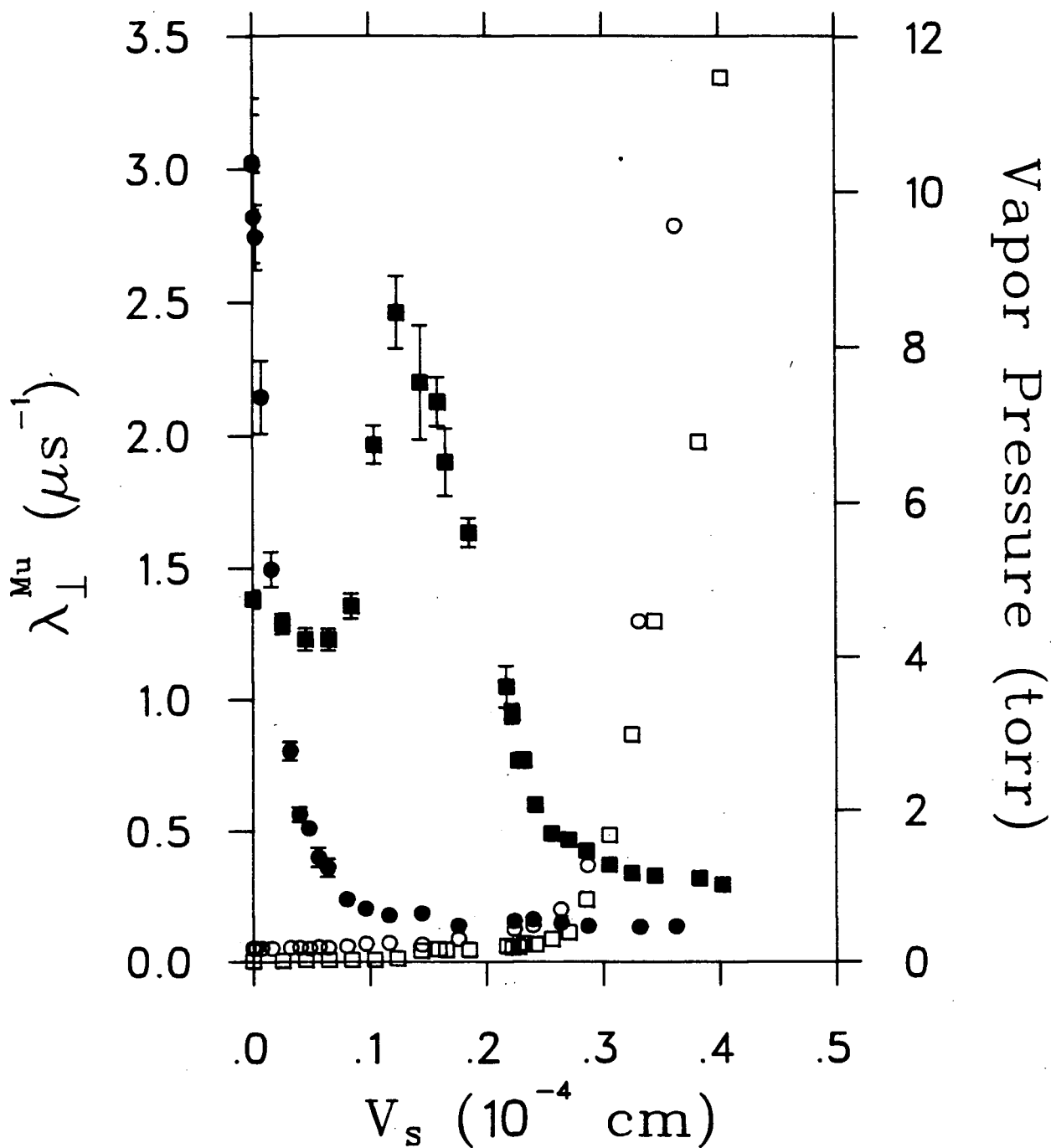
Figure IV.9 Transverse field muonium relaxation rate at 6.0 ± 0.1 K versus ^{4}He coverage (measured in terms of specific volume V_s) for silica prepared at 110 °C (circles) and at 600 °C (squares). The filled symbols correspond to the relaxation rate and the open symbols correspond to the vapor pressure (right hand scale). Notice that the vapor pressure increases rapidly at monolayer completion.

host sites. With these assumptions, one can adopt the following model: At zero coverage the muonium atoms are presumed stationary, but in this case the muonium atoms may occupy either the host sites or the deep potential wells. As the coverage is increased from zero, the helium is adsorbed preferentially into the deep potential wells. At some critical coverage, which looks to be about 20% of a monolayer, the helium atoms fill up the fissures sufficiently to form "bridges" over which a muonium atom may diffuse rapidly until it reaches a "normal" trap site. As the coverage is increased beyond this point, the behavior mimics the 110 °C data; $\lambda_{\perp}^{Mu}$ decreases monotonically with increasing coverage because the chance of encountering the silica surface decreases with increasing coverage.

IV.B.2 Muonium Asymmetry Versus ^{4}He Coverage

Measurements of the muonium asymmetry were also made as a function of surface coverage at 6.0 ± 0.1 K. The relative asymmetry (for one of the positron telescopes) is plotted against the specific volume V_s of ^{4}He adsorbed onto the silica surface in Figure IV.10. The data show that the muonium asymmetry decreases with increasing surface coverage, suggesting that the charge exchange cross section is significant at the helium-silica interface. Unfortunately, it is not possible to draw any conclusions from these data regarding the origins and mechanics of muonium formation in the silica powders (i.e., surface or bulk formation), since the precise role played by the adsorbed helium atoms in the charge exchange interaction at the He-SiO$_2$ interface is not as yet known. Two possibilities for this phenomenon are put forth in Chapter V.
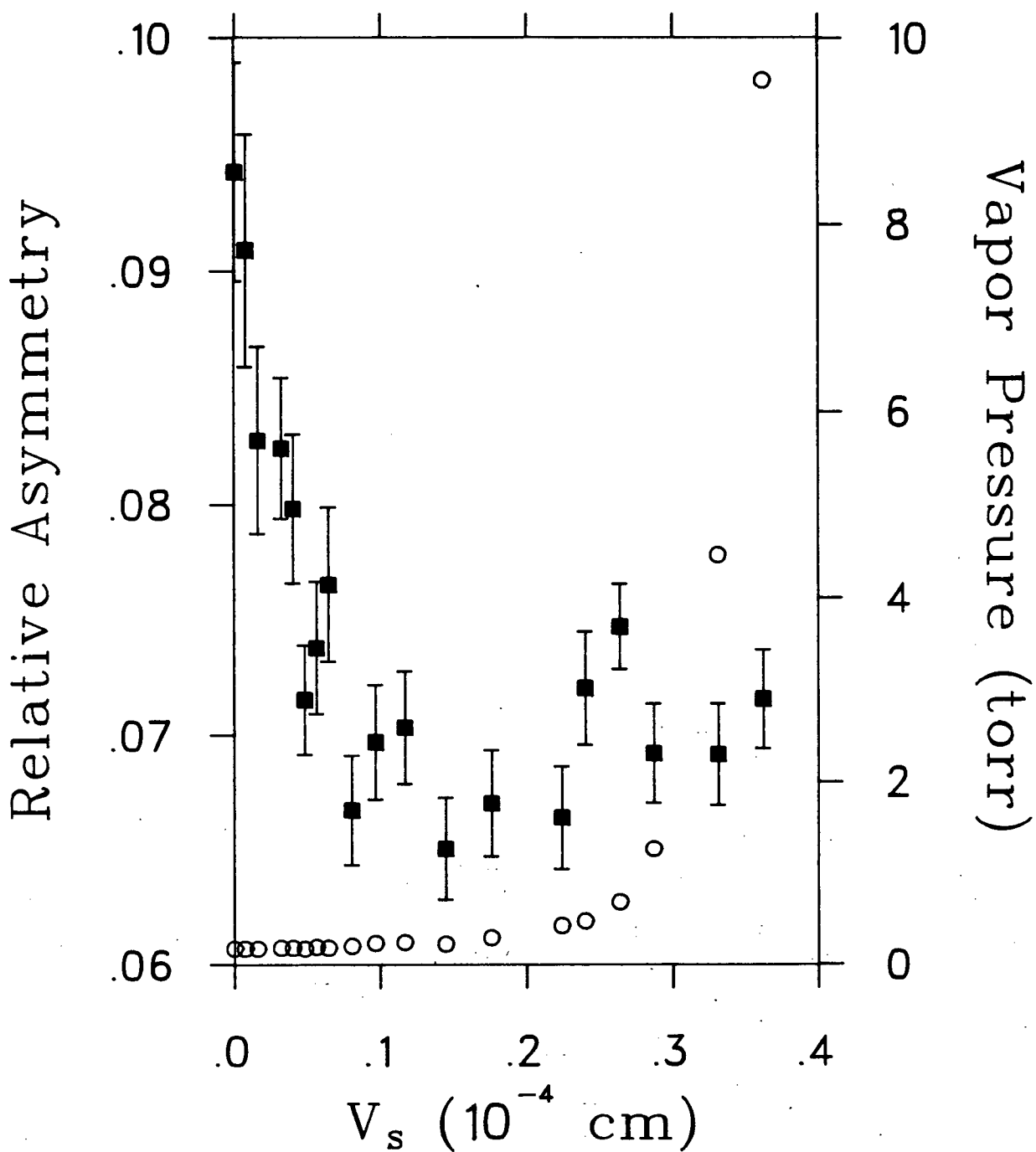
<u>Figure IV.10</u> Transverse field muonium asymmetry versus ^{4}He coverage (closed squares) for sample $SiO_2(4)$ prepared at 110 °C. The corresponding vapor pressure data are represented by the open circles.

IV.C Muonium on the Surface of Supported Platinum Catalysts

The behavior of muonium on the surface of platinum loaded silica was studied by measuring the transverse field muonium relaxation rate $\lambda_\perp^{Mu}$ as a function of temperature, over the temperature range 5 K < T < 100 K, for samples prepared with varying levels of Pt loading. Since a great deal of information has already been acquired concerning the behavior of muonium on the surface of the 35 Å Cab-O-Sil (EH-5) powder, this material was selected as the support material for the Pt loaded catalyst samples. These samples were prepared following the procedures described elsewhere [13], which include reduction in a mixture of H_2 and He at 500 °C for a period of one hour (see section II.C.3). Four levels of Pt loading were chosen for these initial tests; 0.001%, 0.01%, 0.1% and 1.0%, by weight. A control sample containing no Pt (unloaded), but otherwise prepared following the same procedures, was also measured. Some of the specifics of these samples and the target vessels are given in Table II.4(b).

As already discussed in Chapter II, these samples were evacuated and warmed to a temperature of about 100 °C for a period of ten hours prior to the experiment. This was done to remove physisorbed water from the silica surface. Since no other surface treatment was done, the supported platinum particles, which average 10 Å or less in radius, were presumed to be covered with approximately a monolayer of chemisorbed oxygen.

IV.C.1 Unloaded Silica Support

The temperature dependence of the transverse field relaxation rate $\lambda_\perp^{Mu}$ was measured for the H-reduced control sample, containing no Pt loading. The results of these measurements are shown in Figure IV.11, along with the
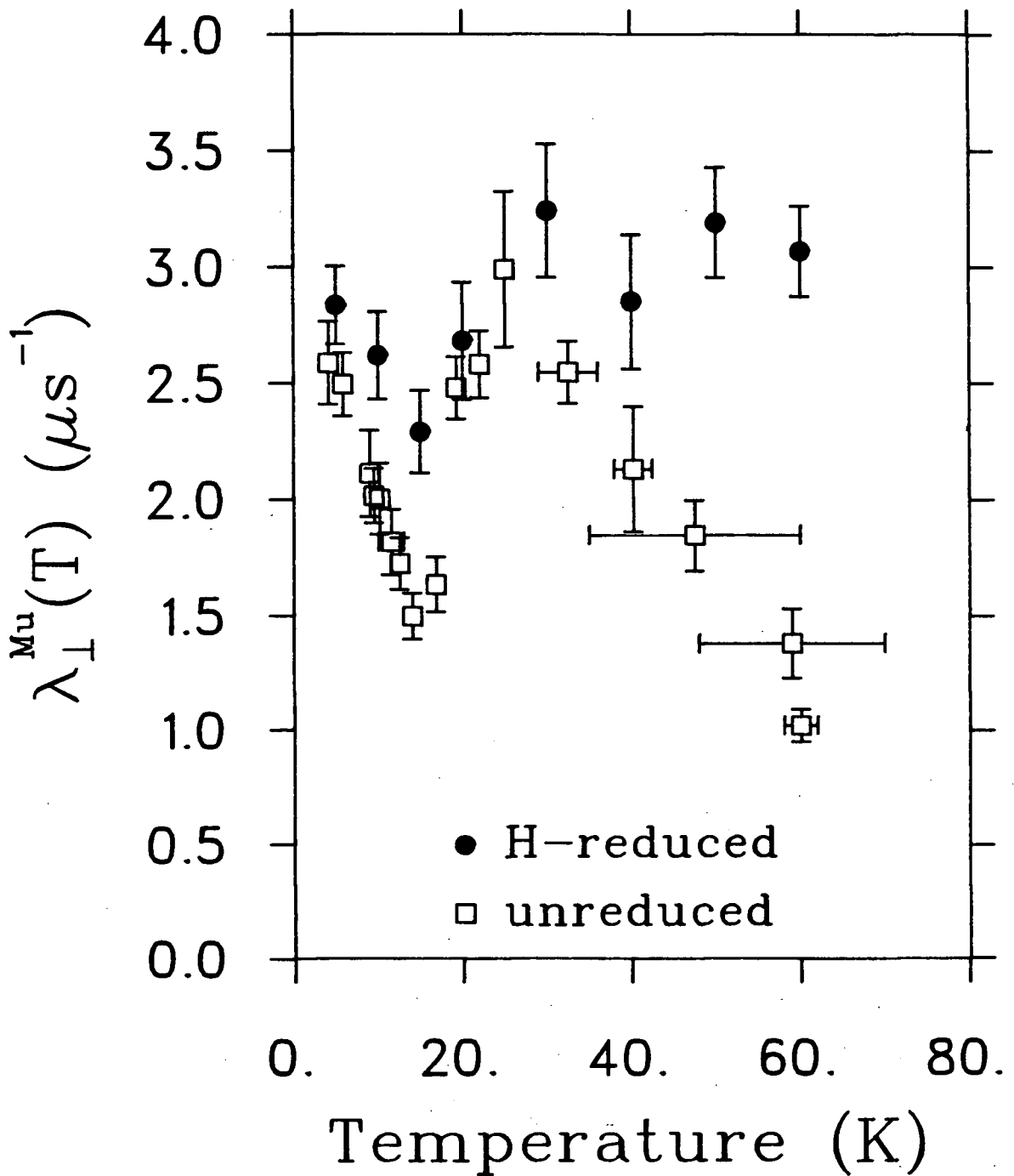
Figure IV.11 Transverse field muonium relaxation rate versus temperature
for unreduced and hydrogen-reduced silica. The filled circles represent the
data taken with the reduced material (sample Pt(1) prepared at 100 °C), and
the open squares are the data taken with unreduced silica (sample SiO_2(1)
prepared at 110 °C).

corresponding results for the unreduced material (sample SiO_2(1) prepared at 110 °C). Comparison of these data suggests roughly the same diffusion and trapping behavior for the H-reduced sample as observed for the unreduced sample. Without evidence to the contrary, the two surface sites observed for the reduced sample can be assumed to be of the same nature as the corresponding sites of the unreduced material, but the greatly increased width of the high temperature peak in the latter is indicative that the hydrogen reduction affects the high temperature sites (traps) more than the low temperature sites (host sites). The data in Figure IV.11 are interpreted following the same line of reasoning as presented for the unreduced silica.

The assumption that the muonium atoms are stationary at low (< 8 K) temperatures, for both the reduced and the unreduced silica, is based on two observations. First, the physisorption of helium gas at 6 K sharply decreases $\lambda_\perp^{Mu}$ as one nears monolayer completion, indicating that the muonium atoms are outside the powder grains and spending a large portion of their lives on the surface. Second, $\lambda_\perp^{Mu}(T)$ for the H-reduced silica was found to be totally independent of the Pt loading at low temperatures. The absence of a Pt loading dependence at low temperatures implies that during their lifetime, the muonium atoms cannot diffuse over distances comparable to the mean separation between Pt particles. With the loadings that have been studied, the mean separation between Pt particles corresponds to spacings of 50 or more SiO-H groups. These distances can easily be spanned by a diffusing muonium atom moving at thermal velocities, for temperatures as low as 5 K; their failure to do so provides further evidence that the muonium atoms are indeed stationary on silica surfaces at low temperatures.

IV.C.2 Platinum Loaded Silica: 0.001% and 0.01%

The effects of extremely light (0.001% and 0.01%) Pt loading on the
transverse field muonium relaxation rate is shown in Figure IV.12. For the
reasons discussed previously, the muonium atoms are again assumed to be
frozen in a surface host site at low temperatures. As the temperature is
increased above about 10 K, $\lambda_{\perp}^{Mu}(T)$ decreases, presumably due to motional
narrowing, in the same manner as for the unloaded sample. At higher
temperatures, one observes that for both samples $\lambda_{\perp}^{Mu}(T)$ continues to
decrease monotonically with only the 0.001% loading still indicating a
slight hint of a trapping peak. The relaxation rates for these two samples
eventually become indistinguishable, leveling off at about 0.5 μs^{-1}.

These results can be understood by first recalling that only with a
loaded silica catalyst can H_2 molecules be dissociated to form atomic
hydrogen. It is clear also that the high temperature peak observed at about
25 K in both the unreduced and reduced, unloaded samples, can be expected to
be a trap for atomic hydrogen as well as muonium. Bearing this in mind, one
can postulate that this trap site might be filled, or otherwise neutralized,
by the atomic hydrogen generated in the reduction step of the loading
procedure. If this model is correct, it would explain the lack of a
trapping peak for the Pt loaded samples, in which large quantities of atomic
hydrogen can be generated upon H-reduction, whereas for the case of the
unloaded H-reduced sample, where there is very little atomic hydrogen
generated, the trapping peak is quite pronounced.

Similarly pronounced effects of catalyst loading, using hydrogen
reduction techniques, have been observed in magnetic susceptibility studies
[14] of palladium loaded silica catalysts, as well as in ESR studies [15] of
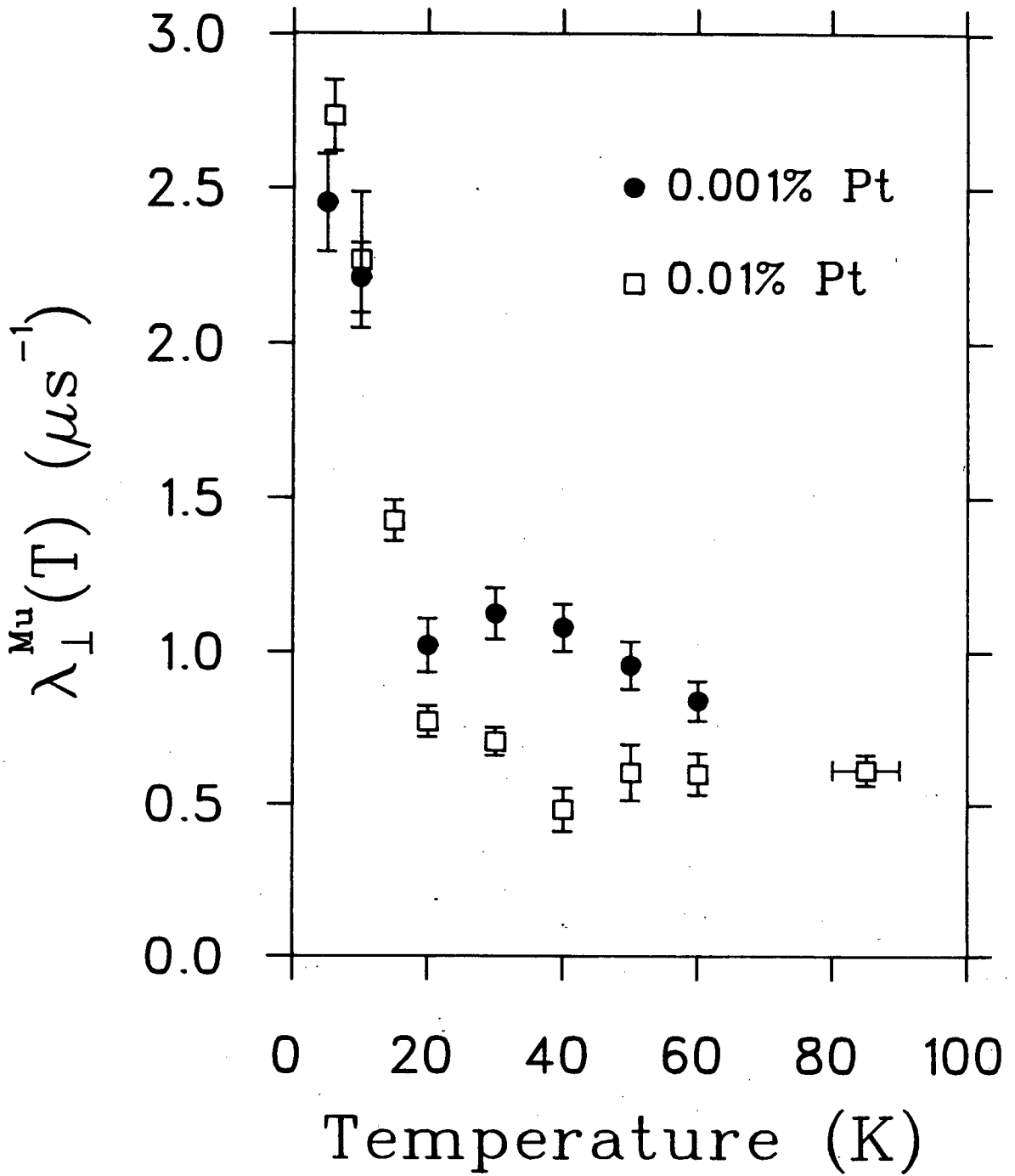
Figure IV.12 Transverse field muonium relaxation rate versus temperature for 0.001% (filled circles) and 0.01% (open squares) platinum loaded SiO_2.

platinum loaded silica catalysts. In both of these two cases, the observed effect was attributed to Fe^{3+} impurities (10 - 100 ppm) present in the silica support, which were reduced to metallic iron by the hydrogen treatment. As has already been mentioned, the iron contamination for the Cab-O-Sil EH-5 material has been measured to be ~6 ppm [12]. Since one might also expect a similar effect (although not as pronounced) when the unreduced silica is baked at 600 °C, it may be possible to attribute the high temperature trap site to iron impurities. The beauty of this hypothesis is twofold; not only does it explain why, upon hydrogen reduction, the trapping peak disappears (H atoms occupy the traps), but it also provides a paramagnetic ion which can interact with the Mu atoms through spin exchange processes. Because relaxations arising from spin exchange interactions are in general not decoupled in small longitudinal fields, this hypothesis provides an explanation for the unquenched component in the longitudinal field data of Figure IV.7. The possibility of an interaction with an electronic dipole moment also exists.

IV.C.3 Platinum Loaded Silica: 0.1% and 1.0%

In Figure IV.13, the muonium relaxation rate $\lambda_\perp^{Mu}$ is shown as a function of temperature for platinum loadings of 0.1% and 1.0%. Of particular interest are the data obtained for the 0.1% sample. At low temperatures, $\lambda_\perp^{Mu}(T)$ is essentially the same as for the other four samples, indicating that the muonium atoms are stationary. As the temperature is increased beyond about 10 K, $\lambda_\perp^{Mu}(T)$ experiences a sharp decrease and reaches a minimum at about 20 K. Between 20 K and 30 K, $\lambda_\perp^{Mu}(T)$ rises sharply, and thereafter continues to rise slowly with temperature toward the value obtained for the
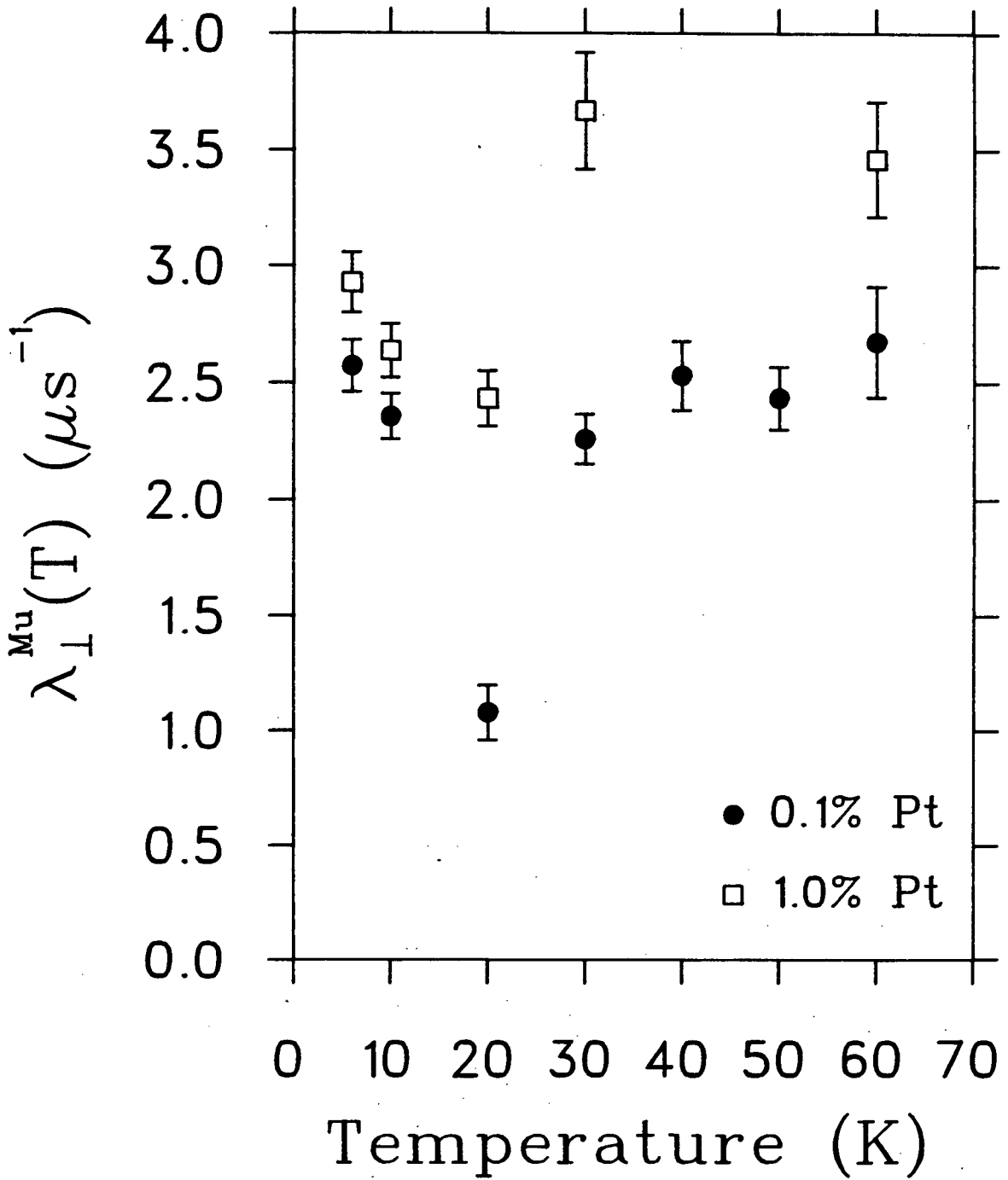
<u>Figure IV.13</u> Transverse field muonium relaxation rate versus temperature
for 0.1% (filled circles) and 1.0% (open squares) platinum loaded SiO_2.

1.0% sample in the same temperature region. In a similar fashion, the data obtained for the 1.0% sample indicate a slight minimum in $\lambda_{\perp}^{Mu}(T)$ at about 20 K, which is followed by a sharp rise to a value of about 3.6 μs^{-1} at 30 K. Above 30 K, $\lambda_{\perp}^{Mu}(T)$ fluctuates with an average value of about 3.5 μs^{-1}.

The interpretation of these results is relatively straightforward if one assumes the possibility of a chemical reaction between the muonium atoms and the oxygen-covered platinum surface. Bearing this in mind one can assume that at 0.1% loading, the muonium atoms do not diffuse fast enough during their lifetime to encounter a platinum partical until the temperature reaches about 30 K, above which $\lambda_{\perp}^{Mu}(T)$ continues to increase in a manner which can be described by the $T^{1/2}$ behavior expected for thermal diffusion. One can continue this line of reasoning and assume then that the 1.0% sample contains a sufficiently high concentration of platinum particles that the muonium atoms have a very high probability of encountering a platinum atom or aggregate even at extremely low hop rates. Believing this model to be an accurate description of the relevant physics, one then concludes that the effectively constant relaxation rate above 30 K, observed for the 1.0% sample, arises from a chemical reaction of muonium at the platinum surface. The rate for this reaction is found to be 3.5 ± 0.15 μs^{-1} which, owing to the isotopic relationship between muonium and hydrogen, should constitute an upper bound for the reaction rate of atomic hydrogen with oxygen-coated platinum.

This interpretation should be susceptible to experimental tests with zero and longitudinal field methods, since (as mentioned in Chapter III) chemical reactions leading to diamagnetic molecular species do not cause relaxation of the μ^+ spin polarization in zero or longitudinal field.

CHAPTER V — CONCLUSIONS AND FUTURE DIRECTIONS

V.A. Summary of Results

The results and discussions presented in this dissertation have

provided information regarding the diffusion and trapping of muonium atoms

on the surface of fine silica powders, as well as the nature of the spin

relaxation mechanisms involved. Experiments have also provided evidence

indicating charge exchange processes ocurring at the silica surfaces for

sub–monolayer ^{4}He coverages.

V.A.1 Diffusion and Trapping

Measurements of the temperature dependence of the transverse field

muonium relaxation rate, have indicated the existence of two different types

of sites (host and trap sites) for muonium on the silica surface. The host

sites were defined to be the most common. The interpretation of the data

follows accordingly; at low temperatures, two-dimensional diffusion and

trapping of muonium is observed, with desorption occuring at high (>100 K)

temperatures. This diffusion and trapping behavior was further shown to be

a strong function of the surface hydroxyl concentration. A three-state

model was subsequently developed [1,2], which assumes the relaxation at

every site to be due entirely to random local magnetic fields. A comparison

of the data for high and low surface hydroxyl concentrations was then made

using this model. One of the more important observations arising from this

was that as the surface hydroxyl concentration is reduced the surface hop

rate for muonium is enhanced at low temperatures (see Figure IV.4). The

interpretation of this suggests that the surface hydroxyls serve to inhibit

surface diffusion of the muonium atoms. This hypothesis is substantiated

further by a recent hydrogen chromotography study [3] in which similar

behavior for hydrogen atoms on silica surfaces was reported.

The host site desorption energy (i.e., the activation energy for

desorption of a Mu atom from a host site on the silica surface), obtained by

summing the host site activation energy E_0 and the energy E_f, was also found

to be strongly dependent upon the sample preparation. From the results

given in Table IV.1, the host site desorption energies for the 110 °C and

600 °C preparations are 275 (+118/-51) K and ~105 K, respectively.

Although the assumption of random local magnetic fields was later shown

to be somewhat inappropriate, the semi-quantitative understanding afforded

by the three-state model proved quite valuable. Studies were later

conducted to ascertain the true nature of the relaxation mechanisms for

muonium at both surface sites. The resulting conclusions are summarized in

the following section. ·

V.A.2 Relaxation Mechanisms

Using zero and longitudinal field μSR techniques, it was shown that a

dipole-dipole interaction (presumably between the muonium atom and the

hydroxyl protons) is in fact not the predominant relaxation mechanism for

muonium on the silica surface. This was deduced by first noting that the

relaxation for muonium in the host sites can be easily decoupled by a

longitudinal field on the order of a few Gauss, thereby leaving only two

possibilities; random local magnetic fields (RLMF) or random anisotropic

hyperfine distortions (RAHD). Further discrimination was then done by

considering the observed zero and longitudinal field long time behaviors in

the context of a static versus dynamic muonium atom; it was found that if

one assumes RLMF, the zero field long time behavior is inconsistent with a

static muonium atom, and the longitudinal field decoupling behavior is

inconsistent with a dynamic system. From these arguments then, a random

anisotropic distortion of the muonium hyperfine interaction was deduced to

be the principal contributor to the relaxation, especially for muonium in

the host sites.

A theory was developed which describes the time evolution of the μ^+

spin polarization for a completely anisotropic muonium hyperfine

interaction. The approach taken here involves expanding the hyperfine

tensor in terms of spherical harmonics and using the expansion coefficients

to parameterize the distortion. Expressions for the static μ^+ spin

relaxation functions, both in zero and "high" external magnetic field, were

then calculated assuming "zero average" Lorentzian and Lorentzian-like

distributions of the distortion parameters. By comparing this theory with

the data, it was shown that both a cylindrical distortion (normal to the

silica surface) and a planar distortion (in the plane of the surface) are

required to fully explain the data. The zero field relaxation function,

assuming both cylindrical and planar distortions, was used to fit the low

temperature (static limit) data. The quality of the fits obtained for both

the 110 °C and 600°C preparations was reasonable (typically, $1 < \chi^2/\text{deg.fr.}$

< 2), but not excellent. In these fits, the muonium asymmetry was allowed

to vary and was found to be consistent with the associated transverse field

data. The relatively high χ^2 values may be directly related to the

Lorentzian approximation adopted for the frequency distributions, which

allows infinite distortions. It is also important to remember that the

Lorentzian distributions assumed in the calculations had zero averages. If the actual distributions have non-zero averages, one would expect an oscillation superimposed on the relaxation. It is, however, impossible to tell from the data whether there is a small amplitude oscillation, but if present it could also account for the high χ^2 values.

The fits of the zero field random anisotropic hyperfine relaxation functions to the data indicate that the cylindrical component σ_{20} increases while the planar component σ_{22}^M decreases with increasing surface hydroxyl concentration. Assuming this phenomenon to be due entirely to the electrostatic interaction between the muonium electron and the electrons of the neighboring hydroxyl groups, one can in principle extract information regarding the effect of the induced electrostatic interaction on the muonium site symmetry. For instance, the fact that the hyperfine distortion observed for high hydroxyl concentrations (110 °C preparation) is shown to have an enhanced cylindrical component and a diminished planar component, as compared to the case of low hydroxyl concentrations (600 °C preparation), suggests that the electrostatic interaction between the muonium atom and the hydroxyl groups is repulsive. Although this interpretation does indeed provide a satisfactory explanation for the observed behavior, one cannot disregard the possibility that this result could merely be a manifestation of a combined relaxation interaction involving both random anisotropic hyperfine distortions and random local magnetic fields due to the hydroxyl protons at the surface.

Dynamical relaxation functions were also calculated by substituting the static functions into the strong collision model [4]. The resulting dynamic functions, for Lorentzian and Lorentzian-like distributions, were found to

be completely independent of the hop frequency at early times, which is inconsistent with the motional narrowing behavior observed for muonium in bulk fused SiO_2 and on the surface of fine silica powders. A modified Lorentzian distribution was therefore tested and found to provide the appropriate motional narrowing behavior. However, since the "correct" form of the distribution cannot be deduced from existing knowledge, the data cannot yield "absolutely calibrated" quantitative values for the hop rates.

The nature of the relaxation mechanism(s) at the trap sites was also investigated and found to be partially consistent with relaxation due to random ansisotropic hyperfine distortions. However, longitudinal field decoupling measurements have indicated a small component of the relaxation which is largly unaffected by the fields applied. This component is further seen to be more prominent in the data taken with the 110 ˇC preparation than in that obtained for the 600 °C preparation. The most likely candidate for this unquenched component is a spin exchange or perhaps a dipole-dipole interaction between the Mu atom and an Fe^{3+} ion. Moreover, Fe^{3+} would be reduced to metallic iron upon hydrogen reduction. The baking procedures employed in the present study might well produce enough atomic hydrogen to significantly reduce the paramagnetic content in the silica powder which would then be reflected in the decoupling behavior in longitudinal field. This possibility has been further substantiated by the platinum loaded silica studies, which are summarized in section V.A.4.

V.A.3 Muonium Formation Probability

Transverse field measurements of the muonium asymmetry versus helium coverage (at 6.0 ± 0.1 K) have shown that the muonium asymmetry decreases

with increasing surface coverage. Although these data suggest that the charge exchange cross section is significant at the silica surfaces, it is impossible to say at this time what role the helium atoms play in the charge exchange process. One possibility is that the helium atoms are relatively passive and only serve to cover up the surface, thereby impairing surface muonium formation. If this interpretation is correct, these data clearly show that muonium formation is partially surface related, as postulated in Chapter I. There is, however, another possibility which casts the helium atoms in a more active role, where they might act to dissociate the muonium atoms at the surface. Consider, for instance, the scenario in which the helium ions, produced in the ionization trail of the stopping μ^+, are able to capture the electrons of newly formed muonium atoms. This process would indeed leave the muons in a diamagnetic state, thereby removing them from the precessing muonium ensemble. Because of these two possibilities, one can say nothing about the origins of muonium formation, since one cannot distinguish between muonium formed at the silica surface and subsequently dissociated, or muonium which is formed in the grains and diffuses to the surface where it is then dissociated.

V.A.4 Catalytic Chemistry

These investigations were also extended to the study of the interactions of muonium with the surface of a silica-supported platinum catalyst. From the results obtained for the temperature dependence of the transverse field muonium relaxation rate, an upper limit of $3.5 \pm 0.15 \ \mu s^{-1}$ was deduced for the reaction rate of muonium with an oxygen-covered platinum surface. These experiments have also provided information concerning the nature of the

trapping site observed for muonium. Specifically, it was observed that the relaxation at the trap sites is completely neutralized for small ($\sim$0.01% Pt) platinum loadings, whereas for an unloaded sample (0% Pt), the trapping peak is quite pronounced. This effect was found to be correlated with the large amount of atomic hydrogen which is generated by the hydrogen reduction methods employed in the preparation of the platinum loaded silica catalyst. Similarly pronounced effects of catalysts loading, using hydrogen reduction techniques, have been observed both in magnetic susceptibility and ESR studies of metal loaded silica catalysts. In these cases, the observed effect was attributed to Fe^{3+} impurities, which were reduced to metallic iron by the hydrogen treatment. The utility of adopting the hypothesis that the trap site is an Fe^{3+} ion not only affords one with an explanation why, upon hydrogen reduction, the trapping peak disappears, but it also provides a paramagnetic ion which can interact with the muonium atoms through spin exchange or dipole-dipole (electronic dipole) processes. This hypothesis can thus account for the unquenched relaxation component observed at the trap site for the sample prepared at 110 °C, and perhaps also explain why the effect may be less prominent for the sample prepared at 600 °C, where enough atomic hydrogen may be generated by the baking procedure to partially neutralize the Fe^{3+} centers.

V.B. Future Directions

The work presented in this dissertation has provided the ground work for many new investigations, both experimental and theoretical, ranging from surface catalysis to surface physics. A few of the more immediately accessible avenues are discussed here.

V.B.1. Theoretical

The spin relaxation theory for a random anisotropic hyperfine
interaction (RAHD), derived in Appendix I, was developed to explain the data
obtained for muonium in bulk fused quartz and for muonium on the surface of
fine silica powders. However, only a few appropriately selected distortion
symmetries were considered, and the functions were derived only for the zero
and "high" external field limits. Further calculations assuming a non-zero
ω_{21} component should therefore be done, and the low external field limit
investigated, before a complete understanding of the static relaxation
functions for a random anisotropic hyperfine distortion can be obtained.
Moreover, these functions should be derived allowing for non-zero averages
for the distortion parameter distributions, since some of the data do seem
to exhibit small amplitude oscillations which are superimposed on the
relaxation.

The dynamic zero field RAHD model discussed in Chapter III was found to
be unsuitable for fitting the data because it exhibits no early time
dependence on hop rate (i.e., no motional narrowing), while the data exhibit
motional narrowing with increasing hop rate. This behavior was found to be
a manifestation of assuming Lorentzian and Lorentzian-like distributions,
for the distortion parameters. More thought must therefore be given to the
choice of distribution function so that a proper motional narrowing theory
can be developed. The modified Lorentzian distribution, discussed in
Chapter III does have the required features (finite second moment and an
exponential-like initial decay), and could be used for this purpose. Once
this is done, extensions can be made to a multi-state model for diffusion in
the presence of traps.

V.B.2 Experimental

This research has laid the foundations for future experimental studies along two complimentary paths; one involving the study of chemical reactions of muonium with various reactants on the silica (or other) powder surfaces and another concerning the interactions of positive muons and muonium with macroscopic surfaces.

Consider first the study of muonium reactions. In this line of study, the silica powder plays the role of an inert substrate which simultaneously provides a way of producing muonium in vacuum as well as an inert surface on which reactants can be stabilized. There are two distinct aspects of this study which should be considered. The first of these aspects is the reaction of muonium with physisorbed molecules, such as ethylene and oxygen, with the prime goal being to measure and compare the two-dimensional and three-dimensional reaction rates. The second aspect concerns the reaction of muonium with metal loaded catalysts. Because of the enormous interest in hydrogen catalysis with metal loaded catalysts, the study of a hydrogen-like probe such as muonium interacting with a metal loaded catalyst should provide an excellent opportunity for μSR to make a significant contribution to a rapidly expanding field. An immediate benefit that can be forseen is that muonium can provide information about the intermediate reactions that occur at short times, which are currently not observable by any other technique.

Preliminary studies of both of these aspects have already been made, with the results obtained for muonium on the surface of a platinum loaded catalyst being reported in this dissertation. All of the studies to date, however, were made in a low (< 10 G) transverse magnetic field. If one's

goal is to measure the reaction rate of muonium with a reactant stabilized

on the silica surface, it will be necessary to distinguish between

relaxation due to chemical reactions and relaxation due to the interactions

of muonium with the silica substrate itself. This could be accomplished by

repeating these measurements in zero and longitudinal field.

The observed functional dependence of the muonium formation probability

on the fractional surface coverage begs further investigation aimed at

determining the origins of muonium formation in these powders. Indeed, the

two possibilities mentioned earlier for the role played by the physisorbed

helium atoms are both very interesting, if only from an atomic physics point

of view. To determine the true role played by the physisorbed atoms in the

charge exchange process, it will be necessary to repeat these experiments

using different adsorbates. It would also be interesting to alter the

substrate in a systematic way, such as changing the surface hydroxyl

concentration.

Now consider the possibility of investigating the interactions of μ^+

and muonium atoms with macroscopic crystalline surfaces. A particularly

interesting topic to lead of these investigations arises from a recent

positron experiment [5]. This experiment shows that when e^+ of keV energies

are implanted into ionic single crystals, they are reemitted isotropically

from the solids with a continuum of energies having a maximum approximately

equal to the band gap energy (typically ~10-20 eV). Positronium (Ps) was

also observed to be emitted. Results also indicate that the emission of

both e^+ and Ps is associated with positronium diffusing to the surface of

these crystals where there exists some branching ratio for e^+ as opposed to

Ps emission. An explanation for this phenomenon has been proposed which

assumes a finite concentration of acceptor sites at the crystalline surface, such that the e^+ is Auger-emitted when the Ps electron combines with such a site. Assuming that one can draw certain analogies between the behavior of positrons and positive muons, and that the mechanism(s) responsible for the re-emission of positrons would also be involved in the analogous phenomenon for positive muons, this line of research would have the added benefit that one can draw guidance from earlier positron experiments. In addition, this research could conceivably lead the way to producing an ultra-low energy (0-10 keV) μ^+ beam. A detailed description of the physics involved, along with a possible test case experiment, is given in Appendix II.

APPENDIX I — THE TIME EVOLUTION OF THE μ^+ SPIN POLARIZATION IN MUONIUM

FOR A GENERALLY ANISOTROPIC HYPERFINE INTERACTION

In this Appendix, the time evolution of the μ^+ spin polarization for a positive muon in the neutral atomic state (muonium, μ^+e^-) is discussed for the case of an anisotropically distorted muonium hyperfine interaction. The associated static spin relaxation function is also calculated for a few selected symmetries. Because the research presented in this dissertation is primarily concerned with muonium on the surface of powders, where there is no well defined crystal orientation, the discussion will be directed accordingly.

AI.A Observables — Crystal and Detector Frames

There are two frames of reference associated with solid state μSR experiments, the crystal frame (designated by the coordinates x', y', z') and the detector frame (x, y, z). Observations are of course made in the detector frame; however, the time evolution of the observables is generally more readily described in terms of the crystal frame, where the symmetries of the problem can be explicitly incorporated. These two reference frames are related by the Euler angles (α, β, γ) through the second rank rotation tensor

$$\underset{\approx}{R}(\Omega) = \exp(-i\underset{\approx z}{J}\alpha) \cdot \exp(-i\underset{\approx y}{J}\beta) \cdot \exp(-i\underset{\approx z}{J}\gamma)$$

and the inverse rotation tensor   (AI.1)

$$\underset{\approx}{R}(\bar{\Omega}) = \exp(+i\underset{\approx z'}{J}\gamma) \cdot \exp(+i\underset{\approx y'}{J}\beta) \cdot \exp(+i\underset{\approx z'}{J}\alpha)$$

where the $\underset{\approx i}{J}$ are the respective infinitesimal rotation generators [1]. With

these defintions, one can define the unit vector transformations and inverse

transformations as $\vec{x}_i = \underset{\approx}{R}(\bar{\Omega})\cdot\vec{x}'_i$ and $\vec{x}'_i = \underset{\approx}{R}(\Omega)\cdot\vec{x}_i$, respectively.

AI.A.1 Spin Relaxation Functions

As for any observable, the time evolution of the μ^+ spin polarization

for a generally anisotropic muonium hyperfine interaction is, in the

Heisenberg picture, given by the equation

$$
\begin{aligned}
\underset{\sim}{P}_{op}(t) &= \exp\left[i(2\pi/h)Ht\right]\underset{\sim}{P}_{op}\exp\left[-i(2\pi/h)Ht\right] \\
&= 2\ \exp\left[i(2\pi/h)Ht\right]\underset{\sim}{S}^{\mu}_{op}\exp\left[-i(2\pi/h)Ht\right]
\end{aligned}
\tag{AI.2}
$$

where H is the spin Hamiltonian of the system and $\underset{\sim}{S}^{\mu}_{op}$ is the muon spin

operator. The time evolution of the spin polarization for an individual

muon, is then represented by the second rank time autocorrelation tensor

defined as

$$
\begin{aligned}
\underset{\approx}{g}(t) &= \frac{1}{4}\ \mathrm{Tr}\left\{\underset{\sim}{P}_{op}(t)\ \underset{\sim}{P}_{op}\right\} \\
&= \frac{1}{4}\ \mathrm{Tr}\left\{\exp\left[i(2\pi/h)Ht\right]\ \underset{\sim}{P}_{op}\exp\left[-i(2\pi/h)Ht\right]\ \underset{\sim}{P}_{op}\right\}
\end{aligned}
\tag{AI.3}
$$

Defining the eigenstates of the Hamiltonian as $|\psi_i\rangle$ with the corresponding

eigenenergies $\xi_i = (h/2\pi)\omega_i$, and recalling the definition of a trace of an

operator product, Equation AI.3 can be written as

$$
\underset{\approx}{g}(t) = \frac{1}{4}\ \sum_{ij}\exp(i\omega_{ij}t)\ \langle\psi_i|\ \underset{\sim}{P}_{op}\ |\psi_j\rangle\langle\psi_j|\ \underset{\sim}{P}_{op}\ |\psi_i\rangle
\tag{AI.4}
$$

where we define the transition frequencies $\omega_{ij} = (\omega_i - \omega_j)$. By separating

the expression given in Equation AI.4 into the diagonal and off diagonal

parts one obtains

$$g(t) = \frac{1}{4} \sum_i \langle\psi_i| \underset{\sim}{P}_{op} |\psi_i\rangle\langle\psi_i| \underset{\sim}{P}_{op} |\psi_i\rangle$$

$$+ \frac{1}{2} \sum_{i<j} Re\{\exp(i\omega_{ij}t) \langle\psi_i| \underset{\sim}{P}_{op} |\psi_j\rangle\langle\psi_i| \underset{\sim}{P}_{op} |\psi_j\rangle^*\} \qquad (AI.5)$$

By definition, $\langle\psi_i| \underset{\sim}{P}_{op} |\psi_j\rangle = \vec{x} P^x_{ij} + \vec{y} P^y_{ij} + \vec{z} P^z_{ij}$, such that, in terms

of its cartesian components, $\underset{\sim}{g}(t)$ can be written as

$$g(t) = \frac{1}{4} \sum_i \{\overleftrightarrow{xx} (P^x_{ii})^2 + \overleftrightarrow{yy} (P^y_{ii})^2 + \overleftrightarrow{zz} (P^z_{ii})^2$$

$$+ (\overleftrightarrow{xy} + \overleftrightarrow{yx})P^x_{ii}P^y_{ii} + (\overleftrightarrow{xz} + \overleftrightarrow{zx})P^x_{ii}P^z_{ii} + (\overleftrightarrow{yz} + \overleftrightarrow{zy})P^y_{ii}P^z_{ii}\}$$

$$+ \frac{1}{2} \sum_{i<j} \cos(\omega_{ij}t)\{\overleftrightarrow{xx} |P^x_{ij}|^2 + \overleftrightarrow{yy} |P^y_{ij}|^2 + \overleftrightarrow{zz} |P^z_{ij}|^2 \qquad (AI.6)$$

$$+ (\overleftrightarrow{xy} + \overleftrightarrow{yx})Re(P^x_{ij}P^{y*}_{ij}) + (\overleftrightarrow{xz} + \overleftrightarrow{zx})Re(P^x_{ij}P^{z*}_{ij}) + (\overleftrightarrow{yz} + \overleftrightarrow{zy})Re(P^y_{ij}P^{z*}_{ij})\}$$

$$- \frac{1}{2} \sum_{i<j} \sin(i\omega_{ij}t)\{(\overleftrightarrow{xy} - \overleftrightarrow{yx})Im(P^x_{ij}P^{y*}_{ij}) + (\overleftrightarrow{xz} - \overleftrightarrow{zx})Im(P^x_{ij}P^{z*}_{ij})$$

$$+ (\overleftrightarrow{yz} - \overleftrightarrow{zy})Im(P^y_{ij}P^{z*}_{ij})\}$$

Since $\underset{\sim}{g}(t)$ is a second rank tensor in three-dimensional space, it can

be expanded in terms of (1) the second rank unit tensor $\underset{\sim}{U}$, (2) a set of

traceless antisymmetric second rank tensor, constructed from the dot product

of the Levi-Cevita tensor $\underset{\equiv}{\varepsilon}$ and the detector frame spherical vectors $\underset{\sim m}{E}^1$, and

(3) the traceless symmetric second rank detector frame spherical tensors $\underset{\approx m}{E}^2$.

The resulting expansion gives

$$g(t) = g_{00} \underset{\sim}{U} - \frac{i}{\sqrt{2}} \sum_{m=-1}^{1} g_{1m} \underset{\sim m}{E}^1 \cdot \underset{\equiv}{\varepsilon} + \sum_{m=-2}^{2} g_{2m} \underset{\approx m}{E}^2 \qquad (AI.7)$$

The transformation to spherical tensors is made in order to provide a more

convenient set of vectors and tensors for the rotational transformations

between the crystal frame and the detector frame. In terms of their

cartesian components ($\vec{x}$, $\vec{y}$ and $\vec{z}$), the spherical covariant vectors $\underset{\sim}{E}{}^1_m$ and

the corresponding contravariant vectors $\underset{\sim}{E}{}^{1m} = \left(\underset{\sim}{E}{}^1_m\right)^*$ are given as

$$\underset{\sim}{E}{}^1_1 = \frac{1}{\sqrt{2}}\left(\vec{x} - i\vec{y}\right) \quad ; \quad \underset{\sim}{E}{}^{11} = -\frac{1}{\sqrt{2}}\left(\vec{x} + i\vec{y}\right)$$

$$\underset{\sim}{E}{}^1_0 = -i\vec{z} \quad ; \quad \underset{\sim}{E}{}^{10} = i\vec{z} \tag{AI.8}$$

$$\underset{\sim}{E}{}^1_{-1} = -\frac{1}{\sqrt{2}}\left(\vec{x} + i\vec{y}\right) \quad ; \quad \underset{\sim}{E}{}^{1-1} = \frac{1}{\sqrt{2}}\left(\vec{x} - i\vec{y}\right)$$

By definition of the Levi-Cevita operator $\underset{=}{\epsilon}$, the antisymmetric spherical

tensors can be written as

$$\underset{\sim}{E}{}^1_1 \cdot \underset{=}{\epsilon} = \frac{1}{\sqrt{2}}\left[\left(\vec{\vec{yz}} - \vec{\vec{zy}}\right) - i\left(\vec{\vec{zx}} - \vec{\vec{xz}}\right)\right]$$

$$\underset{\sim}{E}{}^1_0 \cdot \underset{=}{\epsilon} = -i\left[\left(\vec{\vec{xy}} - \vec{\vec{yx}}\right)\right] \tag{AI.9}$$

$$\underset{\sim}{E}{}^1_{-1} \cdot \underset{=}{\epsilon} = -\frac{1}{\sqrt{2}}\left[\left(\vec{\vec{yz}} - \vec{\vec{zy}}\right) + i\left(\vec{\vec{zx}} - \vec{\vec{xz}}\right)\right]$$

The symmetric spherical tensors can also be written in terms if their

cartesian components with the result

$$\underset{\approx}{E}{}^2_0 = \sqrt{2/3}\left[-\vec{\vec{zz}} + \frac{1}{2}\left(\vec{\vec{xx}} + \vec{\vec{yy}}\right)\right]$$

$$\underset{\approx}{E}{}^2_{\pm 1} = \pm\frac{1}{2}\left[\left(\vec{\vec{xz}} + \vec{\vec{zx}}\right) \mp i\left(\vec{\vec{yz}} + \vec{\vec{zy}}\right)\right] \tag{AI.10}$$

$$\underset{\approx}{E}{}^2_{\pm 2} = -\frac{1}{2}\left[\left(\vec{\vec{xx}} - \vec{\vec{yy}}\right) \mp i\left(\vec{\vec{xy}} + \vec{\vec{yx}}\right)\right]$$

At this point it is convenient to define a few identities. From

Equation AI.9, one can write

$$\vec{z} = i\left(\underset{\sim}{E}{}^1_0\right) = -i\left(\underset{\sim}{E}{}^{10}\right)$$

$$\vec{x} = \frac{-i}{\sqrt{2}}\left(\underset{\sim}{E}{}^1_1 - \underset{\sim}{E}{}^1_{-1}\right) = \frac{i}{\sqrt{2}}\left(\underset{\sim}{E}{}^{11} - \underset{\sim}{E}{}^{1-1}\right) \tag{AI.11}$$

$$\vec{y} = \frac{1}{\sqrt{2}}\left(\underset{\sim}{E}{}^1_1 + \underset{\sim}{E}{}^1_{-1}\right) = \frac{1}{\sqrt{2}}\left(\underset{\sim}{E}{}^{11} + \underset{\sim}{E}{}^{1-1}\right)$$

Combining the identities given in Equation AI.11 with the definitions of Equation AI.10, the second rank symmetric spherical tensors can be constructed from the spherical vectors such that one has

$$\underset{\approx}{E}{}^2_0 = \sqrt{2/3}\,[(\underset{\sim}{E}{}^1_0\,\underset{\sim}{E}{}^1_0) + \tfrac{1}{2}(\underset{\sim}{E}{}^1_{-1}\,\underset{\sim}{E}{}^1_{+1} + \underset{\sim}{E}{}^1_{+1}\,\underset{\sim}{E}{}^1_{-1})]$$

$$\underset{\approx}{E}{}^2_{\pm 1} = \frac{1}{\sqrt{2}}\,[(\underset{\sim}{E}{}^1_0\,\underset{\sim}{E}{}^1_{\pm 1}) + (\underset{\sim}{E}{}^1_{\pm 1}\,\underset{\sim}{E}{}^1_0)] \qquad\qquad (AI.12)$$

$$\underset{\approx}{E}{}^2_{\pm 2} = [(\underset{\sim}{E}{}^1_{\pm 1}\,\underset{\sim}{E}{}^1_{\pm 1})]$$

The covariant and contravariant spherical vectors, which now define the physical space, obey the following cross product relations

$$\left(\underset{\sim}{E}{}^{10} \times \underset{\sim}{E}{}^{10}\right) = \left(\underset{\sim}{E}{}^{11} \times \underset{\sim}{E}{}^{11}\right) = \left(\underset{\sim}{E}{}^{1-1} \times \underset{\sim}{E}{}^{1-1}\right) = 0$$

$$\left(\underset{\sim}{E}{}^{10} \times \underset{\sim}{E}{}^{11}\right) = i\vec{z} \times \left(\frac{-i}{\sqrt{2}}\right)(\vec{x} + i\vec{y}) = \frac{-i}{\sqrt{2}}(i\vec{y} + \vec{x}) = \underset{\sim}{E}{}^{11}$$

$$\left(\underset{\sim}{E}{}^{10} \times \underset{\sim}{E}{}^{1-1}\right) = i\vec{z} \times \left(\frac{i}{\sqrt{2}}\right)(\vec{x} - i\vec{y}) = \frac{i}{\sqrt{2}}(i\vec{y} - \vec{x}) = -\underset{\sim}{E}{}^{1-1} \qquad (AI.13)$$

$$\left(\underset{\sim}{E}{}^{11} \times \underset{\sim}{E}{}^{1-1}\right) = \tfrac{1}{2}(\vec{x} + i\vec{y}) \times (\vec{x} - i\vec{y}) = -i\vec{z} = -\underset{\sim}{E}{}^{10}$$

By combining Equations AI.6 and AI.7, and utilizing the results of Equations AI.8 - AI.12, the nine detector frame components $g_{lm}(t)$ of the relaxation tensor are defined as

$$g_{00}(t) = \tfrac{1}{3}\,\underset{\approx}{U} : \underset{\approx}{g}(t) = (1/12)\Big\{ \sum_i [(P^x_{ii})^2 + (P^y_{ii})^2 + (P^z_{ii})^2] $$
$$ + 2\sum_{i<j} \cos(\omega_{ij}t)[\,|P^x_{ij}|^2 + |P^y_{ij}|^2 + |P^z_{ij}|^2\,]\Big\} \qquad (AI.14)$$

$$g_{10}(t) = -\frac{i}{\sqrt{2}}\,\left(\underset{\sim}{E}{}^{10} \cdot \underset{\underline{\approx}}{\varepsilon}\right) : \underset{\approx}{g}(t) = -\frac{1}{\sqrt{2}}\sum_{i<j} \sin(\omega_{ij}t)[\,\mathrm{Im}(P^x_{ij}P^{y*}_{ij})\,] \qquad (AI.15)$$

$$g_{1\pm1}(t) = -\frac{i}{\sqrt{2}}(\underset{\sim}{E}^{1\pm1}\cdot\underset{\sim}{\varepsilon}) : g(t) = \mp\frac{1}{2}\sum_{i<j}\sin(\omega_{ij}t)[Im(P^y_{ij}P^{z*}_{ij})$$

$$\mp iIm(P^x_{ij}P^{z*}_{ij})] \tag{AI.16}$$

$$g_{20}(t) = \underset{\approx}{E}^{20} : g(t) = \frac{1}{4}\sqrt{2/3}\left\{\sum_i\left[\frac{1}{2}[(P^x_{ii})^2 + (P^y_{ii})^2] - (P^z_{ii})^2\right]\right.$$

$$\left. + 2\sum_{i<j}\cos(\omega_{ij}t)\left[\frac{1}{2}(|P^x_{ij}|^2 + |P^y_{ij}|^2) - |P^z_{ij}|^2\right]\right\} \tag{AI.17}$$

$$g_{2\pm1}(t) = \underset{\approx}{E}^{2\pm1} : g(t) = \pm\frac{1}{4}\left\{\sum_i\frac{1}{2}[P^x_{ii}P^z_{ii} \pm iP^y_{ii}P^z_{ii}]\right.$$

$$\left. \pm 2\sum_{i<j}\cos(\omega_{ij})[Re(P^x_{ij}P^{z*}_{ij}) \pm iRe(P^y_{ij}P^{z*}_{ij})]\right\} \tag{AI.18}$$

$$g_{2\pm2}(t) = \underset{\approx}{E}^{2\pm2} : g(t) = -\frac{1}{4}\left\{\sum_i\frac{1}{2}[(P^x_{ii})^2 - (P^y_{ii})^2 \mp iP^x_{ii}P^y_{ii}]\right.$$

$$\left. + \sum_{i<j}\cos(\omega_{ij}t)[|P^x_{ij}|^2 - |P^y_{ij}|^2 \mp iRe(P^x_{ij}P^{y*}_{ij})]\right\} \tag{AI.19}$$

Because all observations are made in the detector frame, whereas the symmetries are defined in the crystal frame, it is necessary to relate the detector frame observables $g_{lm}(t)$ to the crystal frame observables $g'_{lm}(t)$. This is done via the rotation operation, such that

$$g_{LM}(t) = \sum_m g'_{Lm}(t) R^{(L)}_{Mm}(\bar{\Omega}) \tag{AI.20}$$

where $R^{(L)}_{mM}(\bar{\Omega})$ are the matrix elements of the rotation tensor $\underset{\approx}{R}(\bar{\Omega})$, defined in Equation AI.1.

With these definitions, the dynamics of the μ^+ spin is found to involve nine observable detector frame relaxation functions, which are constructed from the nine detector frame components $g_{lm}(t)$ of the relaxation tensor

[2,3]. Specifically, there are three longitudinal (l) relaxation functions, in the direction of the local field, defined as

$$g_1^c(t) = g_{00}(t) - \sqrt{2/3}\, g_{20}(t)$$

$$g_1^{sc}(t) = \text{Im}\{g_{11}(t)\} + \text{Re}\{g_{21}(t)\} \qquad\qquad (AI.21)$$

$$g_1^{ss}(t) = -\text{Re}\{g_{11}(t)\} + \text{Im}\{g_{21}(t)\}$$

three coplanar-transverse (ct) relaxation functions, which are in the plane defined by the field direction and the incoming muon spin polarization

$$g_{ct}^c(t) = -\text{Im}\{g_{11}(t)\} + \text{Re}\{g_{21}(t)\}$$

$$g_{ct}^{sc}(t) = g_{00}(t) + \frac{1}{2}\sqrt{2/3}\, g_{20}(t) - \text{Re}\{g_{22}(t)\} \qquad\qquad (AI.22)$$

$$g_{ct}^{ss}(t) = -\sqrt{1/2}\, g_{10}(t) - \text{Im}\{g_{22}(t)\}$$

and three perpendicular-transverse (pt) relaxation functions, which are directed perpendicular to both the field and the incoming muon spin polarization.

$$g_{pt}^c(t) = \text{Re}\{g_{11}(t)\} + \text{Im}\{g_{21}(t)\}$$

$$g_{pt}^{sc}(t) = \sqrt{1/2}\, g_{10}(t) - \text{Im}\{g_{22}(t)\} \qquad\qquad (AI.23)$$

$$g_{pt}^{ss}(t) = g_{00}(t) + \frac{1}{2}\sqrt{2/3}\, g_{20}(t) + \text{Re}\{g_{22}(t)\}$$

It is convenient to work in the vector space spanned by the detector frame eigenfunctions $|m_\mu, m_e\rangle$ of the unperturbed (vacuum) muonium isotropic hyperfine Hamiltonian. Defining the axis of quantization to be along the magnetic field, one has

$$|1\rangle = |+,+\rangle \qquad ; \quad |2\rangle = |-,-\rangle$$

$$|3\rangle = s|+,-\rangle + c|-,+\rangle \qquad ; \quad |4\rangle = c|+,-\rangle - s|-,+\rangle \tag{AI.24}$$

where $c = \cos(\lambda/2)$, $s = \sin(\lambda/2)$ and $\lambda = \arcsin[1/(1+x^2)^{1/2}]$. The dimensionless quantity $x = |\underset{\sim}{B}|/B_0$ is the specific field parameter where B_0 (= 1585 G) is the hyperfine field for isotropic muonium in the ground state in vacuum. The labels of the second and third eigenfunctions given in Equation AI.24 have been interchanged with respect to the standard notation [4-6] in order that the hyperfine Hamiltonian can be partially written down in block diagonal form. In general the eigenfunctions $|\psi_i\rangle$ of a specific hyperfine Hamiltonian can be expressed as linear combinations of the isotropic muonium basis vectors $|k\rangle$ given in Equation AI.24, such that one may write

$$H|\psi_i\rangle = \xi_i |\psi_i\rangle = \xi_i \sum_i c_{ik} |k\rangle \tag{AI.25}$$

Utilizing this result, one can then write

$$\langle \psi_i|\underset{\sim}{P}_{op}|\psi_j\rangle = [\ \vec{x}\ P^x_{ij} + \vec{y}\ P^y_{ij} + \vec{z}\ P^z_{ij}] = \sum_k c^*_{ik}\ c_{jk}\ \langle k|\underset{\sim}{P}_{op}k1\rangle$$

$$+ \sum_{k<1} [c^*_{ik}\ c_{j1}\ \langle k|\underset{\sim}{P}_{op}|1\rangle + c^*_{i1}\ c_{jk}\ \langle k|\underset{\sim}{P}_{op}|1\rangle^*] \tag{AI.26}$$

Solving for the three detector frame polarization components, one then has

$$P^x_{ij} = \cos(\lambda/2)[A_{13} + A_{24}] + \sin(\lambda/2)[A_{23} - A_{14}]$$

$$P^y_{ij} = i\{\cos(\lambda/2)[B_{13} - B_{24}] - \sin(\lambda/2)[B_{23} + B_{14}]\} \tag{AI.27}$$

$$P^z_{ij} = [C_{12}] - \cos(\lambda)[C_{34}] + \sin(\lambda)[A_{34}]$$

where we have defined $A_{kl} = [c_{ik}^* c_{jl} + c_{il}^* c_{jk}]$, $B_{kl} = [c_{ik}^* c_{jl} - c_{il}^* c_{jk}]$ and

$C_{kl} = [c_{ik}^* c_{jk} - c_{il}^* c_{jl}]$. Note that in zero field, $\lambda = \pi/2$.

AI.B The Spin Hamiltonian for Isolated Muonium

The spin Hamiltonian for an isolated muonium atom in a magnetic field $\underset{\sim}{B}$, assuming a generally anisotropic muonium hyperfine is given by

$$H = H^{zee} + H^{hf}$$
$$= (h/2\pi)\left(\gamma_e \underset{\sim}{S}_{op}^e - \gamma_\mu \underset{\sim}{S}_{op}^\mu\right) \cdot \underset{\sim}{B} + (h/2\pi) \underset{\approx}{W} : \left(\underset{\sim}{S}_{op}^e \underset{\sim}{S}_{op}^\mu\right) \tag{AI.28}$$

where γ_e and γ_μ are the respective magnetogyric ratios of the electron and the muon, $\underset{\sim}{S}_{op}^e$ and $\underset{\sim}{S}_{op}^\mu$ are the spin operators and $\underset{\approx}{W}$ is a second rank tensor (in three-dimensional space) representing the contact hyperfine interaction. Although this Hamiltonian is discussed in some detail elsewhere [7], a somewhat different but equivalent evaluation is given here which facilitates the calculation of the time evolution of the μ^+ spin polarization, for a generally ansisotropic muonium hyperfine interaction, and the corresponding zero, longitudinal and transverse field spin relaxation functions.

AI.B.1 Evaluation of the Hyperfine Term

Because the isotropic muonium basis given in Equation AI.24 is defined with respect to the detector frame, it is easiest to evaluate the hyperfine Hamiltonian in this frame. Since $\underset{\approx}{W}$ is a second rank tensor in three dimensional space, it can also be expanded in terms of (1) the second rank unit tensor $\underset{\approx}{U}$, (2) a set of traceless antisymmetric second rank tensors,

constructed from the dot product of the Levi-Cevita tensor $\underset{=}{\epsilon}$ and the detector frame spherical vectors $\underset{\sim m}{E^1}$, and (3) the traceless symmetric second rank detector frame spherical tensors $\underset{\approx m}{E^2}$. However, because the hyperfine tensor $\underset{\approx}{W}$ involves only dipole-dipole and contact interactions, both of which have reflection symmetry, the antisymmetric part of the hyperfine tensor is identically zero (i.e., $w_{10} = w_{1\pm1} = 0$). The resulting expansion gives

$$\underset{\approx}{W} = w_{00} \underset{\approx}{U} + \sum_{m=-2}^{2} w_{2m} \underset{\approx m}{E^2} \tag{AI.29}$$

where the symmetry of the anisotropic hyperfine tensor $\underset{\approx}{W}$ is defined by the crystal frame coefficients ω_{Lm}, which are related to the detector frame coefficients via the rotational transformation

$$w_{LM} = \sum_{m} \omega_{Lm} R_{Mm}^{(L)}(\bar{\Omega}) \tag{AI.30}$$

The spin operators for the electron and the muon can be written in terms of the contravariant spherical vectors as

$$
\begin{aligned}
\underset{\sim op}{S^{\alpha}} &= S_x \vec{x} + S_y \vec{y} + S_z \vec{z} \\
&= \frac{i}{\sqrt{2}} S_x^{\alpha} (\underset{\sim}{E^{11}} - \underset{\sim}{E^{1-1}}) + \frac{1}{\sqrt{2}} S_y^{\alpha} (\underset{\sim}{E^{11}} + \underset{\sim}{E^{1-1}}) - i S_z^{\alpha} \underset{\sim}{E^{10}}
\end{aligned} \tag{AI.31}
$$

where $\alpha = \{\mu, e\}$. By combining like terms in $\underset{\sim}{E^{11}}$ and $\underset{\sim}{E^{1-1}}$, one obtains

$$\underset{\sim op}{S^{\alpha}} = \frac{i}{\sqrt{2}} (\underset{\sim}{E^{11}}) S_-^{\alpha} - \frac{i}{\sqrt{2}} (\underset{\sim}{E^{1-1}}) S_+^{\alpha} - i (\underset{\sim}{E^{10}}) S_z^{\alpha} \tag{AI.32}$$

where we define

$$S_-^{\alpha} = (S_x^{\alpha} - i S_y^{\alpha}) \quad \text{and} \quad S_+^{\alpha} = (S_x^{\alpha} + i S_y^{\alpha}) \tag{AI.33}$$

The three operators S^α_-, S^α_+ and S^α_z completely define the vector operator $\underset{\sim}{S}^\alpha_{op}$ and turn out to be more convenient. They obey the commutation relations

$$[S^\alpha_z, S^\alpha_+] = S^\alpha_+ \quad ; \quad [S^\alpha_z, S^\alpha_-] = -S^\alpha_- \quad ; \quad [S^\alpha_+, S^\alpha_-] = 2S^\alpha_z \quad \text{(AI.34)}$$

Utilizing the operations given in Equation AI.13, one obtains the cross product of the electron and muon spin operators, namely

$$
\begin{aligned}
(\underset{\sim}{S}^e_{op} \times \underset{\sim}{S}^\mu_{op}) = \{ & \frac{1}{2} (\underset{\sim}{E}^{11} \times \underset{\sim}{E}^{1-1}) S^e_- S^\mu_+ + \frac{1}{\sqrt{2}} (\underset{\sim}{E}^{11} \times \underset{\sim}{E}^{10}) S^e_- S^\mu_z \\
& + \frac{1}{2} (\underset{\sim}{E}^{1-1} \times \underset{\sim}{E}^{11}) S^e_+ S^\mu_- - \frac{1}{\sqrt{2}} (\underset{\sim}{E}^{1-1} \times \underset{\sim}{E}^{10}) S^e_+ S^\mu_z \\
& + \frac{1}{\sqrt{2}} (\underset{\sim}{E}^{10} \times \underset{\sim}{E}^{11}) S^e_z S^\mu_- - \frac{1}{\sqrt{2}} (\underset{\sim}{E}^{10} \times \underset{\sim}{E}^{1-1}) S^e_z S^\mu_+ \}
\end{aligned}
\quad \text{(AI.35)}
$$

Using the identities for the cross products of the spherical vectors given in Equation AI.13, one can rewrite Equation AI.35 as

$$
\begin{aligned}
(\underset{\sim}{S}^e_{op} \times \underset{\sim}{S}^\mu_{op}) = \{ & \frac{1}{2} (-\underset{\sim}{E}^{10}) S^e_- S^\mu_+ + \frac{1}{\sqrt{2}} (-\underset{\sim}{E}^{11}) S^e_- S^\mu_z \\
& + \frac{1}{2} (+\underset{\sim}{E}^{10}) S^e_+ S^\mu_- - \frac{1}{\sqrt{2}} (+\underset{\sim}{E}^{1-1}) S^e_+ S^\mu_z \\
& + \frac{1}{\sqrt{2}} (+\underset{\sim}{E}^{11}) S^e_z S^\mu_- - \frac{1}{\sqrt{2}} (-\underset{\sim}{E}^{1-1}) S^e_z S^\mu_+ \}
\end{aligned}
\quad \text{(AI.36)}
$$

This cross product relation is not used in the present work because the antisymmetric part of the hyperfine tensor $\underset{\approx}{W}$ is identically zero.

At this point we have a set of convenient spin operators, expressed in terms of the crystal frame spherical vectors, and so we can rewrite the hyperfine Hamiltonian in terms of these operators. First consider the isotropic part of the hyperfine Hamiltonian. In terms of the spherical vectors, the second rank unit tensor is written

$$\underset{\approx}{U} = - \underset{\sim}{E}^1_0 \underset{\sim}{E}^1_0 + (\underset{\sim}{E}^1_1 \underset{\sim}{E}^1_{-1} + \underset{\sim}{E}^1_{-1} \underset{\sim}{E}^1_1) \quad \text{(AI.37)}$$

Thus the trace part of the hyperfine Hamiltonian becomes

$$H_{00}^{hf} = (h/2\pi) \ w_{00} \ [- \underset{\sim}{E}_0^1 \ \underset{\sim}{E}_0^1 + (\underset{\sim}{E}_1^1 \ \underset{\sim}{E}_{-1}^1 + \underset{\sim}{E}_{-1}^1 \ \underset{\sim}{E}_1^1)] : (\underset{\sim}{S}_{op}^e \ \underset{\sim}{S}_{op}^\mu) \qquad (AI.38)$$

and substituting the expressions for the electron and muon spin operators

given in Equation AI.32 into Equation AI.38, yields the result

$$H_{00}^{hf} = (h/2\pi) \ w_{00} \ [S_z^e \ S_z^\mu + \frac{1}{2} (S_+^e \ S_-^\mu + S_-^e \ S_+^\mu)] \qquad (AI.39)$$

By combining the definitions of Equation AI.12 and the expressions for

the electron and muon spin operators, given in Equation AI.32, the five

terms of the symmetric traceless part of the hyperfine Hamiltonian become

$$H_{22}^{hf} = - \frac{1}{2} (h/2\pi) \ w_{22} \ (S_-^e \ S_-^\mu) \qquad (AI.40)$$

$$H_{21}^{hf} = \frac{1}{2} (h/2\pi) \ w_{21} \ (S_z^e \ S_-^\mu + S_-^e \ S_z^\mu) \qquad (AI.41)$$

$$H_{20}^{hf} = \sqrt{2/3} (h/2\pi) \ w_{20} \ [- S_z^e \ S_z^\mu + \frac{1}{4} (S_+^e \ S_-^\mu + S_-^e \ S_+^\mu)] \qquad (AI.42)$$

$$H_{2-1}^{hf} = - \frac{1}{2} (h/2\pi) \ w_{2-1} (S_z^e \ S_+^\mu + S_+^e \ S_z^\mu) \qquad (AI.43)$$

$$H_{2-2}^{hf} = - \frac{1}{2} (h/2\pi) \ w_{2-2} (S_+^e \ S_+^\mu) \qquad (AI.44)$$

The result of operating on the space spanned by the isotropic muonium

eigenvectors $|k\rangle$ with the operators S_z^α, S_+^α and S_-^α can be easily understood

by first considering their effect on the single particle eigenkets, $|j,m\rangle_\alpha$

(equal to $|\frac{1}{2}, \frac{1}{2}\rangle_\alpha$ or $|\frac{1}{2}, \frac{-1}{2}\rangle_\alpha$ for spin 1/2). Thus one can write [1]

$$S_z^\alpha \ |j,m\rangle_\alpha = m_\alpha \ |j,m\rangle_\alpha \qquad (AI.45)$$

$$S_+^\alpha \ |j,m\rangle_\alpha = \sqrt{j(j+1) - m_\alpha(m_\alpha+1)} \ = |j,m+1\rangle_\alpha \ ; \ \text{for} \ m_\alpha = \frac{-1}{2}$$
$$= \quad 0 \quad ; \ \text{for} \ m_\alpha = \frac{+1}{2} \qquad (AI.46)$$

$$S_-^\alpha \, |j,m\rangle_\alpha = \sqrt{j(j+1) - m_\alpha(m_\alpha - 1)} \quad = |j,m-1\rangle_\alpha \; ; \; \text{for } m_\alpha = \frac{+1}{2} \tag{AI.47}$$

$$= \quad 0 \qquad ; \; \text{for } m_\alpha = \frac{-1}{2}$$

Returning now to the two-spin eigenstates of Equation AI.24, one can define the operations

$$S_z^e \, S_z^\mu \, |1\rangle = \frac{1}{4} \, |1\rangle \qquad ; \quad S_z^e \, S_z^\mu \, |2\rangle = \frac{1}{4} \, |2\rangle$$

$$S_z^e \, S_z^\mu \, |3\rangle = -\frac{1}{4} \, |3\rangle \qquad ; \quad S_z^e \, S_z^\mu \, |4\rangle = -\frac{1}{4} \, |4\rangle \tag{AI.48}$$

$$S_-^e \, S_-^\mu \, |1\rangle = \qquad |2\rangle \qquad ; \quad S_-^e \, S_-^\mu \, |2\rangle = \quad 0$$

$$S_-^e \, S_-^\mu \, |3\rangle = \quad 0 \qquad ; \quad S_-^e \, S_-^\mu \, |4\rangle = \quad 0 \tag{AI.49}$$

$$S_+^e \, S_+^\mu \, |1\rangle = \quad 0 \qquad ; \quad S_+^e \, S_+^\mu \, |2\rangle = \qquad |1\rangle$$

$$S_+^e \, S_+^\mu \, |3\rangle = \quad 0 \qquad ; \quad S_+^e \, S_+^\mu \, |4\rangle = \quad 0 \tag{AI.50}$$

$$S_z^e \, S_-^\mu \, |1\rangle = \frac{c}{2} \, |3\rangle - \frac{s}{2} \, |4\rangle \; ; \; S_z^e \, S_-^\mu \, |2\rangle = \quad 0$$

$$S_z^e \, S_-^\mu \, |3\rangle = -\frac{s}{2} \, |2\rangle \qquad ; \; S_z^e \, S_-^\mu \, |4\rangle = -\frac{c}{2} \, |2\rangle \tag{AI.51}$$

$$S_-^e \, S_z^\mu \, |1\rangle = \frac{s}{2} \, |3\rangle + \frac{c}{2} \, |4\rangle \; ; \; S_-^e \, S_z^\mu \, |2\rangle = \quad 0$$

$$S_-^e \, S_z^\mu \, |3\rangle = -\frac{c}{2} \, |2\rangle \qquad ; \; S_-^e \, S_z^\mu \, |4\rangle = \frac{s}{2} \, |2\rangle \tag{AI.52}$$

$$S_z^e S_+^\mu |1\rangle = 0 \quad ; \quad S_z^e S_+^\mu |2\rangle = -\frac{s}{2}|3\rangle - \frac{c}{2}|4\rangle \tag{AI.53}$$

$$S_z^e S_+^\mu |3\rangle = \frac{c}{2}|1\rangle \quad ; \quad S_z^e S_+^\mu |4\rangle = -\frac{s}{2}|1\rangle$$

$$S_+^e S_z^\mu |1\rangle = 0 \quad ; \quad S_+^e S_z^\mu |2\rangle = -\frac{c}{2}|3\rangle + \frac{s}{2}|4\rangle \tag{AI.54}$$

$$S_+^e S_z^\mu |3\rangle = \frac{s}{2}|1\rangle \quad ; \quad S_+^e S_z^\mu |4\rangle = \frac{c}{2}|1\rangle$$

$$S_+^e S_-^\mu |1\rangle = 0 \quad ; \quad S_+^e S_-^\mu |2\rangle = 0 \tag{AI.55}$$

$$S_+^e S_-^\mu |3\rangle = sc|3\rangle - s^2|4\rangle \quad ; \quad S_+^e S_-^\mu |4\rangle = c^2|3\rangle - sc|4\rangle$$

$$S_-^e S_+^\mu |1\rangle = 0 \quad ; \quad S_-^e S_+^\mu |2\rangle = 0 \tag{AI.56}$$

$$S_-^e S_+^\mu |3\rangle = sc|3\rangle + c^2|4\rangle \quad ; \quad S_-^e S_+^\mu |4\rangle = -s^2|3\rangle - sc|4\rangle$$

With these operations defined, the matrix elements of the generally anisotropic hyperfine Hamiltonian in the isotropic muonium representation can be derived. We begin with the isotropic part H_{00}^{hf} and calculate the matrix elements to obtain

$$H_{00}^{hf} = (h/2\pi)\frac{W_{00}}{4}\begin{bmatrix} 1 & 0 & 0 & 0 \\ 0 & 1 & 0 & 0 \\ 0 & 0 & -(1-4sc) & 2(c^2-s^2) \\ 0 & 0 & 2(c^2-s^2) & -(1+4sc) \end{bmatrix} . \tag{AI.57}$$

In a similar manner, the matrix elements of the five terms of the symmetric traceless part of the generally anisotropic hyperfine Hamiltonian can be calculated giving

$$H_{22}^{hf} = \left(h/2\pi\right) \frac{w_{22}}{4} \begin{bmatrix} 0 & 0 & 0 & 0 \\ -1 & 0 & 0 & 0 \\ 0 & 0 & 0 & 0 \\ 0 & 0 & 0 & 0 \end{bmatrix} \qquad (AI.58)$$

$$H_{21}^{hf} = \left(h/2\pi\right) \frac{w_{21}}{4} \begin{bmatrix} 0 & 0 & 0 & 0 \\ 0 & 0 & -(c+s) & -(c-s) \\ (c+s) & 0 & 0 & 0 \\ (c-s) & 0 & 0 & 0 \end{bmatrix} \qquad (AI.59)$$

$$H_{20}^{hf} = \frac{h \sqrt{2/3}}{2\pi} \frac{w_{20}}{4} \begin{bmatrix} -1 & 0 & 0 & 0 \\ 0 & -1 & 0 & 0 \\ 0 & 0 & (1+2sc) & (c^2-s^2) \\ 0 & 0 & (c^2-s^2) & (1-2sc) \end{bmatrix} \qquad (AI.60)$$

$$H_{2-1}^{hf} = \left(h/2\pi\right) \frac{w_{2-1}}{4} \begin{bmatrix} 0 & 0 & -(c+s) & -(c-s) \\ 0 & 0 & 0 & 0 \\ 0 & (c+s) & 0 & 0 \\ 0 & (c-s) & 0 & 0 \end{bmatrix} \qquad (AI.61)$$

$$H_{2-2}^{hf} = \left(h/2\pi\right) \frac{w_{2-2}}{4} \begin{bmatrix} 0 & -1 & 0 & 0 \\ 0 & 0 & 0 & 0 \\ 0 & 0 & 0 & 0 \\ 0 & 0 & 0 & 0 \end{bmatrix} \cdot \qquad (AI.62)$$

AI.B.2 Evaluation of the Zeeman Term

To evaluate the Zeeman Hamiltonian, it is again easier to work in the

detector frame with the magnetic field $\underset{\sim}{B}$ directed along the z-axis.
Recalling the expressions for the electron and muon spin operators given in
Equation AI.32, the Zeeman Hamiltonian becomes

$$H^{zee} = \left(h/2\pi \right) \left[\gamma_e \, S_z^e - \gamma_\mu \, S_z^\mu \right] \, |\underset{\sim}{B}| \qquad \qquad (AI.63)$$

Operating on the eigenstates of the isotropic muonium basis, given in
Equation AI.24, one has for the electron spin operator

$$S_z^e \, |1\rangle = + \tfrac{1}{2} \, |1\rangle \qquad \qquad ; \qquad S_z^e \, |2\rangle = - \tfrac{1}{2} \, |2\rangle$$

$$S_z^e \, |3\rangle = (\tfrac{1}{2} - s^2)|3\rangle - sc|4\rangle \quad ; \quad S_z^e \, |4\rangle = (\tfrac{1}{2} - c^2)|4\rangle - sc|3\rangle$$

and for the muon spin operator $\qquad \qquad \qquad \qquad \qquad \qquad (AI.64)$

$$S_z^\mu \, |1\rangle = + \tfrac{1}{2} \, |1\rangle \qquad \qquad ; \qquad S_z^\mu \, |2\rangle = - \tfrac{1}{2} \, |2\rangle$$

$$S_z^\mu \, |3\rangle = (\tfrac{1}{2} - c^2)|3\rangle + sc|4\rangle \quad ; \quad S_z^\mu \, |4\rangle = (\tfrac{1}{2} - s^2)|4\rangle + sc|3\rangle$$

With these operations defined, the Zeeman Hamiltonian in the detector frame
is given by

$$H^{zee} = \left(h/2\pi \right) \begin{bmatrix} \omega_{Mu} & 0 & 0 & 0 \\ 0 & -\omega_{Mu} & 0 & 0 \\ 0 & 0 & \omega_{Mu}-a & -sc(\gamma_e+\gamma_\mu) \\ 0 & 0 & -sc(\gamma_e+\gamma_\mu) & \omega_{Mu}-b \end{bmatrix} \qquad (AI.65)$$

where $\omega_{Mu} = \tfrac{1}{2} (\gamma_e - \gamma_\mu)|\underset{\sim}{B}|$, $a = (\gamma_e s^2 + \gamma_\mu c^2)|\underset{\sim}{B}|$ and $b = (\gamma_e c^2 + \gamma_\mu s^2)|\underset{\sim}{B}|$.

AI.C Isolated Muonium in Zero Field

In zero field, one has $s = c = 1/\sqrt{2}$. In this case, one can transform
to the crystal frame and write the total Hamiltonian in terms of the crystal

frame coefficients ω_{Lm}, namely

$$H = (h/2\pi) \frac{1}{4} \begin{bmatrix} (\omega_{00}-\omega'_{20}) & -\omega_{2-2} & -\omega'_{2-1} & 0 \\ -\omega_{22} & (\omega_{00}-\omega'_{20}) & -\omega'_{21} & 0 \\ \omega'_{21} & \omega'_{2-1} & (\omega_{00}+2\omega'_{20}) & 0 \\ 0 & 0 & 0 & -3\omega_{00} \end{bmatrix} \qquad (AI.66)$$

where we have defined $\omega'_{jk} = \sqrt{2}\,\omega_{jk}$, with the exception that $\omega'_{20} = \sqrt{2/3}\,\omega_{20}$.

Deriving the crystal and detector frame relaxation functions for a specific hyperfine Hamiltonian is in general straight forward. To calculate the relaxation due to some random distortion of the muonium hyperfine interaction, one averages over the associated ω_{Lm}'s. However, since ω_{00} is in general quite large and unobservable due to timing limitations, one can ignore the oscillatory terms containing ω_{00}, which simply implies ignoring the singlet component of the muonium ensemble, and only take an average over the appropriate ω_{2m}'s, each of which have some distribution $f_{2m}(\omega_{2m})$. With the data presented in this dissertation, it is in general not possible to discriminate between an ω_{21} distortion as opposed to ω_{22} contributions. This being the case, the possible contribution of an ω_{21} component to the relaxation of the μ^+ spin polarization is omitted in the remaining discussions.

In the case of powders in zero applied field, the axis of symmetry of the hyperfine distortion for each muonium atom is oriented randomly. When taking an ensemble average one averages over the Euler angles which, by definition of spherical harmonics, forces all of the detector frame $g_{Lm}(t)$ to zero except $g_{00}(t)$. Because of this averaging, only three of the nine detector frame observable relaxation functions, given in Equations AI.21 –

AI.23, survive; $g_1^c(t)$, $g_{ct}^{sc}(t)$ and $g_{pt}^{ss}(t)$. Furthermore, these three functions are identical and equal to $g_{00}(t)$, which simply reflects the fact that the spin relaxation function is isotropic in the detector frame. With this understanding, the general form of the zero field spin relaxation function, due to random anisotropic hyperfine distortions, for the case of powders, is then given by the equation

$$g_{00}^{rh}(t) = \int_{-\infty}^{\infty} d\omega_{2m} f_{2m}(\omega_{2m}) \cdots \int_{-\infty}^{\infty} d\omega_{2m'} f_{2m'}(\omega_{2m'}) \, g_{00}(t,\omega_{2m},\cdots,\omega_{2m'}) \quad (AI.67)$$

Since all of the zero and transverse field spin relaxation data presented in this dissertation appear qualitatively to exhibit an exponential decay at early times, the ω_{2m}'s are assumed to be distributed according to Lorentzian and Lorentzian-like distributions. This choice of distribution function is purely phenomenological, since the actual function is not known.

AI.C.1 Relaxation Due to a Cylindrical Distortion

Take as an example a cylindrical distortion of the muonium hyperine as in the case of anomolous muonium [8]. In this case, the hyperfine distortion is cylindrically symmetric about some given axis. Assuming that all of the muonium atoms in the ensemble have hyperfine distortions that are symmetric about the z-axis, the Hamiltonian of Equation AI.66 becomes

$$H = (h/2\pi)\frac{1}{4}\begin{bmatrix} (\omega_{00}-\omega_{20}') & 0 & 0 & 0 \\ 0 & (\omega_{00}-\omega_{20}') & 0 & 0 \\ 0 & 0 & (\omega_{00}+2\omega_{20}') & 0 \\ 0 & 0 & 0 & -3\omega_{00} \end{bmatrix} \quad (AI.68)$$

As stated earlier, the eigenfunctions $|\phi_i\rangle$ of a specific hyperfine Hamiltonian can be expressed as linear combinations of the isotropic muonium

basis vectors $|k\rangle$ given in Equation AI.24. Since the Hamiltonian in Equation AI.68 is diagonal in the isotropic muonium representation, one has the coefficients $c_{ik} = \delta_{ik}$ with the eigenvalues ξ_i equal to the diagonal elements, namely

$$\xi_1 = \left(h/8\pi\right)\left(\omega_{00} - \sqrt{2/3}\;\omega_{20}\right) \quad ; \quad \xi_2 = \left(h/8\pi\right)\left(\omega_{00} - \sqrt{2/3}\;\omega_{20}\right)$$
$$\xi_3 = \left(h/8\pi\right)\left(\omega_{00} + 2\sqrt{2/3}\;\omega_{20}\right) \quad ; \quad \xi_4 = \left(h/8\pi\right)\left(-3\omega_{00}\right) \tag{AI.69}$$

with the corresponding transition frequencies

$$\omega_{12} = 0 \qquad\qquad\qquad ; \quad \omega_{23} = \frac{1}{4}\left(-3\sqrt{2/3}\;\omega_{20}\right)$$
$$\omega_{13} = \frac{1}{4}\left(-3\sqrt{2/3}\;\omega_{20}\right) \quad ; \quad \omega_{24} = \frac{1}{4}\left(4\omega_{00} - \sqrt{2/3}\;\omega_{20}\right) \tag{AI.70}$$
$$\omega_{14} = \frac{1}{4}\left(4\omega_{00} - \sqrt{2/3}\;\omega_{20}\right) \quad ; \quad \omega_{34} = \frac{1}{4}\left(4\omega_{00} + 2\sqrt{2/3}\;\omega_{20}\right)$$

Using Equation AI.27 one can then calculate the crystal frame polarization components, namely

$$
\begin{array}{llll}
P^x_{ii} = 0 & ; \; P^y_{ii} = 0 & ; \; P^z_{11} = 1, & P^z_{22} = -1 \\[4pt]
 & & ; \; P^z_{33} = -\cos\lambda, & P^z_{44} = \cos\lambda \\[4pt]
P^x_{12} = 0 & ; \; P^y_{12} = 0 & ; \; P^z_{12} = 0 \\[4pt]
P^x_{13} = c & ; \; P^y_{13} = ic & ; \; P^z_{13} = 0 \\[4pt]
P^x_{14} = -s & ; \; P^y_{14} = -is & ; \; P^z_{14} = 0 & \qquad (AI.71) \\[4pt]
P^x_{23} = s & ; \; P^y_{23} = -is & ; \; P^z_{23} = 0 \\[4pt]
P^x_{24} = c & ; \; P^y_{24} = -ic & ; \; P^z_{24} = 0 \\[4pt]
P^x_{34} = 0 & ; \; P^y_{34} = 0 & ; \; P^z_{34} = \sin\lambda
\end{array}
$$

which simplify further in zero field where $\lambda = \pi/2$, thus $c = s = 1/\sqrt{2}$.

Since all of the crystal frame coefficients in the cylindrically

distorted Hamiltonian are set equal to zero except ω_{00} and ω_{20}, the only non-zero crystal frame relaxation functions are $g'_{00}(t)$ and $g'_{20}(t)$. By Substituting the values of Equation AI.71 into Equation AI.14, and using the definitions of Equation AI.70, the former becomes

$$g'_{00}(t) = \frac{1}{6} \left\{ 1 + \cos\left[\left(\omega_{00} + \frac{1}{2}\omega'_{20}\right)t\right] + 2\cos\left[\left(\frac{3}{4}\omega'_{20}\right)t\right] \right. \\ \left. + 2\cos\left[\left(\omega_{00} - \frac{1}{4}\omega'_{20}\right)t\right] \right\}$$
(AI.72)

Similarly substituting the values of Equation AI.71 into Equation AI.17, along with the transition frequencies defined in Equation AI.70, the expression for the latter can be derived, namely

$$g'_{20}(t) = \frac{1}{2}\sqrt{2/3} \left\{ -1 - \cos\left[\left(\omega_{00} + \frac{1}{2}\omega'_{20}\right)t\right] + \cos\left[\left(\frac{3}{4}\omega'_{20}\right)t\right] \right. \\ \left. + \cos\left[\left(\omega_{00} - \frac{1}{4}\omega'_{20}\right)t\right] \right\}$$
(AI.73)

To derive an expression for the observable relaxation due to random hyperfine distortions, we treat the terms oscillating at or near ω_{00} as averaged to zero and only average over ω_{20}. In this case, the frequency distribution is one-dimensional and, assuming a Lorentzian distribution, is given by

$$f_{20}(\omega_{20}) = \frac{1}{\pi} \left[\frac{\sigma_{20}}{\omega_{20}^2 + \sigma_{20}^2}\right]$$
(AI.74)

where σ_{20} is the width parameter of the distribution, and the factor of $1/\pi$ is a normalization constant. In the case of a powder, averaging over the Euler angles forces all of the detector frame $g_{2m}(t)$ components to zero except $g_{00}(t)$. By combining Equations AI.72 and AI.74 with the definition of Equation AI.67, one can then write for powders

$$g_{00}^{rh}(t) = \frac{2}{\pi} \frac{\sigma_{20}}{6} \int_o^\infty d\omega_{20} \left[\omega_{20}^2 + \sigma_{20}^2\right]^{-1} \left[1 + 2\cos(\frac{3}{4} \sqrt{2/3} \, \omega_{20}t)\right] \qquad (AI.75)$$

Performing the integration in Equation AI.81, then yields

$$g_{00}^{rh}(t) = \frac{1}{6} + \frac{1}{3} \exp(- \frac{3}{4} \sqrt{2/3} \, \sigma_{20} \, t) \qquad (AI.76)$$

Notice that as $t \to \infty$, this function tends to 1/6 (or 1/3 of the initial polarization of the triplet muonium ensemble). The time independent 1/3 component of the ensemble spin polarization (residual polarization) arises because there exists a non-trivial zero frequency. This can be understood intuitively by noting that for a random hyperfine interaction, 1/3 of the time the cylindrical distortion axis is directed along the z-axis of the detector frame, (i.e., along the initial muon spin polarization).

AI.C.2 Relaxation Due to a Planar Distortion

Now consider the time evolution of the μ^+ spin for the case of a planar distortion of the muonium hyperfine interaction. In this case, one has the Hamiltonian

$$H = \left(h/2\pi\right) \frac{1}{4} \begin{bmatrix} \omega_{00} & -\omega_{2-2} & 0 & 0 \\ -\omega_{22} & \omega_{00} & 0 & 0 \\ 0 & 0 & \omega_{00} & 0 \\ 0 & 0 & 0 & -3\omega_{00} \end{bmatrix} \qquad (AI.77)$$

Since this Hamiltonian is block diagonal, the first two energy eigenvalues can be calculated by diagonalizing the 2×2 block

$$\begin{vmatrix} (\omega_{00} - \omega) & -\omega_{2-2} \\ -\omega_{22} & (\omega_{00} - \omega) \end{vmatrix} = 0 = \omega^2 - 2(\omega_{00}\omega) + \omega_{00}^2 - (\omega_{22}^M)^2 \qquad (AI.78)$$

where we define $\omega = \xi(8\pi/h)$, and $\omega_{22}^M = \sqrt{(\omega_{22})(\omega_{2-2})} = \left[(\omega_{22}^R)^2 + (\omega_{22}^I)^2\right]^{1/2}$.

Solving Equation AI.78 for ω then gives

$$\xi_{1,2} = (h/2\pi) \frac{1}{4} \left[\omega_{00} \pm \omega_{22}^{M} \right] \qquad \text{(AI.79)}$$

To compute the eigenfunctions $|\psi_1\rangle$ and $|\psi_2\rangle$ corresponding to these

eigenvalues, one solves the set of coupled linear equations

$$\begin{aligned} (\omega_{00}-\omega)u_1 + (-\omega_{2-2})u_2 &= 0 \\ (-\omega_{22})u_1 + (\omega_{00}-\omega)u_2 &= 0 \end{aligned} \qquad \text{(AI.80)}$$

where u_1 and u_2 are the components of the eigenvectors. Solving Equation

AI.80 for $\omega = \omega_1$ and $\omega = \omega_2$, one obtains respectively

$$u_2 = -\frac{\omega_{22}}{\omega_{22}^{M}} u_1 = -e^{i\phi_{22}} u_1 \quad \text{and} \quad u_2 = +\frac{\omega_{22}}{\omega_{22}^{M}} u_1 = +e^{i\phi_{22}} u_1 \qquad \text{(AI.81)}$$

where $\phi_{22} = \arccos(\omega_{22}^{R}/\omega_{22}^{M}) = \arcsin(\omega_{22}^{I}/\omega_{22}^{M})$. From Equation AI.81 and the

usual normalization conditions, one can obtain expressions for both $|\psi_1\rangle$ and

$|\psi_2\rangle$. Thus one can write

$$|\psi_1\rangle = \frac{1}{\sqrt{2}} \left[|1\rangle + e^{i\phi_{22}} |2\rangle \right] \quad ; \quad |\psi_2\rangle = \frac{1}{\sqrt{2}} \left[|1\rangle - e^{i\phi_{22}} |2\rangle \right]$$

$$|\psi_3\rangle = |3\rangle \qquad\qquad ; \quad |\psi_4\rangle = |4\rangle \qquad \text{(AI.82)}$$

with the corresponding eigenvalues

$$\begin{aligned} \xi_1 &= (h/2\pi) \frac{1}{4} (\omega_{00} + \omega_{22}^{M}) \quad ; \quad \xi_2 = (h/2\pi) \frac{1}{4} (\omega_{00} - \omega_{22}^{M}) \\ \xi_3 &= (h/2\pi) \frac{1}{4} (\omega_{00}) \qquad\quad ; \quad \xi_4 = (h/2\pi) \frac{1}{4} (-3\omega_{00}) \end{aligned} \qquad \text{(AI.83)}$$

The transition frequencies are therefore given as

$$\begin{aligned} \omega_{12} &= \frac{1}{4} (2\omega_{22}^{M}) && ; && \omega_{23} = \frac{1}{4} (-\omega_{22}^{M}) \\ \omega_{13} &= \frac{1}{4} (\omega_{22}^{M}) && ; && \omega_{24} = \frac{1}{4} (4\omega_{00} - \omega_{22}^{M}) \\ \omega_{14} &= \frac{1}{4} (4\omega_{00} + \omega_{22}^{M}) && ; && \omega_{34} = \frac{1}{4} (4\omega_{00}) \end{aligned} \qquad \text{(AI.84)}$$

Again utilizing the expressions given in Equation AI.27, one can calculate

the crystal frame polarization components. To do this we first write down

the eigenstate expansion coefficients c_{ik}, namely

$$c_{11} = \frac{1}{\sqrt{2}} \quad ; \quad c_{12} = +\frac{1}{\sqrt{2}} e^{i\phi_{22}} \quad ; \quad c_{13} = 0 \quad ; \quad c_{14} = 0$$

$$c_{21} = \frac{1}{\sqrt{2}} \quad ; \quad c_{22} = -\frac{1}{\sqrt{2}} e^{i\phi_{22}} \quad ; \quad c_{23} = 0 \quad ; \quad c_{24} = 0 \qquad \text{(AI.85)}$$

$$c_{3k} = \delta_{3k} \quad ; \quad c_{4k} = \delta_{4k}$$

Substituting these coefficients into Equation AI.24 then gives

$$P^x_{ii} = 0 \qquad\qquad ; \quad P^y_{ii} = 0 \qquad\qquad ; \quad P^z_{ii} = 0$$

$$P^x_{12} = 0 \qquad\qquad ; \quad P^y_{12} = 0 \qquad\qquad ; \quad P^z_{12} = 1$$

$$P^x_{13} = \frac{1}{\sqrt{2}}\left[c + se^{-i\phi_{22}}\right] \quad ; \quad P^y_{13} = \frac{i}{\sqrt{2}}\left[c - se^{-i\phi_{22}}\right] \quad ; \quad P^z_{13} = 0$$

$$P^x_{14} = \frac{-i}{\sqrt{2}}\left[s - ce^{-i\phi_{22}}\right] \quad ; \quad P^y_{14} = \frac{-i}{\sqrt{2}}\left[s + ce^{-i\phi_{22}}\right] \quad ; \quad P^z_{14} = 0 \qquad \text{(AI.86)}$$

$$P^x_{23} = \frac{1}{\sqrt{2}}\left[c - se^{-i\phi_{22}}\right] \quad ; \quad P^y_{23} = \frac{i}{\sqrt{2}}\left[c + se^{-i\phi_{22}}\right] \quad ; \quad P^z_{23} = 0$$

$$P^x_{24} = \frac{-i}{\sqrt{2}}\left[s + ce^{-i\phi_{22}}\right] \quad ; \quad P^y_{24} = \frac{-i}{\sqrt{2}}\left[s - ce^{-i\phi_{22}}\right] \quad ; \quad P^z_{24} = 0$$

$$P^x_{34} = 0 \qquad\qquad ; \quad P^y_{34} = 0 \qquad\qquad ; \quad P^z_{34} = \sin\lambda$$

where, in zero field, $\lambda = \pi/2$ and $c = s = 1/\sqrt{2}$. By substituting the

expressions given in Equation AI.86 into Equation AI.14, and recalling the

definitions of the transition frequencies given in Equation AI.84, one

obtains for zero field

$$g'_{00}(t) = \frac{1}{6}\left\{\cos\left[\left(\frac{1}{2}\omega^M_{22}\right)t\right] + 2\cos\left[\left(\frac{1}{4}\omega^M_{22}\right)t\right]\right.$$
$$\left. + \cos\left[\left(\omega_{00} - \frac{1}{4}\omega^M_{22}\right)t\right] + \cos\left[\left(\omega_{00} + \frac{1}{4}\omega_{22}\right)t\right] + \cos\left[\left(\omega_{00}\right)t\right]\right\}$$

$$\text{(AI.87)}$$

Similarly substituting the values of Equation AI.86 into Equation AI.19, the zero field expression for $g_{22}(t)$ is found to be

$$g'_{22}(t) = \frac{1}{4}\{\cos[(\omega_{00} + \frac{1}{4}\omega^M_{22})t] - \cos[(\omega_{00} - \frac{1}{4}\omega^M_{22})t]\}\exp(-i\phi_{22}) \quad \text{(AI.88)}$$

To obtain the relaxation function for random planar anisotropies, one once again ignores the ω_{00} terms and only averages over ω_{22}. In this case, the frequency distribution $f_{22}(\omega^M_{22}, \phi_{22})$ is two-dimensional and, assuming a Lorentzian-like distribution, is of the form given by

$$f_{22}(\omega^M_{22}, \phi_{22}) = \frac{4}{\pi} \frac{\sigma^M_{22} \omega^M_{22}}{[(\omega^M_{22})^2 + (\sigma^M_{22})^2]^2} \cdot (2\pi)^{-1} \quad \text{(AI.89)}$$

where σ^M_{22} is the width of the frequency distribution, and $2/\pi^2$ is a normalization constant. The distribution defined in Equation AI.89 assumes a zero average, even though ω^M_{2m} is positive-definate. At first this might seem inconsistent, except that Equation AI.89 is the distribution function for a complex number; although the magnitude ω^M_{2m} is positive-definate, the orientations of the associated vector are distributed over all directions in a plane. In the case of powders, an ensemble average is made by averaging over the Euler angles, which as earlier stated, forces all of the detector frame relaxation tensor components to zero except for $g_{00}(t)$. By combining Equations AI.87 and AI.89 with the definition of Equation AI.67, and ignoring the ω_{00} terms, one then obtains for powders

$$g^{rh}_{00}(t) = \frac{4}{\pi}\frac{\sigma^M_{22}}{6} \int_0^\infty d\omega^M_{22} \frac{(\omega^M_{22})^2}{[(\omega^M_{22})^2 + (\sigma^M_{22})^2]^2} \{\cos[\frac{1}{2}\omega^M_{22}t] + 2\cos[\frac{1}{4}\omega^M_{22}t]\} \quad \text{(AI.90)}$$

where the integration over the phase angle ϕ_{22} has been done, and the extra factor of ω^M_{22} is the Jacobian arising from the coordinate transformation

from the coordinates ω_{22}^R, ω_{22}^I and ϕ_{22} to ω_{22}^M. By performing the integration, one finally obtains

$$g_{00}^{rh}(t) = \frac{1}{6}\left(1 - \frac{\sigma_{22}^M}{2}t\right)\exp\left(-\frac{\sigma_{22}^M}{2}t\right) + \frac{1}{3}\left(1 - \frac{\sigma_{22}^M}{4}t\right)\exp\left(-\frac{\sigma_{22}^M}{4}t\right) \quad \text{(AI.91)}$$

Notice that as $t \to \infty$, this function tends to zero. This result reflects the fact that, unlike in the case of a cylindrical distortion, there are no zero frequency terms in $g_{00}'(t)$. The simple analytic result of Equation AI.91 arises from the assumption of a "Lorentzian-like" distribution. If instead a true two-dimensional Lorentzian is assumed, the result is not analytic.

AI.C.3 Cylindrical and Planar Distortions Combined

Now consider the time evolution of the μ^+ spin assuming both a cylindrical and a planar distortion. In this case, one has the Hamiltonian

$$H = (h/2\pi)\,\frac{1}{4}\begin{bmatrix} (\omega_{00}-\omega_{20}') & -\omega_{2-2} & 0 & 0 \\ -\omega_{22} & (\omega_{00}-\omega_{20}') & 0 & 0 \\ 0 & 0 & (\omega_{00}+2\omega_{20}') & 0 \\ 0 & 0 & 0 & -3\omega_{00} \end{bmatrix} \quad \text{(AI.92)}$$

Because this Hamiltonian is of the same form as that of the simple planar distortion, given in Equation AI.77, its eigenfunctions $|\psi_i\rangle$ are the same

$$|\psi_1\rangle = \frac{1}{\sqrt{2}}\left[\,|1\rangle + e^{i\phi_{22}}\,|2\rangle\right] \quad ; \quad |\psi_2\rangle = \frac{1}{\sqrt{2}}\left[\,|1\rangle - e^{i\phi_{22}}\,|2\rangle\right]$$

$$|\psi_3\rangle = |3\rangle \qquad\qquad\qquad ; \quad |\psi_4\rangle = |4\rangle \qquad\qquad \text{(AI.93)}$$

Since this Hamiltonian is block-diagonal, the first two energy eigenvalues can of course be calculated by solving the secular equation

$$\begin{vmatrix} (\omega_{00}-\omega_{20}')-\omega & -\omega_{2-2} \\ -\omega_{22} & (\omega_{00}-\omega_{20}')-\omega \end{vmatrix} = 0 = \omega^2 - 2\omega(\omega_{00}-\omega_{20}')$$

$$+ (\omega_{00}-\omega_{20}')^2 - (\omega_{22}^M)^2 \quad \text{(AI.94)}$$

Solving Equation AI.94, the four eigenvalues of this Hamiltonian are

$$\xi_{1,2} = \left(h/2\pi \right) \frac{1}{4} \left[\left(\omega_{00} - \sqrt{2/3} \ \omega_{20} \right) \pm \omega_{22}^{M} \right]$$

(AI.95)

$$\xi_{3} = \left(h/2\pi \right) \frac{1}{4} \left(\omega_{00} + 2 \sqrt{2/3} \ \omega_{20} \right) \quad ; \quad \xi_{4} = \left(h/2\pi \right) \frac{1}{4} \left(-3 \ \omega_{00} \right)$$

with the corresponding transition frequencies

$$\omega_{12} = \frac{1}{4} \left(2\omega_{22}^{M} \right) \qquad ; \qquad \omega_{23} = \frac{1}{4} \left(-3\sqrt{2/3} \ \omega_{20} - \omega_{22}^{M} \right)$$

$$\omega_{13} = \frac{1}{4} \left(-3\sqrt{2/3} \ \omega_{20} + \omega_{22}^{M} \right) \qquad ; \qquad \omega_{24} = \frac{1}{4} \left(4\omega_{00} - \sqrt{2/3} \ \omega_{20} - \omega_{22}^{M} \right) \quad \text{(AI.96)}$$

$$\omega_{14} = \frac{1}{4} \left(4\omega_{00} - \sqrt{2/3} \ \omega_{20} + \omega_{22}^{M} \right) \ ; \quad \omega_{34} = \frac{1}{4} \left(4\omega_{00} + 2\sqrt{2/3} \ \omega_{20} \right)$$

Because the eigenstates of the combined Hamiltonian are the same as those of the planar distortion Hamiltonian, the eigenstate expansion coefficients c_{ik} of the combined Hamiltonian are equal to those quoted in Equation AI.85. Consequently, the crystal frame polarization components, which are derived through the use of Equation AI.27, are the same as those given in Equation AI.86. By substituting the the results of Equation AI.86, as well as the transition frequencies of Equation AI.96, into Equation AI.14, one obtains an expression for $g_{00}'(t)$ in zero field, namely

$$g_{00}'(t) = \frac{1}{6} \left\{ \cos\left[\left(\frac{1}{2} \ \omega_{22}^{M}\right)t\right] + \cos\left[\frac{1}{4}\left(-3\omega_{20}' + \omega_{22}^{M}\right)t\right] \right.$$

$$+ \cos\left[\frac{1}{4}\left(\omega_{00} - \omega_{20}' + \omega_{22}^{M}\right)t\right] + \cos\left[\frac{1}{4}\left(-3\omega_{20}' - \omega_{22}^{M}\right)t\right] \qquad \text{(AI.97)}$$

$$\left. + \cos\left[\left(\omega_{00} - \frac{1}{4} \ \omega_{20}' - \frac{1}{4} \ \omega_{22}^{M}\right)t\right] + \cos\left[\left(\omega_{00} + \frac{1}{2} \ \omega_{20}'\right)t\right] \right\}$$

where $\omega_{20}' = \sqrt{2/3} \ \omega_{20}$. In a similar manner one can obtain expressions for the crystal frame components $g_{20}'(t)$ and $g_{22}'(t)$, such that one has

$$g_{20}'(t) = \frac{1}{2} \sqrt{2/3} \left\{ -\cos\left[\left(\frac{1}{2} \ \omega_{22}^{M}\right)t\right] + \cos\left[\frac{1}{4}\left(-3\omega_{20}' + \omega_{22}^{M}\right)t\right] \right.$$

$$+ \cos\left[\left(\omega_{00} - \frac{1}{4} \ \omega_{20}' + \frac{1}{4} \ \omega_{22}^{M}\right)t\right] + \cos\left[\frac{1}{4}\left(-3\omega_{20}' - \omega_{22}^{M}\right)t\right] \qquad \text{(AI.98)}$$

$$\left. + \cos\left[\left(\omega_{00} - \frac{1}{4} \ \omega_{20}' - \frac{1}{4} \ \omega_{22}^{M}\right)t\right] + \cos\left[\left(\omega_{00} + \frac{1}{2} \ \omega_{20}'\right)t\right] \right\}$$

and

$$g'_{22}(t) = \frac{1}{4}\{- \cos[(-\frac{3}{4} \omega'_{20} + \frac{1}{4} \omega^M_{22})t] + \cos[\omega_{00} - \frac{1}{4} \omega'_{20} + \frac{1}{4} \omega^M_{22})t]$$

$$+ \cos[(-\frac{3}{4} \omega'_{20} - \omega^M_{22})t] - \cos[(\omega_{00} - \frac{1}{4} \omega'_{20} - \frac{1}{4} \omega^M_{22})t]\} \qquad (AI.99)$$

$$\times \{\exp(-i\phi_{22})\}$$

respectively.

The relaxation function for the combination of random cylindrical and planar anisotropies can be calculated by ignoring the unobservable ω_{00} terms and averaging over ω_{20} and ω^M_{22}. In this case, the frequency distribution $f(\omega_{20}, \omega^M_{22})$ is simply given by the product of the ω_{20} and ω^M_{22} distributions as defined in Equations AI.74 and AI.89, respectively, namely

$$f(\omega_{20}, \omega^M_{22}) = f(\omega_{20}) \cdot f(\omega^M_{22}, \phi_{22})$$

$$= \{\frac{1}{\pi} \frac{\sigma_{20}}{(\omega_{20})^2 + (\sigma_{20})^2}\} \{\frac{4}{\pi} \frac{\sigma^M_{22} \omega^M_{22}}{[(\omega^M_{22})^2 + (\sigma^M_{22})^2]^2} (2\pi)^{-1}\} \qquad (AI.100)$$

For powders, one averages over the Euler angles, and by combining Equations AI.97 and AI.100 with the definition of Equation AI.67, and ignoring the ω_{00} terms, one then obtains the expression

$$g^{RH}_{00}(t) = \frac{2}{3\pi^2} (\sigma_{20} \sigma^M_{22}) \int_{-\infty}^{\infty} d\omega_{20} [(\omega_{20})^2 + (\sigma_{20})^2]^{-1}$$

$$\times \int_{o}^{\infty} d\omega^M_{22} (\omega^M_{22})^2 [(\omega^M_{22})^2 + (\sigma^M_{22})^2]^{-2} \{\cos[\frac{1}{2} \omega_{22} t] \qquad (AI.101)$$

$$+ \cos[\frac{1}{4}(-3\sqrt{2/3} \omega_{20} + \omega^M_{22})t] + \cos[\frac{1}{4}(-3\sqrt{2/3} \omega_{20} - \omega^M_{22})t]\}$$

where the integration over the angle ϕ_{22} has already been performed, and

where the extra ω_{22}^M factor is again the Jacobian of the coordinate transformation. Performing the integrations over ω_{20} and ω_{22}^M yields the simple analytic result

$$g_{00}^{rh}(t) = \frac{1}{6} \left(1 - \frac{1}{2} \sigma_{22}^M t\right) \exp\left(-\frac{1}{2} \sigma_{22}^M t\right)$$
$$+ \frac{1}{3} \left(1 - \frac{1}{4} \sigma_{22}^M t\right) \exp\left[-\frac{1}{4}(\sigma_{22}^M + 3\sqrt{2/3}\ \sigma_{20})t\right] \tag{AI.102}$$

A check of the limiting cases shows that as $\omega_{22}^M \to 0$, Equation AI.102 approaches the expression for a cylindrical distortion given in Equation AI.76, and that as $\omega_{20} \to 0$, Equation AI.102 simplifies to Equation AI.91 for a planar distortion. Furthermore, because of the planar contribution to the hyperfine distortion, the spin polarization of the muonium ensemble tends to zero at long times.

AI.D Isolated Muonium in an External Magnetic Field

In the presence of an external magnetic field, the frequencies as well as the amplitudes are dependent upon the Euler angles. Assuming both a cylindrical and a planar distortion of the muonium hyperfine interaction, the total Hamiltonian is

$$H = \frac{h}{8\pi} \begin{bmatrix} (\omega_{00} + 4\omega_{Mu} - w_{20}) & -w_{2-2} & -w_{2-1} & 0 \\ -w_{22} & (\omega_{00} - 4\omega_{Mu} - w_{20}) & -w_{21} & 0 \\ -w_{21} & -w'_{2-1} & (\omega_{00} + 4\Gamma + (1+2sc)w_{20}) & \zeta w_{20} \\ 0 & 0 & \zeta w_{20} & (-3\omega_{00} - 4\Gamma + (1-2sc)w_{20}) \end{bmatrix} \tag{AI.103}$$

where $\Gamma = \frac{1}{2} \omega_{00}[(1 + x^2)^{1/2} - 1]$, $\zeta = 2(c^2 - s^2)$ and the w_{2m} are the detector

frame hyperfine coefficients which are related to the crystal frame

coefficients ω_{2m} through the rotational transformation defined in Equation

AI.30. Calculating the applied field spin relaxation function from the

Hamiltonian of Equation AI.103, for all applied fields is a somewhat

difficult problem. However, this problem becomes considerably easier for

certain limiting cases

Consider the problem in the limit of "high fields", (i.e., $\omega_{Mu} \gg \sigma_{2m}$).

In this limit, one can approximate the total Hamiltonian by its diagonal

components and write

$$H = \frac{h}{8\pi} \begin{bmatrix} (\omega_{00}+4\omega_{Mu}-w_{20}) & 0 & 0 & 0 \\ 0 & (\omega_{00}-4\omega_{Mu}-w_{20}) & 0 & 0 \\ 0 & 0 & (\omega_{00}+4\Gamma+(1+2sc)w_{20}) & 0 \\ 0 & 0 & 0 & (-3\omega_{00}-4\Gamma+(1-2sc)w_{20}) \end{bmatrix} \quad \text{(AI.104)}$$

where w_{20} is the detector frame coefficient which is related to the crystal

frame coefficients through the rotational transformations defined in

Equation AI.30, namely

$$w_{20} = \sqrt{2/3} \sum_{m} \omega_{2m} R_{2m}^{(2)} \quad \text{(AI.105)}$$

Since this Hamiltonian is diagonal, the energy eigenvalues are simply given

by the diagonal elements, namely

$$\xi_1 = (h/2\pi) \tfrac{1}{4}[\omega_{00}+4\omega_{Mu}-w_{20}] \quad ; \quad \xi_2 = (h/2\pi) \tfrac{1}{4}[\omega_{00}-4\omega_{Mu}-w_{20}]$$

$$\text{(AI.106)}$$

$$\xi_3 = (h/2\pi) \tfrac{1}{4}[\omega_{00}+4\Gamma+(1+2sc)w_{20}] \quad ; \quad \xi_4 = (h/2\pi) \tfrac{1}{4}[-3\omega_{00}-4\Gamma+(1-2sc)w_{20}]$$

and the corresponding transition frequencies are then

$$\omega_{12} = 2\omega_{Mu} \qquad\qquad ; \quad \omega_{23} = -\omega_{Mu}-\Gamma-\tfrac{1}{2}(1+sc)w_{20}$$

$$\omega_{13} = \omega_{Mu}-\Gamma-\tfrac{1}{2}(1+sc)w_{20} \qquad ; \quad \omega_{24} = \omega_{00}-\omega_{Mu}+\Gamma-\tfrac{1}{2}(1-sc)w_{20} \quad (AI.107)$$

$$\omega_{14} = \omega_{00}+\omega_{Mu}+\Gamma-\tfrac{1}{2}(1-sc)w_{20} \qquad ; \quad \omega_{34} = \omega_{00}+2\Gamma+scw_{20}$$

The eigenfunctions of this Hamiltonian are of course the isotropic

eigenstates give in Equation AI.24 and so the eigenfunction expansion

coefficients are just $c_{ik} = \delta_{ik}$. Combining this with the expressions for

the detector frame polarization components given in Equation AI.27, gives

$$P_{ii}^{x} = 0 \qquad ; \quad P_{ii}^{y} = 0 \qquad ; \quad P_{11}^{z} = 1, \qquad P_{22}^{z} = -1,$$

$$P_{33}^{z} = -\cos\lambda, \; P_{44}^{z} = \cos\lambda$$

$$P_{12}^{x} = 0 \qquad ; \quad P_{12}^{y} = 0 \qquad ; \quad P_{12}^{z} = 0$$

$$P_{13}^{x} = c \qquad ; \quad P_{13}^{y} = ic \qquad ; \quad P_{13}^{z} = 0$$

$$P_{14}^{x} = s \qquad ; \quad P_{14}^{y} = -is \qquad ; \quad P_{14}^{z} = 0 \qquad\qquad (AI.108)$$

$$P_{23}^{x} = s \qquad ; \quad P_{23}^{y} = -is \qquad ; \quad P_{23}^{z} = 0$$

$$P_{24}^{x} = c \qquad ; \quad P_{24}^{y} = -ic \qquad ; \quad P_{24}^{z} = 0$$

$$P_{34}^{x} = 0 \qquad ; \quad P_{34}^{y} = 0 \qquad ; \quad P_{34}^{z} = \sin\lambda$$

Substituting the results of Equation AI.114 into Equations AI.14, AI.15 and

AI.17, one obtains for the detector frame

$$g_{00}(t) = \tfrac{1}{6} (1 + \cos^2\lambda) + \tfrac{1}{3} \{\cos^2(\lambda/2)[\cos(\omega_{13}t) + \cos(\omega_{24}t)]$$
$$+ \sin^2(\lambda/2)[\cos(\omega_{14}t) + \cos(\omega_{23}t)] + \tfrac{1}{2} \sin^2\lambda[\cos(\omega_{34}t)]\} \qquad (AI.109)$$

and

$$g_{20}(t) = \tfrac{1}{2} \sqrt{2/3} \{-(1 + \cos^2\lambda) - \sin^2\lambda[\cos(\omega_{34}t)] + \cos^2(\lambda/2)$$
$$\times [\cos(\omega_{13}t) + \cos(\omega_{24}t)] + \sin^2(\lambda/2)[\cos(\omega_{14}t) + \cos(\omega_{23}t)]\} \qquad (AI.110)$$

Evaluating Equation AI.112, one writes

$$w_{20} = \sqrt{2/3} \ \{\omega_{20} \ R_{00}^{(2)}(\bar{\Omega}) + \omega_{22} \ R_{02}^{(2)}(\bar{\Omega}) + \omega_{2-2} \ R_{0-2}^{(2)}(\bar{\Omega})\} \tag{AI.111}$$

From the definition of the rotation matrix elements $R_{mM}^{(L)}(\Omega)$, Equation AI.111 becomes

$$w_{20} = \sqrt{2/3} \ \{\omega_{20} \ P_2(\cos\beta) + \omega_{22}^M \ \sqrt{4\pi/5} \ [e^{i\phi_{22}} \ Y_{22}^*(-\beta,-\alpha) \\ + e^{-i\phi_{22}} \ Y_{2-2}^*(-\beta,-\alpha)]\} \tag{AI.112}$$

where $P_2(\cos\beta)$ is the Legendre polynomial and the $Y_{LM}(-\beta,-\alpha)$ are the spherical harmonics which define the rotational transformation. Recalling the associated complex conjugate relationships, Equation AI.112 becomes

$$w_{20} = \frac{1}{2} \ \{\sqrt{2/3} \ \omega_{20} \ (3\cos(\beta) - 1) + \omega_{22}^M \ \sin^2(\beta) \ \cos(\phi_{22} + 2\alpha)\} \tag{AI.113}$$

Because we now have cylindrical symmetry, the relaxation functions for a random anisotropic hyperfine interaction for powders are calculated by

$$g_{L0}^{rh}(t) = \int_{-\infty}^{\infty} d\omega_{20} \int_{0}^{\infty} d\omega_{22}^M (\omega_{22}^M) \ f(\omega_{20}, \ \omega_{22}^M) \int d\bar{\Omega} \ g_{L0}(t) \tag{AI.114}$$

where $L = 0$ and 2 and $f(\omega_{20}, \ \omega_{22}^M)$ is the combined distribution function defined in Equation AI.100. If it is further assumed that the applied field is low with respect to the hyperfine field (i.e., $x \ll 1$), one has $c = s = 1/\sqrt{2}$, $\Gamma = 0$ and $\cos\lambda = 0$. With this one can ignore the singlet state, (i.e., ignore the ω_{00} terms in the $g_{L0}(t)$'s), and derive an expression for the triplet muonium relaxation function. For the case of L=0, Equation AI.114 becomes

$$g_{00}^{rh}(t) = \frac{1}{6} + \frac{1}{3} \int_{-\infty}^{\infty} d\omega_{20} \int_{0}^{\infty} d\omega_{22}^M \ (\omega_{22}^M)^2 \ f(\omega_{20}, \omega_{22}^M) \\ \times \int d\bar{\Omega} \ \cos(\omega_{Mu}t) \ \cos(\frac{3}{4} \ w_{20}t) \tag{AI.115}$$

and for the case L=2 in Equations AI.114 gives

$$g_{20}^{rh}(t) = -\frac{1}{2}\sqrt{2/3} + \frac{1}{2}\sqrt{2/3} \int_{-\infty}^{\infty} d\omega_{20} \int_{0}^{\infty} d\omega_{22}^{M} (\omega_{22}^{M})^2 f(\omega_{20},\omega_{22}^{M})$$

$$\times \int d\bar{\Omega} \cos(\omega_{Mu}t) \cos(\frac{3}{4} w_{20}t) \qquad (AI.116)$$

By integrating over the ω_{2m}'s first, Equation AI.115 becomes

$$g_{00}^{rh}(t) = \frac{1}{6} + \frac{1}{3}(2\pi)^{-1}(4\pi)^{-1}\cos(\omega_{Mu}t) \int_{0}^{\pi} d\beta \sin\beta \int_{0}^{2\pi} d\alpha \int_{0}^{2\pi} d\phi_{22} \qquad (AI.117)$$

$$\times \exp\{-\frac{3}{8}\sqrt{2/3}\,\sigma_{20}|3\cos^2\beta - 1|t - \frac{3}{8}\sin^2\beta\,\sigma_{22}^{M}|\cos(\phi_{22}+ 2\alpha)|t\}$$

which can be written as

$$g_{00}^{rh}(t) = \frac{1}{6} + \frac{1}{3}\left[\frac{\cos(\omega_{Mu}t)}{\pi}\right] \int_{0}^{\pi} d\beta \sin\beta \int_{0}^{\pi/2} d\theta \qquad (AI.118)$$

$$\{\exp[-\frac{3}{8}\sin^2\beta\,\sigma_{22}^{M}t\,\cos\theta] \exp[-\frac{3}{8}\sqrt{2/3}\,\sigma_{20}t\,|3\cos^2\beta - 1|]\}$$

In a similar manner, the case L=2 gives

$$g_{20}^{rh}(t) = -\frac{1}{2}\sqrt{2/3} + \frac{1}{2}\sqrt{2/3}\left[\frac{\cos(\omega_{Mu}t)}{\pi}\right] \int_{0}^{\pi} d\beta \sin\beta \int_{0}^{\pi/2} d\theta \qquad (AI.119)$$

$$\{\exp[-\frac{3}{8}\sin^2\beta\,\sigma_{22}^{M}t\,\cos\theta] \exp[-\frac{3}{8}\sqrt{2/3}\,\sigma_{20}t\,|3\cos^2\beta - 1|]\}$$

Now one can consider the motion of the μ^+ spin polarization in the context of the conventional field geometries; longitudinal and transverse field.

AI.D.1 Longitudinal Field Relaxation Function

The longitudinal relaxation function can be easily calculated from the definitions of the longitudinal relaxation functions given in Equation AI.21. In the limiting case under discussion, the only non-zero longitudinal relaxation function is $g_1^c(t)$. Since this function is a

linear combination of both $g_{00}^{rh}(t)$ and $g_{20}^{rh}(t)$, one has

$$g_1^c(t) = g_{00}^{rh}(t) - \sqrt{2/3}\ g_{20}^{rh}(t) = \frac{1}{2} \qquad \text{(AI.120)}$$

which simply means that the hyperfine interaction of the triplet muonium

ensemble is completely decoupled for $\omega_{Mu} \gg \sigma_{2M}$.

AI.D.2 Transverse Field Relaxation Function

The detector frame observable transverse relaxation functions are

defined in Equations AI.22 and AI.23. For the "high field" limiting case

under consideration, one observes that there is only one non-zero

coplanar-transverse and one non-zero perpendicular-transverse relaxation

function, $g_{ct}^{sc}(t)$ and $g_{pt}^{ss}(t)$, respectively, which are equivalent. Thus one

can write

$$g_{ct}^{sc}(t) = g_{pt}^{ss}(t) = (2\pi)^{-1}\cos(\omega_{Mu}t) \int\limits_{o}^{\pi} d\beta\ \sin\beta \int\limits_{o}^{\pi/2} d\theta$$

$$\{\exp[-\frac{3}{8} \sin^2\beta\ \sigma_{22}^M t\ \cos\theta]\ \exp(-\frac{3}{8}\ \sqrt{2/3}\ \sigma_{20}t\ |3\cos^2\beta - 1|)\} \qquad \text{(AI.121)}$$

which can be calculated numerically. For early times ($t \to 0$), one can

expand the integrand to obtain the approximate expression

$$g_{ct}^{sc}(t) = g_{pt}^{ss}(t) = \frac{1}{2}\ \cos(\omega_{Mu}t)\ \exp[-(\frac{\sqrt{2}}{6}\ \sigma_{20} + \frac{2}{\pi\sqrt{6}}\ \sigma_{22}^M)t] \qquad \text{(AI.122)}$$

As a matter of convention, the $\cos(\omega_{Mu}t)$ part of Equation AI.122 is usually

omitted from the definition of the transverse field relaxation function.

By comparing the initial slope (m_{zf}) of the zero field relaxation

function given in Equation AI.102, with the initial slope (m_{tf}) of the

transverse field function of Equation AI.122, one can define the ratio

$$\frac{m_{zf}}{m_{tf}} = \sqrt{3} \frac{\left[1 + 4/\sqrt{6} \left(\sigma_{22}^{M}/\sigma_{20}\right)\right]}{\left[1 + \sqrt{12} \frac{1}{\pi}(\sigma_{22}^{M}/\sigma_{20})\right]} \approx \sqrt{3} \qquad (AI.123)$$

Thus, one finds that $m_{zf} > m_{tf}$, indicating that the rate of depolarization is greater in zero than in transverse field.

APPENDIX II - ULTRA-LOW ENERGY MUON PRODUCTION (μSOL)

In recent years, the development of high flux positron beams has made it possible to study atomic scattering cross sections, the interaction of positrons with surfaces as well as the spectroscopy of positronium atoms in vacuum [1-4]. The analogous experiments with positive muons are at present impractical since comparable μ^+ beams do not as yet exist. The state of the art method for producing slow μ^+ involves tuning the secondary channel to lower momenta P, thereby collecting and transporting μ^+ which originate from π^+ decaying inside the pion production target. These muons are, for lack of a better term, called subsurface muons. It can be easily argued that the subsurface μ^+ rate R is proportional to $P^{7/2}$ multiplied by an appropriate decay factor. For 10 keV (1.5 MeV/c), the subsurface μ^+ rate at 100 μA for the M13 secondary channel at TRIUMF would be approximately

$$R = \frac{1.4 \times 10^6 \, \text{sec}^{-1}}{\left(29.8 \, \text{MeV/c}\right)^{7/2}} \, P^{7/2} \, e^{-t_f/\tau_\mu} \approx 8.0 \, \text{sec}^{-1} \qquad \text{(AII.1)}$$

where t_f is the time of flight through the channel (3.66 x 10^{-6} sec for M13) and τ_μ is the mean muon lifetime ($\sim$ 2.2 μs). Clearly, this rate is not acceptable from a practical experimental perspective.

The need for an ultra-low energy (0 to ~10 keV), high flux μ^+ beam is somewhat self evident. Such a beam if developed can be immediately utilized in the study of:

(1) Electron-Muon Capture Spectroscopy - By scattering slow μ^+ at grazing incidence to a surface, one can study electron pick-up processes involved in μ^+e^- and $\mu^+e^-e^-$ formation as a function of the surface properties and magnetic ordering. This type of experiment has already been done for D^+ ions [5].

(2) <u>Adatom Adsorption on Surfaces</u> - The ability to adsorb μ^+ or Mu on well characterized surfaces will provide information regarding surface properties as well as the effect of a reduced dimensionality on the evolution of the muon spin polarization.

(3) <u>Charge Exchange Cross Sections</u> - Measurements of the muonium formation probability as a function of incident μ^+ energy (down to thermal energies) would provide valuable information to help discriminate between spur and hot atom mechanisms.

(4) <u>Molecular Ion Formation</u> - Muon molecular ion formation has been observed in He and Ne [6], but it is not as yet known at what stage of thermalization the molecular ion is formed. The correlation between the μ^+ incident energy (down to thermal energies) and molecular ion formation would help decipher the mechanisms involved.

A slow Mu beam could be produced by passing the low energy μ^+ beam through a thin foil (or gas jet) and taking advantage of the large electron capture cross section. The resulting slow Mu beam could then be utilized in experiments such as:

(1) <u>Muonium Lamb Shift</u> - Recently measured to an accuracy of 1% at TRIUMF [7], this experiment becomes a significant test of QED if an accuracy of 100 ppm can be obtained. Slow μ^+ fluxes in excess of 10^3/sec at 1 MeV/c would make a precision experiment possible.

(2) <u>Muonium to Anti-Muonium Conversion</u> - A low energy Mu beam would of course benefit these studies, but to be competitive with existing experimental scenarios the Mu flux would have to be in excess of 10^4/sec.

In what follows, the investigation of possible μ^+ emission from surfaces is proposed which utilizes the knowledge gained in low energy positron production research with the appropriate analogies drawn between positrons and positive muons. The ultimate goal of this research would of course be the development of an ultra-low energy (0 to ~10 keV) μ^+ beam.

AII.1 Current Status of Slow Positron Production

The beam moderation techniques employed in the production of slow e^+

beams involve single crystal metal moderators and utilize the existence of a

negative work function for positrons at the moderator surface. Normally a

backscattering geometry is used where the high energy positrons originate

from a radioactive source (^{22}Na for instance) which is mounted facing the

moderator surface. The beta-decay positrons are implanted into the crystal

and become thermalized with a stopping distribution corresponding to an

exponential attenuation law [8]. Some of the implanted e$^+$ are able to

diffuse back to the surface before annihilating, and a fraction of those are

then emitted from the moderator surface as a result of a negative work

function mechanism. The conversion efficiency ξ for present day moderated

beams, defined as the ratio of the slow e$^+$ yield to the total number of fast

positrons emitted from the source, is generally on the order of 10^{-3}.

By analogy with the electron case, the work function Φ_+ of the

positron in a metal is given by

$$\Phi_+ = - D - \mu_p \tag{AII.2}$$

where D is a potential due to the surface dipole layer and μ_p is the

positron chemical potential inside the metal. The positron chemical

potential incorporates two terms. The first contribution to μ_p arises

from the positron-ion interaction (Bloch wave energy). This interaction

along with the surface dipole layer act to expel the positron from the

metal. The second contribution to μ_p is the electron-positron correlation

energy, which is of course an attractive potential acting to bind the

positron to the metal surface.

Considering the mass of the muon in comparison to that of the positron,

one can conclude that for a metal moderator a μ^+ negative work function is

not such a likely candidate to be used in the production of an ultra-slow μ^+

beam, primarily because the attractive $e^--\mu^+$ correlation energy would be

about 1 R_∞ rather than the 1/2 R_∞ as is the case for e^--e^+ correlations.

Also, the added kinetic energy arising from Bloch wave kinematics, which is

on the order of a few electron volts for e^+, becomes negligible for the

heavier μ^+. From this one can conclude that, at least for metal moderators,

the μ^+ affinities are probably not negative. For insulators, however, the

μ^+ affinities may very well be negative because in this case the $e^--\mu^+$

correlations are in general small. Another emission process, which has been

observed for e^+ implanted in ionic single crystals, produces e^+ having

kinetic energies on the order of the band gap energy of the solid. This

mechanism and its possible application to μ^+ emission is discussed in detail

in the following pages.

AII.2 Band Gap Emission of e^+ from Ionic Crystal Surfaces

Recent positron experiments [9] show that when e^+ of keV energies are

implanted into ionic single crystals they are reemitted isotropically from

the solids with a continuum of energies having a maximum approximately equal

to the band gap energy (typically on the order of 10 to 20 eV). Operating

under the assumption that the mechanism(s) responsible for the reemission of

positrons would also be involved in the analogous phenomena for μ^+, a brief

synopsis of the e^+ experiments, along with the current understanding of the

mechanism(s) involved, are given here.

Five alkali-halides (LiF, NaF, NaCl, KCl, KBr) and four other ionic

solids (SiO_2, Al_2O_3, MgO, CaF_2) were studied in all. The alkali halide

samples were oriented with the (100) axis normal to the emitting surface, as

was the MgO crystal. The SiO_2 crystal was z-cut, the Al_2O_3 sample was

oriented with the c-axis normal to the emitting surface and the CaF_2

orientation was believed to be (110). The experiments were performed in a

vacuum of 5 x 10^{-10} Torr, with the samples heated to about 330 °C, and the

surface contamination was estimated to be somewhat less than a monolayer.

A beam of 500 eV positrons was incident on the surface of the samples

and the axial component of the reemitted positron spectrum was measured.

The energy spectra obtained for each of the nine ionic crystals show a

characteristic continuum of energies with the maximum energy approximately

equal to the band gap of the individual solids. These experiments were

repeated for 1500 eV incident positrons, with the results showing no

statistically significant deviation from the 500 eV data. The angular

distribution of the emission spectra was also studied and found to be

approximately isotropic.

In addition to emitting positrons, it was found that all nine samples

also emit positronium (Ps). To discriminate between different possible

emission processes, for both e^+ and Ps, the dependence of the Ps formation

probability on the incident e^+ energy was studied. Results from these

studies as well as from positron diffraction experiments, have lead to the

conclusion that at least for LiF and NaF, the emission of both e^+ and Ps can

be associated with Ps diffusing to the surface of the crystal moderator.

Approximately 60% of the incident e^+ form Ps in these samples, with about

60% of the Ps atoms that diffuse back to the surface being dissociated,

thereby re-emitting the positron.

In 1972 it was postulated that Ps could be field-ionized in the process

of leaving a surface [10]. This, however, does not explain the anomalously

large emission energies or the correlation with the band gap energy of the solid. An alternate explanation [9] is that the positron is Auger-emitted when the Ps electron falls into an acceptor state at the surface. With this model, the maximum energy E^e_{max} of the emitted e^+, corresponding to the Ps electron recombining with a hole at the bottom of the valence band is given by the expression

$$E^e_{max} = (E_g + \Delta E_v) - (E^{Ps}_b + \Phi^e_+) \qquad (AII.3)$$

where E_g is the band gap energy, ΔE_v is the width of the valence band, E^{Ps}_b is the binding energy of Ps on the surface of the solid and Φ^e_+ is the positron work function. Plugging the values for NaF into Equation AII.3 gives $E^e_{max} = 11.8(6)$ eV, which agrees well with the experimental result [9] of 12.3 +/- 0.7 eV. Since one does not normally expect long-lived holes in the valence band, however, Equation AII.3 represents an overestimate.

The origin of the surface acceptor states is not yet known. Normally, one would not expect holes below the the Fermi energy E_f (about 4.5 eV below the bottom of the conduction band for air cleaved NaF at 300 °C [9]). However, electron-hole pairs are produced in the ionization trail of the incident e^+ beam, and possibly some of the holes survive long enough to migrate to the surface. In any case, the branching ratio for e^+ emission as opposed to Ps emission is equal to the surface density of acceptor states multiplied by the electron capture cross section. As mentioned earlier the branching ratio for e^+ vs Ps emission has been found [9] to be about 60%.

For these initial experiments the alkali halide samples were prepared by cleaving in air. Subsequent experiments on vacuum-cleaved samples of NaF and LiF were also performed [9] with the results indicating the same general

positron emission spectra as found for the air-cleaved samples,
except for a few slight differences. In particular, Φ_+^e for the air-cleaved
NaF and LiF crystals is equal to +0.5 eV and -0.7 eV, respectively [9].
However, for the vacuum-cleaved samples of both NaF and LiF, Φ_+^e was found to
be positive. Thus even though the positron work function is not negative,
positron emission of band gap energies is still observed. This is important
to note in light of the fact that the μ^+ work function for these materials
is expected to be positive.

AII.3 Comparison of e^+ and μ^+ WRT Band Gap Emission

Although some tend to view the muon as a heavy electron, the behavior
of muonium (Mu) in solids is more reminiscent of hydrogen rather than Ps.
The diffusion constant D for Mu in these materials can be estimated by
considering experiments involving Mu emission from fine SiO_2 powders [11].
Using a diffusion model [12] originally applied to positronium, it was found
that $D \sim 10^{-7}$ cm^2/s at room temperature. The diffusivity in single crystals
would of course be greater than this with a good room temperature estimate
being $D \sim 10^{-5}$ cm^2/s. In comparison, the diffusion constant for positrons
in the same materials is about 10^{-3} cm^2/s. With a diffusion constant of
10^{-5}, the diffusion length $(\tau_\mu D)^{1/2}$ is then about 5×10^{-6} cm. Heating to
higher temperatures would of course enhance the diffusion. The stopping
distribution of surface μ^+ in these materials has a range of about 0.05 cm.
Clearly, tuning to subsurface momenta would increase the probability for the
μ^+ to reach the surface within their lifetime, but considering the loss in
incident flux as the beam momentum is reduced, no net increase in the

reemitted beam flux is forseen.

In addition to diffusivity, the formation probability for Mu as opposed to Ps must be considered. As mentioned earlier, roughly 60% of the incident positrons form positronium. In comparison the muonium formation probabilities for single crystals of NaF and LiF at room temperature, deduced from the observed missing fractions in the μ^+ spectra, are 98 ± 5% [13] and 44 ± 6% [13,14], respectively. The muonium fraction will be reflected in the slow μ^+ moderation efficiency.

To estimate the maximum emission energy for μ^+ one requires values for the muonium binding energy E_b^{Mu} on the surface of the solid and the μ^+ work function Φ_+^μ, which are as yet not well known. However, in analogy with Ps studies, the maximum Mu kinetic energy is the negative of its work function Φ^{Mu}, which is given by

$$\Phi^{Mu} = \left(E_b^{Mu} - R_\infty\right) + \left(\Phi_-^e + \Phi_+^\mu\right) \qquad (AII.4)$$

where Φ_-^e is the electron affinity at the bottom of the conduction band. Using Equation AII.4, one can rewrite Equation AII.3 as

$$E_{max}^\mu = \left(E_g + \Delta E_v\right) - \Phi^{Mu} - R_\infty + \Phi_-^e \qquad (AII.5)$$

A negative muonium work function has been postulated to explain the emission of Mu from finely divided SiO_2 powders. A conservative estimate of Φ^{Mu} would be $\Phi^{Mu} \approx 0\pm1$ eV. For NaF and LiF, E_g is 11.5 eV and 13.7 eV, respectively [15]. The width of the valence band is $\Delta E_v = 4.0(5)$ eV [9] and $\Phi_-^e \approx 0\pm1$ eV for both crystals. Thus, the maximum kinetic energies of the emitted μ^+ for NaF and LiF are estimated to be

$$E^\mu_{max}(NaF) = 1.9 \pm 2 \text{ eV}$$

$$E^\mu_{max}(LiF) = 4.1 \pm 2 \text{ eV}$$

(AII.6)

The branching ratio y_o for μ^+ emission as opposed to Mu emission is difficult to estimate. However, the problem is somewhat simplified since the surface density of acceptor states is likely to be a property of the sample preparation. Thus one is left only with evaluating the electron capture cross section at the surface for Mu as opposed to Ps. Because the binding energy of Mu is approximately twice that of Ps, one would expect the electron capture cross section at the surface to decrease accordingly. As has already been mentioned, the higher binding energy and mass of Mu as compared to Ps also shifts the maximum energy for μ^+ emission to lower energies with respect to the e^+ spectra. From these considerations the branching ratio y_o for μ^+ vs Mu should be roughly equal to one half times the branching ratio for e^+ vs Ps emission weighted by the fraction of e^+ emitted in the energy range $(E^e_{max} - E^\mu_{max})$ to E^e_{max}. Thus, a good estimate for the μ^+ branching ratio would then be 5-10%. In any case, measurement of y_o is one of the goals of these experiments. One last point to be made is that in both NaF and LiF the μ^+ spin in the muonium state depolarizes due to superhyperfine interactions of the Mu electron with neighboring nuclei.

AII.4 Calculations for Positive Muon Emission Yield

To make a theoretical estimate of the slow μ^+ conversion efficiency ξ_μ for μ^+ emission, one needs to know:

   (1) The stopping distribution f(x) of the incident beam
   (2) The bulk diffusion constant D for thermalized muonium
   (3) The fraction F(T) of muonium formed (formation probability)
   (4) The branching ratio y_o for energetic μ^+ emission

Consider the random walk problem where the muons are incident on the surface of a homogeneous moderator of thickness d as shown in Figure AII.1, and subsequently thermalize in the muonium state. Once thermalized, the Mu atoms diffuse approximately randomly through the lattice until they reach one of the moderator surfaces where there exists some finite probability for μ^+ emission. With this geometry and taking into account the finite lifetime of the muon, the conversion efficiency ξ_μ can be written [16]

$$\xi_\mu = \frac{1}{2} \left(F(T) y_o \right) \int_o^\infty dt \; e^{-t/\tau_\mu} \int_o^d dx \; f(x) \; R(t;\vec{x}) \qquad \text{(AII.7)}$$

where $R(t;\vec{x})$ is the rate at which a Mu starting at $\vec{x}_o$ at time t=0 appears at the surface. The factor of 1/2 arises since we are neglecting the other surface. It can be shown that [16,17]

$$R(t;\vec{x}) = (2t)^{-1} (4\pi Dt)^{-1/2} \left[x \, e^{-x^2/4Dt} + (d-x) \, e^{-(d-x)^3/4Dt} \right] \qquad \text{(AII.8)}$$

A beam of 30 MeV/c muons with a momentum spread of $\Delta P/P \approx 10\%$ will stop approximately uniformly over a distance r defined by the minimum and maximum mean ranges of the beam particles, namely

$$r \approx \text{Range(30 MeV/c)} - \text{Range(27 MeV/c)} = 2.35 \times 10^{-2} \text{ cm} \qquad \text{(AII.9)}$$

With this approximation, the stopping distribution f(x) in Equation AII.7 can be assumed to be uniform and given by $f(x) = 1/r$. Since the mean stopping distance r is large compared to the diffusion length $(\tau_\mu D)^{1/2}$, the expression for $R(t;\vec{x})$ given in Equation AII.8 clearly breaks down into two components of equal magnitude corresponding to the arrival rate of Mu at
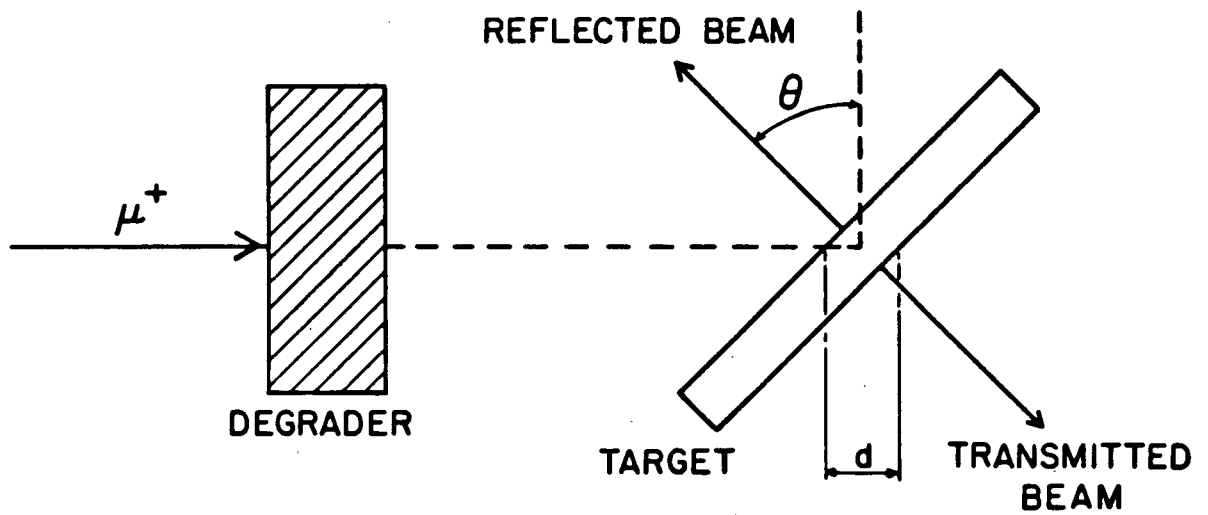
Figure AII.1 Target geometry showing both reflection and transmission modes. In transmission mode degrading is provided by the target itself.

each of the two surfaces. Thus $R(t;\vec{x})$ for each surface can be simplified to give

$$R(t;\vec{x}) = (2t)^{-1} (4\pi Dt)^{-1/2} [x\ e^{-x^2/4Dt}] \qquad \text{(AII.10)}$$

Substituting this expression into Equation AII.7 and letting $d \to \infty$ (i.e., ignoring the second surface), the slow μ^+ conversion efficiency ξ_μ is written

$$\xi_\mu = \frac{1}{2}[F(T)y_0]\ \frac{1}{r}\ \int_o^\infty dt\ e^{-t/\tau_\mu} (2t)^{-1}(4\pi Dt)^{-1/2} \int_o^\infty dx\ x\ e^{-x^2/4Dt}$$

$$= \frac{1}{2}[F(T)y_0]\ \frac{1}{r}\ (\tau_\mu D)^{1/2}\ = y_0\ (9.78\text{x}10^{-5}); \quad \text{for NaF}$$

$$\text{(AII.11)}$$

$$= y_0\ (4.4\text{x}10^{-5})\ ;\quad \text{for LiF}$$

This efficiency ($\sim 10^{-5}$ for a conservative value of y_0) is of course not very good, it does, however, translate into 10 such muons per second for muon intensities such as available from M13 or M20 and $\sim 10^3$ per second if the moderator could be placed close to the pion production target. If the proposed emission process exists for μ^+ it should be observable using one of TRIUMF's surface muon beams, and once observed steps can be taken to improve the above efficiency. These steps could include the development of high surface area moderators, investigating ways of increasing the density of surface acceptor states, increasing the muonium diffusion length as well as investigating other moderators. Producing a polarized μ^+ beam, which utilizes surface emission processes, will require the application of a large (~ 10 G) magnetic field to quench the effects of superhyperfine interactions.

AII.5 Prototype Apparatus

The apparatus designed for the initial search for the emission of μ^+ from solid surfaces is shown in Figure AII.2. It consists of a scattering chamber and target assembly, combined with a DQQ spectrometer which is designed to momentum select the extracted muons and focus them onto a channeltron detector. Although all of the vacuum components have been designed to be consistent with ultra-high vacuum requirements, the initial experiments will employ borrowed, non-bakable components which will limit the attainable vacuum to about 10^{-9} Torr. The scattering chamber is designed in such a way as to allow the spectrometer section to be mounted in either a transmission or reflection geometry, simply by rotating the apparatus by 180°.

The target assembly will be held at a potential V_1 of about +10 kV with respect to a grounded grid thereby providing an electric field to accelerate muons which are emitted from the surface. A second grid, which lies between the target and the grounded grid will have an independently variable potential V_2 applied to it which will allow a first order measurement of the emission energy spectra. Provisions have also been made for heating the targets to enhance the Mu diffusion rate. The initial target assembly will be relatively simple and target changes will require venting the system using dry nitrogen. In the future a bakable, remotely controllable target ladder will be introduced with more sophisticated temperature control capability.

AII.6 Measurements

In transmission mode the μ^+ beam is incident on a moderator of suitable
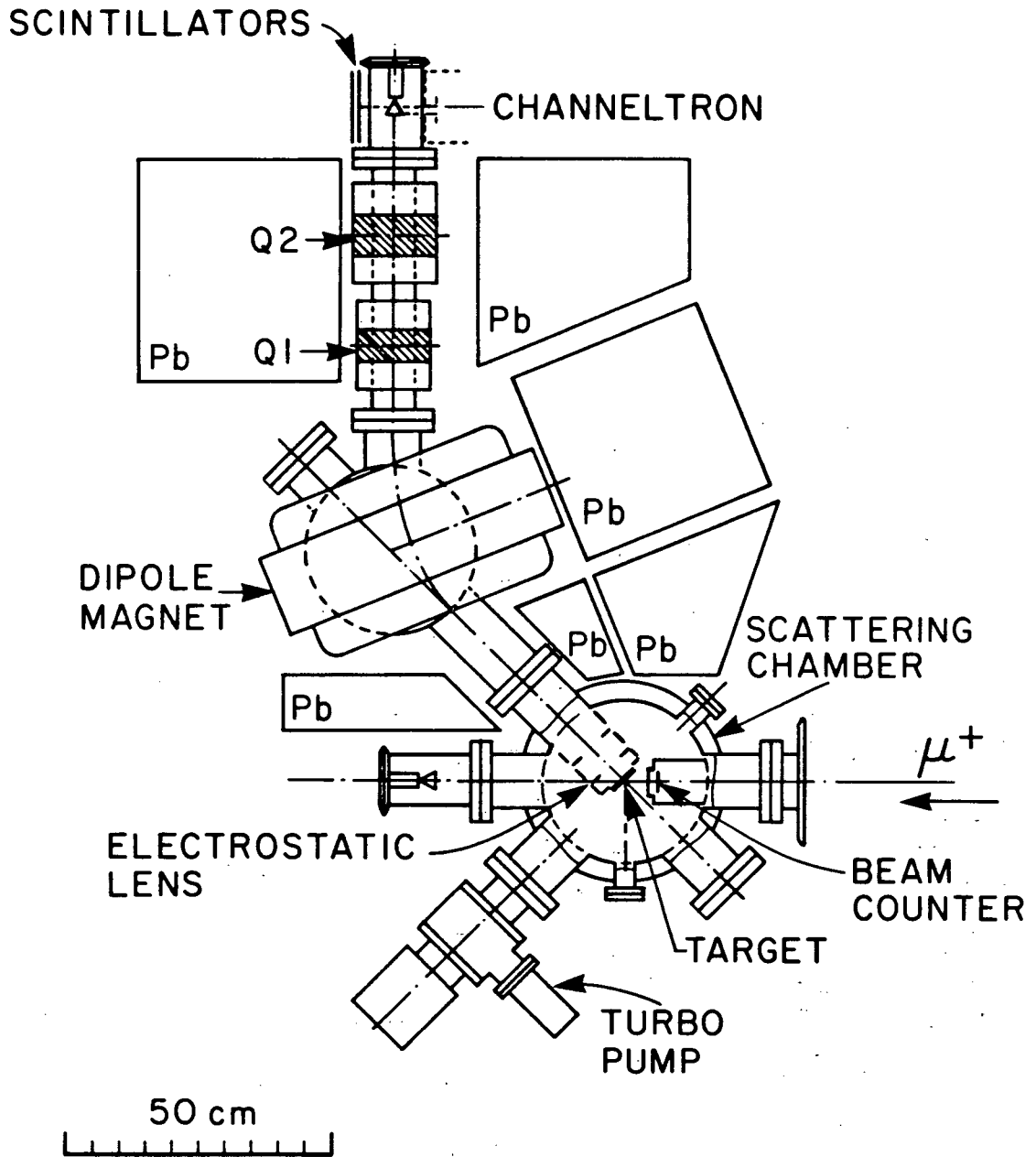
Figure AII.2 μSOL scattering chamber and DQQ spectrometer (shown here in transmission geometry).

thickness such that the muons are stopped at or near the downstream surface.
In reflection mode the incident μ^+ beam must be degraded upstream of the
extraction grids to such an energy that the μ^+ will stop at or near the
upstream surface of the moderator. Multiple scattering in the degrader will
clearly reduce the effective incident beam rate in reflection geometry,
however background rates, especially due to beam positrons, may also be
reduced. In some cases, single crystal samples having the appropriate
thickness for transmission geometry may not be readily available. In light
of these considerations, both transmission and reflection geometries will
have to be tested.

The basic measurement to be made is the time of flight (TOF) between an
incident beam μ^+ which fires the beam counter and the subsequent detection
of a slow μ^+ in the channeltron. Surface emitted μ^+ should give a
characteristic spectrum which begins about 370 ns after the μ^+ start pulse.
From Equation AII.11, the shape of this spectrum is expected to be

$$R(t) = \frac{C}{2} (D/\pi)^{1/2} \frac{e^{-t/\tau_\mu}}{\sqrt{t}} \cdot \exp(-\lambda t) \quad ; \quad C = \left[F(T) \, y_o \, \frac{1}{r} \right] \qquad (AII.12)$$

with the number of events observed within a finite gate width τ_g given by

$$N(\tau_g) = C \int_o^{\tau_g} dt \, R(t) = \frac{C}{2} D^{1/2} \left[\lambda + \frac{1}{\tau_\mu} \right]^{-1/2} erf\left[\sqrt{\tau_g (\lambda + 1/\tau_\mu)} \right] \qquad (AII.13)$$

Here the λ parameter represents the rate of loss of Mu from the diffusing
muonium ensemble, and is included to account for possible losses of Mu due
to chemical reactions, etc., in the crystal.

Epithermal μ^+ or $\mu^+ e^- e^-$ which are produced by multiple scattering and
charge exchange processes in the target and accepted by the spectrometer
system, will gennerally be distributed at higher velocities as compared to
μ^+ arising from surface emission, and will therefore give rise to prompt

events. Measurement of the epithermal μ^+ of Mu^- ($\mu^+e^-e^-$) yield will likely require the development of an electrostatic lens injection system to increase the acceptance of the spectrometer section. Finalization of an injection system design will depend on the spectra observed with the presently proposed apparatus. Simultaneous with the collecting of the TOF histogram, a μ^+-decay histogram between the channeltron and the positron telescopes, gated by an incident μ^+, will also be accumulated.

The detection efficiency, ε_{ch} of the channeltron for 10 keV μ^+ is expected to be $\sim$0.75, but this needs to be better determined. A measurement of this will therefore be made, possibly as a function of energy, using the three NaI detectors placed strategically around the cone of the channeltron to provide the maximum possible detection solid angle. The NaI detectors will detect the decay positrons from μ^+ stopped in the channeltron and thus determine the absolute flux of stopped muons. These measurements will of course require appropriate veto and coincidence scintillators to correctly define the solid angles and sensitive volume.

The NaI detectors can also be used in coincidence with the channeltron to reduce backgrounds in the TOF spectrum, but with a loss in event rate.

With these considerations, the experimental rate R_{exp} is then

$$R_{exp} = R_o \, \xi_\mu \, erf\left(\sqrt{\tau_g/\tau_\mu}\right) \, \varepsilon_d \, \varepsilon_{ch} \, \varepsilon_{NaI} \quad ; \text{ for } \lambda = 0 \qquad (AII.14)$$

where R_o is the incident μ^+ flux, ε_d is the probability that the μ^+ do not decay in flight, ε_{ch} is the detection efficiency of the channeltron and ε_{NaI} is the detection efficiency and solid angle of the NaI crystal array. For the proposed experiment and apparatus, $R_o \sim 10^6/s$, $\varepsilon_{ch} \sim 0.75$, $\varepsilon_{NaI} \sim$ 0.2 and $\varepsilon_d \sim 0.85$. For a gate width of 2 μs, $erf\left(\sqrt{\tau_g/\tau_\mu}\right)$ is approximately

equal to 0.84. From this, conservative estimates of R_{exp}, for both NaF and LiF, are then

$$R_{exp} \approx y_o \ (10/\text{second}) \ ; \ \text{for NaF}$$
$$\approx y_o \ (\ 5/\text{second}) \ ; \ \text{for LiF} \qquad (\text{calculated for } \lambda = 0) \qquad (\text{AII.15})$$

where the value of y_o is of course different for the two crystals

AII.7 Backgrounds

There are three major sources of backgrounds to be considered; beam positrons, positrons from muons stopped in the moderator and positrons from muons which decay in flight through the spectrometer system. Beam positrons will pass through the moderator and scatter downstream producing bremsstrahlung and annihilation radiation. These beam related backgrounds will reflect the RF structure of the cyclotron and will probably be greater in transmission than in reflection geometry. Because of this, a separated beam is highly desirable. The positrons which arise from μ^+ decaying in the moderator have some probability of being emitted into the acceptance of the spectrometer. These positrons are too energetic to be transported through the spectrometer, but collisions with the walls of the vacuum chamber will produce background radiation which is flat in time. Positrons from μ^+ decaying in flight will also collide with the vacuum chamber walls producing background radiation. In this case, however, the background will not be flat, but will decay with the muon mean lifetime multiplied by some position dependent function. These backgrounds are difficult to estimate but will clearly have to be minimized by shielding the detectors from all sources other than the target, reducing the beam contamination and if feasible reducing the momentum bite of the beam.

This experiment should closely parallel the earlier positron experiment at first using NaF and LiF in the <100> orientation. Depending on the results obtained with the alkali halides, these investigations may be extended to other crystal orientations as well as other materials such as quartz ($E_g \approx 9$ eV) and solid rare gases such as argon ($E_g \approx 19$ eV).

This appendix (with modifications) was submitted as an experimental proposal (E-325) to the December 1984 meeting of the TRIUMF Experimental Evaluation Committee and was accepted at high priority. Preliminary results [18] of the first experiments have indeed shown positive indications of a low energy (<10 eV) component for LiF.

APPENDIX III — COLLISION FREQUENCY OF THERMAL MUONIUM

AIII.A Derivation

Consider a point particle of mass m and mean thermal velocity $\bar{v}$, moving freely in a uniform distribution of N spherical particles of radius R. If one defines the number density to be N/V, where V is the total volume of the sample, the mean free path L is then written

$$L = V \left(\pi R^2 N \right)^{-1} \qquad (AIII.1)$$

By dividing the mean free path L by the mean thermal velocity $\bar{v}$, one obtains the average time $\bar{t}$ between collisions, namely

$$\bar{t} = \frac{L}{\bar{v}} = V \left(\pi R^2 \bar{v} N \right)^{-1} \qquad (AIII.2)$$

Taking the reciprocal of Equation AIII.2 then gives the collision frequency, and substituting the definition of the mean thermal velocity, one has

$$F(T) = \frac{1}{\bar{t}} = \frac{N}{V} \left(\pi R^2 \right) \bar{v} = \frac{N}{V} \left(\pi R^2 \right) \left[\frac{8kT}{\pi m} \right]^{1/2} \qquad (AIII.3)$$

where k is Boltzmann's constant and T is the temperature.

AIII.A.1 Low Density Limit

For low packing densities (neglecting the volume of the solid), the number density is simply given by the equation

$$\frac{N}{V} = \frac{\rho}{M} = \left(\frac{3}{4\pi R^3} \right) \frac{\rho}{\rho_o} \qquad (AIII.4)$$

where M is the mass of one grain (particle), ρ is the mass packing density (i.e., after compression) of the target particles and ρ_o is the mass density of the bulk material (for SiO_2; $\rho_o = 2.2$ g/cm^3). Thus in the low

density limit, the collision frequency is

$$F(T) = \left(\frac{3}{R}\right) \frac{\rho}{\rho_o} \left[\frac{k}{2\pi m}\right]^{1/2} T^{1/2} \qquad \text{(AIII.5)}$$

This equation is, however, not correct if the volume of the solid (i.e., the volume of the N particles) is significant with respect to the total volume of the sample.

AIII.A.2 High Density Limit

In the high packing density limit, the volume of the solid is no longer negligible, so that one must redefine the number density to be the number of particles (grains) per unit "free volume" V_f, namely

$$V_f = \left(V - V_{solid}\right) = V - N\left(\frac{4}{3}\pi R^3\right) = V\left[1 - \frac{N}{V}\left(\frac{4}{3}\pi R^3\right)\right] \qquad \text{(AIII.6)}$$

By combining Equations AIII.4 and AIII.6, one obtains

$$\frac{N}{V_f} = \frac{3}{4\pi R^3} \left[\frac{\rho_o}{\rho} - 1\right]^{-1} \qquad \text{(AIII.7)}$$

Using this "corrected" number density, the collision frequency for the high density limit is

$$F(T) = \frac{3}{R} \left(\frac{k}{2\pi m}\right)^{1/2} \left[\frac{\rho_o}{\rho} - 1\right]^{-1} T^{1/2} \qquad \text{(AIII.8)}$$

Notice that for low densities, Equation AIII.8 reduces to the expression of Equation AIII.5.

Q.E.D.

APPENDIX IV -- TABULATED TRANSVERSE FIELD DATA

$SiO_2(1)$ Prepared at 110 °C; $\lambda_\perp^{Mu}$ Vs Temperature

T (K)	ΔT (K)	$\lambda_\perp^{Mu}$ (μs^{-1})	$\Delta\lambda_\perp^{Mu}$ (μs^{-1})
4.1	0.10	2.59	0.180
5.8	0.20	2.49	0.137
9.0	1.00	2.11	0.186
9.5	0.20	2.02	0.118
10.2	0.20	2.00	0.154
11.5	1.50	1.82	0.142
12.5	0.20	1.72	0.112
14.0	0.30	1.50	0.101
16.8	0.20	1.63	0.118
19.3	0.20	2.48	0.135
22.0	0.20	2.58	0.145
25.0	0.20	2.99	0.336
32.5	3.50	2.55	0.135
40.3	2.30	2.13	0.270
47.5	12.50	1.85	0.153
59.0	11.00	1.38	0.153
60.0	2.00	1.02	0.072
86.0	1.00	0.62	0.046
128.0	1.00	0.51	0.037
300.0	3.00	0.40	0.028

$SiO_2(3)$ Prepared at 600 °C; $\lambda_{\perp}^{Mu}$ Vs Temperature

T (K)	ΔT (K)	$\lambda_{\perp}^{Mu}$ (μs^{-1})	$\Delta\lambda_{\perp}^{Mu}$ (μs^{-1})
4.6	0.05	1.18	0.033
6.0	0.10	1.08	0.052
8.0	0.10	1.01	0.045
10.0	0.10	0.90	0.060
12.0	0.10	0.73	0.035
16.0	0.10	0.51	0.026
18.0	0.10	0.57	0.035
20.0	0.30	0.84	0.036
22.0	0.10	1.13	0.053
24.0	0.30	1.42	0.086
25.0	0.20	1.38	0.052
26.0	0.10	1.68	0.098
28.0	0.10	1.85	0.107
30.0	0.20	2.11	0.108
40.0	2.00	1.97	0.082
50.0	3.00	1.85	0.065
85.0	5.00	1.37	0.074

$SiO_2(2)$ Prepared at 110 °C; $\lambda_\perp^{Mu}$ Vs Temperature

T (K)	ΔT (K)	$\lambda_\perp^{Mu}$ (μs^{-1})	$\Delta\lambda_\perp^{Mu}$ (μs^{-1})
5.8	0.20	2.49	0.137
10.1	0.20	2.13	0.089
13.5	0.20	1.76	0.086
25.0	0.20	3.31	0.206
45.0	0.20	1.59	0.089
58.5	5.50	0.99	0.078
64.0	0.20	1.03	0.057

REFERENCES

CHAPTER I.

[1]   J.H. Brewer, K.M. Crowe, F.N. Gygax and A. Schenck, in <u>Muon Physics</u>, Vol. III, Chapter 7, edited by V.W. Hughes and C.S. Wu, (Academic Press, New York, 1975).

[2]   A. Schenck, in <u>Nuclear and Particle Physics at Intermediate Energies</u>, edited by J.B. Warren, (Plenum, New York, 1976).

[3]   J.H. Brewer and K.M. Crowe, Ann. Rev. Nucl. Part. Sci. $\underline{28}$, 239 (1978).

[4]   C.C Anderson and S.H. Neddermeyer, Phys. Rev. $\underline{51}$, 884 (1937).

[5]   J.C. Street and E.C. Stevenson, Phys. Rev. $\underline{52}$, 1003 (1937).

[6]   E. Segré, <u>Nuclei and Particles</u>, 2nd Edition, Chapter 14, (W.A. Benjamin Publishers, Massuchusettes, 1977).

[7]   K.L. Giovanetti, W. Dey, M. Eckhause, R.D. Hart, R. Hartmann, D.W. Hertzog, J.R. Kane, W.A. Orance, W.C. Phillips, W.F. Vulcan, R.E. Welsh and R.G. Winter, Phys. Rev. D, $\underline{29}$, 343 (1984).

[8]   E. Segré, <u>Nuclei and Particles</u>, 2nd Edition, Chapter 2, (W.A. Benjamin Publishers, Massuchusettes, 1977).

[9]   G. Wentzel, Phys. Rev., $\underline{75}$, 1810 (1949).

[10] G.W. Ford and C.J. Mullin, Phys, Rev. $\underline{108}$, 477 (1957).

[11] R.E. Turner, Phys. Rev. A $\underline{28}$, 3300 (1983).

[12] R.E. Turner and M. Senba, Phys. Rev. A $\underline{29}$, 2541 (1984).

[13] H.S.W Massey and E.H.S. Burhop, in <u>Electronic and Ionic Impact Phenomena</u>, Chapter VIII, (Oxford University Press, Clarendon, London and New York, 1952).

[14] V.W. Hughes, D.W. McColm, K. Ziock and R, Prepost, Phys. Rev. Lett. $\underline{5}$, 63 (1960).

[15] V.I. Goldanskii and V.G. Firsov, Ann. Rev. Phys. Chem. $\underline{22}$, 209 (1971).

[16] Y.C. Jean, J.H. Brewer, D.G. Fleming, D.M. Garner, R.J. Mikula, L.C. Vaz and D.C. Walker, Chem Phys. Lett. $\underline{57}$, 293 (1978).

[17] G. Breit and I.I. Rabi, Phys. Rev. $\underline{38}$, 2082 (1931).

[18] D.E. Casperson, T.W. Crane, A.B. Denison, P.O. Egan, V.W. Hughes, F.G. Mariam, H. Orth, H.W. Reist, P.A. Souder, R.D. Stambaugh, P.A. Thompson and G. zu Putlitz, Phys. Rev. Lett. 38, 956 (1977).

[19] V.G. Nosov and I.V. Yakovleva, JETP 16, 1236 (1963).

[20] I.G. Ivanter and V.P. Smilga, JETP 33, 1070 (1971).

[21] C.P. Slichter, Principles of Magnetic Resonance, 2nd Edition, Chapter 5, (Springer-Verlag, Berlin, Heidelberg, New York, 1980).

[22] C.P. Slichter, Principles of Magnetic Resonance, 2nd Edition, Chapter 3, (Springer-Verlag, Berlin, Heidelberg, New York, 1980).

[23] J.H. Brewer, D.S. Beder and D.P. Spencer, Phys. Rev. Lett. 42, 808 (1979).

[24] J.H. Brewer and D.P. Spencer, Hyperfine Interactions 6, 181 (1979).

[25] J.H. Brewer, D.G. Fleming and D.P. Spencer, in Nuclear and Electronic Resonance Spectroscopies Applied to Materials Science, edited by Kaufman and Shenoy, 487 (Elveier North Holland, 1981).

[26] J.H. Brewer, Hyperfine Interactions 8, 375 (1981).

[27] J.H. Brewer, D.P. Spencer, D.G. Fleming and J.A.R. Coope, Hyperfine Interactions 8, 405 (1981).

[28] W. Brandt and R. Paulin, Phys. Rev. Lett. 21, 193 (1968).

[29] R.F. Kiefl and D.R. Harshman, Phys. Lett. 98A, 447 (1983).

[30] G.M. Marshall, J.B. Warren, D.M. Garner, G.S. Clark, J.H. Brewer and D.G. Fleming, Phys. Lett. 65A, 351 (1978).

[31] J.H. Brewer et al., μSR Newsletter 12, 248, (1977), UCID-3857, Technical Information Division, LBL, Berkeley, CA.

[32] R.F. Kiefl, J.B. Warren, G.M. Marshall, C.J. Oram, J.H. Brewer, D.J. Judd and L.D. Spires, Hyperfine Interactions 6, 185 (1979).

[33] R.F. Kiefl, Ph.D. Thesis, University of British Columbia (1982).

[34] R.F. Kiefl, J.B. Warren, C.J. Oram, G.M. Marshall, J.H. Brewer, D.R. Harshman and C.W. Clawson, Phys. Rev. B 26, 2432 (1982).

[35] K.F. Canter, A.P. Mills, Jr. and S. Berko, Phys. Rev. Lett. 33, 7 (1974).

[36] O.E. Mogensen, J. Chem. Phys. 60, 998 (1974).

[37] Y. Ito and Y. Tabata, Proc. of the 5th International Conf. on Positron Annihilation, 325 (1979).

[38] Y. Ito, B.W. Ng, Y.C. Jean and D.C. Walker, Hyperfine Interactions 8, 355 (1981).

[39] E. Roduner, SIN, Private Communication.

[40] P.W. Percival, E. Roduner and H. Fischer, Chem. Phys. 32, 353 (1978).

[41] R.F. Kiefl, TRIUMF, Private Communication.

[42] Cab-O-Sil Properties and Functions, Cabot Corporation Technical Report (Cabot Corporation, Boston MA).

[43] A.V. Kiselev and V.I. Lygin, Infrared Spectra of Surface Componds (Wiley, New York, 1975).

[44] A.P. Mills and W.S. Crane, Phys. Rev. Lett. 53, 2165 (1984).

[45] K.F. Canter, P.G. Coleman, T.C. Griffith and G.R. Heyland, J. Phys. B 5, L167 (1972).

[46] A.P. Mills, Bell Laboratories, Private Communication.

[47] R. Paulin and G. Ambrosino, J. Physique 29, 263 (1968).

[48] R.F. Kiefl, Hyperfine Interactions 8, 359 (1981).

[49] A. Schmidt-Ott, P. Schurtenberger and H.C. Siegmann, Phys. Rev. Lett. 45, 1284 (1980).

[50] B.D. Perlson and J.A. Weil, J. Mag. Res. 15, 594 (1974).

[51] J.C. King and H.H. Sander, Radiation Effects 26, (1975).

[52] A. Sosin, Radiation Effects 26, 267 (1975).

[53] V.B. Kazanskii and G.B. Pariiskii, Kinet. Katal. 2, 4 (1961).

[54] V.B. Kazanskii and G.B. Pariiskii, Kinet. Katal. 2, 507 (1961).

[55] N. Papp and K.P. Lee, J. Magnetic Resonance 19, 245 (1975).

[56] C. Schwartz, Ann. Phys. (N.Y.) 6, 156 (1959).

[57] P.G.H. Sandars, Proc. Phys. Soc. 92, 857 (1967).

[58] B.J. Finlayson-Pitts, J. Phys. Chem. 86, 3499 (1982).

CHAPTER II

[1]   J.R. Richardson, Nucl. Instrum. and Methods $\underline{24}$, 493 (1963).

[2]   J.B. Warren, Proc. 5th International Cyclotron Conf., edited by R.W. McIlroy, 73 (1969).

[3]   J.B. Warren, in High Energy Physics and Nuclear Structure, 566 (Plenum Press, 1970).

[4]   TRIUMF Annual Reports (1972-1976).

[5]   J.R. Richardson, IEEE Trans. on Nucl. Sci. $\underline{NS-20}$, 207 (1973).

[6]   J.R. Richardson and M.K. Craddock, Proc. 5th International Cyclotron Conf., edited by R.W. McIlroy, 85 (1969).

[7]   R. Baartman, E.W. Blackmore, J. Carey, D. Dohan, G. Dutto, D. Gurd, R.W. Laxdal, G.H. Mackenzie, D. Pearce, R. Poirier and P.W. Schmor, 10th International Conference on Cyclotrons and Their Applications (1984).

[8]   L.P. Robertson, E.G. Auld, G.H. Mackenzie and A. Otter, Proc. 5th International Cyclotron Conf., edited by R.W. McIlroy, 245 (1969).

[9]   C.J. Oram, J.B. Warren, G.M. Marshall and J. Doornbos, Nucl. Instrum. and Methods $\underline{179}$, 95 (1981).

[10] N.M.M. Al-Quazzaz, G.A. Beer, G.R. Mason, A. Olin, R.M. Pearce, D.A. Bryman, J.A. MacDonald, J.-M. Poutissou, P.A. Reeve, M.D. Hasinoff and T. Suzuki, Nucl. Instrum. and Methods $\underline{174}$, 35 (1980).

[11] J.L. Beveridge, TRIUMF, Private Communication.

[12] A.E. Pifer, T. Bowen and K.R. Kendall, Nucl. Instrum. and Methods $\underline{135}$, 35 (1976).

[13] W.P. Trower, Range-Momentum and dP/dx Plots of Charged Particles in Matter, LBL Report No. UCRL-2426, $\underline{4}$, (1966).

[14] R.M. Sternheimer, Phys. Rev. $\underline{117}$, 485 (1960).

[15] A.P. Mills, Jr. and W.S. Crane, Phys. Rev. Lett. $\underline{53}$, 2165 (1984).

[16] J.H. Brewer, K.M. Crowe, F.N. Gygax and A. Schenck, in Muon Physics, Vol. III, Chapter 7, edited by V.W. Hughes and C.S. Wu, (Academic Press, New York, 1975).

[17] J.H. Brewer and K.M. Crowe, Ann. Rev. Nucl. Sci. $\underline{28}$, 240 (1978).

[18] A. Schenck, in Nuclear and Particle Physics at Intermediate Energies, edited by J.B. Warren, (Plenum, New York, 1976).

[19] D.M. Garner, Ph.D. Thesis, University of British Columbia (1979).

[20] Cab-O-Sil Properties and Functions, Cabot Corporation Technical Report (Cabot Corporation, Boston MA).

[21] G.M. Marshall, J.B. Warren, D.M. Garner, G.S. Clark, J.H. Brewer and D.G. Fleming, Phys. Lett. 65A, 351 (1978).

[22] R.F. Kiefl, Ph.D. Thesis, University of British Columbia (1981).

[23] R.F. Kiefl, J.B. Warren, C.J. Oram, G.M. Marshall, J.H. Brewer, D.R. Harshman and C.W. Clawson, Phys. Rev. B 28, 2432 (1982).

[24] B.J. Finlayson-Pitts, J. Phys. Chem. 86, 3499 (1982).

[25] A.V. Kiselev and V.I. Lygin, Infrared Spectra of Surface Compounds, (Wiley, New York, 1975).

[26] L.H. Little, Infrared Spectra of Adsorbed Species, (Academic Press, New York, 1966).

[27] H.A. Benesi, R.M. Curtis and H.P. Studer, J. Catal. 10, 328 (1968).

[28] S. Brunauer, P.H. Emmett and E. Teller, J. Am. Chem. Soc. 60, 309 (1938).

[29] J.E. Benson and M. Boudart, J. Catal. 4, 704 (1965).

[30] J. Stewart, TRIUMF Fortran Source Code "KELVIN" (1982).

[31] Available from the Cern Program Library, Division DD, Cern, CH-1211, Geneva 23, Switzerland.

CHAPTER III

[1] R. Kubo and T. Toyabe, in Magnetic Resonance and Relaxation, edited by R. Blinc, (North-Holland, Amsterdam, 1967).

[2] T. Toyabe, M.Sc. Thesis, University of Tokyo, 1966.

[3] C.P. Slichter, Principles of Magnetic Resonance, 2nd Edition, Chapter 3, (Springer-Verlag, Berlin, Heidelberg, New York, 1980.

[4] R.S. Hayano, Y.J. Uemura, J. Imazato, T. Yamazaki and R. Kubo, Phys. Rev. B 20, 850 (1979).

[5] R.E. Walstedt and L.R. Walker, Phys. Rev. B 9, 4857 (1974).

[6] C. Held and M. Klein, Phys. Rev. Lett. 35, 1783 (1975).

[7] L.R. Walker and R.E. Walstedt, Phys. Rev. B 22, 3816 (1980).

[8] R. Kubo, Hyperfine Interactions 8, 731 (1981).

[9] E. Holzschuh and P.F. Meier, Phys. Rev. B 29, 1129 (1984).

[10] P.F. Meier, Hyperfine Interactions 17-19, 427 (1984).

[11] M. Celio and P.F. Meier, Hyperfine Interactions 17-19, 435 (1984).

[12] D.R. Harshman, R. Keitel and M. Celio, (in preparation).

[13] J.H. Brewer, Hyperfine Interactions 8, 375 (1981).

[14] V.W. Hughes, Ann. Rev. Nucl. Sci. 16, 445 (1966).

[15] R.M. Mobley, J.J. Amato, V.W. Hughes, J.E. Rothberg and P.A. Thompson, J. Chem. Phys. 47, 3074 (1967).

[16] R.J. Mikula, D.M. Garner and D.G. Fleming, J. Chem. Phys. 75, 5362 (1981).

[17] R. Beck, P.F. Meier and A. Schenck, Z. Phys. B 22, 109 (1975).

[18] R. Kubo and K. Tomita, J. Phys. Soc. Japan 9, 888 (1954).

[19] R. Kubo, J. Phys. Soc. Japan 9, 935 (1954).

[20] K.W. Kehr, G. Honig and D. Richter, Z. Phys. B 32, 49 (1978).

[21] P. Albrecht and G. Honig, Informatik 8, 336 (1977).

[22] G. Honig, Ph.D. Thesis, Universität of Dortmund (1978).

[23] M. Borghini, T.O. Niinikoski, J.C. Soulié, O. Hartmann, E. Karlsson, L.O. Norlin, K. Pernestal, K.W. Kehr, D. Richter and E. Walker, Phys. Rev. Lett. 40, 1723 (1978).

[24] W.J. Kossler, A.T. Fiory, W.F. Lankford, J. Lindemuth, K.G. Lynn, S. Mahajan, K.G. Petzinger and C.E. Stronach, Phys. Rev. Lett. 41 1558 (1978).

[25] T. McMullen and E. Zaremba, Phys. Rev. B 18, 3026 (1978).

[26] K.G. Petzinger, Hyperfine Interactions 6, 223 (1979).

[27] K.G. Petzinger, Hyperfine Interactions 8, 639 (1981).

[28] A.T. Fiory, Hyperfine Interactions 6, 261 (1979).

CHAPTER IV

[1]   G.M. Marshall, J.B. Warren, D.M. Garner, G.S. Clark, J.H. Brewer and D.G. Fleming, Phys. Lett. 65A, 351 (1978).

[2]   R.F. Kiefl, Ph.D. Thesis, University of British Columbia (1982).

[3]   R.F. Kiefl, J.B. Warren, C.J. Oram, G.M. Marshall, J.H. Brewer, D.R. Harshman and C.W. Clawson, Phys. Rev. B 26, 2432 (1982).

[4]   Cab-O-Sil Properties and Functions, Cabot Corporation Technical Report (Cabot Corporation, Boston MA).

[5]   R.F. Kiefl, B.D. Patterson, E. Holzschuh, W. Odermatt and D.R. Harshman, Hyperfine Interactions 17-19, 563 (1984).

[6]   D.R. Harshman, R. Keitel, M. Senba, E.J. Ansaldo and J.H. Brewer, Hyperfine Interactions 17-19, 557 (1984).

[7]   D.R. Harshman, R. Keitel, M. Senba, R.F. Kiefl, E.J. Ansaldo and J.H. Brewer, Phys. Lett. 104A, 472 (1984).

[8]   T. McMullen and E. Zaremba, Phys. Rev. B 18, 3026 (1978).

[9]   K.G. Petzinger, Hyperfine Interactions 6, 223 (1979).

[10] K.G. Petzinger, Hyperfine Interactions 8, 639 (1981).

[11] Cab-O-Sil Properties and Functions, Cabot Corporation Technical Report (Cabot Corporation, Boston Mass.).

[12] R.F. Marzke, Arizona State Univ., Private Communication.

[13] H.A. Benesi, R.M. Curtis and H.P. Studer, J. Catal. 10, 328 (1968)

[14] S. Ladas, R.A. Dalla Betta and M. Boudart, J. Catal. 53, 356 (1978).

[15] K.M. Sancier and S.H. Inami, J. Catal. 11, 135 (1968).

CHAPTER V

[1]   D.R. Harshman, R. Keitel, M. Senba, E.J. Ansaldo and J.H. Brewer, Hyperfine Interactions 17-19, 557 (1984).

[2]   D.R. Harshman, R. Keitel, M. Senba, R.F. Kiefl, E.J. Ansaldo and J.H. Brewer, Phys. Lett. 104A, 472 (1984).

[3] L. Anthony, Bell Laboratories, Private Communication.

[4] R. Kubo, J. Phys. Soc. Japan $\underline{9}$, 935 (1954).

[5] A.P. Mills, Jr. and W.S. Crane, Phys. Rev. Lett. $\underline{53}$, 2165 (1984).

APPENDIX I

[1] A. Messiah, Quantum Mechanics, Vol. 2, (Wiley and Sons, New York, 1958).

[2] R.E. Turner, accepted for publication in Hyperfine Interactions.

[3] R.E. Turner, Phys. Rev. B $\underline{31}$, 112 (1985).

[4] J.H. Brewer, K.M. Crowe, F.N. Gygax and A. Schenck, in Muon Physics, Vol. III, Chapter 7, edited by V.W. Hughes and C.S. Wu, (Academic Press, New York, 1975).

[5] J.H. Brewer and K.M. Crowe, Ann. Rev. Part. Sci. $\underline{28}$, 239 (1978).

[6] A. Schenck, in Nuclear and Particle Physics at Intermediate Energies, edited by J.B. Warren, (Plenum, New York, 1976).

[7] D.P. Spencer, Ph.D. Thesis, University of British Columbia (1985).

[8] A. Hinterman, P.F. Meier and B.D. Patterson, Am. J. Phys. $\underline{48}$, 956 (1980).

APPENDIX II

[1] A.P. Mills, Jr., S. Berko and K.F. Canter, in Atomic Physics, Vol. 5, edited by R. Marrus, M. Prior and H. Shugart, (Plenum, New York, 1977).

[2] T.C. Griffith and G.R. Heyland, Physics Reports $\underline{39}$, 169 (1978).

[3] S. Berko and H.N. Pendleton, Ann. Rev. Nucl. Part. Sci. $\underline{30}$, 543 (1980).

[4] A.P. Mills, Jr., Science $\underline{218}$, 335 (1982).

[5] Carl Rau, J. Magnetism and Magnetic Materials $\underline{30}$, 141 (1982).

[6] D.G. Fleming, et al., Chem. Phys. $\underline{82}$, 75 (1983).

[7] C.J. Oram, J.M. Bailey, P.W. Schmor, C.A. Fry, R.F. Kiefl, J.B. Warren, G.M. Marshall and A. Olin, Phys. Rev. Lett. $\underline{52}$, 910 (1984).

[8]   W. Brandt and R. Paulin, Phys. Rev. B 15, 2511 (1977).

[9]   A.P. Mills, Jr. and W.S. Crane, Phys. Rev. Lett. 53, 2165 (1984).

[10] K.F. Canter, P.G. Coleman, T.C. Griffith and G.R. Heyland, J. Phys. B 5, L167 (1972).

[11] G.M. Marshall, J.B. Warren, D.M. Garner, G.S. Clark, J.H. Brewer and D.G Fleming, Phys. Lett. 65A, 351 (1978).

[12] R. Paulin and G. Ambrosino, J. Physique 29, 263 (1968).

[13] G.G. Myasishcheva, Yu.V. Obukhov, V.S. Roganov, L.Ya. Suvorov and V.G. Firsov, Soviet High Energy Chemistry 3, 460 (1969).

[14] E.V. Minaichev, G.G. Myasishcheva, Yu.V. Obukhov, V.S. Roganov, G.I. Savel'ev and V.G. Firsov, Soviet Physics JETP 30, 230 (1970).

[15] A.B. Kunz, in Elementary Excitations in Solids, Molecules and Atoms, Part B, edited by J.T. Devreese, A.B. Kunz and T.C. Collins, 343 (Plenum, London, 1974).

[16] S. Chandrasekhar, Rev. Mod. Phys. 15, 1 (1943).

[17] G.M. Marshall, Ph.D. Thesis, University of British Columbia (1981).

[18] D.R. Harshman, J.B. Warren, J.L. Beveridge, K.R. Kendall, R.F. Kiefl, C.J. Oram, A.P. Mills. Jr., W.S. Crane, A.S. Rupaal and J.H. Turner, (submitted to Phys. Rev. Lett.).

Papers Published in Refereed Journals

Surface Interactions of Muonium in Oxide Powders at Low Temperatures, R.F. Kiefl, J.B. Warren, C.J. Oram, G.M. Marshall, J.H. Brewer, D.R. Harshman, and C.W. Clawson, Physical Review B 26, 2432 (1982).

Giant Muon Knight Shifts in Antimony and Antimony Alloys, J.H. Brewer, D.R. Harshman, E. Koster, H. Schilling, D.Ll. Williams and M.G. Priestly, Solid State Communications 46, 863 (1983).

Positronium in SiO$_2$ Powder at Low Temperature, R.F. Kiefl and D.R. Harshman, Physics Letters 98A, 447 (1983).

Zero-Field Muon-Spin Relaxation in CuMn Spin-Glasses Compared With Neutron and Susceptibility Measurements, Y.J. Uemura, D.R. Harshman, M. Senba, E.J. Ansaldo and A.P. Murani, Physical Review B (Rap. Comm.) 30, 1606 (1984).

Diffusion and Trapping of Muonium on Silica Surfaces, D.R. Harshman, R. Keitel, M. Senba, R.F. Kiefl, E.J. Ansaldo and J.H. Brewer, Phys. Lett. 104A, 472 (1984).

Muon Spin Relaxation in AuFe and CuMn Spin Glasses, Y.J. Uemura, T. Yamazaki, D.R. Harshman, M. Senba and E.J. Ansaldo, Phys. Rev. B 31, 546 (1985).

Study of the Hybrid State of Y$_9$Co$_7$ (2 < T < 6 K) by Means of Zero Field Muon Spin Relaxation, E.J. Ansaldo, D.R. Noakes, J.H. Brewer, R. Keitel, D.R. Harshman, M. Senba, C.Y. Huang and B.V.B. Sarkissian, Solid State Communications 55, 193 (1985).

Level-Crossing Resonance Muon Spin Relaxation in Copper, S.R. Kreitzman, J.H. Brewer, D.R. Harshman, R. Keitel, D.Ll. Williams and E.J. Ansaldo, (accepted for publication in Phys. Rev. Lett.).

MSR Measurement of the Reaction Rate of Muonium with a Supported Platinum Catalyst, R.F. Marzke, W.S. Glaunsinger, D.R. Harshman, J.H. Brewer, R. Keitel, M. Senba, E.J. Ansaldo, D.P. Spencer and D.R. Noakes, (accepted for publication in Chem. Phys. Lett.).

Observation of Muon-Fluorine "Hydrogen Bonding" in Ionic Crystals, J.H. Brewer, S.R. Kreitzman, D.R. Noakes, E.J. Ansaldo, D.R. Harshman and R. Keitel, (submitted to Phys. Rev. B, rapid communications).

Anisotropic Muonium With Random Hyperfine Anisotropies: A New Static Relaxation Theory, R.E. Turner and D.R. Harshman, (sub. to Phys. Rev. B.)

Observation of Low Energy μ+ Emission from Solid Surfaces, D.R. Harshman, J.B. Warren, J.L. Beveridge, K.R. Kendall, R.F. Kiefl, C.J. Oram, A.P. Mills, Jr., W.S. Crane, A.S. Rupaal and J.H. Turner, (submitted to Phys. Rev. Lett.).

Conference Proceedings (Refereed)

Muonium in Al_2O_3 Powder at Low Temperatures, R.F. Kiefl, J.B. Warren, C.J. Oram, J.H. Brewer and D.R. Harshman, in Positron Annihilation, edited by P.G. Coleman, S.C. Sharma and L.M. Diana, 693 (North-Holland Publishing Company, 1983).

Magnetic Susceptibility, Proton NMR and Muon Spin Rotation (μSR) Studies of an Unsupported Platinum Catalyst with Adsorbed H and O, R.F. Marzke, W.S. Glaunsinger, K.B. Rawlings, P. Van Rheenen, M. McKelvy, J.H. Brewer, D.R. Harshman and R.F. Kiefl, in Electronic Structure and Properties of Hydrogen in Metals, edited by P. Jena and C.B. Satterthwaite, (Plenum Publishing Corporation, 1983).

Dynamical Behavior of Muonium on Silica Surfaces, D.R. Harshman, R. Keitel, M. Senba, E.J. Ansaldo and J.H. Brewer, Hyperfine Interactions 17-19, 557 (1984).

Hyperfine Splitting of Muonium in SiO_2 Powder, R.F. Kiefl, B.D. Patterson, E. Holzschuh, W. Odermatt and D.R. Harshman, Hyperfine Interactions 17-19, 563 (1984).

Zero-Field μSR in a Spin Glass CuMn (1.1 at. %): Precise Measurement of Static and Dynamic Effects Below T_g, Y.J. Uemura, T. Yamazaki, D.R. Harshman, M. Senba, J.H. Brewer, E.J. Ansaldo and R. Keitel, Hyperfine Interactions 17-19, 453 (1984).

μ^+SR Study of Some Magnetic Superconductors, C.Y. Huang, E.J. Ansaldo, J.H. Brewer, D.R. Harshman, K.M. Crowe, S.S. Rosenblum, C.W. Clawson, Z. Fisk, S. Lambert, M.S. Torikachvili and M.B. Maple, Hyperfine Interactions 17-19, 509 (1984).

Positive Muon Knight Shift in Graphite and Grafoil, F.N. Gygax, A. Hintermann, A. Schenck, W. Studer, A.J. van der Wal, J.H. Brewer and D.R. Harshman, Hyperfine Interactions 17-19, 383 (1984).

Positive Muons in Antimony Bismuth Alloys, F.N. Gygax, A. Hintermann, A. Schenck, W. Studer, A.J. van der Wal, J.H. Brewer, D.R. Harshman, E. Koster, H. Schilling, D.Ll. Williams and M.G. Priestly, Hyperfine Interactions 17-19, 387 (1984).

Muon Spin Relaxation in $ErRh_4B_4$, D.R. Noakes, E.J. Ansaldo, J.H. Brewer, D.R. Harshman, C.Y. Huang, M.S. Torikachvili, S.E. Lambert and M.B. Maple, J. Appl. Phys. 57, 3197 (1985).

Muonium on Surfaces, D.R. Harshman, (Invited Paper), Proceedings of the European Workshop on the Spectroscopy of Sub-Atomic Species in Non-Metallic Solids, 3-7 Sept. 1985, Vitry-sur-Seine, France, (in preparation).

Papers Published in Unrefereed Journals

Study of the Hybrid State of Y_9Co_7 (2 < T < 6K) by means of Zero Field Muon Spin Relaxation, E.J. Ansaldo, D.R. Noakes, J.H. Brewer, R. Keitel, D.R. Harshman, M. Senba, C.Y. Huang and B.V.B. Sarkissian, μSR-Newsletter 30, 1661 (1984).

LF-μSR Quadrupolar Level Crossing Resonance in Copper at 20K, S.R. Kreitzman, J.H. Brewer, D.R. Harshman, R. Keitel, D.Ll. Williams, K.M. Crowe and E.J. Ansaldo, μSR-Newsletter 30, 1675 (1984).

Observation of Muon-Fluorine "Hydrogen" Bonding in Ionic Crystals, J.H. Brewer, S.R. Kreitzman, D.R. Noakes, E.J. Ansaldo, D.R. Harshman and R. Keitel, μSR-Newsletter 31, 1747 (1985).

Abstracts

Positive Muon Spin Rotation in Magnetic-Superconducting $SmRh_4B_4$, C.Y. Huang, Z. Fisk, C.W. Clawson, K.M. Crowe, S.S. Rosenblum, J.H. Brewer, D.R. Harshman, S.E. Lambert, M.S. Torikachvili and M.B. Maple, APS Meeting, Dallas, Texas, USA, March 1982.

Magnetic Susceptibility, Proton NMR and Muon Spin Rotation (μSR) Studies of Unsupported Platinum Catalysts with Adsorbed H and O, R.F. Marzke, W.S. Glaunsinger, K.B. Rawlings, P. Van Rheenan, M. McKelvy, J.H. Brewer, D.R. Harshman and R.F. Kiefl, APS Meeting, Dallas, Texas, USA, March 1982.

Muonium on Bare Silica Surfaces, D.R. Harshman, R.F. Kiefl and J.H. Brewer, Western Regional Nuclear Physics Conference, Banff, Alberta, Canada, February 1982.

Muonium on Bare Silica Surfaces, D.R. Harshman, R. Keitel, R.F. Kiefl, M. Senba and J.H. Brewer, 2'nd Trieste International Symposium on Statistical Mechanics of Adsorption, Trieste, Italy, July 1982.

Observation of H NMR and of Muon Spin Rotation in Unsupported Platinum, R.F. Marzke, W.S. Glaunsinger, K.B. Rawlings, P. Van Reenen, M. McKelvy, J.H. Brewer, D.R. Harshman and R.F. Kiefl, California Catalysis Society, Annual Fall Meeting, Irvine, California, USA, October 1982.

Behavior of Muonium on Silica Surfaces, D.R. Harshman, J.H. Brewer, M. Senba, R. Keitel and E.J. Ansaldo, CAP Meeting, University of Victoria, Victoria, B.C., Canada, June 1983.

Spin Relaxation in YRh_4B_4 and $SmRh_4B_4$, E.J. Ansaldo, D.R. Harshman, J.H. Brewer, C.Y. Huang, K.M. Crowe and S.S. Rosenblum, CAP Meeting, University of Victoria, B.C., Canada, June 1983.

Diffusion and Trapping of Muonium on Silica Surfaces, D.R. Harshman, J.H. Brewer, M. Senba, R. Keitel and E.J. Ansaldo, California Catalysis Society Annual Fall Meeting, Brea, California, USA, October 1983.

Muonium on Amorphous SiO$_2$ Surfaces, D.R. Harshman, J.H. Brewer, R. Keitel, M. Senba, J.M. Bailey and E.J. Ansaldo, CAP Meeting, Université de Sherbrooke, Sherbrooke, Quebec, Canada, June 1984.

Giant Muon Knight Shifts in Antimony Alloys, J.H. Brewer, D.R. Harshman, E. Koster, S.R. Kreitzman and D.Ll. Williams, CAP Meeting, Université de Sherbrooke, Sherbrooke, Quebec, Canada, June 1984.

Muon Spin Relaxation and Crystalline Electric Field Effects in RERh$_4$B$_4$, R.R. Noakes, E.J. Ansaldo, J.H. Brewer, C.Y. Huang and D.R. Harshman, CAP Meeting, Université de Sherbrooke, Sherbrooke, Quebec, Canada, June 1984.

Muonium Diffusion on Amorphous SiO$_2$ Surfaces, D.R. Harshman, J.H. Brewer, R. Keitel, M. Senba, J.M. Bailey and E.J. Ansaldo, International Chemical Congress of Pacific Basin Societies, Honolulu, Hawaii, USA, December 1984.

Measurement of the Reaction Rate of Muonium with the Surface of a Supported Platinum Catalyst by Muonium Spin Rotation (MSR), R.F. Marzke, W.S., Glaunsinger, D.R. Harshman, E.J. Ansaldo, R. Keitel, D.R. Noakes, M. Senba and J.H. Brewer, APS Meeting, Baltimore, Maryland, USA, March 1985.

Measurement of the Reaction Rate of Muonium with the Surface of a Supported Platinum Catalyst by Muonium Spin Rotation (MSR), R.F. Marzke, W.S. Glaunsinger, D.R. Harshman, E.J. Ansaldo, R. Keitel, D.R. Noakes, M. Senba and J.H. Brewer, California Catalysis Society Annual Spring Meeting, Menlo Park, California, USA, April 1985.

Special Oral Presentations (Invited Talks)

Muonium on Silica Surfaces, D.R. Harshman, Invited Talk, µSR Journal Seminar, Dept. of Physics, Univ. of California at Berkeley, Berkeley, Ca., USA, 16 February 1983.

Behavior of Muonium on SiO$_2$ Surfaces, D.R. Harshman, Invited Talk, Solid State Seminar, Department of Physics, The Univ. of British Columbia, Vancouver, B.C., Canada, 28 February 1985.

Muonium on Silica Surfaces, D.R. Harshman, Invited Talk, presented at AT&T-Bell Laboratories, Murray Hill, New Jersey, USA, 4 April 1985.

The Interaction of Muonium With Silica Surfaces, D.R. Harshman, Invited Talk, Physics-Astronomy Seminar, Department of Physics, Western Washington University, Bellingham, Washington, USA, 15 May 1985.

Muonium on Surfaces, D.R. Harshman, Invited Talk, European Workshop on the Spectroscopy of Sub-Atomic Species in Non-Metallic Solids, 3-7 Sept. 1985, Vitry-sur-Seine, France.

The Interactions of Muonium with Surfaces, D.R. Harshman, Invited Talk, presented at Lawrence Livermore National Laboratory, Livermore, California, USA, 21 October 1985.